The effects of electronic quenching on the collision dynamics of OH(A) with Kr and Xe

A thesis submitted for the degree of Doctor of Philosophy

Tom Perkins

New College, University of Oxford

Hilary Term, 2014

The effects of electronic quenching on the collision dynamics of OH(A) with Kr and Xe

Tom Perkins, New College
A thesis submitted for the degree of Doctor of Philosophy
Hilary Term, 2014

Abstract

This thesis presents an experimental and theoretical study of the collision dynamics of $OH(A^2\Sigma^+)$ with Kr and Xe. These two systems both exhibit a significant degree of electronically non-adiabatic behaviour, and a particular emphasis of the work presented here is to characterise the competition and interplay between electronic quenching on the one hand, and electronically adiabatic collisional processes on the other. Quenching takes place close to the bottom of the deepest potential well for both systems. In collisions that remain in the excited electronic state, this same region of the potential is also largely responsible for rotational energy transfer (RET) and the collisional depolarisation of angular momentum. Therefore, the direct competition between these processes suppresses the cross-sections for RET and collisional depolarisation from their expected value in the absence of quenching.

To investigate this, experiments were carried out to measure cross-sections for the collisional transfer of electronic, vibrational and rotational energy in OH(A, $v = 0, 1$) + Kr and OH(A, $v = 0$) + Xe. In addition, measurements were made of the $\boldsymbol{j} - \boldsymbol{j'}$ correlation – that is, the relationship between the angular momentum of the OH radical before and after a collision – in collisions with Kr and Xe, using the experimental technique of *Zeeman quantum beat spectroscopy*. Collisions with both Kr and Xe tend to effectively depolarise the angular momentum of the OH radical, due to the very anisotropic character of the potential on which the process occurs. Electronic quenching, which plays an essential role in both systems, is more prevalent with xenon as the crossing to the ground state potential is located in a more accessible location.

These experimental results were compared with single surface quasi-classical trajectory (QCT) calculations, where the overestimate of rotational energy transfer or collisional depolarisation helps to elucidate the degree to which the presence of quenching suppresses these processes. Surface hopping QCT was then used to account for non-adiabatic transitions in the theory, which led to an improvement in agreement with experiment. However, standard surface hopping QCT theory failed to account for the full extent of quenching in these two systems.

A major focus of this work is therefore on the development of an extension to standard surface hopping QCT theory to incorporate rovibronic couplings. In non-linear configurations, the excited state of the OH + Kr, Xe systems has A' symmetry, while the ground state is split into symmetric (A') and antisymmetric (A'') components. For these symmetry reasons, coupling is restricted to the two states of the same symmetry, however a rotation of the correct (A'') symmetry can induce transitions to the A'' state too. Inclusion of all three electronic states, and the relevant couplings between them, is found to be crucial for a proper description of experimental reality.

Publications

1. Molecular photofragment orientation in the photodissociation of H_2O_2 at 193 nm and 248 nm.

Y.-P. Chang, M. Brouard, R. Cireasa, T. Perkins and S. A. Seamons, *Phys. Chem. Chem. Phys.*, **13**, 8213, (2011).

2. A new potential energy surface for OH(A)-Kr: The van der Waals complex and inelastic scattering.

H. Chadwick, M. Brouard, Y.-P. Chang, C. J. Eyles, T. Perkins, S. A. Seamons, J. Kłos, M. H. Alexander and F. J. Aoiz, *J. Chem. Phys.*, **137**, 154305, (2012).

3. Electronic Quenching of OH $A^2\Sigma^+$ Induced by Collisions with Kr Atoms.

J. H. Lehman, M. I. Lester, J. Kłos, M. H. Alexander, P. J. Dagdigian, D. Herráez-Aguilar, F. J. Aoiz, M. Brouard, H. Chadwick, T. Perkins and S. A. Seamons, *J. Phys. Chem. A*, **117**, 13481, (2013).

4. The collisional depolarization of OH($A^2\Sigma^+$) and NO($A^2\Sigma^+$) with Kr.

H. Chadwick, M. Brouard, Y.-P. Chang, C. J. Eyles, G. McCrudden, T. Perkins, S. A. Seamons, J. Kłos, M. H. Alexander, P. J. Dagdigian, D. Herráez-Aguilar and F. J. Aoiz, *J. Chem. Phys.*, **140**, 054306, (2014).

5. Collisional depolarisation in electronically excited radicals.

H. Chadwick, M. Brouard, T. Perkins and F. J. Aoiz, *Int. Rev. Phys. Chem.*, **33**, 79, (2014).

6. Surface-hopping QCT of OH($A^2\Sigma^+$) + Kr: extension to the $1A''$ state.

T. Perkins, D. Herráez-Aguilar, M. Brouard, G. McCrudden, F. J. Aoiz and J. Kłos, in preparation (2014).

7. Experimental and quasi-classical trajectory studies of OH($A^2\Sigma^+$) + H_2: rotational energy transfer and collisional depolarization.

M. Brouard, H. Chadwick, J. Lawlor, T. Perkins, S. A. Seamons, P. Stevenson, F. J. Aoiz and J. M. Bowman, in preparation (2014).

8. Potential energy surface and classical dynamics of rotational energy transfer in OH($A^2\Sigma^+$) + H_2.

M. Brouard, H. Chadwick, J. Lawlor, T. Perkins, S. A. Seamons, P. Stevenson, F. J. Aoiz, J. M. Bowman *et al.*, in preparation (2014).

9. *OH(A) + Xe PES paper*

J. Kłos, M. Brouard, G. McCrudden, T. Perkins, S. A. Seamons, F. J. Aoiz, D. Herráez-Aguilar and M. H. Alexander, in preparation (2014).

10. *OH(A) + Xe results paper, including OH(A, $v = 1$) + Kr*

M. Brouard, G. McCrudden, T. Perkins, S. A. Seamons, F. J. Aoiz, D. Herráez-Aguilar, M. H. Alexander and J. Kłos, in preparation (2014).

Acknowledgements

First of all, I would like to thank my supervisor, Prof. Mark Brouard, for his help, support, guidance, vision and advice over the past four years. Mark's endless enthusiasm and ability to keep his cool even in the face of experimental disaster have helped to make my time in research an enjoyable one, and he has always been available to answer questions or offer advice.

During my time in the Brouard group, it has been a pleasure and a privilege to work with some truly exceptional people. Special mention must of course go to, in roughly chronological order, D.Phil. students Chris Eyles, Yuan-Pin Chang, Helen Chadwick, Scott Seamons and Garreth McCrudden, and Part II students Paul Stevenson and John Lawlor, for all their help and assistance, both experimentally on the LIF rig and also with theory. I would also like to acknowledge the essential contributions of the other group members, past and present, to the smooth progress of the work in this thesis via all the tea, biscuits, cake and helpful discussions (in the pub or otherwise).

The theoretical work in this thesis on QCT and TSH-QCT calculations would not have been possible without the help of Prof. Javier Aoiz and Diego Herráez-Aguilar of the Universidad Complutense in Madrid, and I am very grateful to both for all their hard work, help and advice on this over the course of this project. In particular, I would like to thank Diego for providing the original two-state version of the surface hopping QCT code that was modified and extended to include rovibronic effects in the present work.

I would also like to thank Prof. Jacek Kłos and Prof. Millard Alexander (University of Maryland) and Prof. Paul Dagdigian (Johns Hopkins University) for calculating the potential energy surfaces and couplings used in this work, and also carrying out quantum scattering calculations. In addition, I am grateful to Prof. Marsha Lester and Julia Lehman (University of Pennsylvania) for their contribution to this stimulating collaboration in the form of experimental OH(X) product state distributions.

Experimental work is often a battle against Murphy's Law* and the less well-known Chadwick's Law,† and this thesis would be rather empty were it not for the efforts of all in Lab Services, Mechanical Workshops and the Electronics Workshop in the PTCL, and CRL Lab Services. Particular thanks go to Paul Mitchell for his help in fixing anything and everything that went wrong with the experiment, and John Adams for all his work on our temperamental excimer lasers.

The support of the Department of Chemistry through a Doctoral Training Award, and of New College, Oxford through a generous travel grant, is also gratefully acknowledged.

Finally, I would like to end by thanking my family and friends for their unwavering support over the past four years, and Ina for all her support, patience and everything else besides.

* "Everything that can go wrong, will"

† "It is a stupid experiment that refuses to work"

Contents

Chapter 1

Introduction

1.1 Motivation

The OH radical is the most important scavenging radical in the troposphere, generated from the reaction between $O(^1D)$ (from the photolysis of O_3) and H_2O.[1] It determines the atmospheric lifetime of methane via the reaction[1]

$$OH + CH_4 \rightarrow H_2O + CH_3 \tag{1.1}$$

and is one of the main oxidants present in the troposphere and lower stratosphere.[2] As well as this, OH radicals are implicated in stratospheric ozone destruction[3] and many other areas of atmospheric chemistry.[4] Energy transfer data, particularly rates, are therefore of great importance for accurate measurements of atmospheric OH, which feed into computer models of many processes.[2,4]

Apart from this, though, small open-shell radicals like OH act as a prototype for fundamental collision dynamics, and the conclusions drawn from studies of their behaviour can be brought to bear on larger and more complex problems. For example, studies of the collisions of OH radicals with rare gas atoms can give insight into OH + H_2 collisions,[5] which are crucial to the understanding of combustion processes. Nearly half a century of experience with techniques such as laser spectroscopy, ion imaging and molecular beams

permits exquisitely detailed measurements of nearly all observable aspects of a collision or half-collision.[6–8]

The interaction between two molecules – in this thesis, an OH radical in its first excited, $A^2\Sigma^+$ state and a krypton or xenon atom – is governed by the masses of the species involved, but also by the *potential energy surface* (PES).[7–10] This is a (hyper)surface which expresses the potential energy of interaction as a function of all the co-ordinates of the system (for example, bond lengths and angles). Detailed experimental studies of molecular collisions provide evidence for the positions and characters of wells, barriers and diverse other features of the PES on which the encounter takes place. In the case of small, triatomic systems such as those studied here, it is possible to compare these experimental results to dynamical calculations performed on *ab initio* theoretical PESs, something which quickly becomes impractical (without significant approximations) for larger systems. In this way, experiment and theory move forward in tandem, with data measured in the lab providing an exacting test of theory, and theoretical insights helping to rationalise and explain the dynamics observed experimentally.

The work in this thesis extends previous studies of OH(A) and NO(A) in collisions with lighter rare gases, such as in refs. 11–24, as well as studies of similar systems (such as NO(X), CN(A) or OH(X) with rare gases) reviewed in refs. 25,26. With Kr and Xe, the collider gases used in this work, a whole new range of collisional outcomes is opened up compared to those previously studied. In collisions of NO(A) with rare gases, or OH(A) with the lighter rare gases (He, Ar), everything takes place on one potential energy surface, *i.e.* the collision is electronically elastic. However, collisions with krypton and xenon are able to *quench* the electronically excited OH($A^2\Sigma^+$) to its ground electronic state, $X^2\Pi$.[27,28] We therefore move from the study of collisions on a single potential energy surface to those that evolve across *three* – the excited $A^2\Sigma^+$ state and the two components of the ground state, which become non-degenerate when the symmetry is lowered away from linearity.

These so-called *non-adiabatic* effects (those occurring over multiple potential energy surfaces) are ubiquitous in chemistry (see section 1.3), and the present work offers an

opportunity to study them in a simple model system with a high level of detail. In particular, a major theme of this project will be the competition between electronically elastic and inelastic processes. For example, to what extent does electronic quenching to the ground (X) state compete with rotational energy transfer within the excited, A state? Are the same features of the excited state PES responsible for both, or do they occur on separate regions of the potential?

In addition to scalar rates, the present work aims to investigate vector correlations as explained in the next section. This provides an extra level of detail above that obtained from energy transfer cross-sections, leading to a better test of theory and a greater understanding of the collision dynamics.

1.2 Collision dynamics and vector correlations

A non-reactive collision between an atom A and a diatom BC can be fully specified by four vectors[8] (see section 3.2). These are the initial and final relative velocities, $\boldsymbol{k}$ and $\boldsymbol{k'}$, and the initial and final angular momenta of BC, $\boldsymbol{j}$ and $\boldsymbol{j'}$. (Note that throughout this thesis, primes refer to quantities after a collision.) These four vectors are shown in figure 1.1.

The full four-vector correlation, which contains all the information about the collision, can be integrated over various vectors to obtain lower-order correlations.[8,29–33] These are often clearer to interpret and easier to deal with, taking one aspect of the collision at a time. In particular, the most commonly investigated correlation is the *differential cross-section* or *DCS*, which is the correlation between $\boldsymbol{k}$ and $\boldsymbol{k'}$ that describes the angular scattering of the products. Forward scattering mostly derives from high impact-parameter,* glancing blow collisions, where the reaction or process of interest occurs at larger separations – one well-studied example of this is a harpoon reaction such as $K + I_2 \rightarrow KI + I$.[7,8] More head-on collisions (rebound dynamics) lead to backward scattering, for example

*See chapter 3

$K + CH_3I \rightarrow KI + CH_3$,[8,34] and an isotropic, statistical DCS indicates a long-lived collision complex, in which all memory of the initial velocities is lost.

In this thesis, the focus will be more on the correlation between $\boldsymbol{j}$ and $\boldsymbol{j'}$, as shown in figure 1.1. The extent to which the plane or sense of rotation is disturbed – quantum mechanically, the change in occupation of the m_j sublevels – provides a guide to the character of the potential felt during the collision. This can be compared between different kinds of collision, for example rotationally elastic or inelastic, to ascertain the different features of the PES responsible for each. A large change in the direction of $\boldsymbol{j'}$ with respect to $\boldsymbol{j}$ indicates that the collision was influenced by a very attractive or anisotropic region of the PES; less of a change shows that flatter features of the PES governed this particular collision.

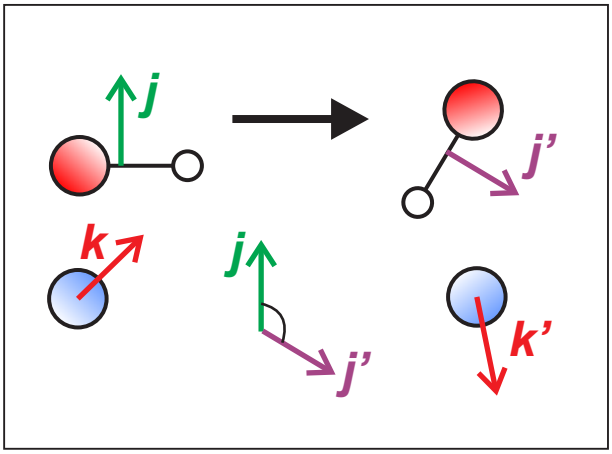

Figure 1.1: The vectors $\boldsymbol{k}$, $\boldsymbol{k'}$, $\boldsymbol{j}$ and $\boldsymbol{j'}$ for an atom + diatom collision. The angle shown is the $\boldsymbol{j} - \boldsymbol{j'}$ 'tilt angle,' $\theta_{jj'}$.

One important concept in this work is *polarisation*, a preferred plane or sense of rotation in the lab frame (quantum mechanically, a preference for certain values of m_j over others) – see chapter 3. In the experiments described in chapter 4, an initially polarised distribution of $\boldsymbol{j}$ is created via excitation with a polarised laser beam. Over time, collisions destroy this polarisation and the distribution of $\boldsymbol{j'}$ becomes more anisotropic. Monitoring the decay of bulk polarisation with time gives information on the probability distribution of $\theta_{jj'}$, *i.e.* the $\boldsymbol{j} - \boldsymbol{j'}$ correlation.

1.3 The Born-Oppenheimer approximation and non-adiabatic effects

As mentioned above, a major reason for choosing to study the OH(A) + Kr, Xe systems in this thesis is because of electronic quenching in these systems. Adiabatic potential energy surfaces are calculated by solving the time-independent Schrödinger equation with the nuclear positions fixed, then repeating this at a variety of nuclear configurations. This takes advantage of the *Born-Oppenheimer approximation*, where the large difference between the masses of nuclei and electrons is invoked to assume that the nuclei can be considered not to move on the timescale of electron motion.[35] However, near a potential crossing, finite nuclear velocities can lead to the breakdown of this approximation in so-called *non-adiabatic* behaviour[8] – see chapter 2.

The ground and excited state potentials of OH + Kr, Xe cross at linear HO–Rg configurations.[21,28] (Previous OH(A) + Rg depolarisation studies are reviewed extensively in refs. 24–26.) Unlike for the OH + He, Ar systems, where such crossings are located high on the repulsive wall of the OH(A) + Rg PES, here the region of crossing is readily accessible at thermal collision energies. The *conical intersection*[36–39] (see chapter 2) between the OH(X) + Rg and OH(A) + Rg potentials – and the area around it – will therefore act as an efficient funnel for transferring electronic population from the excited to the ground potential state.

Such intersections are commonly observed in photochemistry,[39–41] notably in the famously anomalous behaviour shown by azulene, which shows fluorescence from the S_2 state due to a conical intersection leading to radiationless transitions between S_1 and S_0.[42,43] A conical intersection is also implicated in the photoisomerisation of retinal[44] in the rhodopsin protein involved in vision. Moreover, biological molecules such as nucleobases and amino acids are vulnerable to damage by UV radiation.[45] Increased photostability comes from fast, efficient deactivation pathways, which often involve several conical intersections.[45–47] In this way, the excited state lifetime is kept too short for any reaction

to occur.

In addition, non-adiabatic effects are ubiquitous in electron transfer processes such as in ion-molecule reactions or electrochemistry,[41] particularly at surfaces, where the band structure of many closely spaced electronic states leads to a breakdown of the Born-Oppenheimer approximation.[48]

Rovibronic couplings, where coupling to a rotation or vibration of the correct symmetry allows transfer of population between two electronic states of different symmetry, are also important in this thesis, as shown in chapters 2 and 6. Away from linearity, the doubly degenerate $X^2\Pi$ electronic state of OH + Rg splits into two states of A' and A'' symmetry (symmetric and antisymmetric with respect to reflection in the scattering plane), and the excited state has A' symmetry. As well as couplings between the two symmetric states, the state of A'' symmetry can be coupled to the other two by these rovibronic effects, as set out in section 2.4.

1.4 Experimental techniques

The techniques used in this thesis to measure cross-sections (see chapter 3) for electronic quenching, rotational and vibrational energy transfer and collisional depolarisation of angular momentum are set out in chapter 4, and the recent review by Paterson *et al.*[25] gives an account of the various experimental approaches taken to investigate such quantities.

The first requirement for the experiment is that processes should occur under *single collision* conditions, so that the results of the collisional process are not lost from view before they can be detected. This necessitates the use of a vacuum chamber and suitable pumping scheme, as described in section 4.7.

A method is also needed of specifying the initial quantum state of the OH radical, which in this work is done with laser excitation. The bandwidth of the dye laser used is sufficiently narrow to excite OH to a single (N, j) level in its excited (A) electronic state, and the laser wavelength is also tunable, enabling experiments on a selection of initial

states. Other methods of initial state selection include electric fields, for example when using a hexapole to separate out a single lambda-doublet state of NO(X) via the Stark effect.[18,22,49–57] It is even possible to select a particular conformer of a molecule using an inhomogenous electric field to spatially separate it from other conformers.[58–60]

The final quantum state distribution of OH, of course, depends on the collisional processes under study, but often a single state is selected for detection in some way. In this thesis, this is done by resolving the OH(A) fluorescence using a monochromator, with higher resolution resulting in the detection of fluorescence from a single excited (N, j) state and lower resolution collecting fluorescence from all products. Otherwise, a second laser can be used for detection, either in a photon-based method such as $(1 + 1')$ laser-induced fluorescence or optical-optical double resonance,[25] or with a method based around the detection of ions such as resonance-enhanced multiphoton ionisation (REMPI) or Rydberg tagging.[8] Many non-linear methods are also in use, such as four-wave mixing or polarisation spectroscopy – for more details see ref. 25 and chapter 4.

For the investigation of vector correlations, control is required over the initial $\boldsymbol{k}$ and/or $\boldsymbol{j}$ vectors, in addition to some means of measuring the final distribution of $\boldsymbol{k'}$ and/or $\boldsymbol{j'}$. Here, the initial angular momentum vector ($\boldsymbol{j}$) distribution is controlled by polarising the excitation laser, resulting in an oriented or aligned (see chapter 3) distribution of vectors, and the extent of polarisation of $\boldsymbol{j'}$ is followed over time by monitoring the polarisation of the emitted fluorescence. Control over $\boldsymbol{k}$ is often achieved through the use of molecular beam techniques,[8,33] and the magnitude of the initial velocity can be finely controlled using Stark[61,62] or Zeeman[63] deceleration, or other techniques such as Photostop,[64,65] to produce a narrow, cold velocity distribution. As for the resolution of $\boldsymbol{k'}$, this can be achieved by rotating the detector or by the popular and versatile technique of velocity-mapped ion imaging.[66,67].

1.5 Theoretical techniques

The field of reaction dynamics is one in which theory and experiment have a particularly close relationship. The experimental analysis of single collisions with the methods referred to above can be directly compared to the results of *ab initio* calculations, which are computationally feasible for the kinds of simple systems studied in this work. Each extra level of insight afforded by more sophisticated experiments provides a stronger test for theory, and the computational exploration of novel phenomena spurs the development of methods aimed at observing them in the lab.

The basic idea of the theoretical methods discussed here is to simulate the dynamics of molecular collisions using scattering calculations. These calculations are performed on potential energy surfaces that have been obtained using electronic structure theory. The initial conditions (positions and momenta of the atoms, quantum states) are set and the motion of the atoms is propagated over the PES in some way, resulting in final positions, momenta and quantum states.

Quantum mechanically, the wave nature of matter is represented by using the *scattering matrix*, $\mathbf{S}$, to relate the incoming and outgoing wavefunctions:[10]

$$\mathbf{S}|\psi^J_{\text{in}}\rangle = |\psi^J_{\text{out}}\rangle \tag{1.2}$$

The elements of the $\mathbf{S}$ matrix, S_{if}, are probability amplitudes for scattering from an initial state $|i\rangle$ to a final state $|f\rangle$ at a given energy.[8] Note that the wavefunction is decomposed into contributions from different *partial waves* with different values of the total angular momentum, J. (See section 3.1). The superposition of these partial waves (in a double summation) leads to interference effects that are absent in classical calculations.

This time-independent treatment of quantum scattering usually involves solving the *close-coupled* equations.[68] It is also possible to represent quantum scattering in a time-dependent manner, where a wavepacket corresponding to a particular initial state $|i\rangle$ is propagated in time.[8] These methods tend to scale better than time-independent methods,

which require a large number of rovibrational states to be coupled in to the calculations, but have the disadvantage that the wavepacket moves slower at low collision energies.[8]

Classically, Newton's laws of motion are used to propagate trajectories for the nuclei over the potential energy surface. These trajectories are independent and do not interfere, as there is no concept of phase. Each trajectory starts with a set of selected initial conditions and leads to a certain outcome; a Monte Carlo average over a large number of such trajectories, with different initial conditions, is performed to compare with experimental data.

One of the main conceptual advantages of classical trajectory methods over quantum scattering calculations is that everything is observable – there is no analogue of the uncertainty principle, which can sometimes make quantum methods slightly more 'black box' in character. They are also much more scalable with increasing size and complexity of the system under study. However, quantum effects such as tunneling, resonances, spin and (importantly) interference are left out, which makes a particular difference at lower collision energies. Various semiclassical methods have been proposed to include some or other of these effects in trajectory calculations – see chapter 5.

Possibly the most important quantum effect left out of classical trajectory calculations is *quantisation* – the trajectories can start off with any energy, rather than in a specific quantum state. The quasi-classical trajectory (QCT) method,[69] explained further in chapter 5, starts the trajectories in a quantised initial state, but the propagation is still classical in nature. This leads to continuous values for the final energy, angular momentum and so on, which are binned in some way to quantised values at the end of the trajectory. In many cases, the QCT method gives results that are in quantitative agreement with quantum scattering calculations,[70] as long as the situations where its approximations may break down are kept in mind. One such case is to do with zero point energy, where energy put into (for example) a vibrational mode at the start of a calculation can leak out into other degrees of freedom, in conflict with quantum mechanics.

1.5.1 Non-adiabatic theoretical techniques

The kinds of theoretical calculations described above can be extended to include non-adiabatic effects of the types discussed in section 1.3. Diabatisation of the adiabatic potential energy surfaces (see chapter 2) yields the couplings required. In the time-dependent picture, the wavepacket evolves across multiple potential energy surfaces at once, with the diabatic potential couplings governing the transfer of population between the different electronic states.

In a recent review article,[41] as well as an earlier book chapter,[71] Tully gives a perspective on current approaches to non-adiabatic dynamics calculations. The full set of coordinates is separated into a 'fast' and a 'slow' subset; in most cases, as here, the fast subset is the electronic coordinates and the slow subset is the nuclear coordinates. This way, the separation corresponds to the Born-Oppenheimer approximation.

The fast, electronic coordinates are treated using quantum mechanics, and the slow coordinates can be treated in a variety of ways. In this subsection, we will consider the treatment of the nuclear coordinates by quantum methods (e.g. wavepackets or path integrals)[41] or by classical mechanics. For conciseness, the many semiclassical methods will not be discussed in depth here, but they include the Miller-Meyer-Stock-Thoss formalism combined with semiclassical methods;[72] the quantum-classical Liouville equation,[73,74] where the nuclear density matrix is propagated over several coupled states; multiple spawning,[75] where a swarm of Gaussian wavepackets propagates over many surfaces at once; or so-called quantum trajectory methods.[76,77†] A very recent review of non-adiabatic dynamics calculations, with a focus on ultrafast spectroscopy, is given in ref. 78.

Having separated the system into one 'fast' quantum subsystem, and one 'slow' subsystem that may be quantum or classical, it is important to include feedback in both directions between them, which Tully refers to as 'entanglement'.[41] Table 1.1 compares two models in which the slow subsystem is treated classically with two models in which it

[†]Note that references given here are representative examples only and are not meant to be comprehensive; for a fuller review consult ref. 41.

is treated quantum mechanically, according to whether this entanglement is fully included.

Considering first the time-dependent Hartree (TDH),[79] or time-dependent self-consistent field (TDSCF) method, the slow coordinates have an influence on the fast ones by influencing non-adiabatic transitions. However, motion in the fast degrees of freedom takes place in the average field of the slow ones — the system evolves on one, average mean-field PES, so this back-reaction is only approximately included. Taking the classical limit of this method leads to the Ehrenfest method,[80] where a classical trajectory (for the nuclear motion) is propagated on the mean-field PES. This method has the drawback that a trajectory moving on an average potential is often not realistic. For example, in the systems discussed in this thesis, a weighted average potential would involve some OH(X) and OH(A) character, and would not resemble either the ground or excited state very much — it would be difficult to assign the final trajectory to one state.

Including the quantum back-reaction in a more consistent way extends the TDH method to the multi-configurational MCTDH method,[81] where a different wavefunction describes the evolution of the nuclear coordinates for motion on each electronic state. In the limit of a complete basis, this method would be exact (but the basis must be truncated in practice.) The classical analogue of the MCTDH method would be *trajectory surface-hopping* (TSH) QCT,[82,83] the method employed in this thesis.[‡] In this stochastic method, the electronic state populations are propagated simultaneously to the classical integration of the equations of motion, and determine the probability at each timestep that the trajectory will switch from one PES to another. Motion of the nuclei can induce transitions between adiabatic electronic states (see chapter 2), and the 'quantum back-reaction' takes the form of a different PES being used to calculate the forces on the nuclei in each electronic state. A good comparison between the TSH and Ehrenfest methods, with derivations, is contained in ref. 84.

At all times, the trajectory moves on a single adiabatic PES, unlike other semiclassical methods such as Ehrenfest theory, where it evolves on a weighted average PES. The

[‡]Note that this is a classical *analogue*, not a formal limit.[84]

	Nuclear coordinates	
Full 'entanglement'	Classical	Quantum
Yes	TSH	MCTDH
No	Ehrenfest	TDH (TDSCF)

Table 1.1: Comparison of several commonly-used methods for non-adiabatic calculations.[41,71]

sudden switching of trajectories from one potential energy surface to another may appear unrealistic on the single-trajectory level, but an ensemble of trajectories will contain some that hop at earlier or later times, leading to a gradual transfer of population from one PES to the other. Forbidding hops that are energetically impossible (classically speaking, i.e. without tunneling) in the TSH method provides an *approximate* means of maintaining detailed balance and stopping energy flowing from the classical subsystem into the quantum one, which can sometimes be a problem with the Ehrenfest and related methods (see figure 3 of ref. 41).

The TSH method can be implemented in a number of ways, but one of the most widely-used methods for its simplicity, efficiency and intuitive picture of the dynamics is the *fewest-switches* surface hopping method,[83] which is explained in chapter 6.

1.6 Outline of this thesis

This thesis begins in chapters 2 and 3 with a discussion of the theoretical concepts that are made use of in this work. These include angular momentum polarisation, vector correlations, potential energy surfaces and the various types of coupling between them, definitions of key quantities in reaction dynamics and the spectroscopy of the OH radical. The experimental methods employed are then set out in chapter 4, with a description of the theory behind the technique of Zeeman quantum beat spectroscopy (ZQBS) and an explanation of how the data are analysed. Chapter 5 presents the theoretical methods used in this work, principally quasi-classical trajectory (QCT) calculations. All relevant details of the calculations are given, and the tensor opacity formalism used to obtain quasi

open-shell results is also presented here. The trajectory surface hopping (TSH) method is set out at the beginning of chapter 6, and a new three-state TSH method that includes rovibronic couplings between potentials of different symmetry is then developed to extend the existing theory to take account of all relevant electronic states. This third method is described for the first time in chapter 6 of this work.

Experimental results for electronic quenching, rotational energy transfer and collisional depolarisation of OH(A, $v = 0$) with Kr and Xe are compared with theory in chapter 7, and further theoretical results are presented for further characterisation of the dynamics of these systems. For the OH(A, $v = 0$) + Kr system, theoretical rotational state distributions of the OH(X) products of quenching are compared to experimental results obtained elsewhere. Chapter 8 presents experimental results for quenching, collisional energy transfer (both vibrational and rotational) and collisional depolarisation in the OH(A, $v = 1$) + Kr system and compares these to the OH(A, $v = 0$) + Kr system, as well as results with other quencher gases obtained elsewhere.

Chapter 9 summarises the main conclusions of this thesis and suggests possible directions for future work.

Chapter 2

Theory: Spectroscopy, potentials and couplings

This chapter describes some of the core theoretical concepts used in the present work. First, the spectroscopy of the OH radical is described for use in the following chapters, and this leads on to a discussion of the potential energy surfaces characterising its interaction, in its X and A electronic states, with Kr and Xe. The discussion then moves to adiabatic and diabatic potentials and potential couplings, with a consideration of how the mixing of different electronic states will be treated. The different types of coupling in the present systems will be delineated, including conical intersections (electrostatic coupling) and roto-electronic couplings.

2.1 The OH radical: spectroscopy

This thesis concerns collisions of the OH radical with Kr and Xe atoms, and so it is useful to summarise here its spectroscopy.[85] Note that, throughout this thesis, vectors are denoted by bold italic type: $\boldsymbol{j}$, their magnitudes are expressed as $|\boldsymbol{j}|$ and the corresponding quantum numbers are denoted by italics: j.

The ground, X, and first excited, A, electronic states are dealt with in this work, and

have the electronic configurations

$$\mathrm{OH}(\mathrm{X}^2\Pi) : (1\sigma)^2(2\sigma)^2(3\sigma)^2(1\pi)^3$$
$$\mathrm{OH}(\mathrm{A}^2\Sigma^+) : (1\sigma)^2(2\sigma)^2(3\sigma)^1(1\pi)^4$$

Both of these states are doublets, having a single unpaired electron.

The $\mathrm{OH}(\mathrm{A}^2\Sigma^+)$ state, collisions of which form the main object of study in this thesis, is a Σ state as its unpaired electron is in a σ orbital. Thus Λ, the component of electronic orbital angular momentum $\boldsymbol{L}$ along the internuclear axis, is zero, meaning that the radical can be well described by Hund's case (b). Note that Λ is a good quantum number, while L is not.

In case (b) coupling, the angular momentum of nuclear rotation, $\boldsymbol{R}$, is strongly coupled to Λ to give $\boldsymbol{N}$; in the special case of a Σ radical such as OH(A), $\boldsymbol{R} \equiv \boldsymbol{N}$. $\boldsymbol{N}$ then couples to the electron spin, $\boldsymbol{S}$, giving $\boldsymbol{j}$, the total angular momentum exclusive of nuclear spin. As OH(A) is a doublet radical, $S = \frac{1}{2}$ and so $j = N \pm \frac{1}{2}$.

These two *spin-rotation* levels will be labelled as f_1 ($j = N + S$) and f_2 ($j = N - S$). They are split by the spin-rotation coupling, $\gamma(\boldsymbol{N} \cdot \boldsymbol{S})$, giving an energy splitting between f_1 and f_2 levels of the same N state of $\gamma(N + \frac{1}{2})$. For the OH(A) radical, the spin-rotation coupling constant γ is 0.2244 cm^{-1} in $v = 0$ and 0.2112 cm^{-1} in $v = 1$.[86] This constant reflects the interaction between the magnetic moment of the electron and the magnetic field of the rotating nuclei, but also contains second-order contributions from spin-orbit interactions and other interactions with the X state, which can sometimes dominate the first-order part[87].

In the $^{16}\mathrm{O}^1\mathrm{H}$ radical, $\boldsymbol{j}$ then couples to the nuclear spin of the proton, $\boldsymbol{I}$, to form the total angular momentum $\boldsymbol{F}$. As $I = \frac{1}{2}$, $F = j \pm \frac{1}{2}$. The isotopic abundances of oxygen and hydrogen in nature are such that other isotopomers of OH will not be considered here. A diagram of Hund's case (b) coupling is given in figure 2.1, and an energy level diagram is shown in figure 2.2.

Considering the collision system made up of OH(A) + Rg, where Rg is a rare gas atom, the orbital angular momentum of the system is labelled ℓ, and the total angular momentum of the triatomic system is then J. $\boldsymbol{J} = \boldsymbol{j} + \boldsymbol{\ell}$ if nuclear spin is neglected, and $\boldsymbol{J} = \boldsymbol{F} + \boldsymbol{\ell}$ if it is included.

The ground state of OH, $X^2\Pi$, also follows Hund's case (b) at high N, as $\boldsymbol{S}$ is uncoupled from the internuclear axis and can instead couple to $\boldsymbol{N}$. In this case, $\Lambda = \pm 1$ but S and I are the same as in the A state, so coupling proceeds as above. At low N, the coupling between $\boldsymbol{R}$ and Λ becomes weaker than spin-orbit coupling, so $\boldsymbol{L}$ instead couples to $\boldsymbol{S}$ in Hund's case (a) scheme (figure 2.3). Neither L nor S are good quantum numbers, but their projections on the internuclear axis Λ and Σ are, as is $\Omega = |\Lambda + \Sigma|$. (Note that N is not a good quantum number in Hund's case (a).) The combined projection Ω couples to $\boldsymbol{R}$ to form $\boldsymbol{j}$, and this then couples to the nuclear spin $\boldsymbol{I}$ to form the total angular momentum $\boldsymbol{F}$.

For OH(X), $\Omega = \frac{3}{2}$ (F_1) or $\frac{1}{2}$ (F_2), corresponding to two spin-orbit manifolds, of which F_2 is the higher in energy by around 140 cm^{-1}.[85]

The wavefunction for Hund's case (a) can be written as[88]

$$|jm\Omega\rangle = \sqrt{\frac{2j+1}{4\pi}} D^{j*}_{m\Omega}(\phi, \theta, 0) \tag{2.1}$$

in which $D^j_{m\Omega}(\phi, \theta, 0)$ is a Wigner rotation matrix[88], but this is not an eigenfunction of the molecular Hamiltonian. Instead, a linear combination of $+\Omega$ and $-\Omega$ states is taken, with defined parity $p = (-1)^{j-\frac{\epsilon}{2}}$:

$$|jm\Omega\epsilon\rangle = \frac{\sqrt{2}}{2}\left(|jm\Omega\rangle + \epsilon|jm-\Omega\rangle\right) \tag{2.2}$$

The $+\Lambda$ and $-\Lambda$ states can be visualised semiclassically as $\boldsymbol{L}$ precessing clockwise or anticlockwise around the internuclear axis.

These pairs of $\pm\epsilon$ states are referred to as Λ-*doublets*, and take the label e ($\epsilon = +1$) or f ($\epsilon = -1$)[88]. They can also be labelled according to the symmetry of the electronic

wavefunction under reflection in the plane of rotation of the molecule — in the case of a Π state molecule like OH(X), the $\Pi(A')$ state is symmetric and the $\Pi(A'')$ state is antisymmetric.[89]

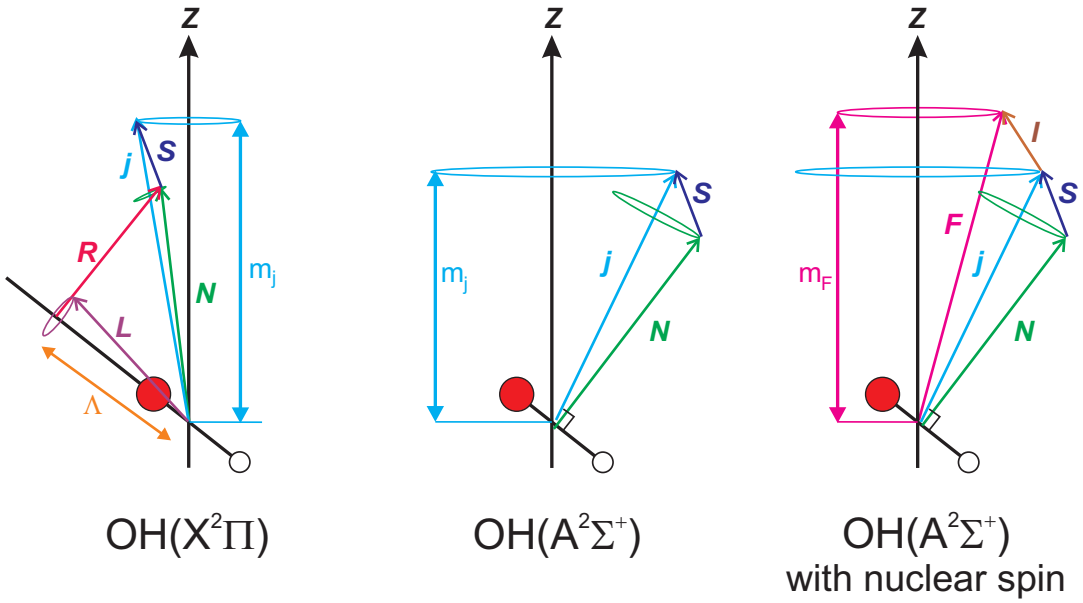

Figure 2.1: Hund's case (b) coupling of angular momenta. Left: OH(X), centre: OH(A), both neglecting nuclear spin. Right: OH(A), including nuclear spin. Symbols as defined in text.

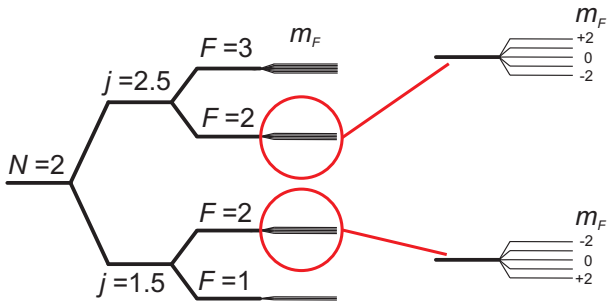

Figure 2.2: Energy levels of OH(A) under Hund's case (b) coupling – splittings not to scale. Note the difference in ordering of the Zeeman sublevels (section 2.1.1) between the two spin-rotation levels.

Transitions between the X and A states in this thesis are labelled with the following Hund's case (b) notation:

$$\Delta N_{f_\Sigma F_\Pi}(N'') \tag{2.3}$$

where N'' is the rotational quantum number of OH(X) and ΔN is the change in N going from the ground to the excited state. This is expressed as a letter: O, P, Q, R, S for

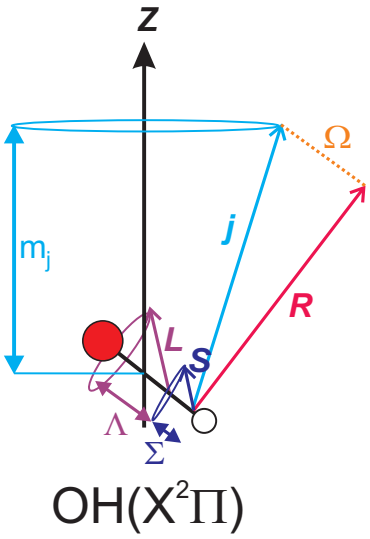

Figure 2.3: Hund's case (a) coupling of angular momenta for OH(X), neglecting nuclear spin. Symbols as defined in text.

ΔN = -2, -1, 0, 1, 2. F_Π is the spin-orbit level of the Π state (F_1 or F_2) and f_Σ is the spin-rotation level of the Σ state (f_1 or f_2).

2.1.1 Zeeman sublevels and g-values

An angular momentum state can be defined as $|Fm_F\rangle$, where F is the total angular momentum quantum number and m_F is the eigenvalue of the $\hat{j}_Z$ operator — classically, the projection of $\boldsymbol{F}$ on the Z axis. As m_F can range from $-F$ to $+F$ in integer steps, the number of 'Zeeman' m_F sublevels is $(2F+1)$. In free space, the choice of Z is arbitrary and so the Zeeman levels are degenerate by the spherical symmetry of the system. However, an external magnetic field imposes a definition of Z along the field axis, which is different from all other directions in space. This breaking of symmetry splits the m_F degeneracy.

The energy splitting between the Zeeman sublevels resulting from application of a magnetic field, $\boldsymbol{B}$, is given by[88]

$$\Delta E_Z = \langle -\boldsymbol{\mu} \cdot \boldsymbol{B} \rangle \tag{2.4}$$

where $\boldsymbol{\mu}$ is the magnetic dipole and the angle brackets denote averaging over all orientations of the molecule.

Considering the interaction of the field with the electron spin $\boldsymbol{S}$, the magnetic dipole moment μ_S is given by

$$\mu_S = g_e \mu_0 (S(S+1))^{0.5} \tag{2.5}$$

where g_e is the Landé g-value of a free electron (2.002) and μ_0 is the Bohr magneton.

Under Hund's case (b), as discussed above, $\boldsymbol{S}$ couples to $\boldsymbol{N}$ to give $\boldsymbol{j}$, and the resulting magnetic dipole moment is

$$\mu_j = g_j \mu_0 m_j \tag{2.6}$$

Likewise, considering coupling to nuclear spin too,

$$\mu_F = g_F \mu_0 m_F \tag{2.7}$$

In these equations, the g-values are

$$g_j = g_e \frac{j(j+1) + S(S+1) - N(N+1)}{2j(j+1)} \tag{2.8}$$

$$g_F \simeq g_j \frac{F(F+1) + I(I+1) - j(j+1)}{2F(F+1)} \tag{2.9}$$

Therefore the Zeeman splitting is given by

$$\Delta E_Z = g_F \mu_0 B \Delta m_F \tag{2.10}$$

The Larmor frequency, ω_L, will be used a lot in this thesis. It is defined as

$$\omega_L = -\frac{g_F \mu_0 B}{\hbar} \tag{2.11}$$

2.2 Potential energy surfaces

2.2.1 Single surface OH(A) + Rg

The *diabatic** Σ-state potential energy surfaces used in this work were calculated by Kłos at the RCCSD(T) level of theory for OH(A) + Kr,[21] and the MRCISD+Q level for OH(A) + Xe.[90] As the reduced masses of OH + Kr and OH + Xe are similar, the PES will be responsible for most of the differences in behaviour between these systems.

The PESs are expressed as a function of the Jacobi coordinates R, the distance between Kr/Xe and the centre of mass of OH; r, the OH bond length and γ, the angle between R and r (such that $\gamma = 0°$ corresponds to the OH–Rg linear configuration) — see figure 2.4. In the surfaces used here, the OH bond length r is fixed at its equilibrium value, $r_e = 1.0121$ Å.[21,90,91].

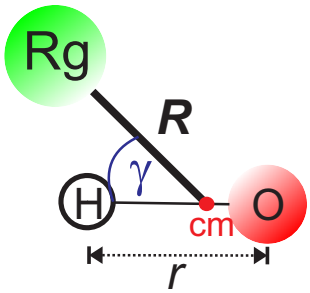

Figure 2.4: Jacobi coordinates R, r and γ as used in this thesis. See text for details.

The interaction between OH($A^2\Sigma^+$) and Kr or Xe is attractive in linear configurations, with deep potential wells in both OH–Rg and HO–Rg geometries. Of these, the oxygen well (HO–Rg) is deeper and at closer range, as seen in figure 2.5. The two wells are separated by a region of repulsion at T-shaped geometries, that extends to long range, longer for Xe than for Kr. The main differences between the OH(A) + Kr, Xe potentials are the strength and range of the attractive forces, with the OH(A) + Xe potential being more attractive, anisotropic and extending to longer range than OH(A) + Kr. Note also that the two wells are separated by a region of repulsion at T-shaped geometries, that extends to longer range for OH(A) + Xe than for OH(A) + Kr.

*A full discussion of 'adiabatic' and 'diabatic' potentials will follow in section 2.3

The attraction between OH(A) and Kr or Xe is very strong, as illustrated by table 2.1 — in particular, the HO–Xe well depth is on the order of a chemical bond, with the HO–Kr well depth around half of this. This fits with the experimentally observed strength of the van der Waals complexes formed by OH(A) with rare gas atoms in the gas phase[11,92–96] although, due to Franck-Condon factors, experimental studies of these complexes provide information mostly about the OH–Rg geometry. The very strong attraction is thought to have contributions from electron correlation and some charge transfer effects at short range[11,21], and induction and dispersion at longer range[21,92]. In collinear geometries, the overlap of OH 3σ and rare gas p_z orbitals could also lead to weak covalent interactions.

The difference in attraction between the wells at either end of the molecule was explained in the case of OH(A) + Ar by noting that charge/dipole and dipole/dipole interactions largely cancel for the OH–Ar configuration, but are additive in the HO–Ar geometry[11,92], and a similar rationalisation is likely to hold for Rg = Kr, Xe also.

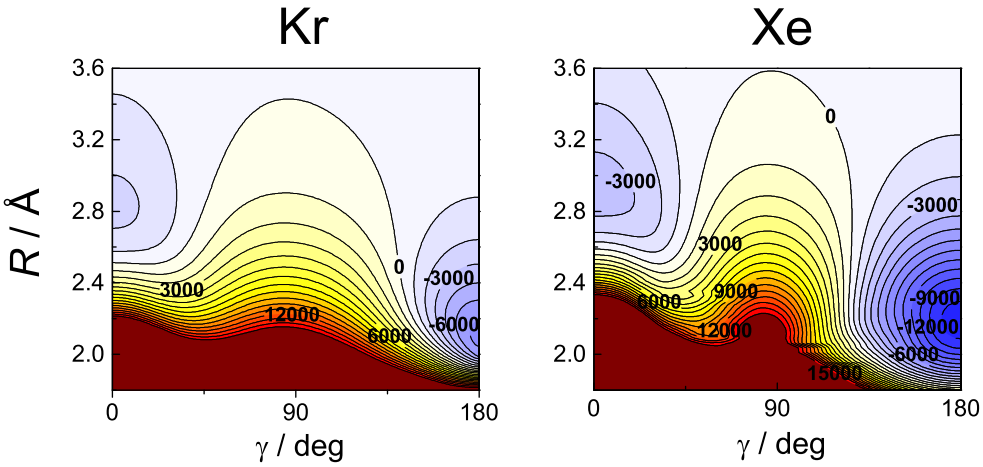

Figure 2.5: Potential energy surfaces for OH(A) + Kr[21] (left) and OH(A) + Xe[90] (right). Energy given in cm^{-1}.

2.2.2 Adiabatic surfaces $1A'$, $1A''$, $2A'$

The symmetry labels of Σ and Π in the subsection above are valid only at linearity ($C_{\infty v}$ symmetry). As the rare gas atom approaches the doubly degenerate OH($X^2\Pi$) state in C_s symmetry, it splits into two states that are respectively symmetric (A') and antisymmetric

Well / bond	D_e / cm^{-1}
OH(A)–Ar[11]	1,219
HO(A)–Ar[11]	1,720
OH(A)–Kr[21]	1,949
HO(A)–Kr[21]	6,079
OH(A)–Xe[90]	3,500
HO(A)–Xe[90]	12,648
I–I (I_2)[97]	12,600
F–F (F_2)[97]	13,300

Table 2.1: Well depths for linear OH(A) + rare gas systems, compared to chemical bond strengths

(A'') with respect to reflection in the *scattering plane*, i.e. the plane containing the three atoms. Note that these labels are *not* the same as the Λ-doublet labels $\Pi(A')$ and $\Pi(A'')$ defined in section 2.1, which concerned reflection symmetry in the plane of *rotation* instead.

These two states will be labelled as $1A'$ and $1A''$ in this thesis, and the excited state ($^2\Sigma^+$ at linearity), which is also symmetric in the scattering plane, will be labelled $2A'$.

The coupled-cluster (CC) calculations used for the OH(A) + Kr PES of ref. 21 succeed in recovering much of the electron correlation energy needed for a good description of the HO–Kr interaction, but are not well suited for a characterisation of the potential crossing region due to their *single-reference* nature. A good discussion of the points raised in this subsection can be found in the tutorial article by Lodi and Tennyson.[98] The CC method assumes that the Hartree-Fock (HF) wavefunction — which, by definition, includes no electron correlation — is a reasonable approximation to the true, exact wavefunction, and tries to obtain an improved wavefunction by expansion in a basis of the eigenfunctions of the Fock operator. The idea is that contributions from excited states become smaller the more those states differ from the HF ground state, so the Hamiltonian is diagonalised in a basis set that includes HF states up to a certain level of excitation. The RCCSD(T) method includes single and double excitations, with an approximate treatment of triple excitations based on perturbation theory. 'Single-reference' means that the expansion is based on only one (reference) HF calculation, meaning that coupled cluster methods

do not work well when the HF wavefunction is not a good approximation to the exact wavefunction.

One such situation is in a region of potential coupling, near to a conical intersection (the HF theory exploits the Born-Oppenheimer approximation). Therefore, the set of three adiabatic PESs $1A'$, $1A''$ and $2A'$ were calculated for OH + Kr using a *multi-reference* method (MRCISD+Q) by Kłos[28]. This aims to describe the PES even in regions where single-reference methods do not work. The +Q refers to the Davidson correction for size-extensivity, which approximates the parts of the electron correlation energy that result from higher-order excitations.[98,99]

The adiabatic OH + Kr MRCISD+Q $2A'$ PES is very similar to the RCCSD(T) PES described in section 2.2, and single-surface QCT calculations on both surfaces are found to give almost the same results. For OH(X, A) + Xe, all three adiabatic PESs are presented in ref. 90 and are calculated with the multi-reference MRCISD+Q theory.

Cuts through the three potentials $1A'$, $1A''$ and $2A'$ are shown for OH + Kr and OH + Xe in figure 2.6. These cuts are taken at the near-linear HO–Rg geometry ($\gamma = 175°$). The close approach of the $1A'$ and $2A'$ potentials results in an avoided crossing, the pathway to which is barrierless. As the position of this crossing is observed to lie below the thermal collision energy, both systems are expected to exhibit significant electronic quenching to the $1A'$ state, and quenching is predicted to be more prevalent in OH(A) + Xe as the crossing lies closer to the bottom of the well, rather than on the repulsive wall as in OH(A) + Kr. For lighter rare gases, no quenching is expected as the crossing lies too high on the repulsive wall (see figure 7.2). These predictions are in accordance with experiment; the quenching cross-sections for OH(A) + He, Ar are negligible while those for OH(A) + Kr, Xe are significant[21,27,28] and similar to the cross-sections observed with diatomic collision partners such as H_2[27].

The $1A''$ state also crosses the $2A'$ state at an easily accessible location for both the Kr and Xe systems. Because of the different symmetry of these potentials, this crossing between adiabatic states is not avoided. As coupling between states of different symmetry

is forbidden, the $1A''$ state would not at first be expected to play a part in quenching, but section 2.4 discusses ways in which a rotation of A'' symmetry can couple to the electronic degrees of freedom in order to lift the symmetry restrictions and couple the $2A'$ and $1A''$ surfaces.

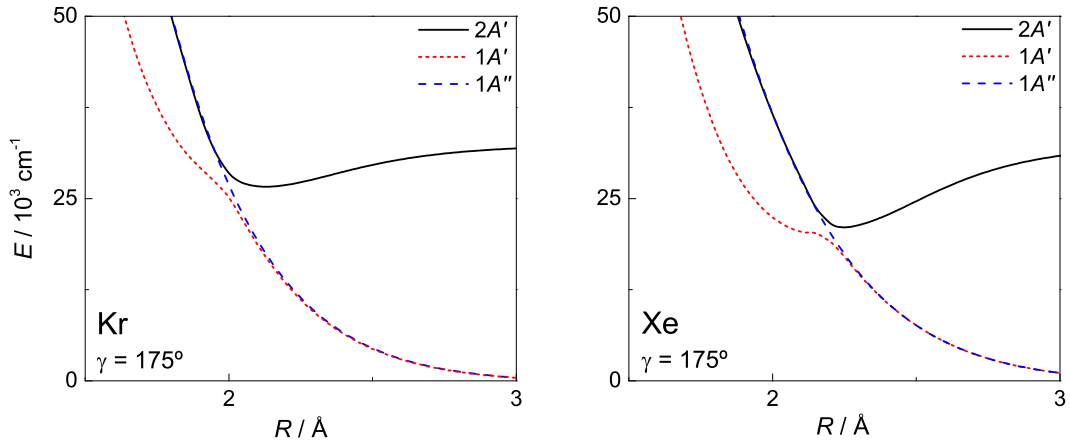

Figure 2.6: Cuts through the adiabatic potentials $1A'$ (red dots), $1A''$ (blue dashes) and $2A'$ (black line) for OH(A) + Kr[28] (left) and OH(A) + Xe[90] (right). Thermal collision energy lies at 32,907 cm^{-1} for the left hand panel and 32,985 cm^{-1} on the right.

To round off this section, the PESs for OH(X) + Xe (the adiabatic $1A'$ and $1A''$ surfaces) used in this work are compared to those calculated by Groenenboom[100] in 2006, using the RCCSD(T) method. These potentials, which succeeded in modelling the inelastic scattering of OH(X) + Xe under molecular beam conditions to a high degree of accuracy,[100] are compared to the MRCISD+Q surfaces used in this work in figure 2.7. As can be seen, the two sets of potentials agree almost entirely, and it is hard to tell them apart by eye.

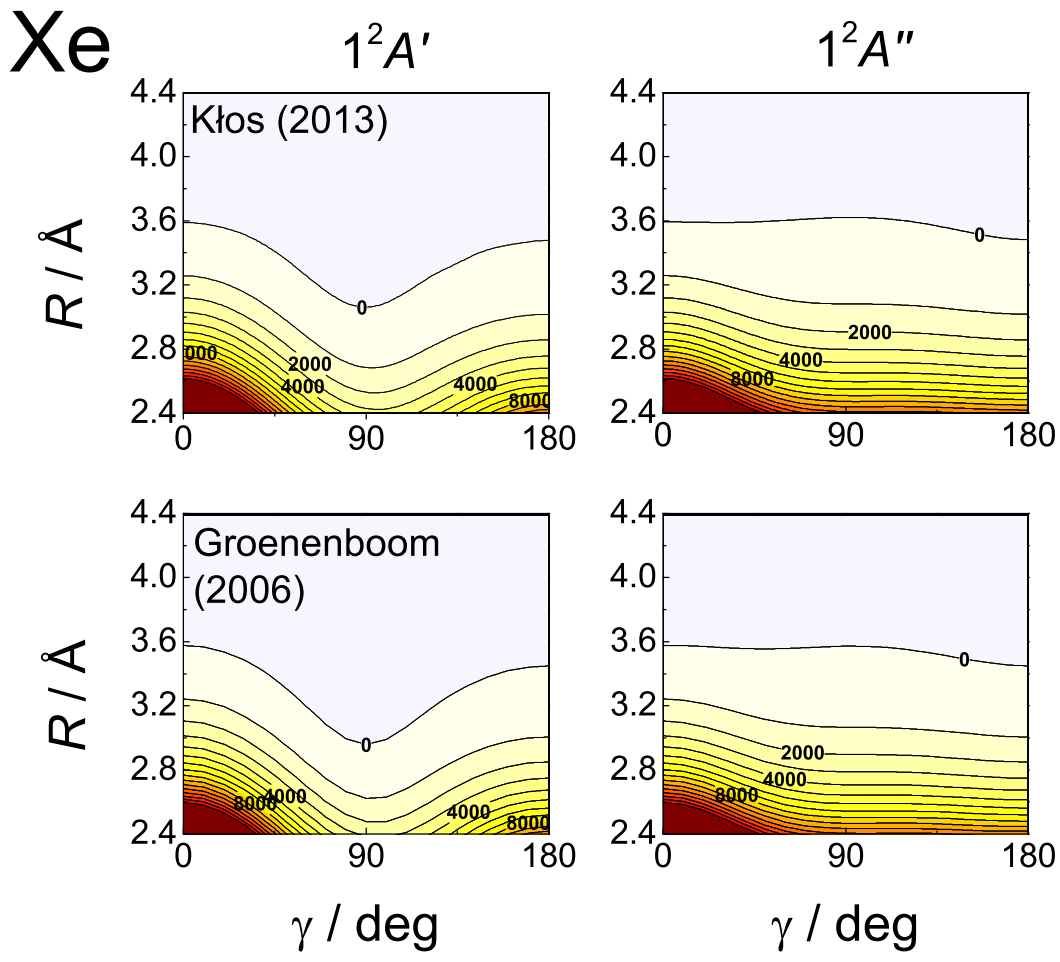

Figure 2.7: Potential energy surfaces for OH(X) + Xe, with the $1A'$ surface on the left and the $1A''$ surface on the right. Energy given in cm^{-1}. Top: Kłos[90], as used in this work, bottom: Groenenboom.[100]

2.3 Couplings and adiabatic to diabatic transformation

2.3.1 Adiabatic and diabatic states

The Born-Oppenheimer approximation[35] invokes a separation between 'fast' electronic co-ordinates and 'slow' nuclear co-ordinates, taking advantage of the large difference between the masses of electrons and nuclei to assume that the nuclei are more-or-less stationary on the timescale of electronic motion. Note that writing the total wavefunction as a product of electronic and nuclear wavefunctions in this way is an approximation, but it has recently been shown that it is in fact possible to do so exactly (with the choice of a different electronic Hamiltonian).[101]

Adiabatic wavefunctions, ϕ_i, are defined as those that diagonalise the Hamiltonian with the nuclear positions fixed:

$$\hat{H}_{\mathrm{el}}(\boldsymbol{x};\boldsymbol{X}) \begin{pmatrix} \phi_{1A'}(\boldsymbol{x},\boldsymbol{X}) \\ \phi_{2A'}(\boldsymbol{x},\boldsymbol{X}) \\ \phi_{1A''}(\boldsymbol{x},\boldsymbol{X}) \end{pmatrix} = \begin{pmatrix} U_{1A'}(\boldsymbol{x};\boldsymbol{X}) & 0 & 0 \\ 0 & U_{2A'}(\boldsymbol{x};\boldsymbol{X}) & 0 \\ 0 & 0 & U_{1A''}(\boldsymbol{x};\boldsymbol{X}) \end{pmatrix} \begin{pmatrix} \phi_{1A'}(\boldsymbol{x},\boldsymbol{X}) \\ \phi_{2A'}(\boldsymbol{x},\boldsymbol{X}) \\ \phi_{1A''}(\boldsymbol{x},\boldsymbol{X}) \end{pmatrix} \tag{2.12}$$

where $\boldsymbol{x}$ and $\boldsymbol{X}$ are vectors of the (fast) electronic and (slow) nuclear coordinates respectively. $\hat{H}_{\mathrm{el}}$ is the Hamiltonian minus the nuclear kinetic energy term ($\hat{H} - \hat{T}_N$).

Repeating the calculation at different fixed nuclear positions maps out an adiabatic potential energy surface; it is these adiabatic PESs that are the product of *ab initio* electronic structure calculations.

By definition, the adiabatic potential energy matrix (in equation (2.12)) is diagonal, and so coupling between adiabatic states is *kinetic* — finite nuclear velocities can cause couplings between these states. This constitutes a breakdown of the Born-Oppenheimer approximation, as electronic and nuclear motion can no longer be considered on different timescales.

To illustrate the adiabatic separation and investigate non-adiabatic couplings, the total wavefunction $\Phi(\boldsymbol{x}, \boldsymbol{X}, t)$ can be expanded in the product of the electronic wavefunction, $\phi(\boldsymbol{x}, \boldsymbol{X})$ and the nuclear wavefunction, $\psi(\boldsymbol{X}, t)$.[8]

$$\Phi(\boldsymbol{x}, \boldsymbol{X}, t) = \sum_i \psi_i(\boldsymbol{X}, t)\phi_i(\boldsymbol{x}, \boldsymbol{X}) \tag{2.13}$$

Using this in the time-dependent Schrödinger equation,

$$i\hbar\frac{\partial\Phi(\boldsymbol{x}, \boldsymbol{X}, t)}{\partial t} = \left(\hat{T}_N - \hat{H}_{\text{el}}\right)\Phi(\boldsymbol{x}, \boldsymbol{X}, t) \tag{2.14}$$

Left-multiplying by $\phi_j^*(\boldsymbol{x}, \boldsymbol{X})$ and integrating over the electronic co-ordinates then gives[8,38,41,82,102]

$$i\hbar\frac{\partial\psi_j}{\partial t} = \left[\hat{T}_N + U_j\right]\psi_j - \sum_i \hat{\Lambda}_{ji}\psi_i \tag{2.15}$$

in which the operator $\hat{\Lambda}_{ji}$ accounts for non-adiabatic coupling between the electronic states $|\phi_i\rangle$ and $|\phi_j\rangle$:

$$\hat{\Lambda}_{ji} = \delta_{ji}\hat{T}_N - \langle\phi_j|\hat{T}_N|\phi_i\rangle \tag{2.16}$$

Using the fact that $\hat{T}_N = -\frac{\hbar^2}{2\mu}\nabla^2$,

$$\hat{\Lambda}_{ji}\psi_i = -\frac{\hbar^2}{2\mu}\delta_{ji}\nabla^2\psi_i + \frac{\hbar^2}{2\mu}\langle\phi_j|\nabla^2|\phi_i\rangle\psi_i \tag{2.17}$$

in which the first term is zero when considering $i \neq j$. Applying the identity $\nabla^2 ab = b\nabla^2 a + a\nabla^2 b + 2\nabla a\nabla b$,

$$\hat{\Lambda}_{ji}\psi_i = \frac{\hbar^2}{2\mu}\left[\psi_i\langle\phi_j|\nabla^2|\phi_i\rangle + \langle\phi_j|\phi_i\rangle\nabla^2\psi_i + 2\langle\phi_j|\nabla|\phi_i\rangle\nabla\psi_i\right] \tag{2.18}$$

which, as $i \neq j$, means that

$$\hat{\Lambda}_{ji} = \frac{\hbar^2}{2\mu}\left(2\boldsymbol{d}_{ji}\nabla + D_{ji}\right) \tag{2.19}$$

in which $\boldsymbol{d}_{ji} = \langle\phi_j|\nabla|\phi_i\rangle$ is the non-adiabatic coupling vector and $D_{ji} = \langle\phi_j|\nabla^2|\phi_i\rangle$, the

scalar second-derivative term, is generally neglected. The derivative operator acts with respect to the nuclear co-ordinates. Note that $\boldsymbol{d}_{ji} = -\boldsymbol{d}_{ij}$, and that $\boldsymbol{d}_{ii} = 0$.

In the Born-Oppenheimer approximation, $\hat{\Lambda}_{ji}$ is zero for $i \neq j$.

Considering a point of degeneracy between two adiabatic potential energy surfaces, $\boldsymbol{d}_{ij}$ (see equation (2.19)) can be expressed in a more illuminating form by starting with the electronic Schrödinger equation:

$$\begin{aligned}
\hat{H}_{\mathrm{el}}\phi_i =& U_i\phi_i \\
\nabla\left(\hat{H}_{\mathrm{el}}\phi_i\right) =& \nabla\left(U_i\phi_i\right) \\
\hat{H}_{\mathrm{el}}\nabla\phi_i + (\nabla\hat{H}_{\mathrm{el}})\phi_i =& U_i\nabla\phi_i + (\nabla U_i)\phi_i \\
\langle\phi_j|\hat{H}_{\mathrm{el}}\nabla|\phi_i\rangle + \langle\phi_j|\nabla\hat{H}_{\mathrm{el}}|\phi_i\rangle =& U_i\langle\phi_j|\nabla|\phi_i\rangle + \nabla U_i\delta_{ji}
\end{aligned} \tag{2.20}$$

The right hand side of this expression becomes $U_i\boldsymbol{d}_{ij} + 0$, and the left hand side can be simplified by noting that

$$\begin{aligned}
\langle\phi_j|\hat{H}_{\mathrm{el}}\nabla|\phi_i\rangle =& \langle\phi_j|\hat{H}_{\mathrm{el}}|\nabla\phi_i\rangle \\
=& \langle\nabla\phi_i|\hat{H}_{\mathrm{el}}|\phi_j\rangle^* \\
=& U_j\langle\nabla\phi_i|\phi_j\rangle^* \\
=& U_j\langle\phi_j|\nabla|\phi_i\rangle = U_j\boldsymbol{d}_{ij}
\end{aligned} \tag{2.21}$$

and therefore

$$\boldsymbol{d}_{ij} = \frac{\langle\phi_j|\nabla\hat{H}_{\mathrm{el}}|\phi_i\rangle}{U_i - U_j} \tag{2.22}$$

implying that non-adiabatic coupling becomes infinite at a point of degeneracy.

The *diabatic* representation is defined such that, ideally, the nuclear kinetic energy operator is diagonal. (See section 2.3.2). The kinetic (nuclear momentum) coupling vectors $\boldsymbol{d}_{ji}$ vanish and the coupling between potentials is contained in the off-diagonal elements of the potential energy matrix, V_{ji}. This avoids singularities such as the one demonstrated in

equation (2.22). Unfortunately, it is not possible to form exact diabatic states V_k, as not all components of $\boldsymbol{d}_{ji}$ can be made to go to zero simultaneously, so in practice approximate diabatic states must be used[103].

A qualitative measure of the applicability of the Born-Oppenheimer approximation can be gained from the Massey parameter.[8,83,104] This is defined as

$$\zeta = \left| \frac{\hbar \dot{\boldsymbol{z}} \cdot \boldsymbol{d}_{ji}}{U_j - U_i} \right| \tag{2.23}$$

in which $\dot{\boldsymbol{z}}$ is the nuclear velocity vector and U_k is the adiabatic potential energy of state $|k\rangle$.

When the energy gap between the two states is large, the non-adiabatic coupling $\boldsymbol{d}_{ji}$ is small and the nuclei are moving slowly — i.e. when the Massey parameter is small — the system behaves according to the Born-Oppenheimer approximation, evolving on one adiabatic PES. As the nuclei are moving slowly with respect to the electronic timescale, the electrons have time to arrange themselves into a new configuration at each new set of nuclear positions. Conversely, when the value of ζ approaches unity (near a curve crossing, a region of strong coupling or when the nuclei are moving fast) then a transition between adiabatic states becomes more likely, as it is harder to decouple the electronic and nuclear motions.

The Massey parameter is closely linked to the simple one-dimensional Landau-Zener model of non-adiabatic transfer.[8,105,106] This gives the probability P of non-adiabatic transfer for a two-state system assuming that, in the region of potential crossing, $\dot{\boldsymbol{z}}$ and the diabatic potential coupling V_{ji} are both constant and that the diabatic potentials V_k are linear:

$$P = \exp\left(\frac{-2\pi V_{ji}^2}{\hbar \dot{\boldsymbol{z}} \frac{\partial V_i - V_j}{\partial R}} \right) \tag{2.24}$$

2.3.2 Adiabatic to diabatic transformation

The adiabatic and diabatic representations set out in the previous subsection can be linked by an orthogonal transformation.[107–110] We first recast equation (2.12), using ϕ_i to represent the *adiabatic* electronic wavefunctions:

$$\hat{H}_{\mathrm{el}}(\boldsymbol{x};\boldsymbol{X}) \begin{pmatrix} \phi_{1A'}(\boldsymbol{x},\boldsymbol{X}) \\ \phi_{2A'}(\boldsymbol{x},\boldsymbol{X}) \\ \phi_{1A''}(\boldsymbol{x},\boldsymbol{X}) \end{pmatrix} = \mathbf{A} \begin{pmatrix} \phi_{1A'}(\boldsymbol{x},\boldsymbol{X}) \\ \phi_{2A'}(\boldsymbol{x},\boldsymbol{X}) \\ \phi_{1A''}(\boldsymbol{x},\boldsymbol{X}) \end{pmatrix} \tag{2.25}$$

in which the adiabatic potential energy matrix $\mathbf{A}$ is

$$\begin{pmatrix} U_{1A'}(\boldsymbol{x};\boldsymbol{X}) & 0 & 0 \\ 0 & U_{2A'}(\boldsymbol{x};\boldsymbol{X}) & 0 \\ 0 & 0 & U_{1A''}(\boldsymbol{x};\boldsymbol{X}) \end{pmatrix} \tag{2.26}$$

In the *diabatic* basis, with electronic wavefunctions φ_i,

$$\hat{H}_{\mathrm{el}}(\boldsymbol{x};\boldsymbol{X}) \begin{pmatrix} \varphi_{\Pi_{A'}}(\boldsymbol{x};\boldsymbol{X}) \\ \varphi_{\Sigma_{A'}}(\boldsymbol{x};\boldsymbol{X}) \\ \varphi_{\Pi_{A''}}(\boldsymbol{x};\boldsymbol{X}) \end{pmatrix} = \mathbf{D} \begin{pmatrix} \varphi_{\Pi_{A'}}(\boldsymbol{x};\boldsymbol{X}) \\ \varphi_{\Sigma_{A'}}(\boldsymbol{x};\boldsymbol{X}) \\ \varphi_{\Pi_{A''}}(\boldsymbol{x};\boldsymbol{X}) \end{pmatrix} \tag{2.27}$$

with the diabatic potential energy matrix, $\mathbf{D}$, being[109]

$$\begin{pmatrix} V_{\Pi_{A'}}(\boldsymbol{x};\boldsymbol{X}) & V_{12} & 0 \\ V_{12} & V_{\Sigma}(\boldsymbol{x};\boldsymbol{X}) & 0 \\ 0 & 0 & V_{\Pi_{A''}}(\boldsymbol{x};\boldsymbol{X}) \end{pmatrix} \tag{2.28}$$

Note the difference in notation between the diabatic states here, $\Pi_{A'}$ and $\Pi_{A''}$, and the OH(X) lambda-doublet levels of section 2.1, $\Pi(A')$ and $\Pi(A'')$. (This notation is chosen for compatibility with ref. 28.)

The adiabatic and diabatic representations are linked by a simple rotation.[107–110] In the

case where roto-electronic couplings are ignored, $\phi_{1A''} = \varphi_{\Pi_{A''}}$ — the state of A'' symmetry cannot couple to the states of A' symmetry, so is the same in both representations. This model with two coupled states can be characterised by a 2x2 rotation matrix featuring a single *mixing angle*, χ:[28,111]

$$\begin{pmatrix} U_{1A'} & 0 \\ 0 & U_{2A'} \end{pmatrix} = \mathbf{C}_2 \begin{pmatrix} V_{\Pi_{A'}} & V_{12} \\ V_{12} & V_{\Sigma} \end{pmatrix} \mathbf{C}_2^T \tag{2.29}$$

in which

$$\mathbf{C}_2 = \begin{pmatrix} \cos\chi & \sin\chi \\ -\sin\chi & \cos\chi \end{pmatrix} \tag{2.30}$$

χ describes the degree of mixing of the adiabatic wavefunctions, with a value of zero corresponding to the adiabatic limit, and a value of $\pm\frac{\pi}{4}$ to the diabatic limit.

When couplings to the third state, $\varphi_{\Pi_{A''}}$, are not neglected, a 3x3 rotation matrix, $\mathbf{C}_3$, parametrised by three mixing angles, describes the linear transformation between the adiabatic and diabatic representations. $\mathbf{C}_3$ can be formed by multiplying together three individual matrices that only feature one of the three mixing angles each. This can be done in any order, resulting in different definitions of these angles due to the non-commutativity of matrix multiplication. In this thesis, $\mathbf{C}_3$ is defined by[111]

$$\begin{pmatrix} U_1 & 0 & 0 \\ 0 & U_2 & 0 \\ 0 & 0 & U_3 \end{pmatrix} = \mathbf{C}_3 \begin{pmatrix} V_{\Pi_{A'}} & V_{12} & V_{13} \\ V_{12} & V_{\Sigma} & V_{23} \\ V_{13} & V_{23} & V_{\Pi_{A''}} \end{pmatrix} \mathbf{C}_3^T \tag{2.31}$$

in which

$$\mathbf{C}_3 = \begin{pmatrix} \cos\alpha\cos\beta - \sin\alpha\sin\omega\sin\beta & \sin\alpha\cos\omega & \cos\alpha\sin\beta + \sin\alpha\sin\omega\cos\beta \\ -\sin\alpha\cos\beta - \cos\alpha\sin\omega\sin\beta & \cos\alpha\cos\omega & -\sin\alpha\sin\beta + \cos\alpha\sin\omega\cos\beta \\ -\cos\omega\sin\beta & -\sin\omega & \cos\omega\cos\beta \end{pmatrix} \tag{2.32}$$

Like χ in the case of two mixed states, α describes the mixing of states $|\Sigma_{A'}\rangle$ and $|\Pi_{A'}\rangle$. The angle β couples $|\Pi_{A'}\rangle$ and $|\Pi_{A''}\rangle$, and the third angle ω is responsible for the coupling between $|\Sigma_{A'}\rangle$ and $|\Pi_{A''}\rangle$. If the angles β and ω are both set to zero, the situation reverts to the same as that in equation (2.30), with $\alpha \equiv \chi$.

2.3.3 Diabatisation

The theory of collision-induced electronic transitions between a $^2\Pi$ and a $^2\Sigma^+$ state of a diatomic molecule was formulated in the 1986 paper of Alexander and Corey.[109,112] This fully quantum theory uses an electronically *diabatic* basis, in which[109]

$$|\Pi_{A'}\rangle = \frac{\sqrt{2}}{2}\left[|\Lambda = 1\rangle - |\Lambda = -1\rangle\right] \tag{2.33}$$

$$|\Pi_{A''}\rangle = \frac{\sqrt{2}}{2}\left[|\Lambda = 1\rangle + |\Lambda = -1\rangle\right] \tag{2.34}$$

As roto-electronic couplings are not included in this formalism, the $|\Pi_{A''}\rangle$ state is identical to the adiabatic state $1A''$. V_{12} is the diabatic potential coupling as in equation (2.30), and the diabatic potentials V_Π and V_2 are defined using[109]

$$V_{\Pi_{A'}} = V_\Pi - V_2 \tag{2.35}$$

$$V_{\Pi_{A''}} = V_\Pi + V_2 \tag{2.36}$$

The four diabatic potentials V_Σ, V_{12}, V_2 and V_Π thus define the basis. They can be obtained from the three adiabatic potentials $U_{1A'}$, $U_{2A'}$, $U_{1A''}$ and the mixing angle χ via[109]

$$V_\Sigma = U_{1A'}\sin^2\chi + U_{2A'}\cos^2\chi \tag{2.37}$$

$$V_\Pi = \frac{1}{2}\left[U_{1A'}\cos^2\chi + U_{2A'}\sin^2\chi + U_{1A''}\right] \tag{2.38}$$

$$V_{12} = \frac{1}{2}\sin 2\chi\left[U_{1A'} - U_{2A'}\right] \tag{2.39}$$

$$V_2 = \frac{1}{2}\left[-U_{1A'}\cos^2\chi - U_{2A'}\sin^2\chi + U_{1A''}\right] \tag{2.40}$$

Note that the differences between these equations and those in ref. 109 are because, here, the ground X state is $^2\Pi$ and the excited A state is $^2\Sigma^+$. In the papers of Alexander and Corey,[109,112] the system considered was CN + He, where the $^2\Sigma^+$ state is the ground (X) state and the excited (A) state is $^2\Pi$.

In the diabatic basis, V_Σ governs scattering in the excited $|\Sigma^+\rangle$ state, and scattering in the Π state is ruled by V_Π and V_2. V_{12} is the diabatic coupling between the symmetric $|\Sigma^+\rangle$ and $|\Pi_{A'}\rangle$ states; the asymmetric $|\Pi_{A''}\rangle$ state is not coupled to either of the symmetric states.

The mixing angle χ is obtained from *ab initio* calculations as described in ref. 28. The adiabatic states $|1A'\rangle$ and $|2A'\rangle$ are quasi-diabatised[28] to obtain the (approximate) diabatic states $|\Sigma_{A'}\rangle$, $|\Pi_{A'}\rangle$ and the mixing angle, as in equation (2.30). These diabatic states are shown in figure 2.8, together with the $1A'$ and $2A'$ adiabatic surfaces.

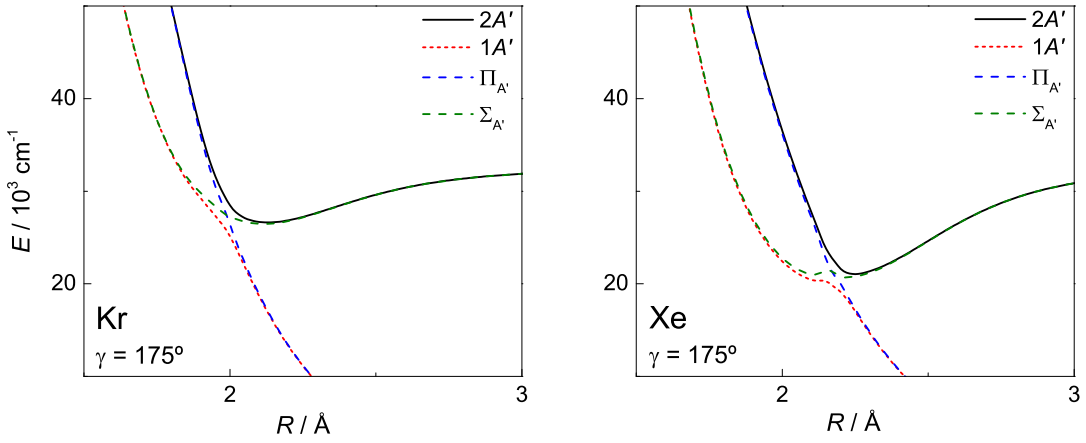

Figure 2.8: Cuts through the adiabatic potentials $1A'$ (red dots) and $2A'$ (black line), and diabatic potentials $\Pi_{A'}$ (blue dashes) and $\Sigma_{A'}$ (green dashes) for OH(X,A)+Kr[21,28] (left) and OH(X,A)+Xe[90] (right). Thermal collision energy lies at 32,907 cm^{-1} for the left hand panel and 32,985 cm^{-1} on the right.

2.3.4 Conical intersections

To summarise the points made in the previous subsections, the *adiabatic* representation is one in which the potential energy matrix, $\mathbf{A}$, is diagonal. Non-adiabatic coupling is kinetic, governed by off-diagonal elements of $\hat{\mathbf{\Lambda}}$, i.e. $\boldsymbol{d}_{ij}$. In the *diabatic* representation,

the kinetic couplings are set to zero (or as near as possible). Instead, the potential energy matrix $\mathbf{D}$ is non-diagonal, with the off-diagonal elements representing potential couplings between diabatic states.

By transforming to the diabatic representation, the singularity of infinite coupling at a potential crossing (equation (2.22)) is removed, as the couplings are now local potential terms rather than non-local derivative operators. Equation (2.15) now becomes

$$i\hbar\frac{\partial\psi_j}{\partial t} = \left[T_N + V_{jj}\right]\psi_j \tag{2.41}$$

or, in matrix form,

$$i\hbar\frac{\partial\boldsymbol{\psi}}{\partial t} = \left[T_N\boldsymbol{I} + \boldsymbol{V}\right]\boldsymbol{\psi} \tag{2.42}$$

Following ref. 39, the coordinate vector of the point of degeneracy is $\boldsymbol{R}_0$, and $\boldsymbol{R}$ is the displacement from $\boldsymbol{R}_0$. At $\boldsymbol{R}_0$, the adiabatic and diabatic bases are taken to be equal.[39] Expanding in a Taylor series about $\boldsymbol{R}_0$,

$$\boldsymbol{V}(\boldsymbol{R}) = \boldsymbol{V}(\boldsymbol{R}_0) + \boldsymbol{V}^{(1)} + \boldsymbol{V}^{(2)} + \ldots \tag{2.43}$$

The first-order elements around $\boldsymbol{R}_0$ can be expressed in the adiabatic basis as[39]

$$V_{kl}^{(1)x} = \left[\langle k|\frac{\partial\hat{H}_{\mathrm{el}}}{\partial R_x}|l\rangle\right]R_x \tag{2.44}$$

and we adopt the notation (for a two-state system)

$$\boldsymbol{V}_{11}^{(1)} = \boldsymbol{\kappa}_1\cdot\boldsymbol{R} \quad , \quad \boldsymbol{V}_{22}^{(1)} = \boldsymbol{\kappa}_2\cdot\boldsymbol{R} \quad , \quad \boldsymbol{V}_{12}^{(1)} = \boldsymbol{\lambda}\cdot\boldsymbol{R} \tag{2.45}$$

Now, considering a two-state system in which $\phi = c_1\phi_1 + c_2\phi_2$, the secular equations are[8]

$$\begin{pmatrix} V_{11}-E & V_{12} \\ V_{12} & V_{22}-E \end{pmatrix}\begin{pmatrix} c_1 \\ c_2 \end{pmatrix} = 0 \tag{2.46}$$

which leads to the pair of solutions

$$E_{\pm} = \frac{1}{2}\left[(V_{11} + V_{22}) \pm \sqrt{(V_{11} - V_{22})^2 + 4V_{12}^2}\right] \tag{2.47}$$

This means that the conditions for a point of degeneracy between the two adiabatic potentials are that $V_{11} = V_{22}$ and $V_{12} = 0$. In order to satisfy these, at least two independent nuclear degrees of freedom are needed — for diatomic molecules, there is only one (the internuclear separation), leading to the famous *non-crossing rule*.[113] However, for polyatomic systems, it is possible for potential energy surfaces to touch or intersect.[37]

The reason why at least two degrees of freedom are necessary is because there needs to be a *tuning* co-ordinate — which brings the adiabatic states closer in energy, up to a point of degeneracy, while keeping $V_{12} = 0$ — and a *coupling* co-ordinate, which reduces the symmetry of the system to induce $V_{12} \neq 0$, thus causing the states to avoid a crossing. Moving along either of these co-ordinates lifts the degeneracy, while motion along the remaining $F-2$ co-ordinates (where $F = 3N-6$ is the total number of degrees of freedom for N atoms) can take place without doing so. The tuning and coupling co-ordinates define the so-called *branching space*.

For the OH–Rg systems discussed in this thesis, there are three atoms and so $F-2 = 1$, meaning that adiabatic potential crossings can take place at isolated points. In higher-dimensional systems, it is possible to have seams of such intersections — a well-studied example of this is the OH(X,A)–H_2 system.[5,114–116] In the OH(X,A)–Kr/Xe systems, the tuning co-ordinate (conventionally called $\boldsymbol{g}$) corresponds to motion of the rare gas atom radially towards and away from OH in the linear configuration, while the coupling co-ordinate, $\boldsymbol{h}$, is motion away from linearity. This is a symmetry-induced intersection, where, at linearity, the potentials are of different symmetry (Σ and Π) and so can cross; motion along $\boldsymbol{g}$ retains this symmetry while motion along $\boldsymbol{h}$ reduces it. When two states have the same symmetry, it is possible to have an 'accidental' intersection, where it just so happens that $V_{11} = V_{22}$ and $V_{12} = 0$ at a certain point.

A plot of the OH–Kr adiabatic potentials in the $\boldsymbol{g} - \boldsymbol{h}$ co-ordinate system is shown in figure 2.9, demonstrating the point of degeneracy and how motion along either $\boldsymbol{g}$ or $\boldsymbol{h}$ breaks this degeneracy.

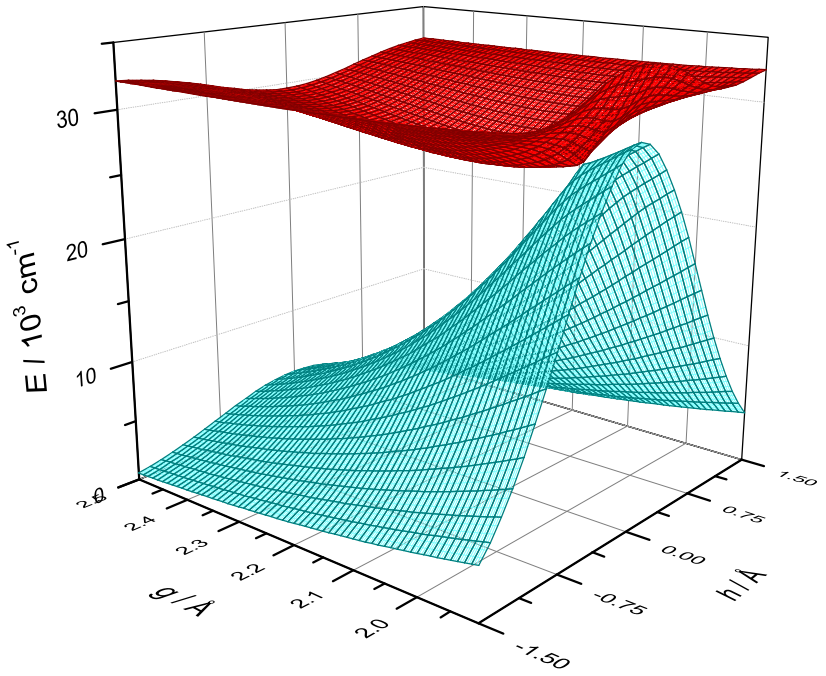

Figure 2.9: *g-h* plot of the adiabatic potential energy surfaces for OH(A) + Kr[28], with $1A'$ displayed in blue and $2A'$ in red. An expanded version of the conical intersection is shown in figure 2.10. Here, $\boldsymbol{g}$ corresponds to motion of Kr radially towards and away from OH in the linear configuration, and $\boldsymbol{h}$ is motion orthogonal to this (away from linearity).

Intersections such as these are often referred to as 'conical' intersections. Taking $(V_{11} - V_{22})$ as the x coordinate and V_{12} as y, equation (2.47) describes a double cone (diabolo) with its vertex at the point of degeneracy.[36] This can be seen in figure 2.10, which is an expanded view of figure 2.9. For this reason, conical intersections are also sometimes called 'diabolical points'.[38,117]. Close to degeneracy, $(V_{11} - V_{22})^2 \simeq (\boldsymbol{\kappa}_1 - \boldsymbol{\kappa}_2) \cdot \boldsymbol{R}$, the gradient difference vector ($\boldsymbol{g}$), and $V_{12} \simeq \boldsymbol{\lambda} \cdot \boldsymbol{R}$, the non-adiabatic coupling vector ($\boldsymbol{h}$). This means that degeneracy is lifted (to first order) on moving in the $\boldsymbol{g} - \boldsymbol{h}$ plane, and the almost linear dependence of the energy on moving away produces the 'diabolo' double-cone effect, as shown in figure 2.11.

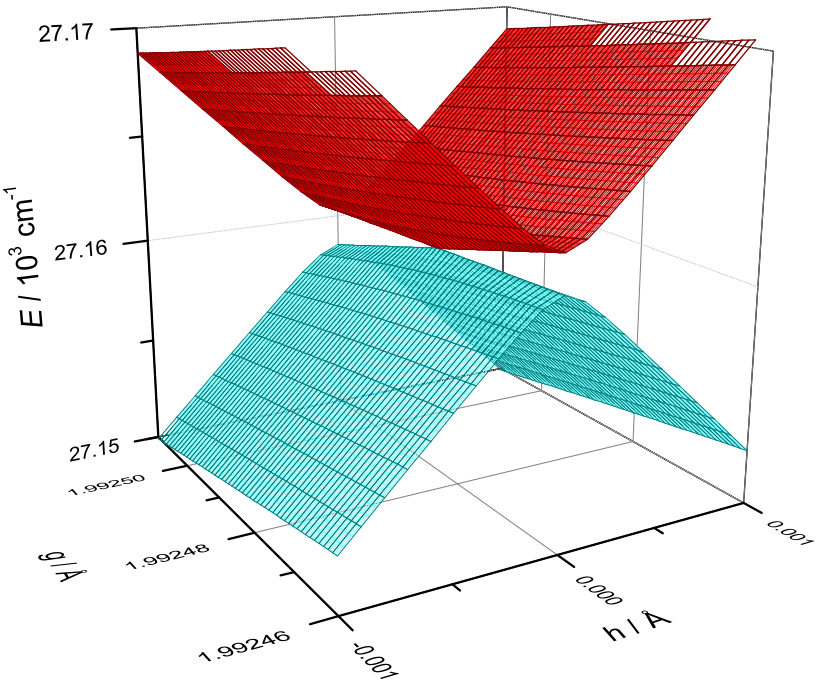

Figure 2.10: g-h plot of the adiabatic potential energy surfaces for OH(A) + Kr[28], with $1A'$ displayed in blue and $2A'$ in red. This figure is an expanded version of figure 2.9, and $\boldsymbol{g}$ and $\boldsymbol{h}$ have the same meanings as in that figure.

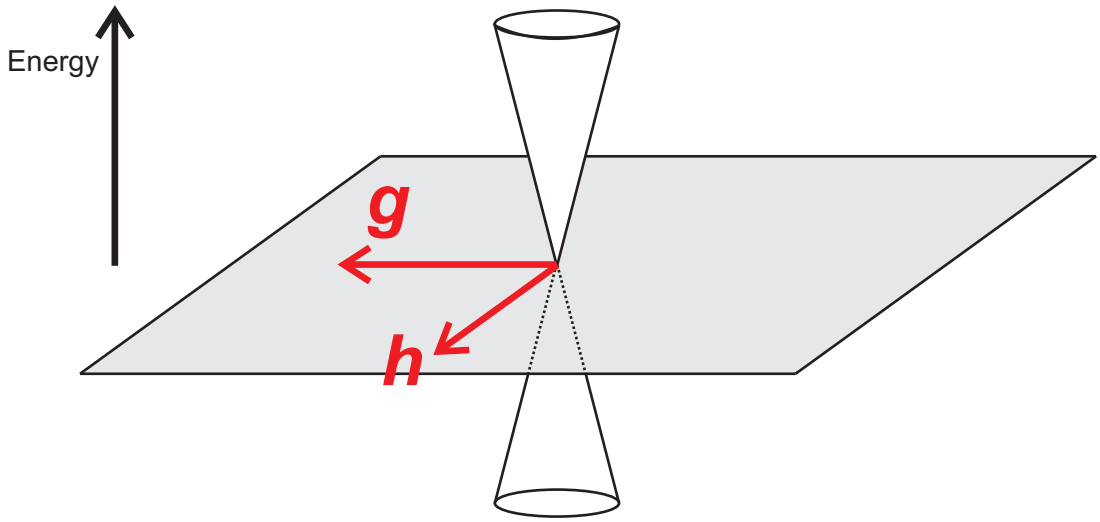

Figure 2.11: Diagram of a conical intersection, showing the $\boldsymbol{g} - \boldsymbol{h}$ branching plane

Longuet-Higgins developed a prescription for locating a conical intersection.[37] If the wavefunction changes sign on completing an adiabatic closed loop on the PES, there must be a point within that loop where the wavefunction is discontinuous — implying an intersection with another PES. The phase shift acquired by the wavefunction after an odd number of circuits around the conical intersection — even if the intersection itself is unreachable at that energy — is known as the geometric, or Berry, phase[36,118,119] and has been seen to have demonstrable, though small, interference effects in reactions such as H + H_2.[120] However, it is still a challenge to discern these effects experimentally.[121] Transforming to a diabatic basis means that these effects no longer need to be accounted for separately.[39] The sign change can easily be seen by considering a two-state system with a wavefunction $\phi = c_1\phi_1 + c_2\phi_2$, like equations (2.46) and (2.47), and, following ref. 36, defining an angle θ via

$$R\cos\theta = \frac{1}{2}(V_{11} - V_{22}) \tag{2.48}$$

$$R\sin\theta = V_{12} \tag{2.49}$$

$$R = \frac{1}{2}\sqrt{(V_{11} - V_{22})^2 + 4V_{12}^2} \tag{2.50}$$

Taking the lower root of equation (2.47), E_-, and substituting into the secular equations (equation (2.46)):

$$c_1(R\cos\theta + R) + c_2 R\sin\theta = 0 \tag{2.51}$$

$$c_1 R\sin\theta + c_2(R - R\cos\theta) = 0 \tag{2.52}$$

both of which lead to

$$\frac{c_1}{c_2} = \frac{\cos\theta - 1}{\sin\theta} = \frac{-\sin\theta}{\cos\theta + 1} = -\tan\frac{\theta}{2} \tag{2.53}$$

giving the real solutions

$$c_1 = \sin\frac{\theta}{2} \quad ; \quad c_2 = -\cos\frac{\theta}{2} \tag{2.54}$$

$$c_1 = -\sin\frac{\theta}{2} \quad ; \quad c_2 = \cos\frac{\theta}{2} \tag{2.55}$$

Moving in a loop around the conical intersection, from $\theta = 0$ to 2π, the wavefunction $\phi = c_1\phi_1 + c_2\phi_2$ will therefore change sign.[36]

As described in chapter 1, in many systems, conical intersections act as a funnel transferring population from one electronic state to another. However, the surfaces are not only coupled at the point of degeneracy itself, but for a region around it. The degree of mixing of adiabatic surfaces is parametrised by the mixing angle, χ, defined in equation (2.30). Given the adiabatic PESs $1A'$, $2A'$ and the diabatic coupling V_{12} from *ab initio* calculations, χ can be calculated by considering the transformation (for a two-state system)

$$\mathbf{D} = \mathbf{C}_2^T\mathbf{A}\mathbf{C}_2 \tag{2.56}$$

leading to

$$\begin{pmatrix} V_{\Pi_{A'}} & V_{12} \\ V_{12} & V_{\Sigma} \end{pmatrix} = \begin{pmatrix} U_{1A'}\cos^2\chi + U_{2A'}\sin^2\chi & (U_{1A'} - U_{2A'})\cos\chi\sin\chi \\ (U_{1A'} - U_{2A'})\cos\chi\sin\chi & U_{2A'}\cos^2\chi + U_{1A'}\sin^2\chi \end{pmatrix} \tag{2.57}$$

which gives the mixing angle via

$$\chi = \frac{1}{2}\arcsin\left(\frac{2V_{12}}{U_{1A'} - U_{2A'}}\right) \tag{2.58}$$

$$= \frac{1}{2}\arctan\left(\frac{2V_{12}}{V_{\Pi_{A'}} - V_{\Sigma}}\right) \tag{2.59}$$

Plots of the mixing angle, χ, for the OH(X,A) + Rg systems are given in the left and right columns of figure 2.12 for Kr and Xe respectively. It can be seen that mixing is largest at closer approaches, and is zero in the linear geometry, increasing to a maximum near

$\gamma \approx 120°$. The mixing angle then decreases to near-zero at the T-shaped configuration, changes sign and there is another region of strong mixing near $\gamma \approx 60°$.

As the OH–Rg minima are further out than the HO–Rg minima, the regions of strong mixing near the hydrogen end are energetically inaccessible.[28] However, the strongly mixed region in HO–Rg near-linear geometries is accessible at thermal collision energies — and, due to the increased depth of the HO–Xe well compared to HO–Kr, there is expected to be more quenching for Xe than Kr due to the strongest mixing being at the bottom of the well, as opposed to on the inner wall as for Kr. Stronger mixing at more bent configurations will favour these geometries for quenching,[28] so the areas of the PES most responsible for quenching are found by balancing the value of χ with the energetic accessibility.

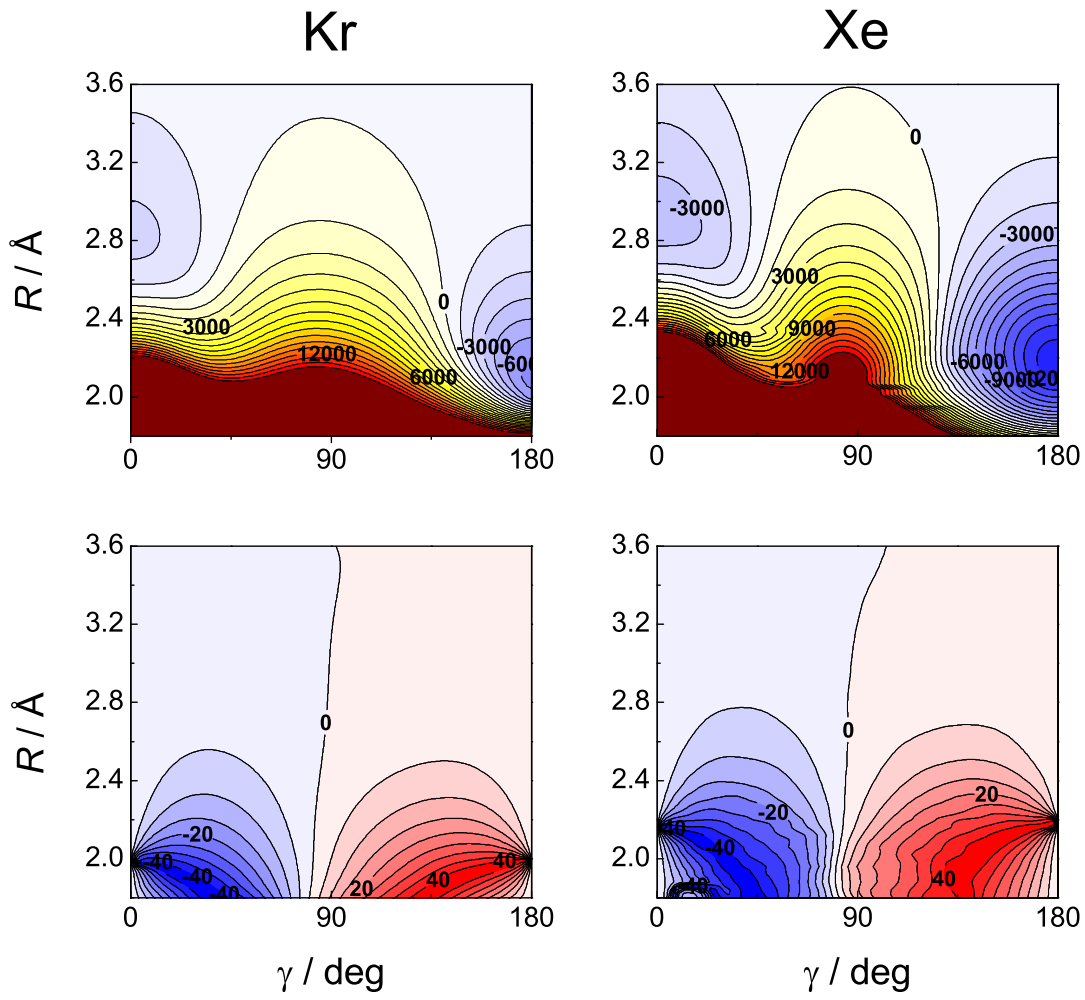

Figure 2.12: Plots of the excited state PES (top) and mixing angle, χ (bottom) for OH(X,A)+Kr[21,28] (left) and OH(X,A)+Xe[90] (right). Energies are given in cm^{-1} and mixing angles in degrees.

2.4 Roto-electronic couplings

As described in section 2.2.2, the approach of a perturber (Kr or Xe atom) to the ground state OH(X) radical lowers the cylindrical $C_{\infty v}$ symmetry of the system to C_s in non-linear configurations.[85,122] Under this symmetry, the electronic wavefunction of the A $^2\Sigma^+$ state is symmetric (A') with respect to reflection in the scattering plane, and the doubly degenerate Π state is split into states of A' and A'' reflection symmetry. These correspond (semiclassically) to the unpaired electron lying in an orbital in (A') or perpendicular to (A'') the scattering plane.

The discussion so far (section 2.3.3) has assumed that coupling can only take place between states of the same symmetry, with the $1A''$ state being the same in the adiabatic and diabatic representations. However, it could also be possible that this state can play a part in the dynamics. An overall rotation of the three-atom system about an axis perpendicular to the O-H bond (x or y, if the O-H bond is z) will be antisymmetric[123] and thus can couple electronic states of different electronic symmetry: $A' \times A'' \times A'' = A'$, the totally symmetric representation.[8,85,122]

This is a different type of coupling to that previously discussed. So far, electrostatic potential couplings (the term V_{12} in the diabatic representation) have described a localised interaction between electronic and nuclear motion — that is, a breakdown of the Born-Oppenheimer approximation — near to a crossing (avoided or real). The roto-electronic couplings introduced in this section are examples of geometric coupling,[124] where the non-applicability of the Born-Oppenheimer approximation derives from the description of electronic motion using a nuclear co-ordinate system that is itself moving. Centrifugal or Coriolis forces act on the electrons — semiclassically, this can be visualised as the cloud of electrons drifting behind the nuclei as the system rotates.[125] This has links to 'gyroscopic perturbations' in triatomic molecules, which are heterogeneous perturbations between states with the same S but different Λ caused by the $\boldsymbol{L}$-uncoupling operator.[126] This kind of coupling applies at all ranges, even if there is no interaction between the

potentials,[124] but, of course, when the potentials are far apart the coupling cannot induce any appreciable mixing.

This thesis considers two kinds of roto-electronic coupling in triatomic systems. These are *Renner-Teller* coupling, which involves the $\hat{J}_z\hat{L}_z$ term in the triatomic Hamiltonian and couples states with $\Delta\Lambda = 0$ (the $\Pi_{A'}$ and $\Pi_{A''}$ states that are degenerate at linearity), and *Coriolis* coupling, which is governed by the $\hat{J}_+\hat{L}_- + \hat{J}_-\hat{L}_+$ term and couples states that have $\Delta\Lambda = \pm 1$ (the $\Sigma_{A'}$ and $\Pi_{A''}$ states).

Renner-Teller (RT) coupling involves bending of a linear complex.[127–129] At linearity, λ, the projection of electronic orbital angular momentum on the linear axis ($\lambda = \pm\Lambda$) is a good quantum number; on bending, this ceases to be the case and coupling is possible for states with non-zero electronic angular momentum.[130,131] The most well-investigated triatomic cases are the NH_2 radical[128,130,131] and the photolysis of $H_2O(\tilde{B})$.[132–134]. The competition between RT and conical intersection channels has been investigated recently by Zhou *et al.*[135], following earlier work by Dixon[136], using quantum mechanical methods.

Coriolis coupling mixes states of different symmetry by means of a rotation – see for example refs. 132,137,138. In contrast to RT coupling, Coriolis coupling can only mix states that differ in their electronic angular momentum by $\Delta\Lambda = \pm 1$.

Recent examples of systems where these kinds of coupling have been investigated include quenching in NH(a)+H and C+H_2,[139,140] and the inclusion of Coriolis coupling in quantum mechanical (QM) studies such as the $O(^1D) + H_2 \rightarrow OH(X) + H$ reaction.[141] RT coupling has been considered in a trajectory surface-hopping model by Santoro, Petrongolo and Schatz for the $N(^2D) + H_2$ system,[131,142] following the QM study of Goldfield *et al.*[130]

Further details of these couplings that are of relevance to the systems considered in this thesis will be discussed in chapter 5.

2.5 Spin-orbit coupling

As the theoretical methods used in this thesis are (quasi-)classical in character, spin-orbit coupling — which derives from the purely quantum concept of spin — is not considered in them. However, it is useful to remember that it may play a part in the systems considered here.

Spin-orbit coupling is the interaction of the electron's intrinsic magnetic moment (from its spin) with the magnetic field generated by its orbital motion.[8] It is present in systems of non-zero S and Λ, and the relevant operator is $\boldsymbol{L} \cdot \boldsymbol{S}$. Recalling section 2.1, $\boldsymbol{L}$ and $\boldsymbol{S}$ couple in Hund's case (a) to form the projection $\Omega = |\Lambda + \Sigma|$, where Ω can be $\frac{3}{2}$ or $\frac{1}{2}$ for OH(X).

States of definite $|\Lambda\Sigma\Omega\rangle$ can be coupled by a spherical perturber:[143,144]

$$\langle \Lambda'\Sigma'\Omega'|\hat{H}_{\mathrm{so}}|\Lambda\Sigma\Omega\rangle = \sum_{\lambda} d^{\lambda}_{\Omega-\Omega',0}(\gamma) H^{\mathrm{so}}_{\lambda,\Omega-\Omega'}(R) \tag{2.60}$$

The $\hat{L}_z\hat{S}_z$ term couples the Π_Ω states, and $\hat{L}_y\hat{S}_y$ and $\hat{L}_x\hat{S}_x$ couple the Σ and Π states. There are terms of both $\Delta\Omega = 0, \pm 2$ connecting the Σ and Π states — in isolated OH (and linear OH–Rg and HO–Rg complexes), the $\Delta\Omega = 0$ terms are non-zero (giving rise to the Λ-doublet splitting) while the $\Delta\Omega = \pm 2$ terms are zero. These terms may not be zero in non-linear complexes.

2.6 Summary

The spectroscopy of the OH radical in its ground and first excited electronic states has been introduced in this chapter, with particular attention paid to the Zeeman sublevels and their interaction with an external magnetic field, which will form the basis of the Zeeman quantum beat spectroscopy technique described in chapter 4. In the rest of this chapter, the potential energy surfaces (PESs) for the interaction of OH(X,A) with Kr and Xe have been shown, and the transformation between electronically adiabatic and diabatic

bases was discussed.

The various types of coupling between different potentials have been considered – electrostatic, rovibrational and spin-orbit. One particular focus has been on the *conical intersection* between the OH(X) and OH(A) potentials in the HO–Rg configuration.

The PESs and concepts from this chapter will be used in the theoretical methods developed in chapters 4 and 6, and these methods will be employed for calculations presented in chapters 6 and 7.

Chapter 3

Theory: Collisions, vectors and polarisation

In this chapter, the basic concepts such as cross-sections and opacity functions that lie at the heart of the discussion in this thesis will be defined for use in later chapters. The theory of angular momentum and its polarisation will then be set out in as far as it is relevant to the present work, with particular attention paid to the classical formalism for better comparison with quasi-classical calculations. The links between the quantum and classical pictures will be explored, and a description will be given of the polarisation of light.

The focus of this chapter is on the notation, formalisms and concepts used in this thesis. The review by Paterson *et al.* compares several considerations of these subjects, giving relations between this and other treatments.[25]

3.1 Opacity functions and cross-sections

The experiments described in this thesis measure thermally averaged rate constants, $k(T)$, for various processes. These are defined as the integral of the excitation function $\sigma(E_t)$ over the Boltzmann distribution of collision energies at a temperature T, where the excitation function simply describes the variation of the *cross-section* for the process of interest with

collision energy, E_t.[145]

$$k(T) = \sqrt{\frac{8k_BT}{\pi\mu}}(k_BT)^{-2}\int_{E_0}^{E_2}\sigma(E_t)E_t\exp\left(\frac{-E_t}{k_BT}\right)\,\mathrm{d}E_t \tag{3.1}$$

In this expression, k_B is the Boltzmann constant and μ is the reduced mass of the system. E_0 is the threshold energy for the process of interest to take place, and E_2 is set high enough to include the whole Boltzmann distribution of collision energies for that temperature.

The cross-section, σ, has units of area, and can be thought of as a 'target area' for collision in simple collision theory.[1,8] It can be related to the rate constant at fixed energy, $k(E_t)$ (as opposed to the thermal rate constant, $k(T)$, of equation (3.1)) by the relative velocity $v_{\mathrm{rel}}(E_t)$[1,8]

$$k(E_t) = v_{\mathrm{rel}}(E_t)\sigma(E_t) \tag{3.2}$$

i.e. $k(E_t)$ is the collision volume swept out by the reactants per unit time.

In a classical collision between two particles A and B, the *impact parameter*, b, can be defined as the perpendicular distance between B and the path of A (see figure 3.1) — if there were no intermolecular potential, b would be the distance of closest approach.[1,8]

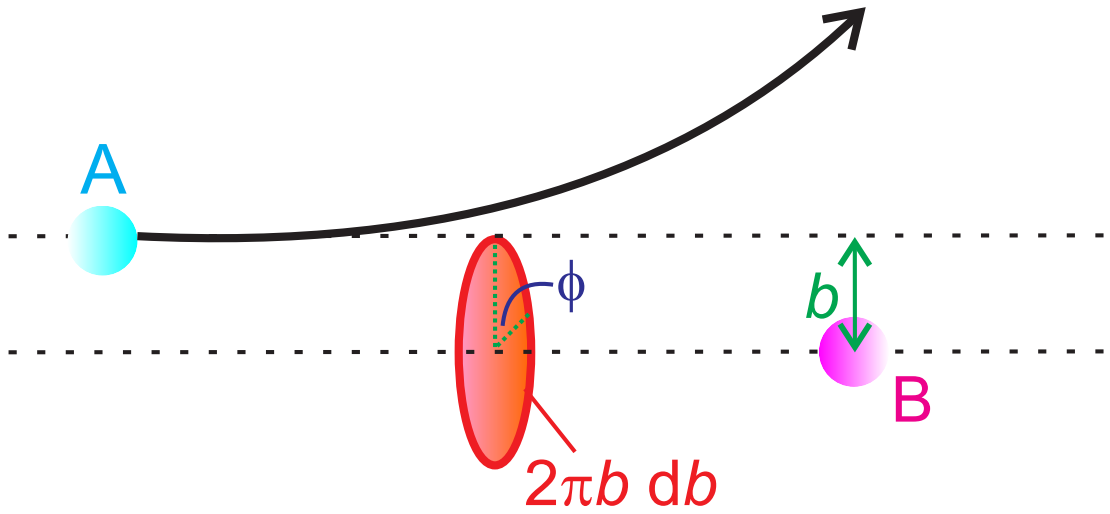

Figure 3.1: Classical collision between two particles, A and B, with impact parameter b

Because the system of figure 3.1 has cylindrical symmetry, averaging over the azimuthal angle ϕ reveals that the area of the ring shown is $2\pi b\,\mathrm{d}b$. The classical cross-section can

now be described as a partial cross-section, $\sigma(b)$, averaged over impact parameter:

$$\sigma = \int_0^{b_{\max}} \sigma(b)\ \mathrm{d}b \tag{3.3}$$

in which $\sigma(b)$ is the probability that the transition of interest takes place multiplied by the area of the ring, $2\pi b$.

$$\sigma(b) = 2\pi b P(b) \tag{3.4}$$

$P(b)$, the transition probability as a function of impact parameter, is known as the *opacity function*. Classically, if $\mathcal{N}_r$ collisions out of $\mathcal{N}_{\mathrm{tot}}$ undergo the transition at impact parameter b, then

$$P(b) = \frac{\mathcal{N}_r(b)}{\mathcal{N}_{\mathrm{tot}}(b)} \tag{3.5}$$

The impact parameter gives the (classical) orbital angular momentum of the system via $|\boldsymbol{\ell}| = \mu v_{\mathrm{rel}} b$, and this corresponds to the quantum mechanical ℓ via $|\boldsymbol{\ell}| = \hbar\sqrt{\ell(\ell+1)}$. As J is the sum of ℓ and j (or F), this relationship between J and b provides a link between the quantum and classical descriptions. The quantum mechanical opacity function can be expressed either as $P(\ell)$ or $P(J)$, with the partial cross-section being given by either of

$$\sigma(\ell) = \frac{\pi}{k_i^2}(2\ell+1)P(\ell) \tag{3.6}$$

$$\sigma(J) = \frac{\pi}{k_i^2}\frac{2J+1}{2j+1}\left[2\min(J,j)+1\right]P(J) \tag{3.7}$$

where k_i is the wavevector (the linear momentum divided by $\hbar$).

In the quantum picture, the integral over b is replaced by a sum over J:

$$\sigma = \sum_J \sigma(J) \tag{3.8}$$

This shows how the experimentally measured rate constants are related to the more fundamental opacity functions. Going deeper into scattering theory, the opacity function

for a transition from state $|i\rangle$ to $|f\rangle$ can be expressed as[10]

$$P(J) = |T_{if}^{J}|^2 \tag{3.9}$$

To explain what this means, we introduce the time-independent picture of quantum scattering.[8,10,146] The incoming molecule is represented as a plane wave interacting with a scattering centre. The *scattering matrix* relates the incoming and outgoing waves:

$$\mathbf{S}|\psi_{\text{in}}^{J}\rangle = |\psi_{\text{out}}^{J}\rangle \tag{3.10}$$

The incoming plane wave can be decomposed into a series of *partial waves* with increasing values of J^* — this is the quantum analogue to classical collisions at different impact parameters, b. Mathematically, this is done by expressing the plane wave as a sum of Bessel functions of the first kind.[10]

It is often more useful to define the *transformation matrix*, $\mathbf{T}$:

$$\mathbf{T}|\psi_{\text{in}}^{J}\rangle = (\mathbf{1} - \mathbf{S})|\psi_{\text{in}}^{J}\rangle = |\psi_{\text{in}}^{J}\rangle - |\psi_{\text{out}}^{J}\rangle \tag{3.11}$$

It is the elements of this matrix that appear in equation (3.9), as the square modulus of these $\mathbf{T}$-matrix elements gives the probability of scattering from $|i\rangle$ to $|f\rangle$ at total angular momentum J.

In general, the state of a system can be described by the *density matrix*. The density operator is given by[147]

$$\hat{\rho} = |\psi\rangle\langle\psi| = \sum_{mn} c_m c_n^* |\psi_m\rangle\langle\psi_n| \tag{3.12}$$

meaning that the elements of the density matrix are

$$\langle\psi_i|\hat{\rho}|\psi_j\rangle = c_i c_j^* \tag{3.13}$$

*In the body-fixed frame; in the space-fixed frame, the decomposition is in ℓ

The diagonal elements thus give the probabilities of the eigenstates, and the off-diagonal elements describe the coherences between them. The expectation value of an arbitrary operator $\hat{Q}$ is[147]

$$\langle \hat{Q} \rangle = \mathrm{Tr}[\hat{\rho}\hat{Q}] \tag{3.14}$$

Considering here a pure, coherent state, the density matrix is diagonal and the wave-function can be expressed as a linear combination of basis functions.

$$|\psi\rangle = \sum_n c_n |\psi_n\rangle \tag{3.15}$$

For a state like this, and also fixing total J using the partial wave expansion, we have

$$|\psi^J_{\mathrm{in}}\rangle = \sum_i c_i |\psi^J_i\rangle \tag{3.16}$$

$$|\psi^J_{\mathrm{out}}\rangle = \sum_f c_f |\psi^J_f\rangle \tag{3.17}$$

In this case, with the incoming partial wave being a single eigenfunction,[10]

$$\begin{aligned} T^J_{fi} =& \langle \psi^J_f | \hat{T} | \psi^J_i \rangle = \langle \psi^J_f | \psi^J_i \rangle - \langle \psi^J_f | \hat{S} | \psi^J_i \rangle \\ =& \langle \psi^J_f | \psi^J_i \rangle - \langle \psi^J_f | \psi^J_{\mathrm{out}} \rangle = \langle \psi^J_f | \psi^J_i \rangle - \sum_n c_n \langle \psi^J_f | \psi^J_n \rangle \\ =& \delta_{fi} - \sum_n \delta_{fn} c_n = \delta_{fi} - c_f \end{aligned} \tag{3.18}$$

Taking the square modulus, as in equation (3.9),

$$|T^J_{fi}|^2 = \delta_{fi} + |c_f|^2 - 2\delta_{fi}\mathrm{Re}(c_f) \tag{3.19}$$

For an inelastic collision, this means that $P(J) = |c_f|^2$, so its limits range from 0 to 1. However, for an elastic collision, the opacity function can range from[18] 0 to 4 — note that the *classical* opacity function for an elastic collision does not converge and tends to unity at high b. This is because there is no cut-off determining how glancing a blow can still

count as a 'collision'; in quantum mechanics the Heisenberg uncertainty principle fulfils this role.

3.2 Vector correlations

An atom-diatom collision, such as the ones considered in this thesis, can be completely specified by four vectors:[8,32,33]

$\boldsymbol{k}$ Initial relative velocity vector

$\boldsymbol{j}$ Initial angular momentum vector of the diatom

$\boldsymbol{k'}$ Final relative velocity vector

$\boldsymbol{j'}$ Final angular momentum vector of the diatom

The full four-vector correlation can be integrated over the appropriate angles to give a lower-order correlation that is more readily interpreted.[19,30,32,33,148]. In this way, there are four possible three-vector correlations. The most useful are the $\boldsymbol{k}-\boldsymbol{k'}-\boldsymbol{j'}$ correlation[149], obtained by integrating over all directions of $\boldsymbol{j}$, which describes the product rotational polarisation with respect to the scattering plane, and the $\boldsymbol{k}-\boldsymbol{j}-\boldsymbol{j'}$ correlation[19], which illustrates the dependence of the collisional depolarisation on the initial velocity vector.

Integrating these distributions over a further vector results in one of six possible two-vector correlations.[32] The $\boldsymbol{k}-\boldsymbol{k'}$ correlation is the familiar differential cross-section (DCS), which is not discussed in this thesis but which has been extensively investigated for many systems, both experimentally and theoretically. Of more interest to the present study is the correlation between $\boldsymbol{j}$ and $\boldsymbol{j'}$, which quantifies the extent of angular momentum depolarisation in the collision. To describe this further, the spatial distribution of $\boldsymbol{j}$ will first be examined, and then the distribution of $\boldsymbol{j'}$ with respect to $\boldsymbol{j}$. Note that, in the present discussion, $\boldsymbol{j}$ stands for the total angular momentum vector of the diatom (OH) — $\boldsymbol{N}$ or $\boldsymbol{F}$ could be used in its place, depending whether electron and/or nuclear spin is being included (see chapter 2).

3.2.1 Lab-frame distribution of $\boldsymbol{j}$

Classically, the lab-frame distribution of $\boldsymbol{j}$ — that is, the two-vector correlation between $\boldsymbol{j}$ and the Z axis — can be expanded in the complex conjugates of modified spherical harmonics.[150,151] This function gives the probability of $\boldsymbol{j}$ lying along the direction specified by the angles (θ_j, ϕ_j):

$$P(\theta_j, \phi_j) = \sum_{k=0}^{\infty} \sum_{q=-k}^{k} \frac{2k+1}{4\pi} a_q^{(k)} C_{kq}^*(\theta_j, \phi_j) \tag{3.20}$$

The expansion coefficients, $a_q^{(k)}$, are given by

$$a_q^{(k)} = \langle C_{kq}(\theta_j, \phi_j) \rangle \tag{3.21}$$

and Hertel-Stoll normalised to obtain real polarisation parameters[152] ($q > 0$):

$$a_{q+}^{\{k\}} = (-1)^q \sqrt{2} \mathrm{Re}\left(a_{+q}^{(k)}\right) \tag{3.22}$$

$$a_{q-}^{\{k\}} = (-1)^q \sqrt{2} \mathrm{Im}\left(a_{+q}^{(k)}\right) \tag{3.23}$$

$$a_0^{\{k\}} = a_0^{(k)} \tag{3.24}$$

Note that the modified spherical harmonics $C_{kq}(\theta_j, \phi_j)$ are related to the spherical harmonics $Y_{kq}(\theta_j, \phi_j)$ by

$$C_{kq}(\theta_j, \phi_j) = \sqrt{\frac{4\pi}{2k+1}} Y_{kq}(\theta_j, \phi_j) \tag{3.25}$$

Quantum mechanically, the direction of $\boldsymbol{j}$ cannot be precisely defined in this way. Instead, the density matrix is expanded in Clebsch-Gordan coefficients:[150,151]

$$\langle jm|\rho|jm'\rangle = \sum_{k=0}^{2j} \sum_{q=-k}^{k} \frac{2k+1}{2j+1} a_q^{(k)} \langle jm, kq|jm'\rangle \tag{3.26}$$

In this expansion, the $a_q^{(k)}$ polarisation parameters are given by

$$a_q^{(k)} = \sum_{mm'} \langle jm|\rho|jm'\rangle \langle jm, kq|jm'\rangle \tag{3.27}$$

To provide a link between the quantum and classical descriptions, it is possible to define a *minimum uncertainty state*, $|\theta_j, \phi_j\rangle$. This is a state in which $\boldsymbol{j}$ is as localised as possible around the direction (θ_j, ϕ_j).[150,151] It can be obtained by taking the state with maximum localisation along $\theta_j = 0$ – that is, $|jj\rangle$ – and rotating it:[150,151]

$$|\theta_j, \phi_j\rangle = \sum_m |jm\rangle D^j_{mj}(\phi_j, \theta_j, 0) \tag{3.28}$$

($D^j_{mj}(\phi_j, \theta_j, 0)$ is a Wigner rotation matrix, as defined in ref. 88.)

The *quantum probability density function*[150,151] then describes the population of this minimum uncertainty state. It can be obtained via[150,151]

$$Q(\theta_j, \phi_j) = \frac{\langle \theta_j, \phi_j|\rho|\theta_j, \phi_j\rangle}{\mathrm{Tr}(\rho)} \tag{3.29}$$

$$= \sum_{k=0}^{2j} \sum_{q=-k}^{k} \frac{2k+1}{4\pi} a_q^{(k)} \langle jj, k0|jj\rangle C^*_{kq}(\theta_j, \phi_j) \tag{3.30}$$

The Clebsch-Gordan coefficient tends to unity in the limit of high j, which makes equations (3.30) and (3.20) correspond.

Using the real, Hertel-Stoll normalised polarisation parameters and modified spherical harmonics,[8]

$$Q(\theta_j, \phi_j) = \sum_{k=0}^{2j} \frac{2k+1}{4\pi} \langle jj, k0|jj\rangle \left[a_0^{\{k\}} C_0^{\{k\}}(\theta_j, \phi_j) + \sum_{q=1}^{2j} a_{q+}^{\{k\}} C_{q+}^{\{k\}}(\theta_j, \phi_j) + a_{q-}^{\{k\}} C_{q-}^{\{k\}}(\theta_j, \phi_j) \right] \tag{3.31}$$

The system considered in the present work is cylindrically symmetric — the measured quantities are resolved in neither $\boldsymbol{k}$ nor $\boldsymbol{k'}$. Therefore $q = 0$ and the distributions can be azimuthally integrated, replacing the spherical harmonics with Legendre polynomials.

Classically, the probability density function becomes

$$P(\theta_j) = \sum_{k=0}^{\infty} \frac{2k+1}{2} a^{(k)} P_k(\cos\theta_j) \tag{3.32}$$

and, in the quantum description,

$$Q(\theta_j) = \sum_{k=0}^{2j} \frac{2k+1}{2} a^{(k)} \langle jj, k0|jj\rangle P_k(\cos\theta_j) \tag{3.33}$$

with the polarisation parameters

$$a^{(k)} = a_0^{(k)} = \langle P_k(\cos\theta_j)\rangle \tag{3.34}$$

The set of $a^{(k)}$ parameters specify the *polarisation* of $\boldsymbol{j}$ in the lab frame. Polarisation parameters of odd rank, k, describe the *orientation* of the angular momentum vectors of the bulk sample of OH radicals. Classically, orientation corresponds to a preferred sense of rotation of the radical — in terms of $|jm\rangle$ state populations, orientation means a preference for positive over negative m (or vice versa). The even-rank polarisation parameters describe the angular momentum *alignment*, which is a propensity to populate high $|m|$ over low $|m|$ states, or low over high — classically, a preferred plane of rotation. Figure 3.2 shows a pictorial description of orientation and alignment.

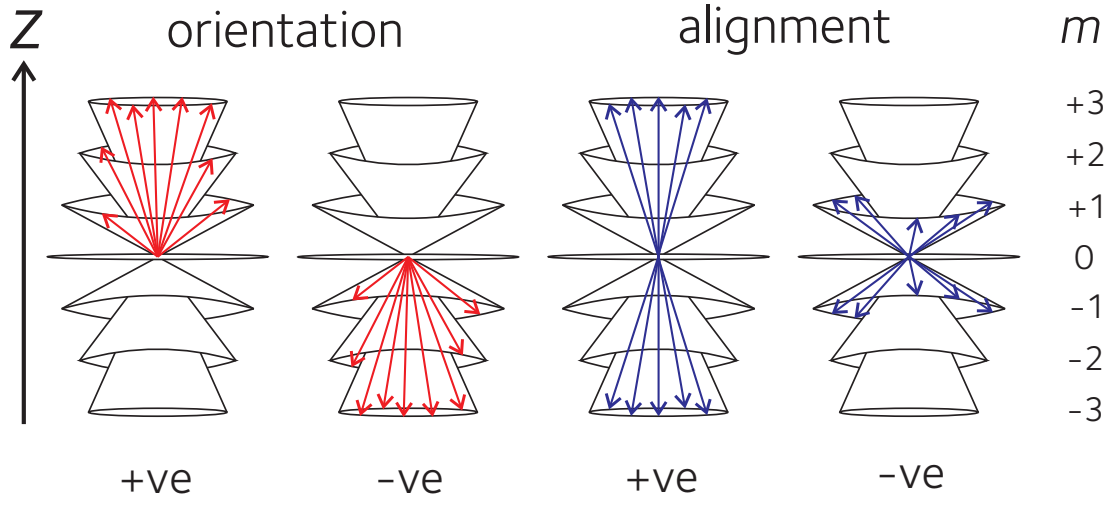

Figure 3.2: Pictorial representation of oriented and aligned distributions of vectors

Angular momentum polarisation can also be described using the density matrix (section 3.1). As described earlier, a pure state can be expressed as[88,147]

$$|\psi_n\rangle = \sum_m c_m^{(n)} |\psi_m\rangle \tag{3.35}$$

and, in the general case of an incoherent superposition of pure states with weights W_n, the density operator $\hat{\rho}$ (equation (3.12)) is

$$\hat{\rho} = \sum_n W_n |\psi_n\rangle\langle\psi_n| \tag{3.36}$$

The elements of the density matrix are therefore

$$\rho_{ij} = \sum_n W_n c_i^{(n)} c_j^{(n)} \tag{3.37}$$

If we consider a pure angular momentum state $|jm\rangle$, the density matrix elements are $\langle jm'|\hat{\rho}|jm\rangle \equiv \rho_{mm'}$. The density matrix can also be expanded using spherical tensor operators[88,147], $T_q^k(j)$

$$\rho = \sum_{kq} \rho_q^k(j) T_q^k(j) \tag{3.38}$$

where

$$T_q^k(j) = \sum_{m'm} (-1)^{j-m} \sqrt{2k+1} \begin{pmatrix} j & j & k \\ m' & -m & q \end{pmatrix} |jm\rangle\langle jm'| \tag{3.39}$$

The *state multipoles* ρ_q^k can be related to the density matrix elements via[147]

$$\rho_{mm'} = \sum_{kq} (-1)^{j-m'} \sqrt{2k+1} \begin{pmatrix} j & j & k \\ m' & -m & q \end{pmatrix} \rho_q^k \tag{3.40}$$

An oriented distribution of angular momenta has at least one non-zero odd-k multipole; an aligned distribution has at least one even-k (not $k = 0$) multipole.[147] The polarisation parameters can be expressed in terms of the state multipoles, or the density matrix

elements, noting that $q = 0$ in a cylindrically symmetric system:[147,153]

$$a^{(k)} = \sum_{m'=-j}^{j} \sum_{m=-j}^{j} \rho_{mm'} \langle jm', k0|jm\rangle \tag{3.41}$$

$$a^{(k)} = \frac{2j+1}{2k+1} \rho_0^k \tag{3.42}$$

3.2.2 $\boldsymbol{j}$-$\boldsymbol{j'}$ correlation

The $\boldsymbol{j}$-$\boldsymbol{j'}$ correlation describes the spatial distribution of the angular momentum vector after a collision with respect to the initial $\boldsymbol{j}$. This distribution can be expanded classically in Legendre polynomials as[12,154]

$$P(\theta_{jj'}) = \sum_k \frac{2k+1}{2} a^{(k)}(j, j') P_k(\cos\theta_{jj'}) \tag{3.43}$$

The depolarisation moments, $a^{(k)}(j, j')$, are given by

$$a^{(k)}(j, j') = \langle P_k(\cos\theta_{jj'})\rangle \tag{3.44}$$

and are a measure of the transfer of polarisation from the initial to the final state, with the odd-k moments dealing with transfer of orientation and the even-k moments with transfer of alignment. This thesis will mostly be concerned with the moments for $k = 1$ and 2, which are those that can be measured experimentally using the 1+1 LIF technique employed here. These have the classical limits[12]

$$-1 \leq a^{(1)} \leq 1 \tag{3.45}$$

$$-\frac{1}{2} \leq a^{(2)} \leq 1 \tag{3.46}$$

with $a^{(1)} = 1$ corresponding to complete retention of orientation, and $a^{(1)} = -1$ implying that the sense of rotation is completely reversed. Similarly, $a^{(2)} = 1$ corresponds to $\boldsymbol{j'} \parallel \boldsymbol{j}$ and $a^{(2)} = -\frac{1}{2}$ to $\boldsymbol{j'} \perp \boldsymbol{j}$.

Quantum mechanically, $a^{(k)}(j,j')$ is identical[12,25] to the tensor transfer coefficients $E^{(k)}(j,j')$ of Corey *et al.*[155], which relate the state multipoles of the density matrix after the collision to the initial state multipoles:

$$\frac{\rho_q^{(k)}(j')}{\rho_0^0(j')} = E^{(k)}(j,j')\frac{\rho_q^{(k)}(j)}{\rho_0^0(j)} \tag{3.47}$$

A further link between the quantum and classical descriptions can be made by defining the *tensor cross-sections*, $\sigma_T^{(k)}$, as

$$\sigma_T^{(k)}(j,j') = a^{(k)}(j,j')\sigma_{jj'} \tag{3.48}$$

These tensor cross-sections quantify how much polarisation is transferred from the initial to the final state during the collision. Note that the zero-order tensor cross-section, $\sigma_T^{(0)}(j,j')$, is the same as the integral cross-section $\sigma_{jj'}$. If $\mathcal{N}_{jj'}$ out of $\mathcal{N}_{\rm tot}$ classical collisions result in the transition $|j\rangle \rightarrow |j'\rangle$ taking place, then

$$\sigma_T^{(k)}(j,j') = \frac{\pi b_{\rm max}^2}{\mathcal{N}_{\rm tot}}\sum_{i=1}^{\mathcal{N}_{jj'}} P_k(\cos\theta_{jj'}^{(i)}) \tag{3.49}$$

The quantum expression for the tensor cross-sections is given by Alexander and Davis as[26,156]

$$\sigma_T^{(k)}(j,j') = \frac{\pi}{k^2}\sum_{JJ'}\sum_{\ell\ell'}(2J{+}1)(2J'{+}1)(-1)^{\ell+\ell'-j-j'+2J}\begin{Bmatrix} j & j & k \\ J & J' & \ell \end{Bmatrix}\begin{Bmatrix} j' & j' & k \\ J & J' & \ell' \end{Bmatrix} T^J_{j'\ell' j\ell} T^{J*}_{j'\ell' j\ell} \tag{3.50}$$

This equation is used with equation (3.48) to calculate quantum mechanical $a^{(k)}(j,j')$ moments. Note that the classical limits for $a^{(k)}(j,j')$ apply to the quantum parameters only in the high-j limit and, in reality, the limits on the quantum $a^{(k)}(j,j')$ depend on j and j'. As stated in ref. 12, for $j' > j$, the quantum limits are greater than the classical ones, and the reverse is true for $j' < j$.

One of the main quantities of interest in this thesis is the collisional depolarisation

cross-section, $\sigma^{(k)}(j, j')$, which specifies the loss of polarisation during the collision, in contrast to the tensor cross-section, which deals with the conservation of polarisation. This is defined as

$$\sigma^{(k)}(j, j') = \sigma_{jj'} - \sigma_T^{(k)}(j, j') = \sigma_{jj'} \left[1 - a^{(k)}(j, j')\right] \tag{3.51}$$

Note that ref. 25 treats the kinetics of collisional depolarisation in detail, giving the relations between the treatment used here and other, related formalisms.

3.3 Tensor opacities – linking the classical and quantum descriptions

The classical and quantum mechanical expressions for integral and tensor cross-sections can be linked by making the assumption that spin, $\boldsymbol{S}$, is a spectator in the collisions considered in this thesis. For the collisions of a $^2\Sigma^+$ radical with a rare gas atom, this is a good assumption — the potential is electrostatic in nature, which does not interact with spin. In the energy-sudden limit, where the spin-rotation constant γ (section 2.1) does not vary on formation of the collision complex, the quantum mechanical expression for the integral cross-section $\sigma_{Nj \to N'j'}$ can be factorised into a *closed-shell* dynamical part containing all the information about the collision dynamics, and a geometric angular momentum coupling part:[12,155–158]

$$\sigma_{Nj \to N'j'} = \frac{\pi}{k_i^2}(2j' + 1) \sum_K \begin{Bmatrix} N & N' & K \\ j' & j & S \end{Bmatrix}^2 P^K(N, N') \tag{3.52}$$

in which $K = |\boldsymbol{N'} - \boldsymbol{N}|$ is the angular momentum transferred in the collision.

The *tensor opacity*, $P^K(N, N')$, contains all the dynamical information in equation (3.52), with the rest of the expression being made up of angular momentum coupling terms. Being independent of spin, it is possible to calculate $P^K(N, N')$ in a classical

calculation, and it is these tensor opacities that provide the link between the classical and quantum mechanical pictures. In this way, it is possible to calculate (quasi) open-shell cross-sections using QCT methods, assuming spin is a spectator.

Quantum mechanically, the tensor opacities are defined as[155,156,158]

$$P^K(N,N') = \frac{1}{2K+1}\sum_{\ell\ell'}|\langle N'\ell'||T^K||N\ell\rangle|^2 \tag{3.53}$$

where the reduced $\hat{T}$-matrix elements are given by[155,156,158]

$$\langle N'\ell'||T^K||N\ell\rangle = (2K+1)(-1)^{N+\ell'}\sum_J(-1)^J(2J+1)\begin{Bmatrix} N & N' & K \\ \ell & \ell' & J \end{Bmatrix} T^J_{N'\ell',N\ell} \tag{3.54}$$

Classically, it is demonstrated in ref. 12 that the tensor opacities can be calculated from the closed-shell integral cross-section resolved in K:

$$P^K(N,N') = \frac{k_i^2}{\pi}(2N+1)\sigma_{NN'}(K) \tag{3.55}$$

These K-resolved cross-sections could be calculated from, for example, a QCT calculation *via*[12]

$$\sigma_{NN'}(K) = \pi b_{\max}^2\frac{\mathcal{N}(K;N,N')}{\mathcal{N}_{\text{tot}}(N)} \tag{3.56}$$

where $\mathcal{N}(K;N,N')$ trajectories out of $\mathcal{N}_{\text{tot}}(N)$ starting in rotational state N end up in rotational state N' after transferring K units of angular momentum.

The tensor opacities can also be used to calculate $a^{(k)}(j,j')$ polarisation parameters[12]:

$$a^{(k)}(j,j') = A\frac{\sum_K(-1)^K\begin{Bmatrix} j & j & k \\ j' & j' & K \end{Bmatrix}\begin{Bmatrix} N & N' & K \\ j' & j & S \end{Bmatrix}^2 P^K(N,N')}{\sum_K\begin{Bmatrix} N & N' & K \\ j' & j & S \end{Bmatrix}^2 P^K(N,N')} \tag{3.57}$$

where

$$A = (-1)^{k-j-j'}\sqrt{2j+1}\sqrt{2j'+1} \tag{3.58}$$

Having linked the depolarisation cross-sections $\sigma^{(k)}_{jj'}$ to the tensor opacities $P^K(N, N')$, it can be noted that it is also possible to calculate m-changing cross-sections from the tensor opacities. In the lab frame, where m is the projection of $\boldsymbol{j}$ on the lab Z axis,[155]

$$\sigma_{Njm\to N'j'm'} = \frac{\pi}{k_i^2}(2j'+1)(2j+1)\sum_{KQ}\begin{pmatrix} j' & K & j \\ -m' & Q & m \end{pmatrix}^2 \begin{Bmatrix} N & N' & K \\ j' & j & S \end{Bmatrix}^2 P^K(N, N') \tag{3.59}$$

thus providing a link between the m-changing cross-sections and the depolarisation cross-sections.

3.4 The polarisation of light

This section gives a brief overview of what is meant by the *polarisation* of light, something that will be referred to extensively in chapters to follow. In the picture of light as a transverse wave, $\boldsymbol{e}$, the polarisation vector of the electric field $\boldsymbol{E}$, is perpendicular to the direction of propagation. Taking the light wave to be travelling along Z, the polarisation vector can be resolved into a linear superposition of waves polarised along X and Y, with a phase shift of δ between them:[147,159]

$$\boldsymbol{e} = \boldsymbol{e}_X \cos\beta + \boldsymbol{e}_Y \exp(i\delta)\sin\beta \tag{3.60}$$

A linear polarised wave has $\delta = 0$, meaning that β is the angle between $\boldsymbol{e}$ and X. Circular polarisation is the case where $\delta = \pm\pi/2$ and $\cos\beta = \sin\beta$, and the general case where $\delta \neq 0$ is known as elliptical polarisation. Representing the wave's angular frequency as

ω,[31]

$$\begin{aligned} \boldsymbol{e}_X =& \mathrm{Re}\left[\cos\beta \exp(-i\omega t)\right] \\ \boldsymbol{e}_Y =& \mathrm{Re}\left[\sin\beta \exp(-i(\omega t + \delta))\right] \end{aligned} \tag{3.61}$$

The link with the photon picture of light becomes clearer when using the helicity representation.[147] The photon is a spin-1 particle, and $\lambda = \pm 1$ is defined as the projection of $\boldsymbol{S}$ along the direction of propagation. Note that the component of the photon's orbital angular momentum in this direction is zero, so λ is also the projection of $\boldsymbol{j}_{\mathrm{phot}}$ along the propagation direction.[147] Therefore

$$\boldsymbol{e}_\pm = \mp \frac{\sqrt{2}}{2} \left[\boldsymbol{e}_X \pm i\boldsymbol{e}_Y\right] \tag{3.62}$$

The classical optics definition[31], which will be used in this thesis, labels $\boldsymbol{e}_+$ as *right*-hand circular polarisation (RCP), and $\boldsymbol{e}_-$ as *left*-hand circular polarisation (LCP), following the Stokes parameter s_3. Unfortunately, the opposite convention applies in quantum physics[147], and care should be taken with the RCP and LCP labels.

By inverting equation (3.62), $\boldsymbol{e}_{X,Y}$ can be expressed as

$$\begin{aligned} \boldsymbol{e}_X =& -\frac{\sqrt{2}}{2}\left[\boldsymbol{e}_+ - \boldsymbol{e}_-\right] \\ \boldsymbol{e}_Y =& -i\frac{\sqrt{2}}{2}\left[\boldsymbol{e}_+ + \boldsymbol{e}_-\right] \end{aligned} \tag{3.63}$$

If the beam of light does not propagate along Z, the equations above must be rotated to the correct frame. This frame will be labelled as xyz to differentiate it from XYZ. In the new frame, the cyclic components $\boldsymbol{e}_Q$ ($Q = -1,0,1$) can be expressed in terms of $\boldsymbol{e}_{Q'}$ in the old frame:[159]

$$\boldsymbol{e}_Q = \sum_{Q'} \boldsymbol{e}_{Q'} D^{(1)*}_{Q'Q}(\chi,\theta,\phi) \tag{3.64}$$

where $D^{(1)}_{Q'Q}(\chi,\theta,\phi)$ is a Wigner rotation matrix.[88] The angle χ is set to zero, as it corre-

sponds to rotation about the direction of propagation and as such is arbitrary.

3.5 Summary

In this chapter, the concepts of polarisation, orientation and alignment have been introduced in quantum and (semi)classical terms. The polarisation of light, discussed in section 3.4, leads to oriented or aligned distributions of angular momentum vectors $\boldsymbol{j}$ in excited OH(A), as described in section 3.2. Collisions with Kr or Xe atoms can destroy the polarisation created by these methods, and the mathematical description of this has been given in terms of the $\boldsymbol{j} - \boldsymbol{j'}$ correlation.

Opacity functions and cross-sections, fundamental concepts in the field of molecular collision dynamics, have been defined and explained, and the formalism of *tensor opacities* used for the treatment of open-shell species in this thesis has been introduced.

The concepts explored in this chapter are relevant to the rest of this thesis. Chapter 4 will set out the methods used to experimentally measure the cross-sections defined here, and the results will be presented in chapters 7 and 8. The techniques used to calculate these quantities from theoretical potential energy surfaces are brought into the discussion in chapters 5 and 6, and applied in the results chapters 7 and 8.

Chapter 4

Experimental methods

4.1 Aim and definitions

The experiments in this thesis measure absolute, thermal rate constants for the following processes (see chapter 1):

- Electronic quenching
- Vibrational energy transfer
- Rotational energy transfer
- Total collisional depolarisation
- Elastic collisional depolarisation

The laser and detection system used can resolve in spin-rotation level, j, but not hyperfine level, F (for OH($A^2\Sigma^+$)). Thus 'elastic' in this section refers to collisions that are elastic in j, and 'rotational energy transfer' is all collisions for which either $N' \neq N$ or $N' = N; j' \neq j$. (The notation used here is defined in section 2.1).

The absolute rate constants, $k(T)$, obtained from the experiment are measured at 300 K and can be written as in chapter 3:

$$k(T) \equiv \langle k \rangle = \langle v_{\text{rel}} \sigma(v_{\text{rel}}) \rangle \tag{4.1}$$

$$= \int_0^\infty v_{\text{rel}} \sigma(v_{\text{rel}}) f_{\text{MB}}(v_{\text{rel}}|T) \, \mathrm{d}v_{\text{rel}} \tag{4.2}$$

$$= \sqrt{\frac{8k_B T}{\pi\mu}} (k_B T)^{-2} \int_0^\infty \sigma(E_t) E_t \exp\left(\frac{-E_t}{k_B T}\right) \mathrm{d}E_t \tag{4.3}$$

where v_{rel} is the relative velocity, E_t is the collision energy, k_B is the Boltzmann constant, T is the temperature and μ is the reduced mass of the system. $f_{\text{MB}}(v_{\text{rel}}|T)$ and $P_{\text{MB}}(E_t|T)$ are the Maxwell-Boltzmann distributions of relative velocities and energies at temperature T respectively.

$k(T)$ can be converted into a flux averaged thermal cross-section, σ, using the thermal mean relative velocity, $\langle v_{\text{rel}} \rangle$.

$$\sigma = \frac{k(T)}{\langle v_{\text{rel}} \rangle} \; ; \quad \langle v_{\text{rel}} \rangle = \left(\frac{8k_{\text{B}} T}{\pi\mu}\right)^{\frac{1}{2}} \tag{4.4}$$

Note that this "thermal *flux averaged* cross-section", σ, is *not* the same as the "thermally averaged cross-section" $\sigma(T) \equiv \langle \sigma \rangle$:

$$\sigma(T) \equiv \langle \sigma \rangle = \int_0^\infty \sigma(v_{\text{rel}}) f_{\text{MB}}(v_{\text{rel}}|T) \, \mathrm{d}v_{\text{rel}} \tag{4.5}$$

$$\sigma = \frac{\int_0^\infty v_{\text{rel}} \sigma(v_{\text{rel}}) f_{\text{MB}}(v_{\text{rel}}|T) \, \mathrm{d}v_{\text{rel}}}{\int_0^\infty v_{\text{rel}} f_{\text{MB}}(v_{\text{rel}}|T) \, \mathrm{d}v_{\text{rel}}} \tag{4.6}$$

and that it is the thermal flux averaged cross-section, σ, that will be referred to as a "cross-section" in the remainder of this thesis. These cross-sections are absolute numbers, and do not need to be scaled in any way for comparison with theory.

4.2 Outline

This section will describe the experimental processes used to measure the above mentioned cross-sections. It will start with an overview of the various techniques used to measure such quantities in different laboratories, before moving in to focus on the methods used in this thesis. A description of how polarised laser light is used to excite ground state OH to the excited $A^2\Sigma^+$ state, creating a polarised distribution of OH(A) angular momentum vectors, begins the discussion, and then the techniques of laser induced fluorescence (LIF) and Zeeman quantum beat spectroscopy (ZQBS) used will be introduced. After presenting the experimental setup, the processes used to analyse and fit the data obtained will be explained, with a description of the error analysis and procedures to simulate experimental data from theoretical results.

4.3 Experimental techniques

As reviewed in detail in ref. 25, the experimental methods used in measurements of angular momentum transfer and depolarisation fall into three main classes. These are: polarised single-photon laser induced fluorescence (LIF), which includes the method of Zeeman quantum beat spectroscopy (ZQBS) used in this work; Optical-optical double resonance (OODR); and non-linear techniques such as polarisation spectroscopy or four-wave mixing.

The theory of polarised LIF is set out in the papers of Case *et al.*[31] and Greene and Zare.[160] A polarised laser is used to excite the sample, and the resonance fluorescence is detected in a polarisation-sensitive manner — the anisotropy of the fluorescence gives information on the polarisation of the sample. Clearly, this method is restricted to the study of excited states, such as the OH(A) state probed in this work. It has been used in early studies of depolarisation of iodine and alkali metal dimers[161–165] and the more recent work on elastic depolarisation of OH(A) by Brinkman and Crosley,[166] as well as in the depolarisation of NO(A) by CO_2[167] and of H_2, HD and D_2 using VUV light.[168] The 1908 study of Wood[169] on collisional depolarisation of Na_2 obviously did not use laser

excitation, but the analysis of polarised fluorescence followed similar lines.

The absorption of polarised light causes the angular momentum of the sample of molecules to become polarised[88], as detailed further in section 4.4. Using linear polarised light results in an aligned distribution of angular momenta. Two experimental geometries are used: $I_{\parallel}$ and $I_{\perp}$, in which the polarisation axes of the laser and of a linear polariser placed in front of the detector are respectively parallel or perpendicular to each other. The difference in the two fluorescence channels, $I_{\parallel} - I_{\perp}$, is a measure of the alignment of the sample, and is normalised to obtain a polarisation ratio R, which depends only on the polarisation and not on the population. The weighted sum, $I_{\parallel} + 2I_{\perp}$, depends only on the excited state population and not on its polarisation, enabling the separation of these two effects. Measuring R as a function of collider pressure enables the determination of a rate constant for collisional disalignment.

$$R = \frac{I_{\parallel} - I_{\perp}}{I_{\parallel} + 2I_{\perp}} \tag{4.7}$$

The reason for using $I_{\parallel} + 2I_{\perp}$ in the denominator, rather than $I_{\parallel} + I_{\perp}$, is because the resulting R is directly proportional (in the classical limit) to the alignment of the sample,[154,170,171] $\langle \cos\theta_{j'} \rangle$.

$$R = \begin{cases} \langle \cos\theta_{j'} \rangle & \text{Q branch} \\ -\frac{1}{2}\langle \cos\theta_{j'} \rangle & \text{P or R branch} \end{cases} \tag{4.8}$$

In some texts, P is used to refer to $(I_{\parallel} - I_{\perp})/(I_{\parallel} + I_{\perp})$, which has a slightly more complicated relationship to $\langle \cos\theta_{j'} \rangle$.[154] R can be viewed as the Laplace transform of a correlation function for depolarisation.[170]

For disorientation measurements, circular polarised light is used to prepare a sample of molecules whose angular momentum distribution is oriented (and also aligned). The polarisation ratio used here is

$$C = \frac{I_L - I_R}{I_L + I_R} \tag{4.9}$$

with I_L and I_R corresponding to left- and right-hand circular polarised light respectively. This ratio does still contain a small contribution from alignment, but, in practice, this is usually within experimental error.

Polarised LIF has the advantage of experimental simplicity, and also separates out the contributions to the signal from population decay and polarisation decay. However, final rotational state resolution is achieved by spectrally resolving the fluorescence, which reduces the signal-to-noise ratio and may not be possible for species with closely-spaced spectra. The use of a monochromator in the current experiments is discussed in section 4.7.6.

Quantum beat spectroscopy (QBS) is a Doppler-free technique that has seen extensive use in molecular spectroscopy, as reviewed in refs. 172–174. Beats between Zeeman,[175,176] hyperfine[177–180] and Stark[181,182] levels have been used to measure various spectroscopic quantities in a variety of small and medium-size molecules. QBS has also been used to measure collisional angular momentum depolarisation in atoms,[183] and its use by Brouard and coworkers[11–16,20,21,184] in the study of depolarisation of the small open-shell radicals OH(A) and NO(A) finds its latest chapter in this thesis. The use of QBS to measure rates of collisional depolarisation is dealt with in detail in the rest of this chapter.

The OODR technique uses a second laser for detection of the state of interest, rather than looking at its fluorescence as in the LIF method above. Similar strategies are $1 + 1'$ LIF, where the state of interest is detected by excitation to a third state and observation of the emission from there, and techniques using detection by REMPI. These experiments are more complex than the simple polarised LIF technique, but have much better rotational state resolution due to the narrow bandwidth light available from the second laser. The polarisation ratios P and C defined above are also used in the OODR method, but analysis is more complicated, as explored in ref. 25. Excitation to the state of interest can be performed with a laser, or by other methods such as stimulated Raman pumping.[25] Examples of this family of techniques include OODR studies of depolarisation in NO(A)[185] and CO,[186] $1 + 1'$ LIF experiments on alkaline earth metal oxides[187] and the

use of stimulated Raman pumping in the ground electronic state of N_2,[188] acetylene[189–191] and HD.[192]

Four-wave mixing (FWM),[193] polarisation spectroscopy (PS)[26] and other non-linear methods have the advantage that they can be applied to almost any combination of electronic states, but can be experimentally difficult if the species of interest cannot be produced in a high enough concentration — the signal falls with the square of the number density.[26] PS is a measure of bulk polarisation, and it is not possible to separate out the effects of polarisation and population decay.[26]

Further details of the various experimental techniques mentioned here, as well as others, can be found in several recent reviews.[25,26]

4.4 Creating a polarised angular momentum distribution

To measure collisional depolarisation, the OH radical is excited to the OH(A) state with polarised laser light, so that the resulting distribution of $\boldsymbol{j}$ is aligned (linear polarised light) or oriented (circular polarised light). This bulk polarisation of $\boldsymbol{j}$ vectors is then lost through collisions with Kr or Xe, and the rate of this process is measured.

Excitation of OH(X) is first treated quantum mechanically, and the results are then compared to those from a classical treatment.

4.4.1 Quantum description

Considering first excitation from a single $|j''m''\rangle$ state by polarised light, the excited state $|j\rangle$ can be written as[88,147]

$$|j\rangle = C' \sum_m |jm\rangle\langle jm|\hat{\boldsymbol{e}} \cdot \hat{\boldsymbol{d}}|j''m''\rangle \tag{4.10}$$

where $\hat{\boldsymbol{e}}$ is the electric field vector of the laser and $\hat{\boldsymbol{d}}$ is the electric dipole moment operator.

The operator $\hat{\boldsymbol{e}} \cdot \hat{\boldsymbol{d}}$ can be expressed as spherical components of $\hat{\boldsymbol{d}}$ in the lab frame, $\hat{\boldsymbol{d}}_p$:[88]

$$\hat{\boldsymbol{e}} \cdot \hat{\boldsymbol{d}} = \begin{cases} \hat{\boldsymbol{d}}_0 & \text{lin, } z = \text{ laser polarisation axis} \\ \hat{\boldsymbol{d}}_{+1} & \text{LCP, } z = \text{ laser propagation axis} \\ \hat{\boldsymbol{d}}_{-1} & \text{RCP, } z = \text{ laser propagation axis} \end{cases} \tag{4.11}$$

Now considering excitation from an isotropic ground state,

$$\rho_i = C'' \sum_{m''} |j''m''\rangle\langle j''m''| \tag{4.12}$$

the excited state density matrix ρ_f is

$$\rho_f = A \sum_{m'',m} \left| \langle jm|\hat{\boldsymbol{e}} \cdot \hat{\boldsymbol{d}}|j''m''\rangle \right|^2 |jm\rangle\langle jm| \tag{4.13}$$

Applying the Wigner-Eckart theorem,[88]

$$\langle jm|\hat{\boldsymbol{d}}_p|j''m''\rangle = (-1)^{j-m} \begin{pmatrix} j & 1 & j'' \\ -m & p & m'' \end{pmatrix} \langle j||\boldsymbol{d}||j''\rangle \tag{4.14}$$

Following ref. 147 and substituting equation (4.14) into equation (4.13),

$$\rho_f = A' \sum_{m} \begin{pmatrix} j & 1 & j'' \\ -m & p & m'' \end{pmatrix}^2 |\langle j||\boldsymbol{d}||j''\rangle|^2 |jm\rangle\langle jm| \tag{4.15}$$

The excited state density matrix must be normalised, and for this the trace is needed:

$$\begin{aligned}\mathrm{Tr}(\rho_f) =& \sum_{m''} A'' \sum_{m} \begin{pmatrix} j & 1 & j'' \\ -m & p & m'' \end{pmatrix}^2 |\langle j||\boldsymbol{d}||j''\rangle|^2 \\ =& A'' \sum_{m''m} \begin{pmatrix} j'' & j & 1 \\ m'' & -m & p \end{pmatrix}^2 |\langle j||\boldsymbol{d}||j''\rangle|^2 \\ =& \frac{1}{3} A'' |\langle j||\boldsymbol{d}||j''\rangle|^2 \end{aligned} \tag{4.16}$$

in which the sum over the squared $3j$-symbol has turned into $1/3$ because of the orthogonality properties of $3j$-symbols.[88]

The normalised density matrix is therefore $\rho = \rho_f/\mathrm{Tr}(\rho_f)$:

$$\rho = 3 \sum_{m} \begin{pmatrix} j & 1 & j'' \\ -m & p & m'' \end{pmatrix}^2 |jm\rangle\langle jm| \tag{4.17}$$

Note that $m'' = m - p$ because of the triangle properties of the $3j$-symbol.[88]

The squared $3j$-symbol can be expanded using the relations to be found in Zare's book:[88]

$$\rho = 3(-1)^{j+j''-p} \sum_{m,k} (2k+1)(-1)^{j-m} \begin{Bmatrix} 1 & 1 & k \\ j & j & j'' \end{Bmatrix} \begin{pmatrix} j & j & k \\ m & -m & 0 \end{pmatrix} \begin{pmatrix} 1 & 1 & k \\ -p & p & 0 \end{pmatrix} |jm\rangle\langle jm| \tag{4.18}$$

Considering the $3j$-symbol $\left(\begin{smallmatrix} 1 & 1 & k \\ -p & p & 0 \end{smallmatrix}\right)$, k can take the integer values 0, 1 and 2 only. This means that single-photon excitation can only alter the multipoles up to rank 2 of the density matrix. For linear polarised light, $p = 0$ and there is a further restriction, since by symmetry

$$\begin{pmatrix} 1 & 1 & k \\ 0 & 0 & 0 \end{pmatrix} = (-1)^{k+2} \begin{pmatrix} 1 & 1 & k \\ 0 & 0 & 0 \end{pmatrix} \tag{4.19}$$

and so k must be even — hence linear polarised light can affect only the multipoles of

$k = 0$ and 2, *i.e.* can align, but not orient, the sample. (See chapter 3).

In order to obtain the multipole moments of the excited state density matrix, equation (4.17) can be used in the following relation:[147]

$$\rho_q^{(k)} = \sum_{mm''} (-2)^{j-m} \sqrt{2k+1} \begin{pmatrix} j & j & k \\ m & -m & -q \end{pmatrix} \langle jm|\rho|jm\rangle \tag{4.20}$$

to obtain (using the shorthand $[x] = 2x + 1$)

$$\rho_q^{(k)} = \sum_{mm''} 3[k]^{3/2} (-1)^{j+j''-p} \begin{pmatrix} j & j & k \\ m & -m & -q \end{pmatrix} \times \begin{pmatrix} j & j & k \\ m & -m & 0 \end{pmatrix} \begin{pmatrix} 1 & 1 & k \\ -p & p & 0 \end{pmatrix} \begin{Bmatrix} 1 & 1 & k \\ j & j & j'' \end{Bmatrix} \tag{4.21}$$

Restricting q to zero and using the relation[88]

$$\sum_{m_1 m_2} \begin{pmatrix} j_1 & j_2 & j \\ m_1 & m_2 & m \end{pmatrix}^2 = \frac{1}{2j+1} \tag{4.22}$$

we obtain

$$\rho_0^{(k)} = 3[k]^{1/2} (-1)^{j+j''-p} \begin{pmatrix} 1 & 1 & k \\ -p & p & 0 \end{pmatrix} \begin{Bmatrix} 1 & 1 & k \\ j & j & j'' \end{Bmatrix} \tag{4.23}$$

Recalling equation (3.42) from chapter 3, the $a^{(k)}$ parameters can be obtained via

$$a^{(k)} = a_0^{(k)} = \frac{2j+1}{2k+1} \rho_0^{(k)} \tag{4.24}$$

and used in equation (3.33) to obtain the quantum probability density function for the population of the minimum uncertainty state, $Q(\theta_j)$.

$$Q(\theta_j) = \frac{1}{2} \left[1 + 3a_0^{(1)} \langle jj, 10|jj\rangle P_1(\cos\theta_j) + 5a_0^{(2)} \langle jj, 20|jj\rangle P_2(\cos\theta_j) \right] \tag{4.25}$$

where

$$a_0^{(k)} = 3\sqrt{2j+1}(-1)^{j+j''-p} \begin{Bmatrix} 1 & 1 & k \\ j & j & j'' \end{Bmatrix} \begin{pmatrix} 1 & 1 & k \\ -p & p & 0 \end{pmatrix} \tag{4.26}$$

In this section, we refer to the $a_0^{(k)}$ parameters as $r_0^{(k)}$, or *extrinsic* polarisation moments. This is because they are produced by laser excitation, rather than being related to the dynamics of the system under study.[8]

4.4.2 Classical description

An instructive comparison to the quantum description of excitation by polarised light considered above is the classical viewpoint, which is perhaps more intuitive. In the limit of high j, of course, the two descriptions become equivalent, and this section will explore the circumstances under which the classical picture is valid.

One way of approaching the problem is to follow Zare's treatment[88,194] of the polarisation of $\boldsymbol{r}$, the bond axis vector, by polarised laser excitation, and change the wavefunction for the molecule in the $\boldsymbol{r}$ basis for that in the $\boldsymbol{j}$ basis,[150,151] as in refs. 18,22. The approach used here is based on a consideration of the classical absorption probability, as in Application 6 of ref. 88 and developed further in ref. 159. This classical derivation will be compared with the high-j limit of the quantum description given in the previous subsection.

The probability that a diatomic radical with transition dipole moment $\boldsymbol{\mu}$ will absorb light with electric field polarisation vector $\boldsymbol{e}$ is proportional to

$$\begin{aligned} P_{\text{abs}} &\propto |\boldsymbol{e} \cdot \boldsymbol{\mu}|^2 \\ &= \left| \sum_{Q=-1}^{+1} \boldsymbol{e}_Q \mu_Q \right|^2 \end{aligned} \tag{4.27}$$

in which $Q = -1, 0, 1$ are the cyclic components in the lab frame xyz (see section 4.4.1).

Considering first the light, right-hand and left-hand circular polarised light propagating along z is expressed as pure $\boldsymbol{e}_{+1}$ and $\boldsymbol{e}_{-1}$ respectively. In the case of linear polarised light

propagating along y with polarisation along x, the appropriate term is found by application of equation (3.64). The polarisation angle β is between $\boldsymbol{e}$ and X is zero, and the required rotation can be described by $\theta = \frac{\pi}{2}$, $\phi = 0$, so[159]

$$\boldsymbol{e}_Q = -\frac{(-1)^Q\sqrt{2}}{2} d^{(1)}_{1Q}\left(\frac{\pi}{2}\right) + \frac{(-1)^Q\sqrt{2}}{2} d^{(1)}_{-1Q}\left(\frac{\pi}{2}\right) \tag{4.28}$$

where $d^{(1)}_{Q'Q}$ is a reduced rotation matrix element.[88] This reveals that this linear polarised light can be described with $\boldsymbol{e}_0$.

In a $\boldsymbol{j}$-fixed coordinate system, the components of the transition dipole can be expressed as[159] μ^Δ, with $\Delta = -1$, 0, 1 for P, Q and R branch transitions respectively. Rotating to the lab frame, in which the direction of the initial $\boldsymbol{j''}$ is specified by $(\theta_{j''}, \phi_{j''})$,[159]

$$\mu^Q = D^{(1)*}_{\Delta Q}(0, \theta_{j''}, \phi_{j''}) = (-1)^Q D^{(1)}_{\Delta Q}(0, \theta_{j''}, \phi_{j''}) \tag{4.29}$$

where $D^{(1)}_{\Delta Q}(0, \theta_{j''}, \phi_{j''})$ is a Wigner rotation matrix element.[88]

Using equation (4.27), the absorption probability is

$$P_{\text{abs}}(\theta_{j''}, \phi_{j''}) = \left| \sum_{Q=-1}^{+1} (-1)^Q \boldsymbol{e}^Q D^{(1)}_{\Delta Q}(0, \theta_{j''}, \phi_{j''}) \right|^2 \tag{4.30}$$

and the probability density function $P(\theta_j, \phi_j)$ is simply $P_{\text{abs}}(\theta_{j''}, \phi_{j''})$ normalised such that

$$\int_0^{2\pi} \int_0^{\pi} P(\theta_j, \phi_j) \sin\theta_j \, \mathrm{d}\theta_j \, \mathrm{d}\phi_j = 1 \tag{4.31}$$

The polarisation moments $a^{(k)}_q$ (chapter 3) can be obtained via[150]

$$a^{(k)}_q = \int_0^{2\pi} \int_{-1}^{1} P(\theta_j, \phi_j) C_{kq}(\theta_j, \phi_j) \, \mathrm{d}(\cos\theta_j) \, \mathrm{d}\phi_j \tag{4.32}$$

Integrating over ϕ_j and expanding in Legendre polynomials gives[8,17,88]

$$P(\theta_j) = \frac{1}{2}\left[1 + 3r^{(1)}_0 P_1(\cos\theta_j) + 5r^{(2)}_0 P_2(\cos\theta_j)\right] \tag{4.33}$$

where the $r_0^{(k)}$ moments are given in Table 4.1.

	$r_0^{(1)}$			$r_0^{(2)}$		
branch	lin	LCP	RCP	lin	LCP	RCP
P	0	$-\frac{1}{2}$	$+\frac{1}{2}$	$-\frac{1}{5}$	$+\frac{1}{10}$	$+\frac{1}{10}$
Q	0	0	0	$+\frac{2}{5}$	$-\frac{1}{5}$	$-\frac{1}{5}$
R	0	$+\frac{1}{2}$	$-\frac{1}{2}$	$-\frac{1}{5}$	$+\frac{1}{10}$	$+\frac{1}{10}$

Table 4.1: Table of *extrinsic* polarisation moments $r_0^{(k)}$ for use with equation (4.33)

Note that, as in the quantum case, only the polarisation moments up to $k = 2$ can be produced by single-photon excitation. Linear polarised light can only align the sample, while circular polarised light can produce both orientation and alignment of the $\boldsymbol{j}$ vectors.

4.4.3 Comparison

Figure 4.1 compares the extrinsic quantum polarisation moments $r_0^{(k)}$ for Q-branch excitation of OH(A←X) at different values of j (where j is the rotational angular momentum quantum number of OH(A)) to their limiting classical values. As j increases, the quantum polarisation moments approach their classical limits, showing that the purely classical formula (equation (4.33)) is a good approximation to reality at high j ($j > 10$) but begins to fail more seriously for lower rotational states ($j < 5$).

Notice that, classically, it is not possible to produce orientation using a Q-branch transition with any polarisation of light, but that this is possible at low j in the quantum picture if circular polarised light is used. Using linear polarised light does not result in orientation with either formalism.

3D representations of the lab frame distributions of j are shown, for Q-branch excitation with linear polarised light, in figure 4.2. These clearly show how, as j increases, the quantum probability density functions approach the classical (correspondence) limit.

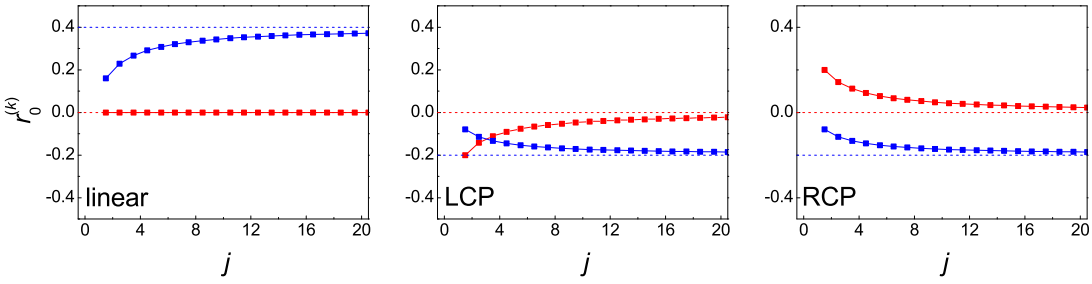

Figure 4.1: Extrinsic polarisation moments $r_0^{(k)}$ for Q-branch excitation with linear (left), left-hand circular (centre) and right-hand circular (right) polarised light. Red and blue are for $k = 1$ and 2 respectively. The solid lines are quantum (equation (4.25)) and the dotted lines are classical (equation (4.33)) – note that the classical and quantum moments use integral and half-integral j respectively.

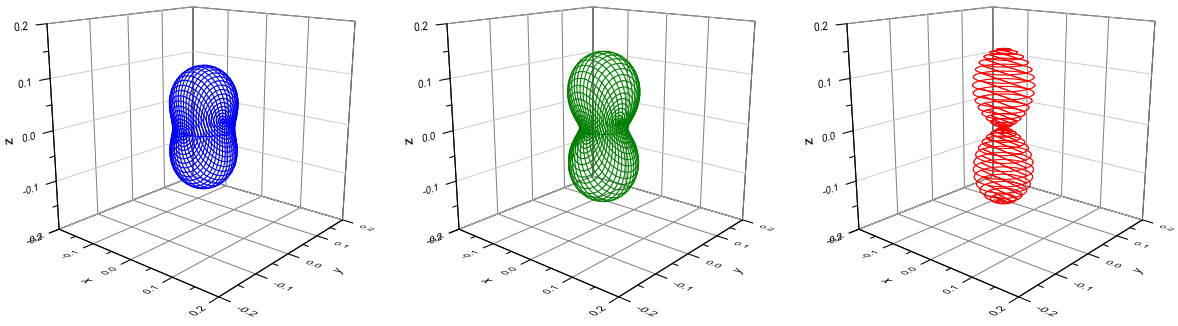

Figure 4.2: Lab frame $\boldsymbol{j}$ distributions for Q-branch excitation with light polarised linearly along the z axis. Left: $j = 2.5$, centre: $j = 25.5$, right: classical ($j = \infty$).

4.5 Collisional depolarisation of rotational angular momentum

After a polarised distribution of $\boldsymbol{j}$ vectors has been prepared, this polarisation can be lost through a number of 'depolarising' processes. These can be non-collisional, for example from the dephasing effect of external magnetic fields or hyperfine depolarisation (both of which are considered in section 4.7.4), or collisional, which is the main process of interest here.

As in equations (4.25) and (4.33), the pre-collision distribution of $\boldsymbol{j}$ can be written as

$$P(\theta_j) = \sum_k \frac{2k+1}{2} r_0^{(k)}(j) P_k(\cos\theta_j) \tag{4.34}$$

Likewise, the distribution of $\boldsymbol{j'}$ after a single collision can be written as

$$P(\theta'_j) = \sum_k \frac{2k+1}{2} \mathcal{P}_0^{(k)}(j') P_k(\cos\theta_{j'}) \tag{4.35}$$

in which[12]

$$\mathcal{P}_0^{(k)}(j') = a^{(k)}(j,j') r_0^{(k)}(j) \tag{4.36}$$

Note that this is valid only when neither $\boldsymbol{k}$ nor $\boldsymbol{k'}$ are defined[12], as in the present experiments. After x collisions, the situation is[13]

$$\mathcal{P}_0^{(k)}(j') = \left[a^{(k)}(j,j')\right]^x r_0^{(k)}(j) \tag{4.37}$$

(This assumes that $a^{(k)}(j,j')$ is the same for subsequent collisions – in practice, the experiment would aim to probe the OH radicals after a single collision).

Now, the pseudo first-order state-to-state collision rate $k_{jj'}$ at a number concentration $[Q]$ of collider, Q, can be written as[12]

$$k_{jj'} = \langle v_{\mathrm{rel}} \sigma_{jj'}(v_{\mathrm{rel}}) \rangle [Q] \tag{4.38}$$

The angle brackets, which denote an average over a Maxwell-Boltzmann distribution of collision energies, will be dropped henceforth to simplify the notation.

The probability that there will be x collisions in a time Δt can be modelled as a Poisson distribution:[13]

$$P(x) = \frac{(k_{jj'}\Delta t)^x}{x!} \mathrm{e}^{-k_{jj'}\Delta t} \tag{4.39}$$

After time Δt has passed, the polarisation moments of the $\boldsymbol{j'}$ distribution are therefore (using the power series expansion of e^x):[13]

$$\begin{aligned}
\mathcal{P}^{(k)}(j';t) &= \sum_x P(x) \left[a^{(k)}(j,j')\right]^x r_0^{(k)}(j) \\
&= \sum_x \frac{\left[k_{jj'}a^{(k)}(j,j')\Delta t\right]^x}{x!} \mathrm{e}^{-k_{jj'}\Delta t} r_0^{(k)}(j) \\
&= \exp\left[k_{jj'}a^{(k)}(j,j')\Delta t\right] \exp[-k_{jj'}\Delta t] r_0^{(k)}(j) \\
&= \exp[-k_d^{(k)}(j,j')\Delta t] r_0^{(k)}(j)
\end{aligned} \tag{4.40}$$

where the collisional depolarisation rate, $k_d^{(k)}(j,j')$, is

$$k_d^{(k)}(j,j') = k_{jj'}\left(1 - a^{(k)}(j,j')\right) \tag{4.41}$$

Note the similarity of this equation to equation (3.51) in chapter 3.

4.6 Zeeman quantum beat spectroscopy

The experimental method used in this thesis is the 1+1 LIF-based method of Zeeman quantum beat spectroscopy (ZQBS), as discussed in section 4.3. This method has the major advantage of the separate measurement of population and polarisation decay, enabling the effects of state-to-state transfer to be teased apart from those of collisional depolarisation.

The ZQBS method takes its name from the coherent excitation of multiple Zeeman

levels (see section 2.1.1) of the OH(A) radical, with an applied magnetic field serving to lift the degeneracy of these levels. Since the excited superposition is not a stationary state, its evolution in time results in a modulation of the fluorescence observed, with the amplitude of these 'quantum beats' being a measure of the bulk polarisation of the sample. The decay of these beats over time thus provides the rate of depolarisation.

A simplified two-state model is presented in the next subsection to clarify the above discussion, and then quantum mechanical and classical presentations of the experimental technique will be given.

The experimental geometry used in this section is as follows, and is illustrated in figure 4.3. The magnetic field is taken to be along $+Z$ in the lab frame, and the laser propagates along $+Y$. In the case of linear polarised light, the polarisation is flipped on alternate shots between 'horizontal' (along X) and 'vertical' (along Z) directions; for circular polarisation, alternate shots change between left and right hand circular polarisation. Note that this axis system (XYZ) is *not* the same as that used to describe the creation of a polarised distribution of j (xyz), where z was either the laser polarisation (linear polarised light) or the laser propagation axis (circular polarised light). The two frames are related by a simple rotation, as in equation (4.50).

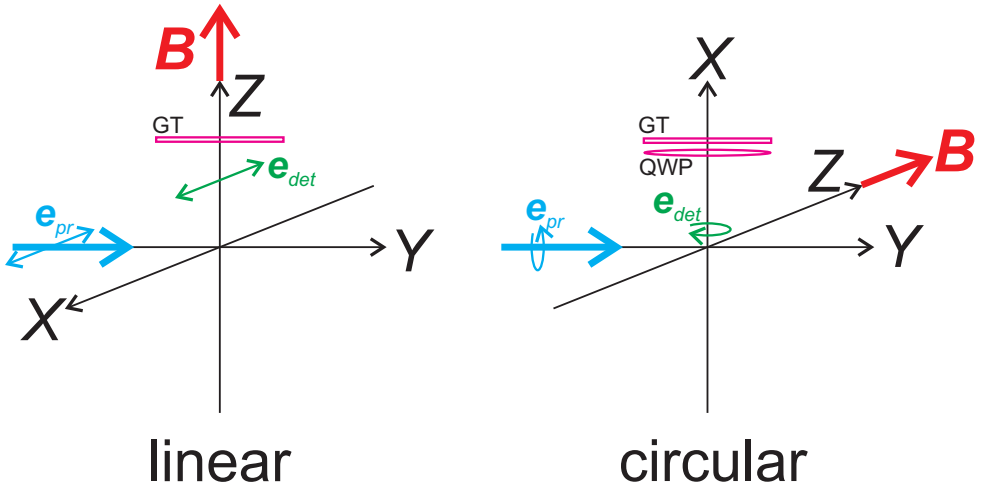

Figure 4.3: Lab frame for excitation with linear (left) or circular (right) polarised light. The detection axis is towards the top of the page. $\boldsymbol{B}$ is the magnetic field and $\boldsymbol{e}_{pr}$ and $\boldsymbol{e}_d$ are the polarisation axes for the probe light and detection respectively. GT: Glan-Taylor linear polariser, QWP: quarter-wave plate.

4.6.1 Two-state quantum model

As explained in section 2.1.1 of chapter 2, the application of a weak magnetic field lifts the degeneracy of the Zeeman levels of OH(A), with the energy splitting being $\Delta E_z = g_F \mu_0 m_F B$ (equation (2.10)). Due to time-energy uncertainty, a finite-time laser pulse has a non-zero spread in energy ('coherence width') — in the case of the 6 ns pulse width of the Nd:YAG-pumped dye laser used in this work, the coherence width is approximately 30 MHz, or around 0.001 cm^{-1}. This is sufficiently wide to excite a superposition of Zeeman levels (as long as the field is not too large), but, as the splitting between the hyperfine levels of OH(A) is greater (on the order of 160 MHz[85]), this superposition does not include levels from different hyperfine manifolds.

The levels included in the excited superposition are determined by the selection rules. Because the absorption probability is given by[88,195] $|\langle jm|\hat{\mu}_Q|j''m''\rangle|^2$, application of the Wigner-Eckart theorem[88] separates out the geometrical terms that give rise to these selection rules.

$$\langle jm|T^k_q|j''m''\rangle = (-1)^{j-m} \begin{pmatrix} j & k & j'' \\ -m & q & m'' \end{pmatrix} \langle j||T^k_q||j''\rangle \tag{4.42}$$

The 3j-symbol in the above equation is responsible for the selection rules in this excitation — since $\boldsymbol{\mu}$ is a tensor of rank 1, $k = 1$ and so $\Delta j = 0, \pm 1$. The m levels excited depend on the polarisation of light, which is taken to propagate along $+y$.

For linear polarised light, we take the polarisation along the X axis, giving $\Delta m = 0, \pm 1$ since $\boldsymbol{e}_X = -\frac{\sqrt{2}}{2}[\boldsymbol{e}_+ - \boldsymbol{e}_-]$. This means that the Zeeman levels excited have a separation of $\Delta m = 2$. Note that the orthogonal polarisation (along Z) is $\boldsymbol{e}_0$, exciting only the level with $m = m''$ — since this geometry does not give rise to a superposition of states, there is no interference and hence no quantum beats.

Circular polarised light has polarisation $\boldsymbol{e} = \frac{\sqrt{2}}{2}[\boldsymbol{e}_Z \pm i\boldsymbol{e}_X]$, thus giving rise to superpositions separated by $\Delta m = 1$ and $\Delta m = 2$. In practice, the second of these is not usually observed experimentally.

Taking a superposition of two levels, $|a\rangle$ and $|b\rangle$, for the sake of example (figure 4.4),

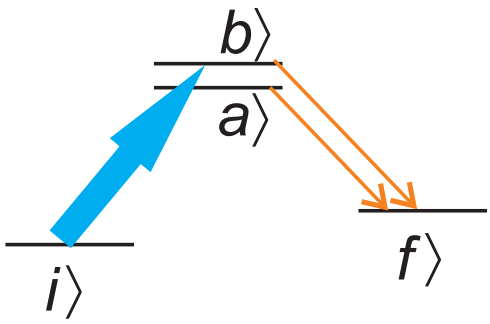

Figure 4.4: Model four-level system to demonstrate Zeeman quantum beats — see text for details.

the excited state wavefunction at time zero is given by[174,175]

$$|\psi(0)\rangle = c_a|a(0)\rangle + c_b|b(0)\rangle \tag{4.43}$$

in which the eigenstates $|a(t)\rangle$ and $|b(t)\rangle$ evolve in time only via a phase factor, so their dependence on t will be dropped:

$$|x\rangle = |x(t)\rangle = |x(0)\rangle e^{-i\omega_x t} \tag{4.44}$$

where $x = a$, b and $\omega_x = E_x/\hbar$. This assumes that the laser pulse is much faster than the relaxation times of $|a\rangle$ and $|b\rangle$, which is the case in the experiments in this work.

If the energy of the laser light is taken to be constant over the whole coherence width, $c_x = \langle x|\hat{\mu}|i\rangle = \mu_{xi}$. Introducing the decay rates[174,175] $\gamma_x = \tau_x^{-1}$,

$$|\psi(t)\rangle \propto \mu_{ai}|a\rangle e^{-(i\omega_a+\gamma_a/2)} + \mu_{bi}|b\rangle e^{-(i\omega_b+\gamma_b/2)} \tag{4.45}$$

This is then substituted into the equation for fluorescence intensity:

$$\begin{aligned} I(t) &\propto |\langle f|\mu|\psi(t)\rangle|^2 \\ &= |\mu_{ai}|^2|\mu_{af}|^2 e^{-\gamma_a t} + |\mu_{bi}|^2|\mu_{bf}|^2 e^{-\gamma_b t} + |\mu_{ai}\mu_{af}\mu_{bi}\mu_{bf}| e^{-(\gamma_a+\gamma_b)t/2}\cos(\omega_{ab}t + \phi) \end{aligned} \tag{4.46}$$

In this equation, $\omega_{ab} = |\omega_a - \omega_b|$ and ϕ is the phase angle.

The cross term in the above equation describes the quantum beats arising from interference between the coherently excited Zeeman levels $|a\rangle$ and $|b\rangle$, hence the name 'Zeeman quantum beat spectroscopy'. Making the assumptions that $\gamma_a = \gamma_b = \gamma$ and that all $|\mu_{ij}|$ are the same, a simpler form can be derived:

$$I(t) \propto \left[1 + r_0^{(k)}(j)\cos(\omega_{ab}t + \phi)\right] \mathrm{e}^{-\gamma t} \tag{4.47}$$

in which the extrinsic polarisation moment $r_0^{(k)}(j)$ describes the initial polarisation of $\boldsymbol{j}$.

The following subsections build on this description to give more quantitative descriptions of ZQBS that are of more use in the analysis of the experiments presented in this thesis.

4.6.2 Quantum model — density matrices

The density matrix treatment of polarised laser excitation set out in section 4.4.1 can be extended to include the effects of an external magnetic field on the excited distribution of j.

Under the effect of a static magnetic field in the Z direction, the elements of the density matrix evolve according to[196]

$$\frac{\partial}{\partial t}\rho_{mm''} = \exp\left[-i\omega_L(m - m'') - \Gamma\right]\rho_{mm''} \tag{4.48}$$

where ω_L is the Larmor frequency and Γ is the relaxation rate. For the purposes of the discussion here, it is more useful to consider the state multipoles rather than the density matrix elements themselves — the conversion can be carried out by using equation (4.20).

Recalling equation (4.23) of section 4.4.1, the initial state multipoles $\rho_0^{(k)}$ of the excited density matrix (given cylindrical symmetry) are

$$\rho_0^{(k)} = 3[k]^{1/2}(-1)^{j+j''-p} \begin{pmatrix} 1 & 1 & k \\ -p & p & 0 \end{pmatrix} \begin{Bmatrix} 1 & 1 & k \\ j & j & j'' \end{Bmatrix} \tag{4.49}$$

However, $\rho_q^{(k)}$ are the state multipoles in the xyz frame of section 4.4, and must be rotated into the XYZ frame used here. The rotated (XYZ) state multipoles will be labelled $\bar{\rho}_q^{(k)}$.

This is done via[88,147]

$$\bar{\rho}_q^{(k)} = \sum_{q'} D^{(k)}_{qq'}(\phi, \theta, 0)\rho_{q'}^{(k)} \tag{4.50}$$

Under both frames, the monopole moment $\bar{\rho}_0^{(0)} = \rho_0^{(0)} = 1$.

In the case of excitation with linear polarised light (where the light is polarised perpendicular to Z), the appropriate rotation is one of $\theta = -\frac{\pi}{2}$, $\phi = 0$ and therefore

$$\bar{\rho}_0^{(2)} = -\frac{1}{2}\rho_0^{(2)} \tag{4.51}$$

$$\bar{\rho}_{\pm1}^{(2)} = 0 \tag{4.52}$$

$$\bar{\rho}_{\pm2}^{(2)} = -\sqrt{\frac{3}{8}}\rho_0^{(2)} \tag{4.53}$$

with all the $k = 1$ moments being zero (no orientation). If the light is polarised along Z, there is no rotation and only the $q = 0$ multipoles are non-zero.

For circular polarised light excitation, the rotation is $\theta = -\frac{\pi}{2}$, $\phi = -\frac{\pi}{2}$ and so

$$\bar{\rho}_0^{(1)} = 0 \tag{4.54}$$

$$\bar{\rho}_{\pm1}^{(1)} = -\frac{i}{\sqrt{2}}\rho_0^{(1)} \tag{4.55}$$

$$\bar{\rho}_0^{(2)} = \frac{-1}{2}\rho_0^{(2)} \tag{4.56}$$

$$\bar{\rho}_{\pm1}^{(2)} = 0 \tag{4.57}$$

$$\bar{\rho}_{\pm2}^{(2)} = \sqrt{\frac{3}{8}}\rho_0^{(2)} \tag{4.58}$$

Using the treatment of Blum,[147] the effect of a magnetic field on the density matrix can be accounted for by a *perturbation coefficient*, $G(j,t)^{Kk}_{Qq}$:

$$\bar{\rho}_q^{(k)}(j,t) = \sum_{KQ} \bar{\rho}_Q^{(K)}(j, t=0)G(j,t)^{Kk}_{Qq} \tag{4.59}$$

In this equation, the perturbation coefficient is[147]

$$G(j,t)^{Kk}_{Qq} = \delta_{Kk} \sum_{Q'} \exp(-i\omega_L Q' t) D^{(K)*}_{QQ'}(\alpha,\beta,0) D^{(K)*}_{qQ}(\alpha,\beta,0) \tag{4.60}$$

where the magnetic field vector has polar angle β and azimuthal angle α in the Lab frame — as the field is along Z here, this simplifies to

$$\bar{\rho}^{(k)}_q(j,t) = \mathrm{e}^{-i\omega_L q t} \bar{\rho}^{(k)}_q(j',t=0) \tag{4.61}$$

Note that the exponential term is a rotation at the Larmor frequency about the magnetic field axis, which is reminiscent of the classical viewpoint discussed in the next subsection. The magnetic field cannot mix multipoles of different rank (k); orientation and alignment cannot be interconverted. Only the phases (reflected in the components, q) change, corresponding to the distribution of $\boldsymbol{j}$ precessing about the field axis.

Following the treatment of Brucat and Zare,[175] we note that, when collisions occur with the initial and final directions of motion unspecified, the rate of relaxation Γ_k is dependent on k but not q. Therefore, using equation (4.61), the excited density matrix evolves as[175]

$$\bar{\rho}(t) = \bar{\rho}^{(0)}_0 \mathrm{e}^{-\Gamma_0 t} + \left[\bar{\rho}^{(2)}_0 + \bar{\rho}^{(2)}_2 \mathrm{e}^{-2i\omega_L t} + \bar{\rho}^{(2)}_{-2} \mathrm{e}^{+2i\omega_L t}\right] \mathrm{e}^{-\Gamma_2 t} \tag{4.62}$$

for light polarised linearly perpendicular to Z, and for light polarised parallel to Z, the evolution includes only the $q = 0$ terms. In the case of circular polarised light, the density matrix evolves as

$$\begin{aligned} \bar{\rho}(t) =& \bar{\rho}^{(0)}_0 \mathrm{e}^{-\Gamma_0 t} \\ &+ \left[\bar{\rho}^{(1)}_1 \mathrm{e}^{-i\omega_L t} + \bar{\rho}^{(1)}_{-1} \mathrm{e}^{+i\omega_L t}\right] \mathrm{e}^{-\Gamma_1 t} \\ &+ \left[\bar{\rho}^{(2)}_0 + \bar{\rho}^{(2)}_2 \mathrm{e}^{-2i\omega_L t} + \bar{\rho}^{(2)}_{-2} \mathrm{e}^{+2i\omega_L t}\right] \mathrm{e}^{-\Gamma_2 t} \end{aligned} \tag{4.63}$$

The relaxation rates Γ_k can be decomposed into collision-free and collisional rates:[197]

$$\Gamma_0 = k_0 + k_1[Q] \tag{4.64}$$

$$\Gamma_k = k_0 + k_1[Q] + k_2^{(k)} + k_3^{(k)}[Q] \tag{4.65}$$

k_0 and $k_1[Q]$ describe the collision-free and collisional loss of population respectively, and $k_2^{(k)}$ and $k_3^{(k)}[Q]$ describe the collision-free and collisional loss of orientation ($k = 1$) or alignment ($k = 2$).[14,25]

An expression for the time-dependent fluorescence intensity can be obtained by considering emission to the final state $|j_f m_f\rangle$:[88]

$$I \propto \sum_{m m_f} \left| \langle j_f m_f | \hat{\boldsymbol{e}}_{\mathrm{det}} \cdot \hat{\boldsymbol{d}} | j(t) \rangle \right|^2 \tag{4.66}$$

The intensity, I, can be expressed as a function of the state multipoles $\rho_0^{(k)}(j)$, the angle θ between $\boldsymbol{e}_{\mathrm{pr}}$ and $\boldsymbol{e}_{\mathrm{det}}$ (see figure 4.3) and the initial and final polarisations p and p', which take the value 0 for linear polarisation and ± 1 for circular polarisation ($+1 =$ LCP, $-1 =$ RCP).[17,88] Note that the state multipoles $\rho_0^{(k)}(j)$ are those in the xyz frame; equations (4.51)-(4.58) are employed in order to transform to and from the XYZ-frame multipoles $\bar{\rho}_q^{(k)}(j)$.

$$I(p, p'; \theta) \propto (-1)^{j_f + j - p'} \sum_k (2k+1)^{1/2} \begin{Bmatrix} 1 & 1 & k \\ j & j & j_f \end{Bmatrix} \begin{pmatrix} 1 & 1 & k \\ -p' & p' & 0 \end{pmatrix} \rho_0^{(k)}(j) P_k(\cos\theta) \tag{4.67}$$

This can be used with the time dependence of $\bar{\rho}_q^{(k)}(j)$ considered above (equations (4.62) and (4.63)) to determine the time-dependent fluorescence intensity for the system considered here.

For example, for linear polarised light with the polarisation parallel to X, which will

be labelled $I_{\parallel}$:[175]

$$I_{\parallel}(t) \propto \left[\begin{Bmatrix} 1 & 1 & 0 \\ j & j & j_f \end{Bmatrix} \rho_0^{(0)} \mathrm{e}^{-\Gamma_0 t} - \begin{Bmatrix} 1 & 1 & 2 \\ j & j & j_f \end{Bmatrix} \sqrt{2} \rho_2^{(0)} \mathrm{e}^{-\Gamma_2 t} P_2 \left(\cos(\omega_L t + \phi) \right) \right] \tag{4.68}$$

For light with the orthogonal polarisation, $I_{\perp}$ contains no quantum beat, as previously noted.

Ref. 198 gives explicit expressions for the fluorescence intensity for the simplified case where excitation is from the pure state $|j = 0, m = 0\rangle$ to $j = 1$.

The analysis of these fluorescence traces for linear and circular polarised light, and the extraction of the rates of depopulation and depolarisation of the excited OH(A), will be dealt with in the section on data analysis (section 4.8).

4.6.3 Classical model — precession of $\boldsymbol{j}$ vectors

The above quantum mechanical picture of the ZQBS technique is complemented by the classical viewpoint, which lends itself more readily to visualisation. In this conception of the experiment, the excited distribution of $\boldsymbol{j}$ vectors precesses about the magnetic field axis at the Larmor frequency (similar to an NMR experiment).

The precession originates from the moment of $\boldsymbol{j}$ arising from the interaction of the magnetic moment, $\boldsymbol{\mu}_j$, with the magnetic field $\boldsymbol{B}$:[159]

$$\frac{\mathrm{d}\boldsymbol{j}}{\mathrm{d}t} = \frac{g_j \mu_0}{\hbar} (\boldsymbol{j} \times \boldsymbol{B}) = -(\boldsymbol{j} \times \boldsymbol{\omega}_L) \tag{4.69}$$

in which the magnetic moment, $\boldsymbol{\mu}_j$ is $(g_j \mu_0/\hbar)\boldsymbol{j}$ and the vector $\boldsymbol{\omega}_L$ is $-(g_j \mu_0/\hbar)\boldsymbol{B}$ (see section 2.1.1).

To model this precession, an active rotation matrix can be used:[88]

$$P(\theta_j, \phi_j; t) = \boldsymbol{R}(0, \omega_L t, 0) P(\theta_j, \phi_j; 0) \tag{4.70}$$

which, using equation (4.33), becomes

$$P(\theta_j;t) = \frac{1}{2}\left[1 + 3r_0^{(1)}P_1(\cos\omega_L t)P_1(\cos\theta_j) + 5r_0^{(2)}P_2(\cos\omega_L t)P_2(\cos\theta_j)\right] \tag{4.71}$$

The emission intensity is given by

$$I(t) = \mathrm{e}^{-k_p t}\int P(\theta_j;t)\,|\boldsymbol{e}\cdot\boldsymbol{\mu}|^2\ \mathrm{d}\theta_j \tag{4.72}$$

where k_p is the rate of loss of population from the excited state. The square modulus term is given by the analogous equation to (4.30):

$$|\boldsymbol{e}\cdot\boldsymbol{\mu}|^2 = \left|\sum_{Q=-1}^{+1}(-1)^Q \boldsymbol{e}_Q D^{(1)}_{\Delta Q}(0,\theta_j,\phi_j)\right|^2 \tag{4.73}$$

thus resulting in the fluorescence intensity[17,88] $I = A\mathrm{e}^{-k_p t}\mathcal{F}$, where $\mathcal{F}$ is tabulated by spectroscopic *emission* branch in Table 4.2.

branch	linear	circular
P	$1-\frac{1}{4}r_0^{(2)}\left[3\cos(2\omega_L t+2\phi)+1\right]$	$1+\frac{3}{2}r_0^{(1)}\cos(\omega_L t+\phi)+\frac{1}{2}r_0^{(2)}P_2\left(\cos(\omega_L t+\phi)\right)$
Q	$1+\frac{1}{2}r_0^{(2)}\left[3\cos(2\omega_L t+2\phi)+1\right]$	$1-r_0^{(2)}P_2\left(\cos(\omega_L t+\phi)\right)$
R	$1-\frac{1}{4}r_0^{(2)}\left[3\cos(2\omega_L t+2\phi)+1\right]$	$1-\frac{3}{2}r_0^{(1)}\cos(\omega_L t+\phi)+\frac{1}{2}r_0^{(2)}P_2\left(\cos(\omega_L t+\phi)\right)$

Table 4.2: Table of factors $\mathcal{F}$ for use in the equation $I = A\mathrm{e}^{-k_p t}\mathcal{F}$

Important points to note from this table include that no quantum beats are observed for orientation when detecting emission on the Q branch, and that, for linear polarised light, the beats in the P and R branches are in phase with each other but out of phase with the beats in Q emission. Therefore unresolved detection will result in a loss in beat amplitude, a point that will be returned to in section 4.7.6.

When using circular polarised light, two sets of beats are observed — one of frequency ω_L for orientation, and one of frequency $2\omega_L$ for alignment. Because of the relative magnitude of $r_0^{(2)}$ relative to $r_0^{(1)}$ for excitation with circular polarised light (Table 4.1), the alignment beats are usually not observable in this thesis, and circular polarised light is

therefore used as a probe of orientation only. In this case, there is no (orientation) beat observed in Q emission, and the beats in the P and R branches cancel out, meaning that no beat will be observed if the emission is not resolved. Section 4.7.6 will deal with this point further.

Figure 4.5 shows two sets of experimental fluorescence traces. Alignment beats, using linear polarised light, are displayed in the left hand panel, and the right hand panel contains representative orientation beats.

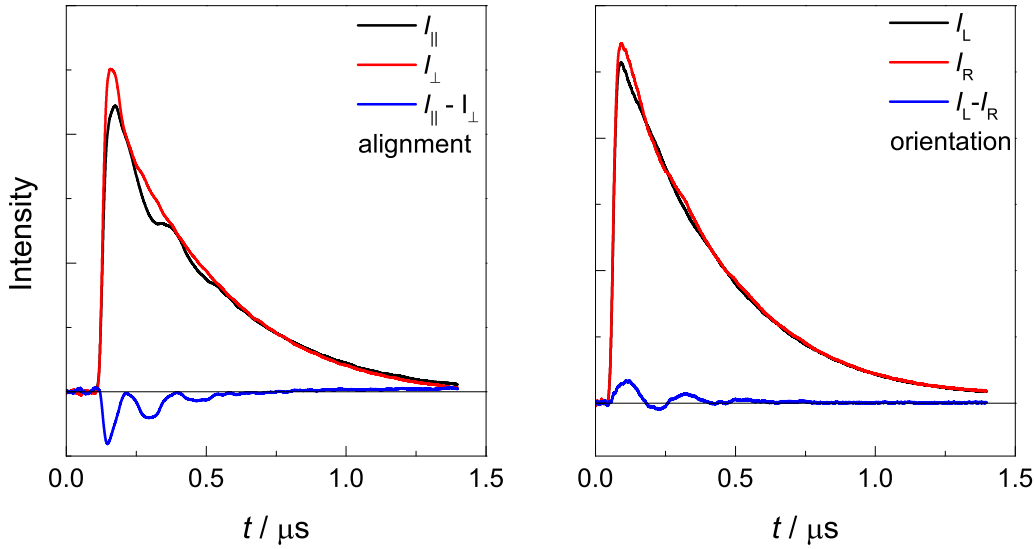

Figure 4.5: Experimental fluorescence from OH(A) excited by linear (left) or circular (right) polarised light. The blue trace displays the difference between the two channels in each case.

4.7 Experimental setup

The apparatus used for the experiments in this thesis is presented in figure 4.6, and the following subsections describe each part in detail. OH radicals are generated from the 193 nm photolysis of nitric acid, which is flowed slowly through the chamber with the collider gas (Kr or Xe). After a delay, during which the nascent OH radicals are translationally thermalised through collisions with the collider gas, a second laser is used to excite them to the $A^2\Sigma^+$ state. The subsequent fluorescence is resolved, collected and analysed as set

out in section 4.8.

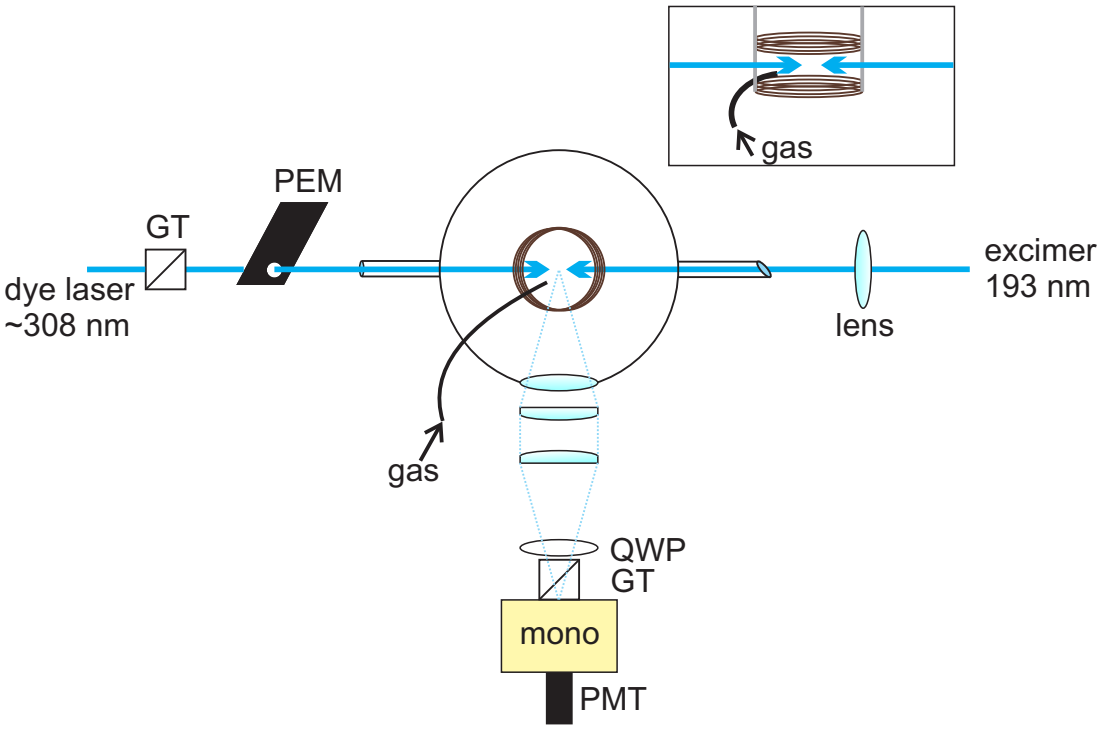

Figure 4.6: The experimental rig used in the experiments described here — see text for details. GT: Glan-Taylor polariser, QWP: Quarter-wave plate, PEM: photo-elastic modulator, PMT: photomultiplier tube, mono: monochromator.

4.7.1 Vacuum chamber and flow system

The experiments in this work were carried out in a cylindrical vacuum chamber, made of stainless steel, with a diameter of approximately 30 cm. The inner walls were painted black to minimise the detection of scattered laser light.

The pressure inside the chamber was maintained at $\sim 1 \times 10^{-3}$ mbar (~ 1 mTorr) by a mechanical rotary pump (Leybold Trivac), and was measured using a Baratron pressure gauge, rated up to 10 Torr. This gauge is a capacitance manometer, which measures true pressure (force per unit area) by means of a diaphragm, and therefore the reading obtained is independent of the type of gas used.

The Baratron gauge was periodically calibrated by evacuating the chamber to $\sim 1 \times 10^{-6}$ mbar with a baffled, oil-filled diffusion pump (Edwards), backed by the same rotary pump mentioned above, and setting the measured pressure to zero. In this low-

pressure regime, the pressure was monitored using a hot-cathode ion gauge (Leybold Ionivac). The diffusion pump was also used to remove any impurities adsorbed on the walls of the chamber between experimental runs.

Because of the corrosive nature of nitric acid, used to generate OH (section 4.7.2), a liquid nitrogen trap was used in the foreline to prevent it entering the rotary pump. This trap could be bypassed and removed for daily venting and cleaning.

The OH(A, $v = 0$) + Kr experiments were carried out by using a steady flow of nitric acid (70% with water, degassed by pumping down for several hours) through a Teflon (PTFE) tube into the centre of the chamber, such that the partial pressure of nitric acid was around 20 mTorr. Kr was added via a separate inlet in partial pressures between 100 and 600 mTorr.

The flow system used in the OH(A) + Xe and OH(A, $v = 1$) + Kr experiments is shown in figure 4.7. Helium carrier gas was flowed through a glass bubbler filled with a 2:3 mixture of 98% sulfuric acid and 70% nitric acid, in order to generate a flow of HNO_3. The reason for the sulfuric acid was to reduce the vapour pressure of water.[27,199] From similar procedures in the literature,[27,199–202] it is believed that the proportion of nitric acid in the He/HNO_3 flow was on the order of 3-5%. A needle valve was used to control the flow of the helium-acid mix into the chamber at around 2-3 standard cubic centimetres per minute (sccm), measured by a Tylan FM-360 flowmeter, such that the partial pressure of the mix inside the chamber was around 100 mTorr. The collider gas (Kr or Xe) was used neat, straight from the gas cylinder (BOC). The flow was controlled within the range 3-10 sccm using a second needle valve and flowmeter, providing a partial pressure of 100-600 mTorr in the chamber. The two flows of helium-acid mix and rare gas were combined in a T-piece and flowed into the chamber through a Teflon (PTFE) tube, which was directed into the centre of the chamber where the laser beams intersected. All parts of the flow system that came into contact with nitric acid vapour were made of stainless steel or Teflon, except for the bubbler itself, which was made of glass. The outlet valve was throttled to maintain the flow at a low rate, since both Kr and Xe are rather expensive. Nevertheless, care was

taken to ensure that the flow was high enough such that a fresh volume of gas was probed on each laser shot.

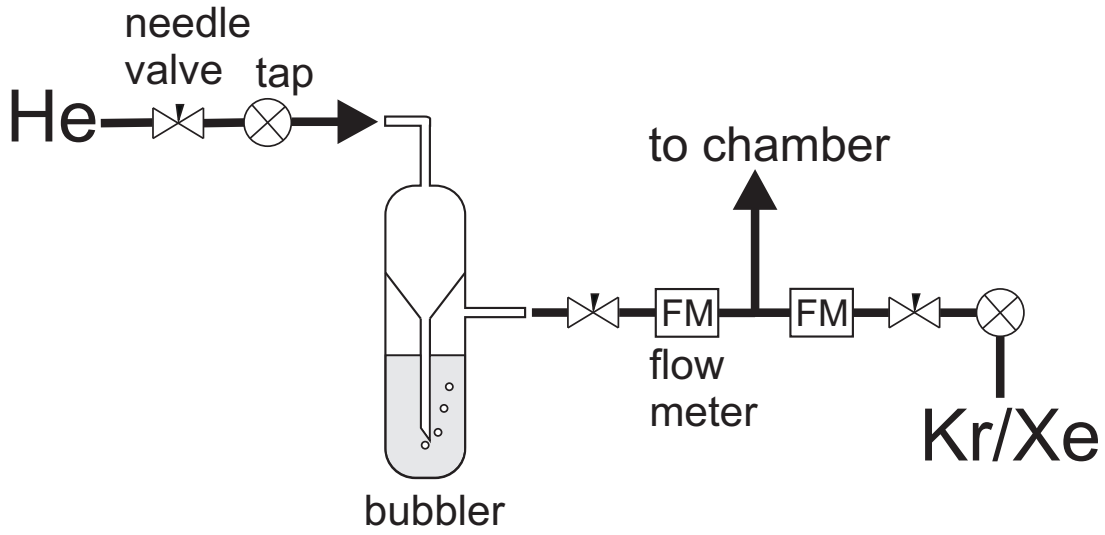

Figure 4.7: The gas flow system used in the experiments in this thesis. See text for details.

Calibration of the flowmeters employed in these experiments was carried out using a burette. A flow of helium passing through the flowmeter under test was used to push a soap bubble through the burette, and its progress was timed between two set points. This procedure measured the time taken for a known volume of helium to flow through the flowmeter, and so the flowmeter reading could be related to the true mass flow rate. Flow rates for gases other than helium could be measured using a correction factor, which is dependent on the density and specific heat capacity of the gas involved. These correction factors are tabulated by various manufacturers, for example ref. 203. For Kr and Xe, the correction factors relative to He are 1.06 and 0.91 respectively. Note that the helium/acid mix was treated as pure helium for the purposes of ascertaining its mass flow rate.

To verify correct calibration of the flowmeters, experimental results for OH(A, $v = 0$) + Kr were collected using the high-flow method, where the partial pressures were measured directly, and the low-flow method, where they were calculated from the ratio of mass flow rates. Fluorescence traces at the same pressures were indistinguishable between the two methods, and the resulting cross-sections agreed to within experimental error, lending a high degree of confidence to the low-flow method's accuracy.

4.7.2 Generation and thermalisation of OH(X) radicals

OH(X) radicals are generated by the 193 nm photolysis of nitric acid vapour in the centre of the chamber. The laser used is an ArF excimer (Coherent COMPex 102) focused just before the probe volume with a biconvex lens. The focus is purposely placed away from the probe volume to avoid any possible multiphoton dissociation of HNO_3.

In previous studies of OH with the present experiment,[11–13,16] the precursor molecule used was hydrogen peroxide. However, the present modifications to the gas flow system (to enable experiments to be carried out using a much lower volume of collider gas) make this impossible because of the tendency of H_2O_2 to dissociate on the stainless steel inner surfaces of the flowmeters. Therefore HNO_3 is used exclusively in this work.

Nitric acid has a large cross-section for absorption of light at 193 nm (1330 Å^2),[204,205] with a branching ratio of[202,206] 0.50 ± 0.05 between the OH + NO_2 and O + HONO channels corresponding to a quantum yield Φ_{OH} of[202,206] 0.33 ± 0.04. Two decay channels produce slow and fast OH(X) radicals,[201] with the overall OH(X) nascent rotational state distribution being peaked at low values of N and falling off fairly rapidly, extending to around $N = 16$ at the highest.[201,207] This is in contrast to the hotter distribution observed from the 193 nm photolysis of H_2O_2, which peaks at[208,209] $N = 12$.

For an experiment run at thermal collision energies, it is important to let the nascent, translationally hot OH(X) fragments relax before exciting them to OH(A). This was done by introducing a delay of between 9 and 30 μs between the photolysis of HNO_3 and the probing of OH(X). The lower end of this delay is in accordance with refs. 27,199 and also with a simple hard-sphere kinetic model of the OH(X) velocity distribution at the lowest pressures used experimentally, as used in refs. 22,184 and 210. Longer delays were used when unresolved fluorescence was being recorded, to avoid a baseline due to emission from OH(A) produced in the photolysis of HNO_3.

4.7.3 Laser system

As described in the previous subsection, an excimer laser was used to produce pulses of 193 nm light for photolysis of nitric acid. The experiment was run at a repetition rate of 10 Hz, and each pulse from the excimer has an energy of 80-100 mJ in a rectangular profile of 2x3 cm. This was focused into the centre of the chamber as described above, down an evacuated side arm of the chamber containing 10 cm-long baffles. The window for the photolysis light is made of fused silica (to maximise UV transmission), and was slanted to direct scattered light away from the photomultiplier field of view. In this experiment, the photolysis radiation was used without polarisation as it acts simply as a source of OH(X). These radicals undergo several collisions before being probed, so any polarisation they may have had will be lost before they are excited to the A state.

The probe beam was propagated along the same axis as the photolysis beam, but in the opposite direction, also through a set of baffles. The window in this case was orthogonal to the direction of propagation, in order to preserve the beam's polarisation.

For $v = 0$ experiments, OH(X) was excited to OH(A) on the (0,0) band using light of wavelengths around 306 to 310 nm. This was produced by using the frequency-doubled (532 nm) output of a flashlamp-pumped Nd:YAG laser (Continuum Surelite III-10) to pump a tunable Lambda Physik LPD-3002 dye laser, operating on Rhodamine 101 dye in methanol. The fundamental laser emission (612-620 nm) was frequency-doubled with a BBO crystal and compensator to produce the required UV laser radiation.

For experiments in which OH(A, $v = 1$) was prepared, the same laser system was used with Rhodamine 6G dye in methanol, which lases at a shorter wavelength (562-569 nm). The frequency-doubled radiation was used to excite OH(X) on the (1,0) band.

At the power used in the experiment, the pulse energy at the exit of the dye laser was approximately 0.5 mJ; by the time the light entered the chamber, this had been reduced to less than 100 μJ by the steering and polarising optics. LIF intensity was monitored carefully as a function of laser power in order to avoid saturation. The beam was irised down to a spot of diameter 2 mm just before the entrance window. As the Helmholtz coils

(see section 4.7.4) have an inner diameter of 5 cm, this means that the probe volume was approximately 600 mm^3.

The wavelength desired was selected from the dye's emission profile by using a diffraction grating. The linewidth of the dye laser emission is[17,211] 0.36 cm^{-1}. It is possible to narrow the linewidth using a Fabry-Perot etalon,[211] but this was not necessary for the resolution required in this thesis — in this work, the whole Doppler profile is excited at once, rather than a subset of molecules with certain velocities.

The YAG laser used in this work produces pulses of 4-6 ns in length, which implies a coherence width of around 27 MHz by time-energy uncertainty.[13,17]. Note that this refers to the energy spread of each individual photon, while the figure of 0.36 cm^{-1} above refers to the range of energies in the whole laser pulse. As the hyperfine levels in OH(A) are split by several hundred MHz,[13,212,213] it is not possible to excite more than one level simultaneously, and so hyperfine beats are not observed in this thesis. The Zeeman levels of OH(A), on the other hand, are more closely spaced, and several levels can be excited coherently by a single photon from this laser system.

The polarisation optics for the probe laser radiation are as shown in figure 4.6. On exit of the laser, the beam is linearly polarised, and a Glan-Taylor prism was used to improve this polarisation before the beam enters a photo-elastic modulator (PEM). The PEM uses the piezoelectric effect in quartz to stretch and compress a fused silica bar. Doing so makes the optical element birefringent — different polarisations of light pass through it at different speeds. The phase difference between the horizontal and vertical components of polarisation is known as the 'retardation'.

For studies of alignment, the PEM alternates between being relaxed (no retardation), where the original polarisation of light is passed, and half-wave retardation, where the PEM acts as a half-wave plate. This rotates the plane of polarisation by 90 degrees. In this way, the probe laser beam was horizontally and vertically polarised on alternate shots.

Orientation studies use circular polarised light, for which the PEM was set to quarter-wave retardation. In this mode, it acts as a quarter-wave plate, and its output was left-

or right-hand circular polarised light on alternate shots.

The polarisation of the probe light was checked on exit of the chamber using a Rochon prism and photodiode, and found to be better than 95%. For checking the polarisation in the circular polarised case, a Fresnel rhomb was used to convert circular to linear polarised light before it entered the Rochon prism.

4.7.4 Magnetic field

A pair of Helmholtz coils (inner diameter 5 cm, separation 2.5 cm, 10 turns) were used to generate a uniform, tunable magnetic field of between 0 and 25 Gauss in the centre of the chamber.[214] As the DC current used in the coils was quite high (up to tens of amps), the coils were pulsed on a millisecond timescale to avoid them heating up, but the field was constant during each acquisition cycle. The uniformity of the field within the coils, and the calibration of the field produced as a function of current, was checked using a Hall probe. It was also possible to verify the field strength using the Zeeman quantum beat frequency, as the g-values of OH(A) are known to a high degree of precision.

To null the effects of the Earth's magnetic field (and other external fields) inside the chamber,[25,215] the Helmholtz coils were surrounded by shielding made of μ metal. This is a nickel-iron-molybdenum alloy of high magnetic permeability, which provides a path for magnetic field lines around the shielded region.[216] Measurements with a Hall probe demonstrated that these measures were effective at isolating the interaction region from external fields.

The uniformity of the field within the coils is important so that the Larmor frequency for a given Zeeman level is the same for all points within the interaction region. If it were not, Zeeman quantum beats with different frequencies would interfere destructively in the observed fluorescence (so-called 'dephasing'), leading to a destruction of the beat. The effects of field inhomogeneity are captured in the rate $k_2^{(k)}$ (section 4.8). This also accounts for hyperfine depolarisation[25] of angular momentum, though this is only significant when j is of the order of $I = 0.5$ and, as such, is not considered further here.

4.7.5 Timing and triggers

The experiment was run at a repetition rate of 10 Hz. The master trigger was provided by a Stanford DG-535 delay generator, and the timing system was as shown in figure 4.8 – note that all instruments were triggered off the rising edge of the respective pulse. The magnetic field was turned on shortly after the master trigger, and remained on for the duration of the acquisition cycle. After being triggered by the master trigger, the PEM sent a signal to the external trigger input of another DG-535 after a delay set to produce the desired retardation, and this signal also acted as the oscilloscope trigger. This second delay unit triggered the excimer laser and, 9 to 30 μs later, the flashlamp and Q-switch of the YAG laser. The latter two triggers were relayed through an opto-electronic isolator to avoid electronic interference.

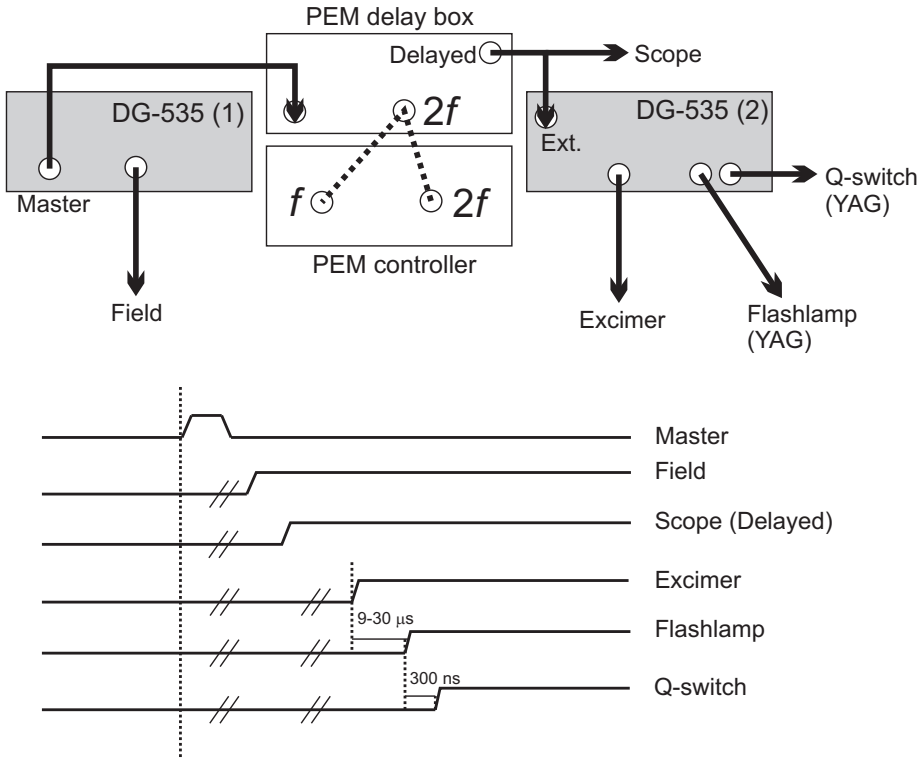

Figure 4.8: Timings for the experiment (not to scale) — see text for details. Note that the connection between the PEM boxes is $2f - 2f$ for alignment studies, $2f - f$ for orientation studies.

4.7.6 Detection optics and monochromator

As shown in figures 4.3 and 4.6, the fluorescence was collected by a set of lenses and then passed through some polarising optics before entering the monochromator. In the case of alignment measurements, this was a linear (Glan-Taylor) polariser; for orientation experiments, a quarter-wave plate was placed before the linear polariser to turn circular to linear polarisation. These optics are necessary to observe a quantum beat in the fluorescence, as detailed in section 4.6. The axis of polarisation of the Glan-Taylor polariser was parallel to the monochromator's preferred axis (because of the direction of lines on the grating) and the quarter-wave plate was set at 45 degrees to this.

Fluorescence was resolved before detection using a Czerny-Turner monochromator (0.3 m, Bentham M300, 2400 lines/mm) with adjustable entrance and exit slits to control the resolution. The maximum resolution attainable was theoretically 0.7 Å, but in practice was closer to 1.0 Å, and the bandwidth with the slits fully opened was 77 Å.

When the monochromator grating is set to λ_m and the slits are adjusted for bandwidth B, the transmission function can be approximated by[17]

$$I(\lambda;\lambda_m) = \exp\left[-4\ln 2\left(\frac{\lambda_m - \lambda}{B}\right)^2\right] \tag{4.74}$$

This function applies when the entrance and exit slits are both set to the same width, which was always the case in this thesis.

After the monochromator, the resolved fluorescence was focused onto the photomultiplier tube with a biconvex lens. The signal output was recorded on a Tektronix TDS 3032B oscilloscope (300 MHz), except for the OH(A, $v = 1$) + Kr experiments, where a Tektronix TDS 220 oscilloscope (100 MHz) was used instead. A home-built switching box, triggered from the 'delayed' output of the PEM controller (the same trigger as the oscilloscope), was used to direct the signal to channel 1 or 2 of the oscilloscope on alternate laser shots, with 'channel 2' being inverted. This ensured that one channel corresponded to $I_\parallel$ and the other to $I_\perp$, or I_L and I_R as the case may be. The oscilloscope digitised and

averaged the signal from several (up to 512) laser shots before sending it to a PC running LabVIEW data acquisition software.

Resolving the fluorescence permits the measurement of rates for a variety of different processes. The unresolved decay in population furnishes electronic quenching cross-sections, or the sum of quenching and vibrational energy transfer (VET) for initial $v = 1$; resolving the emission from a single excited j' state gives cross-sections for quenching plus rotational energy transfer (RET), or the sum of quenching, VET and RET in the case of initial $v = 1$.

For depolarisation measurements, the monochromator is even more necessary, as explained at the end of section 4.6. Oriented samples show no quantum beats in Q-branch emission, and the Zeeman beats in P- and R-branch emission are out of phase, so unresolved detection would not give a beat. Instead, the monochromator was set to the maximum of either the P or R branch, with the slits adjusted to detect all of the emission from that branch but reject emission from the other branches. This was accomplished using the LIFBASE spectral database[217] to simulate the dispersed fluorescence spectrum, and comparing to experimental results from scanning the monochromator grating position. Care was taken not to reject emission from any collisionally populated rotational levels within the same branch — this was checked by recording data at a variety of slit widths.

The measurement of alignment quantum beats is possible without resolving the fluorescence, though greater signal to noise ratios are possible by using the monochromator. This is because the Zeeman quantum beats in P- and R-branch emission are in phase with each other, but out of phase with Q-branch beats, so the cancellation in the unresolved emission is not total.

Figure 4.9 shows simulated quantum beats (see section 4.9) for orientation and alignment measurements using unresolved and resolved emission. It can be seen that there is little to no beat visible for the unresolved orientation results, and the unresolved alignment beat is smaller than the resolved beat.

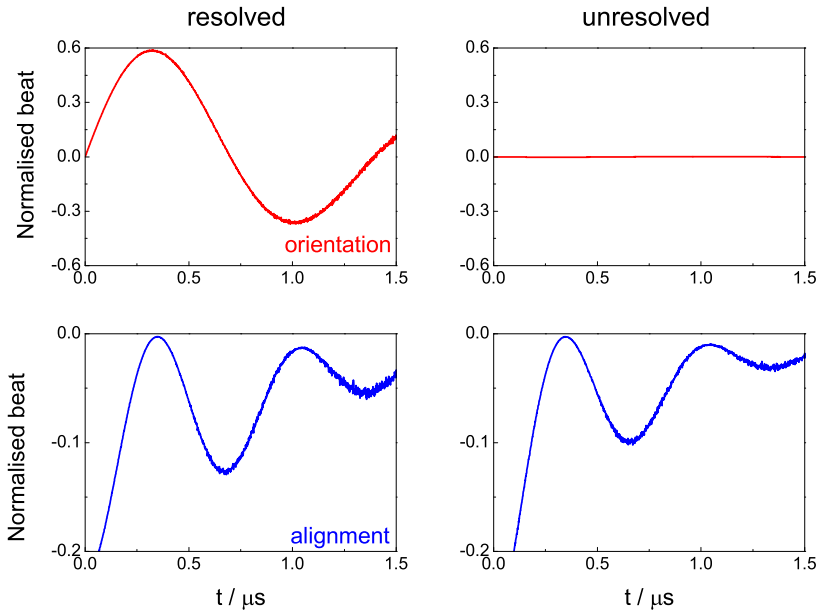

Figure 4.9: Simulated quantum beats (see section 4.9) for orientation (top) and alignment (bottom) measurements of OH(A, $v = 0$, $N = 5$, $j = 5.5$). Excitation on $R_{11}(4)$, detection on $P_{11}(6)$, 100 mTorr Kr. Left panels show resolved measurements (6.8 Å), right panels show unresolved measurements (77 Å). Magnetic field strength 1.4 Gauss (orientation), 2.8 Gauss (alignment).

4.8 Data analysis

The signal on the oscilloscope is split into two channels corresponding to $I_{\parallel}$ and $I_{\perp}$ (linear polarised light) or I_L and I_R (circular polarised light).

Linear polarised light

As in figure 4.6, the two channels of light are specified by the phase angle, ϕ, which is zero for $I_{\parallel}$ and $\pi/2$ for $I_{\perp}$. This means that the decays can be written using the expressions in table 4.2, using zero field for $I_{\perp}$ as there is no beat in this channel:

$$I_{\parallel} = A\mathrm{e}^{-k_p t}\left[1 + m r_0^{(2)} \mathrm{e}^{-k_d^{(2)}[Q]t}(3\cos(2\omega_L t) + 1)\right] \tag{4.75}$$

$$I_{\perp} = A\mathrm{e}^{-k_p t}\left[1 - 2m r_0^{(2)} \mathrm{e}^{-k_d^{(2)}[Q]t}\right] \tag{4.76}$$

in which m is branch-dependent (+ 0.5 for Q, − 0.25 for P and R), and $[Q]$ is the concentration of quencher gas. k_p and $k_d^{(k)}$ are the phenomenological rate for the loss of population, and the rate constant for the loss of polarisation, respectively.

This means that field-off data can be analysed using the weighted sum $I_\parallel + 2I_\perp$, which is sensitive to the decay in population but insensitive to polarisation:

$$I_\parallel + 2I_\perp = 3A\mathrm{e}^{-k_p t} \tag{4.77}$$

and the decay in polarisation can be isolated from the population decay via the *polarisation anisotropy*, R:

$$R = \frac{I_\parallel - I_\perp}{I_\parallel + 2I_\perp} = \frac{1}{3}\left[1 + mr_0^{(2)}\mathrm{e}^{-k_d^{(2)}[Q]t}(3\cos(2\omega_L t) + 1)\right] \tag{4.78}$$

When the field is on, the decay in polarisation is instead isolated by using

$$\frac{I_\parallel - I_\perp}{I_\perp} = \frac{mr_0^{(2)}\mathrm{e}^{-k_d^{(2)}[Q]t}\left(3\cos(2\omega_L t) - 1\right)}{1 - 2mr_0^{(2)}\mathrm{e}^{-k_d^{(2)}[Q]t}} \tag{4.79}$$

and, since it is not possible to isolate the decay in population, k_p is instead obtained by fitting $I_\parallel(t)$ using equation 4.75.

Circular polarised light

For circular polarised light, only the P and R branches are considered, as there is no (orientation) beat in Q branch emission. The magnetic field must be turned on to measure orientation in the experimental geometry used ($\phi = \pm\pi/2$, figure 4.6) — the advantage of the ZQBS technique here is that it enables orientation measurements to be made without pointing the probe laser directly at the detector. Unlike in the case of alignment measurements, there is no orientation measured at $t = 0$, and the field serves to rotate the orientation into the correct plane for detection.

Using tables 4.1 and 4.2, I_L and I_R can be written as

$$I_L = Ae^{-k_p t}\left[1 \mp su\frac{3}{4}e^{-k_d^{(1)}[Q]t}\cos(\omega_L t+\phi) + \frac{1}{20}e^{-k_d^{(2)}[Q]t}P_2\left(\cos(\omega_L t+\phi)\right)\right] \tag{4.80}$$

$$I_R = Ae^{-k_p t}\left[1 \pm su\frac{3}{4}e^{-k_d^{(1)}[Q]t}\cos(\omega_L t+\phi) + \frac{1}{20}e^{-k_d^{(2)}[Q]t}P_2\left(\cos(\omega_L t+\phi)\right)\right] \tag{4.81}$$

where s depends on the excitation branch and u on the detection branch (both +1 for P, -1 for R).

The decay in polarisation is isolated from that in population by fitting the polarisation ratio C:

$$\begin{aligned} C =& \frac{I_L - I_R}{I_L + I_R} = \frac{\frac{\mp 3us}{2}e^{-k_d^{(1)}[Q]t}\cos(\omega_L t+\phi)}{2 + \frac{1}{10}e^{-k_d^{(2)}[Q]t}P_2\left(\cos(\omega_L t+\phi)\right)} \\ \simeq& \mp\frac{3us}{4}e^{-k_d^{(1)}[Q]t}\cos(\omega_L t+\phi) \end{aligned} \tag{4.82}$$

where the second line comes from noting that $2 \gg 0.1$, and so the alignment contribution can be neglected. In this thesis, the experimentally measured C can always be simplified to a cosine multiplied by an exponential decay in the above way.

Fitting and error estimation

For the purpose of fitting, the decays are written as[218–221]

$$I(t) = Ae^{-k_p t}\left[1 + e^{-k_d^{(k)}[Q]t}\sum_F C_F\cos(2\pi\alpha_F Bt+\phi)\right] \tag{4.83}$$

and

$$C(t) = e^{-k_d^{(k)}[Q]t}\sum_F C'_F\cos(2\pi\alpha'_F Bt+\phi) \tag{4.84}$$

where C_F are the hyperfine level-dependent beat amplitudes, B is the field strength and $\alpha_F \simeq 2\frac{\mu_0}{\hbar}g_F$, with $\alpha'_F = \alpha_F/2$.

k_p and $k_d^{(k)}$ can be respectively broken down into terms that are independent of, and

dependent on, the pressure of the collider gas, Q:

$$k_p = k_0 + k_1[Q] \tag{4.85}$$

$$k_d^{(k)} = k_2^{(k)} + k_3^{(k)}[Q] \tag{4.86}$$

k_0 is the inverse of the fluorescence lifetime, τ_0, and k_1 can be identified as the rate constant for collisional loss of population. When the fluorescence is unresolved, this is the quenching rate coefficient (or the sum of quenching and VET, for OH(A, $v = 1$)), and, for rotationally resolved fluorescence, k_1 is the sum of the quenching and RET rate coefficients (or the sum of quenching, VET and RET).

$k_2^{(k)}$ describes the non-collisional loss of polarisation, which is principally due to magnetic field inhomogeneities, and $k_3^{(k)}$ is the rate constant for collisional depolarisation (disorientation and disalignment for $k = 1, 2$ respectively).

The experimental data, comprising decay traces for six (or more) pressures for a given line, is fitted to the above equations globally using a program previously written in the group.[222,223] The program uses a genetic algorithm to minimise the value of χ^2, a merit function given by the square of the difference between the experimental and fitted decays. The advantage of the genetic algorithm is in making sure the global best solution is found, rather than a local minimum of χ^2.

The rates and rate constants k_i, the magnetic field strength, the phase and the beat amplitudes are all treated as adjustable parameters in the fit. Where one of these is known, for example the field strength, this serves as a useful check on the accuracy of the fit. Once the rate constants have been obtained, they are converted into thermally averaged cross-sections as in section 4.1.

An estimate of the experimental error is obtained by taking two standard deviations of the repeated results. When compared to the results of a Monte Carlo error routine described previously,[222,223] the two methods of estimating the error give almost the same answer, which is taken to indicate a 95% confidence interval. In the case of results for

electronic quenching, vibrational energy transfer and rotational energy transfer, *one* standard deviation is instead used for comparison with data in the literature.[27,224–227] When subtracting quantities, for example to get k_{RET} from the sum of $k_Q + k_{\mathrm{RET}}$ and k_Q alone, or to obtain the inelastic depolarisation rate constant from (total - elastic), the errors are propagated according to

$$\begin{aligned} k_X &= k_A \pm k_B \\ \mathrm{err}_X &= \sqrt{(\mathrm{err}_A)^2 + (\mathrm{err}_B)^2} \end{aligned} \tag{4.87}$$

When fitting data that is resolved in j — for RET (summed decays) or elastic depolarisation (normalised difference) — only the first 100 ns of the decay is fitted. This avoids contributions from collisional back-transfer, where an inelastic collision takes the molecule out of the initially prepared j level, but a second inelastic collision takes it back in, from where it emits — and this emission is detected as 'elastic' fluorescence. The fit length of 100 ns was chosen, using Poisson statistics, so that the overwhelming majority of molecules would have undergone one collision or fewer in that time under typical experimental conditions. This length was also varied to check it was short enough for convergence.

Vibrational energy transfer

Fitting the (weighted) summed decays, as above, furnishes the rate constant k_1, which enables (for $v = 0$) the separation of the rate constants for quenching and for RET. However, for $v = 1$ measurements, k_1 in the unresolved and rotationally resolved regimes provides the sums $(k_Q + k_{\mathrm{VET}})$ and $(k_Q + k_{\mathrm{VET}} + k_{\mathrm{RET}})$. Therefore a separate method of obtaining k_{VET} alone is required to separate out the contributions from these three different processes.

The procedure used was similar to refs. 224,226,227. The monochromator was used at high resolution to disperse the fluorescence, and the grating was scanned across the (0,0)

and (1,1) emission bands, which are next to each other but not significantly overlapped. They can therefore be separated by a 'cutoff' of 3123.9 Å, beyond which less than 1% of (0,0) emission can be found.[226] This provides rotationally resolved spectra of these two bands, as demonstrated in figure 4.10.

The laser powers were monitored before and after each scan to ensure they remained constant, and the spectra were recorded using $I_{\parallel} + 2I_{\perp}$ (with no magnetic field), which is independent of polarisation effects. For each monochromator grating position, the entire resolved fluorescence decay in time was recorded, so that an emission spectrum could later be generated for any desired integration time. The whole procedure was repeated at a variety of quencher (here, Kr) pressures.

The total intensity from the (0,0) and (1,1) bands was integrated and converted to populations of the respective vibrational states by[226]

$$\frac{\mathcal{N}_0}{\mathcal{N}_1} = \frac{A_{11}\nu_{11}^3 I_{00}}{A_{00}\nu_{00}^3 I_{11}} \tag{4.88}$$

where A_{00} and A_{11} are Einstein A-coefficients for the (0,0) and (1,1) bands, I_{00} and I_{11} are the respective integrated intensities, and ν_{ii} is the centre frequency of the band. The same Einstein A-coefficients and centre frequencies were used as in ref. 226 for comparison with the literature data.

Time integration of the spectra was performed for a variety of gate lengths between 100 and 500 ns, and the resulting population ratio was extrapolated back to $t = 0$ for each pressure. This enabled the data to be fitted to a straight line as below, without the effects of quenching in $v = 0$, or rotational energy transfer out of the initial (N, j) level, coming into the picture.

$$\frac{\mathcal{N}_0}{\mathcal{N}_1}([\mathrm{Kr}]; t = 0) = k_{\mathrm{VET}}[\mathrm{Kr}] + k_{\mathrm{intercept}} \tag{4.89}$$

The intercept corresponds mainly to VET caused by background gases.

Another way of extracting k_{VET} was by plotting the population ratio against pressure for each integration time to get a time-dependent k_{10}, and then extrapolating to obtain

$k_{\mathrm{VET}} = k_{10}(t = 0)$. The two methods are equivalent, but sometimes the second proved to be more robust. Both methods are illustrated graphically in figure 4.11.

$$\frac{\mathcal{N}_0}{\mathcal{N}_1}([\mathrm{Kr}]; t) = k_{10}(t)[\mathrm{Kr}] + k'_{\mathrm{intercept}} \tag{4.90}$$

The rate constant, as measured, has units of $\mathrm{mTorr}^{-1}\tau^{-1}$; the lifetimes used to convert this to a cross-section are the inverse of k_0 measured from the unresolved fluorescence studies.

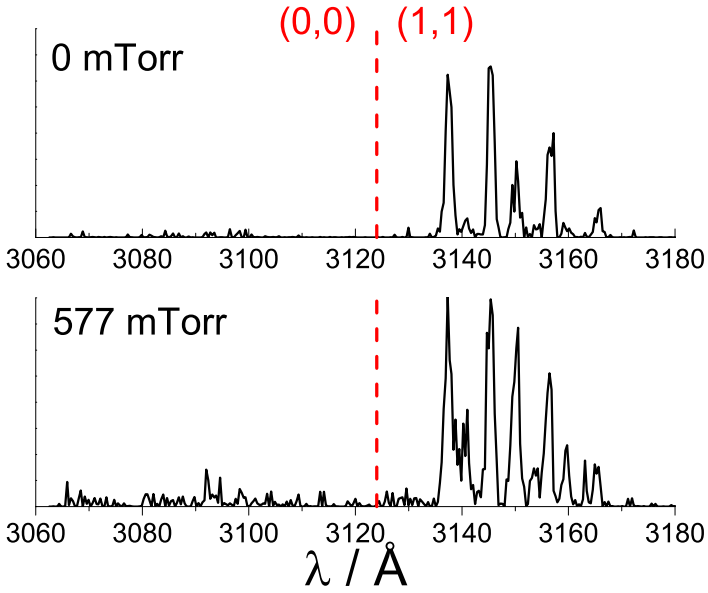

Figure 4.10: Example rotationally resolved fluorescence spectra for emission from OH(A, $v = 0, 1$) + Kr. Pressure as shown in figure, initial level excited $v = 1$, $N = 1$, $j = 1.5$ ($P_{11}(2)$).

4.9 Experimental simulations — dephasing and resolution

To aid in comparison of experiment and theory, fluorescence decays and quantum beats were simulated, starting from theoretical (QCT) rate constants and depolarisation moments. The simulation used a Monte Carlo method previously reported within the group[13,210,223] and recently extended to include the effects of monochromator resolution.[22]

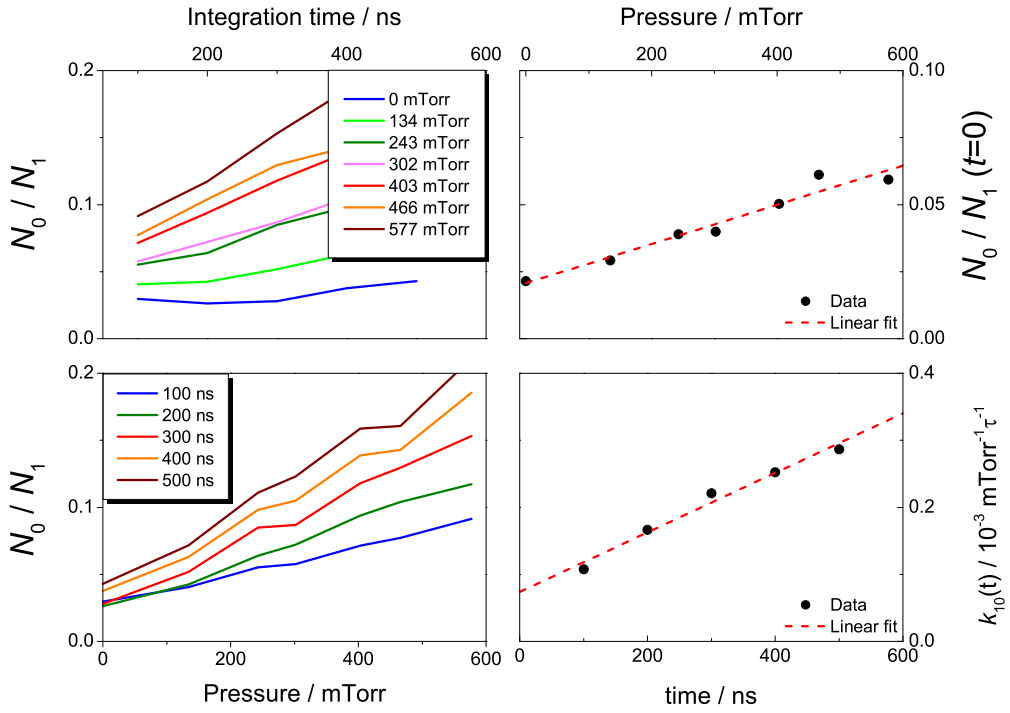

Figure 4.11: Extraction of k_{VET} from dispersed fluorescence spectra, as described in the text. Top row: equation (4.89), bottom row: equation (4.90). Initial level excited $v = 1$, $N = 1$, $j = 1.5$ ($\mathrm{P}_{11}(2)$).

The program integrated the kinetic equations[25] for the population and polarisation of OH(A,$v = 0$,N,j) by simulating around 1×10^7 individual encounters between OH(A) and Kr/Xe. State-to-state probabilities for the collisional transfer of population and polarisation were calculated from the input QCT data, probabilities for fluorescence at each timestep were taken from the experimental radiative lifetimes[217], and a random number was generated at each timestep to decide what the molecule should do. The options open to it were to do nothing (elastic collision), undergo rotational energy transfer, electronic quenching or to fluoresce.

By combining many such encounters, simulated LIF decays were produced and could be analysed in the same way as experimental data. This was useful for comparison between experiment and theory, as well as validating the fitting techniques used (as the required rate constants were already known from the input). More importantly, the effect of changing the monochromator resolution could be tested to ensure that the experimental settings

would not miss emission from any collisionally populated levels, yet would still be able to resolve a quantum beat.

However, the main reason for doing the simulations was to investigate *dephasing* of the quantum beat over time. In an inelastic collision, the $g_{F'}$ value of the final level (and hence the Larmor frequency of the beat) will be different to the inital g_F value. Collisions which change the spin-rotation state of the radical (from $j = N + S$ to $j = N - S$ or vice versa) will have a particularly large difference in beat frequency, as the g_F value changes sign. Over time, the observed quantum beat thus becomes a superposition of beats of differing frequencies, and destructive interference between them results in a loss of beat amplitude. This process is experimentally indistinguishable from collisional depolarisation, and so the experimental $k_3^{(k)}$ will be an overestimate of the true $k_d^{(k)}$, more so at low N where the difference in g_F values is greatest.

The simulations described here concur with simulations of similar systems performed previously in the group[12,13,15,16,22] in their conclusion that dephasing is a minor contribution to the measured $k_3^{(k)}$, making up 10% at most of the observed depolarisation.

4.10 Summary

The experimental methods used in this thesis have been presented and compared with techniques used in other laboratories. The production of polarised OH(A), and its collisional depolarisation, have been considered and the fitting procedures set out. Before presenting the results obtained by employing these methods, the theoretical techniques used in this work will be presented in the following chapters. The results from experiment and theory will then be compared, both with each other and with data from the literature.

Chapter 5

Theoretical methods

This chapter describes the theoretical methods used in this thesis to model collisional energy transfer, depolarisation and related processes in the OH(A,X) + Kr/Xe systems. The potential energy surfaces used have been introduced in section 2.2, and the adiabatic *quasi-classical trajectory (QCT)* method mentioned in chapter 1 will be outlined here, including the tensor opacity formalism employed to generate quasi open-shell cross-sections.

The recent review article by Paterson *et al.* contains a discussion of these and other theoretical techniques for relating the potential energy surface(s) that a collision evolves on to the dynamics, as well as a comparison to relevant experimental data for collisions of diatomic radicals with rare gas atoms.[26]

The systems studied in this thesis both exhibit a significant degree of electronic quenching, which is not included in the adiabatic QCT theory. A non-adiabatic theory, including the ground and excited state potential energy surfaces and the coupling between them, is necessary to take these effects into account. In this work, *trajectory surface-hopping (TSH)* QCT will be adopted for this purpose. Although this will be detailed fully in chapter 6, TSH-QCT builds on all of the concepts introduced in the present chapter for single-surface QCT.

5.1 The QCT method

The quasi-classical trajectory (QCT) method involves integrating the classical equations of motion for the nuclei over a potential energy surface (PES), and was first described by 2013's Nobel laureate Martin Karplus and coworkers in 1965.[69] It builds upon previous classical trajectory studies, for example refs. 9,228–230 but, instead of sampling the initial energies of each molecule randomly, the initial states of each molecule are *quantised*, giving the 'quasi'-classical part of the method's name.[69,70]

After choosing the initial states and propagating the nuclear motion classically over the PES, the final quantum numbers of the products are binned to integer values (by one of a variety of possible methods). Thus the initial and final states are quantised, but everything in between is treated classically. Taking a Monte Carlo average over a batch of trajectories with various initial conditions enables the calculation of rate constants, cross-sections etc.

5.1.1 Equations of motion and coordinate system

In this thesis, the systems treated with QCT are all atom + diatom, which will be labelled A + BC. In the specific case here, A is the rare gas atom (Kr/Xe), B is hydrogen and C is oxygen. The space-fixed coordinate system of figure 5.1 is used, with each atom, X, having a mass m_X, Cartesian coordinates q_i^X $(i = 1, 2, 3)$ and conjugate momenta p_i^X.

The space-fixed classical Hamiltonian is the sum of the kinetic and potential energy:[69]

$$H = \sum_{i=1}^{3} \left[\frac{(p_i^A)^2}{2m_A} + \frac{(p_i^B)^2}{2m_B} + \frac{(p_i^C)^2}{2m_C} \right] + V(q_1^A, q_2^A, \ldots, q_2^C, q_3^C) \tag{5.1}$$

This uses nine coordinates and associated momenta, but only six are needed to describe the system — the motion of the system's centre of mass is a constant of the motion, and can be subtracted out. To do this, the coordinates are recast as Q_{1-9}, with P_{1-9} being their conjugate momenta:[69]

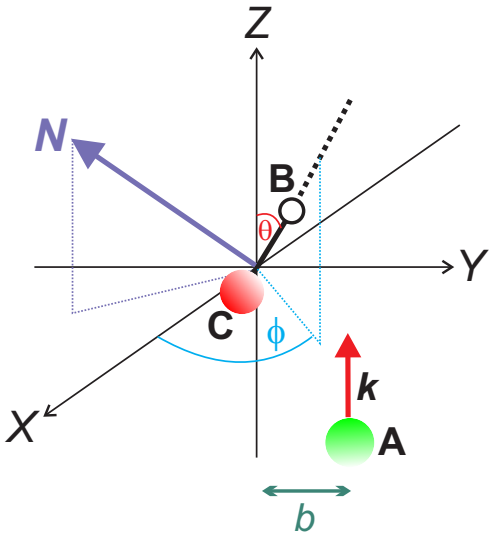

Figure 5.1: Space-fixed frame for QCT calculations. $\boldsymbol{N}$ is the rotational angular momentum vector of diatom BC, θ and ϕ are the polar and azimuthal angles of BC. η (not labelled) is the azimuthal angle of $\boldsymbol{N}$, defining the rotational phase of BC.

$Q_{1,2,3}$: coordinates of C with respect to B

$$[Q_i = q_i^C - q_i^B;\ i = 1, 2, 3]$$

$Q_{4,5,6}$: coordinates of A with respect to centre of mass of BC

$$\left[Q_{i+3} = q_i^A - \left(\frac{m_B q_i^B + m_c q_i^C}{m_B + m_C}\right);\ i = 1, 2, 3\right]$$

$Q_{7,8,9}$: coordinates of system's centre of mass

$$\left[Q_{i+6} = \frac{m_A q_i^A + m_B q_i^B + m_C q_i^C}{m_A + m_B + m_C};\ i = 1, 2, 3\right]$$

The Hamiltonian can now be written as the following, where P_{7-9} have been subtracted out:[69]

$$H = \frac{1}{2\mu_{BC}} \sum_{i=1}^{3} P_i^2 + \frac{1}{2\mu_{ABC}} \sum_{i=4}^{6} P_i^2 + V(R, r, \gamma) \tag{5.2}$$

where μ_{BC} is the reduced mass of BC, $(m_B m_C)/(m_B + m_C)$, and μ_{ABC} is the system's reduced mass, $(m_A(m_B + m_C))/(m_A + m_B + m_C)$.

The potential energy here is expressed as in chapter 2, as a function of the Jacobi coordinates R, r and γ (see figure 2.4).

In these coordinates, Hamilton's equations of motion are[69]

$$\dot{Q}_i = \frac{\partial H}{\partial P_i} = \frac{\partial T}{\partial P_i} \tag{5.3}$$

$$\dot{P}_i = -\frac{\partial V}{\partial Q_i} = -\left(\frac{\partial V}{\partial R}\frac{\partial R}{\partial Q_i} + \frac{\partial V}{\partial r}\frac{\partial r}{\partial Q_i} + \frac{\partial V}{\partial \cos\gamma}\frac{\partial \cos\gamma}{\partial Q_i}\right) \tag{5.4}$$

As well as this, in the present case Lagrangian multipliers are used to fix the bond length of OH throughout the calculation, as in ref. 22. This is because the PESs used have only been calculated for a fixed r_{OH}.

5.1.2 Numerical integration and initial conditions

Around 1×10^5 trajectories were propagated over the potential energy surface by integrating equations (5.3) and (5.4) numerically, using a Hamming predictor-corrector method initialised by a fourth-order Runge-Kutta integration.[231] The accuracy and stability of the integration could be checked by monitoring the conservation of total energy, E, and total angular momentum, J. The initial separation of A and BC was set to a large enough value that the interaction between them is negligible, and checked by varying it to ensure the results do not change. Care was taken to ensure that the results were converged with respect to the integration timestep, which was typically of the order of 60-100 as for the results presented here.

The initial conditions of each trajectory were set by randomly sampling the angles θ, ϕ and η from figure 5.1. ϕ and η were sampled between 0 and 2π and θ was sampled from 0 to π. The present discussion deals with calculations at a fixed collision energy; the case of variable collision energy is considered in section 5.4. For the calculations in this thesis, the fixed collision energy used for comparison with thermal cross-sections was 39 meV (0.039 eV), which corresponds to $\frac{3}{2}k_BT$ at 300 K.

The impact parameter, b, was sampled uniformly between 0 and b_{max}^2, to weight the sampling towards high b as a 'dartboard average'.[8] This is necessary because the probability of a collision between b and $b + \mathrm{d}b$ is $2\pi b\,\mathrm{d}b$ (see chapter 3). b_{max}, the maximum impact

parameter, was set by trial and improvement using small batches of trajectories such that no inelastic collisions occurred past $b = b_{\max}$ and all depolarisation was included. (It is not possible to converge a purely elastic QCT cross-section — see chapter 3).

5.1.3 Binning final states

At the end of each trajectory, the final angular momentum of the BC diatom is $\boldsymbol{N}'$. In this thesis, quantities with primes refer to after the collision, and those without primes refer to before it. The classical vector magnitude is converted to a quantum number, N', via

$$|\boldsymbol{N}'| = \hbar\sqrt{n'(n'+1)} \tag{5.5}$$

The resulting value of N' is not an integer, which is why it is labelled with a lower case letter, n', in equation (5.5). The quantum number N' is obtained by binning n' to an integer value. In the calculations performed in this thesis, this is simply done by rounding n' to the nearest integer (the *histogram binning* method), such that an 'elastic' trajectory is one for which $n' = N \pm 0.5$ (in the closed shell case).

It is also possible to use other methods of binning, such as *Gaussian* binning, which gives a weight W_{GB} to each trajectory, weighting more highly those trajectories for which n' is closest to an integer value.

$$W_{\mathrm{GB}} = \exp\left[-2\left(\frac{n'-N'}{2\delta}\right)^2\right] \tag{5.6}$$

In this method, one trajectory can contribute to several different cross-sections $\sigma_{NN'}$. The analogous expression for histogram binning would be

$$W_{\mathrm{HB}} = \begin{cases} 1 & \text{if } N'-0.5 \leq n' < N'+0.5 \\ 0 & \text{otherwise} \end{cases} \tag{5.7}$$

For the calculations in this thesis, the results of the Gaussian binning method were not

found to be significantly different to those of the histogram binning method.

Also at the end of each trajectory, the angle between $\boldsymbol{N}$ and $\boldsymbol{N}'$ is calculated using the cosine rule:

$$\cos\theta_{NN'} = \frac{\boldsymbol{N}\cdot\boldsymbol{N}'}{|\boldsymbol{N}||\boldsymbol{N}'|} \tag{5.8}$$

5.2 Obtaining experimentally measurable quantities from QCT

The state-to-state collision cross-section, from initial rotational state N to final state N', is given by*

$$\sigma_{NN'} = \pi b_{\max}^2 \frac{\mathcal{N}_{N'}}{\mathcal{N}_{\text{tot}}} \tag{5.9}$$

where $\mathcal{N}_{N'}$ is the number of trajectories, out of a total $\mathcal{N}_{\text{tot}}$ run, that end in the state N'. The closed-shell RET cross-section out of state N is obtained simply by summing over product states:

$$\sigma_N = \sum_{N'} \sigma_{NN'} \tag{5.10}$$

The closed-shell depolarisation parameters $a^{(k)}_{NN'}$ (see chapter 3) are found by

$$a^{(k)}_{NN'} = \langle P_k(\cos\theta_{NN'})\rangle = \frac{1}{N_{N'}}\sum_{i=1}^{\mathcal{N}_{N'}} P_k(\cos\theta^{(i)}_{NN'}) \tag{5.11}$$

$$a^{(k)} = \frac{1}{\sigma_N}\sum_{N'} \sigma_{NN'} a^{(k)}_{NN'} \tag{5.12}$$

and can be used to obtain closed-shell depolarisation cross-sections,

$$\sigma^{(k)}_{NN'} = \sigma_{NN'}(1 - a^{(k)}_{NN'}) \tag{5.13}$$

It is important to note that (as remarked upon briefly in chapter 3) it is not possible

*Note that this expression is only valid for trajectories where the impact parameter is sampled uniformly from 0 to $b^2_{\max}$.

to calculate the elastic collision cross-section, σ_{NN}, with the QCT method. As the impact parameter increases, the collisions become more and more glancing-blow in character, and less likely to change the rotational state, so the opacity function for an elastic collision ($P(b)$) tends to unity. In quantum mechanics, the uncertainty principle provides a 'cut-off' impact parameter, $b_{\max}$, beyond which the interaction no longer counts as a 'collision', so $P(b)$ converges — no such cut-off exists for classical mechanics, and $P(b)$ does not converge. This means that the classical elastic cross-section is infinite, and in practice is determined by the choice of $b_{\max}$ that the user gives to the QCT program as input. The polarisation moments $a^{(k)}_{NN}$ for purely elastic collisions also cannot be converged using QCT. Note, however, that it *is* possible to obtain the open-shell cross-section for purely spin-rotation changing collisions (where $N' = N$ but $j' \neq j$) using the methods in the next section.

Depolarisation cross-sections, on the other hand, can be obtained for elastic collisions using QCT. This is because elastic collisions become less depolarising as b increases, so $P^{(k)}(b)$ does converge once a point is reached where the collisions are too glancing-blow to change the direction of $\boldsymbol{N}$. Therefore, even though the QCT values of $\sigma_{NN'}$ and $a^{(k)}_{NN'}$ are themselves meaningless when $N' = N$, they can be used in equation 5.13 to get a meaningful value of $\sigma^{(k)}_{NN}$.

To obtain opacity functions, $P(b)$, for a particular process, one possible method would be to assign the trajectories that undergo that process to bins in impact parameter, b. However, using this histogram method requires a lot of trajectories to get smooth functions. A better method is to expand $P(b)$ as a Legendre series.[232] Taking as an example the opacity function for $N \rightarrow N'$,

$$P_{NN'}(b) = \frac{\mathcal{N}_{N'}(b)}{\mathcal{N}_{\text{tot}}(b)} = \frac{2\sigma_{NN'}}{\pi b^2_{\max}} g(\beta) \tag{5.14}$$

where $g(\beta)$ is a (truncated) Legendre expansion in the reduced variable β:[232]

$$g(\beta) = \frac{1}{2} + \sum_{n=1}^{M} \alpha_n P_n(\beta) \tag{5.15}$$

$$\alpha_n = \frac{2n+1}{2} \frac{1}{\mathcal{N}_{N'}} \sum_{i=1}^{\mathcal{N}_{N'}} P_n(\beta^{(i)}) \tag{5.16}$$

$$\beta = \frac{2b^2}{b_{\max}^2} - 1 \tag{5.17}$$

The Kolmogorov-Smirnov statistical test is used to decide on the number of terms, M, to include in the Legendre expansion,[231,232] typically aiming for a significance level of around 95%. This usually implies between 4 and 8 terms, but note that, quantum mechanically, M should not exceed $2N$.

Opacity functions for depolarisation can be calculated by expanding $a^{(k)}(b)$ in a similar fashion and using

$$P^{(k)}(b) = P(b)(1 - a^{(k)}(b)) \tag{5.18}$$

As above, neither $P_{NN}(b)$ nor $a_{NN}^{(k)}(b)$ can be converged for elastic collisions, but the depolarisation opacity function $P_{NN}^{(k)}(b)$ can be.

5.3 Quasi open-shell QCT: tensor opacity formalism

Section 3.3 in chapter 3 sets out the tensor opacity formalism used to calculate quasi open-shell cross-sections in QCT, assuming that spin is a spectator.[12] Quantum mechanical expressions for $\sigma_{jj'}$, $a_{jj'}^{(k)}$ and $\sigma_{jj'}^{(k)}$ are given in that section as a function of $P^{(K)}(N, N')$, the spin-independent tensor opacities, which can be calculated using closed-shell QCT calculations. The current section will explain the specifics of how this is implemented.

The magnitude of the angular momentum transfer vector, $\boldsymbol{K} = \boldsymbol{N'} - \boldsymbol{N}$, can be calculated via[12]

$$|\boldsymbol{K}|^2 = |\boldsymbol{N}|^2 + |\boldsymbol{N'}|^2 - 2|\boldsymbol{N}||\boldsymbol{N}| \cos\theta_{NN'} \tag{5.19}$$

and quantised using

$$|\boldsymbol{K}| = \hbar\sqrt{K(K+1)} \tag{5.20}$$

K is then binned to the nearest integer value.

The state-to-state cross-section resolved in K is next worked out using the number of trajectories that go from N to N' with momentum transfer of K, $\mathcal{N}(K;N,N')$:

$$\sigma_{NN'}(K) = \pi b_{\max}^2 \frac{\mathcal{N}(K;N,N')}{\mathcal{N}_{\text{tot}}} \tag{5.21}$$

As in chapter 3, this can then be converted to the tensor opacity via[12]

$$P^K(N,N') = \frac{k_i^2}{\pi}(2N+1)\sigma_{NN'}(K) \tag{5.22}$$

where k_i is the wavevector.

These tensor opacities can then be employed to calculate quasi open-shell cross-sections and depolarisation parameters using the equations in section 3.3.

5.4 Variable collision energy QCT

The discussion so far has explained how QCT calculations are carried out for a fixed collision energy, E_t. However, the experiments in this thesis take place under thermal conditions (300 K), where the collision energy follows a Maxwell-Boltzmann distribution. Therefore it is useful to compare QCT calculations for such a distribution of energies to those carried out at fixed E_t, to verify that the fixed-energy calculations are a good model for the experiment.

This is done by running trajectories with E_t randomly sampled between E_1 and E_2 (in this case, 1 and 125 meV). For each trajectory, the impact parameter b is sampled from 0 to $b_{\max}^2(E_t)$. In previous studies, the function $b_{\max}(E_t)$ was modelled using the line-of-centres model,[22,70,145,233] which is appropriate for a process with a barrier, such as when

calculating $\sigma_{NN'}$. For calculating quenching cross-sections, though, it would be better to have $b_{\max}(E_t)$ falling with collision energy – for a simple Langevin-style capture model,[234] $\sigma_Q \sim E_t^{-0.5}$, and $\sigma_Q \sim b_{\max}^2$, so $b_{\max}(E_t) \sim E_t^{-0.25}$.

By running small batches of trajectories at various fixed collision energies and using these to obtain $b_{\max}$ at that energy, the function $b_{\max}(E_t)$ was fitted to the form[235]

$$b_{\max}(E_t) = 2.8 \times 10^{-8} \left[5.8 \times 10^{-8} + E_t^{-0.2}\right] \tag{5.23}$$

where $b_{\max}(E_t)$ is in cm and E_t is in eV.

Each trajectory is given the weighting[70,145,233]

$$w_i = \frac{b_{\max}^2(E_t)}{D^2} \tag{5.24}$$

where D is taken as the value of $b_{\max}(0.001\text{ eV})$. Note that the value of D is not important, as it will cancel out in equation (5.25).

The expression for the thermal (Maxwell-Boltzmann average) rate constant can be written down directly, without expanding the excitation function:[11]

$$k_{NN'}(T) = \frac{\pi D^2 (E_2 - E_1)}{\mathcal{N}_{\text{tot}}} \sum_{i=1}^{\mathcal{N}_{N'}} w_i \mathcal{P}_{\text{MB}}(E_t^{(i)}|T) v_{\text{rel}}^{(i)} \tag{5.25}$$

where $\mathcal{P}_{\text{MB}}(E_t|T)$ is the Maxwell-Boltzmann distribution of energies at temperature T, and v_{rel} is the relative velocity. This rate constant can be turned into a thermal (flux averaged) cross-section, σ, by simply dividing by the relative velocity $\langle v_{\text{rel}}(T)\rangle$. This is the quantity that should be compared to experiment, as opposed to $\sigma(T) \equiv \langle\sigma\rangle$ (see chapter 4).

The depolarisation parameter at temperature T can also be calculated via[12]

$$a_{NN'}^{(k)}(T) \equiv \langle a_{NN'}^{(k)}\rangle_T = \frac{\sum_{i=1}^{\mathcal{N}_{N'}} w_i v_{\text{rel}}^{(i)} \mathcal{P}_{\text{MB}}(E_t^{(i)}|T) P_k(\cos\theta_{NN'}^{(i)})}{\sum_{i=1}^{\mathcal{N}_{N'}} w_i v_{\text{rel}}^{(i)} \mathcal{P}_{\text{MB}}(E_t^{(i)}|T)} \tag{5.26}$$

If the excitation function (the dependence of the cross-section on collision energy) is required, it can be expanded as a truncated Legendre series much like the opacity function in section 5.2. The expansion, up to the Mth term, is[70,145,233]

$$\sigma_{NN'}(E_t) = \frac{2R}{E_2 - E_1}\left(\frac{1}{2} + \sum_{n=1}^{M} c_n P_n(x)\right) \tag{5.27}$$

with the reduced variable x being

$$x = \frac{2E_t - E_2 - E_1}{E_2 - E_1} \tag{5.28}$$

and R representing

$$R = \int_{E_1}^{E_2} \sigma_{NN'}(E_t)\,\mathrm{d}E_t \simeq \frac{\pi D^2 (E_2 - E_1)}{\mathcal{N}_{\mathrm{tot}}} \sum_{i=1}^{\mathcal{N}_{N'}} w_i \tag{5.29}$$

The Legendre coefficients c_i are given by[70,145,233]

$$c_n = \frac{2n+1}{2}\langle P_n(x)\rangle \tag{5.30}$$

and the Kolmogorov-Smirnov statistical test is used to determine the value of M at which the series will be truncated, exactly as for the opacity functions discussed in the previous section. Integrating $\sigma(E_t)$ over a Maxwell-Boltzmann distribution of collision energies at temperature T gives the thermally averaged cross-section $\sigma(T) \equiv \langle\sigma\rangle$.

It was verified in refs. 21 and 22 that the 300 K cross-sections for OH(A) + Kr single-surface QCT agreed very well with calculations at a fixed collision energy of 0.039 eV, justifying the use of the fixed E_t single-surface data. The methodology here will therefore be used in chapter 6 to confirm that the same conclusion holds for trajectory surface-hopping data.

5.5 Comparison of QCT with QM

Although no quantum mechanical (QM) scattering calculations were performed in this thesis, the quasi-classical data here will be compared to QM calculations carried out elsewhere.[21,235–237] These calculations used the HIBRIDON suite of codes,[238] which solve the close-coupled (CC) equations[68] using a hybrid propagator made up of the log-derivative propagator of Manolopoulos[239] at short range, and the Airy propagator[240] at longer range. Full details of the calculations are contained in refs. 21,237.

QM cross-sections for rotational energy transfer (RET), σ_j, are compared with QCT in chapter 7, and figure 5.2 presents state-to-state resolved $\sigma^{(2)}_{jj'}$ cross-sections for collisional disalignment of OH(A) + Xe. As can be seen, the agreement between single-surface QCT and QM calculations is excellent, validating the use of the QCT method in this thesis. The greatest disagreement is in the $\Delta j = \pm 1$ cross-sections for spin-rotation conserving transitions, which is due to the QCT definition of 'elastic' and the choice of binning method.

5.6 Summary

This chapter has presented the single surface quasi-classical trajectory (QCT) method used in this thesis.The selection of initial conditions, the propagation of trajectories over one or many electronic states, the binning of final angular momenta to integer quantum numbers and the methods of obtaining cross-sections to compare with experiment have all been dealt with in detail, and will be used throughout the rest of this thesis. Methods for extending QCT results to open-shell $^2\Sigma^+$ radicals have been considered, and the results compared to quantum scattering calculations performed elsewhere.

In addition, it has been demonstrated that the use of QCT theory is appropriate for the treatment of this system, as confirmed by comparisons to quantum mechanical calculations.

Chapter 6 will introduce the surface hopping (TSH-QCT) model to include non-

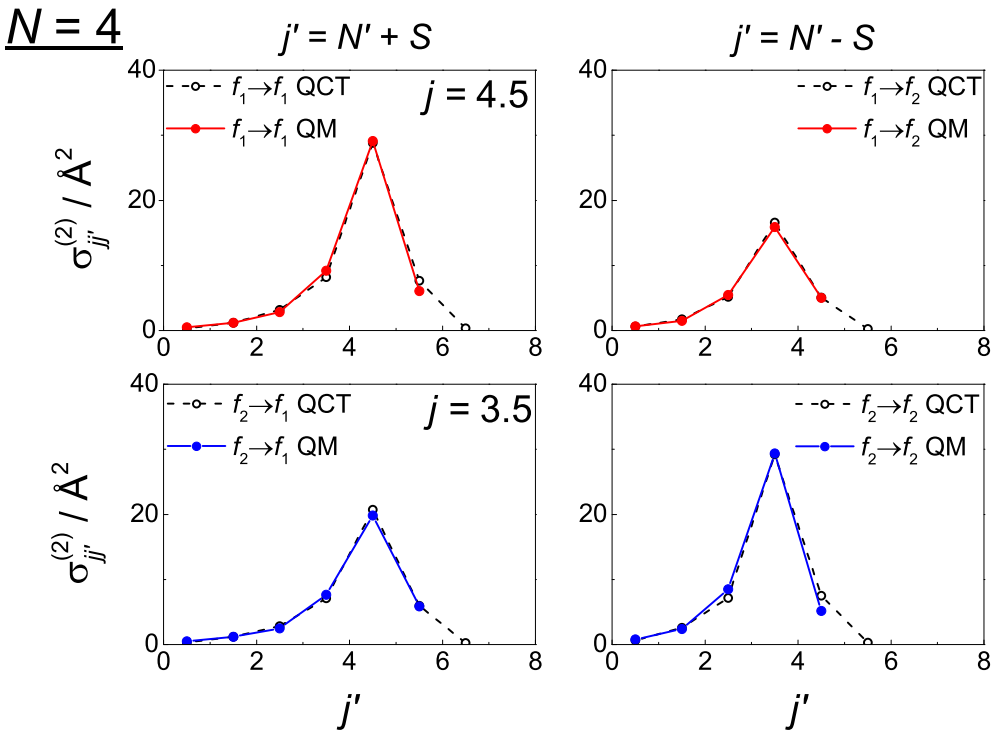

Figure 5.2: Comparison of adiabatic QCT[237] (dashed) and adiabatic QM[235,237] (solid) state-to-state *disalignment* cross-sections for OH(A) + Xe, initial $N = 4$. Initial spin-rotation level f_1 $(N + S)$: top, f_2 $(N - S)$: bottom; final spin-rotation level f_1 $(N + S)$: left, f_2 $(N - S)$: right.

adiabatic effects, and detail a new extension to incorporate the OH(X) + Rg $1A''$ PES. Rovibronic couplings between all three states will be added in to the existing model, which will be fully explained and characterised and then compared to experimental data. After this, the following chapter (chapter 7) will use the methods in this chapter and chapter 6 to compare with experimental data for OH(A) + Kr, Xe.

Chapter 6

A three-state surface hopping model of OH(A,X)+Rg interactions, including rovibronic couplings

In chapter 5, the theory of quasi-classical trajectory (QCT) calculations was presented. The single-surface QCT method described so far is limited to dynamics on one adiabatic potential energy surface (PES). However, one of the main reasons for studying the OH(A) + Kr,Xe systems in this thesis is that they both display significant *non-adiabatic* effects, where more than one PES is involved in the dynamics. (The term 'adiabatic' here refers to electronically adiabatic behaviour). An extension to the theory presented thus far is therefore required to properly model the experimental results in this work. In this thesis, *trajectory surface hopping* (TSH-QCT) theory will be used for this purpose.

As described in chapter 2, for linear configurations of OH + Rg, the ground, X state is a doublet Π state and the excited, A state is $^2\Sigma^+$. Away from linearity, the symmetry of the system is reduced from $C_{\infty v}$ to C_s, which splits the doubly degenerate $^2\Pi$ state into states of A' and A'' symmetry with respect to reflection in the scattering plane. These states are labelled $1A'$ and $1A''$ respectively in this thesis. The excited state is symmetric under such a reflection and is labelled $2A'$ in the C_s point group.

This chapter begins by outlining "standard" TSH-QCT theory, which, so far, has only involved two states: the ground and excited states of A' symmetry ($1A'$ and $2A'$). The

third state, $1A''$, was considered not to be coupled to the other two states of different symmetry, and so was left out of the theory.[23,28]

However, the $1A''$ state can be coupled to the two states of A' symmetry by rovibronic interactions, as introduced in section 2.4. The rest of the present chapter sets out an extension of the two-state surface hopping model to include all three electronic states. Adiabatic-diabatic transformations for a three-state system will be considered before the extension to the theory will be set out and explained in detail. Theoretical results for electronic quenching, and the rotational state distribution of quenched OH(X), will be presented for several different models and compared to non-adiabatic quantum scattering calculations[236] before a full comparison with experiment in chapter 7.

6.1 The fewest-switches algorithm for TSH-QCT

In the trajectory surface hopping (TSH) method,[82] a batch of independent classical trajectories is run, each on one adiabatic PES at a time, just as in the single-surface QCT method. (See section 1.5 and chapter 5). Independent of the 'active' surface that the nuclear trajectory is running on, the electronic coordinates are evolved via quantum mechanics, and provide a means of determining whether or not a 'hop' to another surface occurs at each timestep.

The effect of the classical subsystem on the quantum one is that the regions of the PES accessed by the nuclear trajectory influence the evolution of the electronic state; the effects of the quantum subsystem on the classical nuclear trajectory come about via the active PES determining the forces experienced by the nuclei.

Over the years, a number of variants of surface hopping have been developed. One of the most popular is fewest-switches surface hopping (FSSH) of Tully,[83,84] which is the one employed in the work described here. In this method, each trajectory has its own electronic density matrix, which is propagated simultaneously to the integration of the nuclear motion.

The algorithm used is as follows, and is also summarised in figure 6.1. At each timestep, Hamilton's equations of motion for the nuclei are integrated as in sections 5.1.1 and 5.1.2. The time-dependent Liouville equation for the electronic density matrix is also integrated. The probability (P_{ij}) of a hop from the active PES, $|i\rangle$, to another surface, $|j\rangle$, is calculated as described below, and then a random number is drawn.

This random number, ζ, is used to decide if the trajectory will hop to another PES. If we label the active potential as state 1,

- If $\zeta \leq P_{12}$ then switch to state 2
- If $P_{12} \leq \zeta < P_{12} + P_{13}$ then switch to state 3
- Otherwise, no hop takes place.

If the trajectory does not hop at this timestep, we return to the start and move on to the next timestep. If a hop does occur, the nuclear momenta must be adjusted before moving to the next timestep (section 6.8.1), but note that the density matrix elements are not reset until the end of the trajectory, thus including the effects of coherence.* Just as for adiabatic QCT, the trajectory is over when the separation between atom A and diatom BC is enough that any interaction is negligible.

6.1.1 Justification for the FSSH algorithm

The fewest-switches surface hopping (FSSH) algorithm described above has been justified intuitively by Tully,[83] but has never been rigorously derived from the time-dependent Schrödinger equation. Note, however, that Subotnik *et al.* have recently shown[241] that the FSSH algorithm can be obtained from the quantum-classical Liouville equation, provided that certain conditions are met (mostly to do with decoherence).

There is some inconsistency in that the electronic state is counted twice – each trajectory carries a label of the current state it propagates on, but the electronic wave-

*In fact, TSH suffers from a problem of *overcoherence* — the lack of decoherence. There are a large number of schemes to circumvent this in the literature.[241]

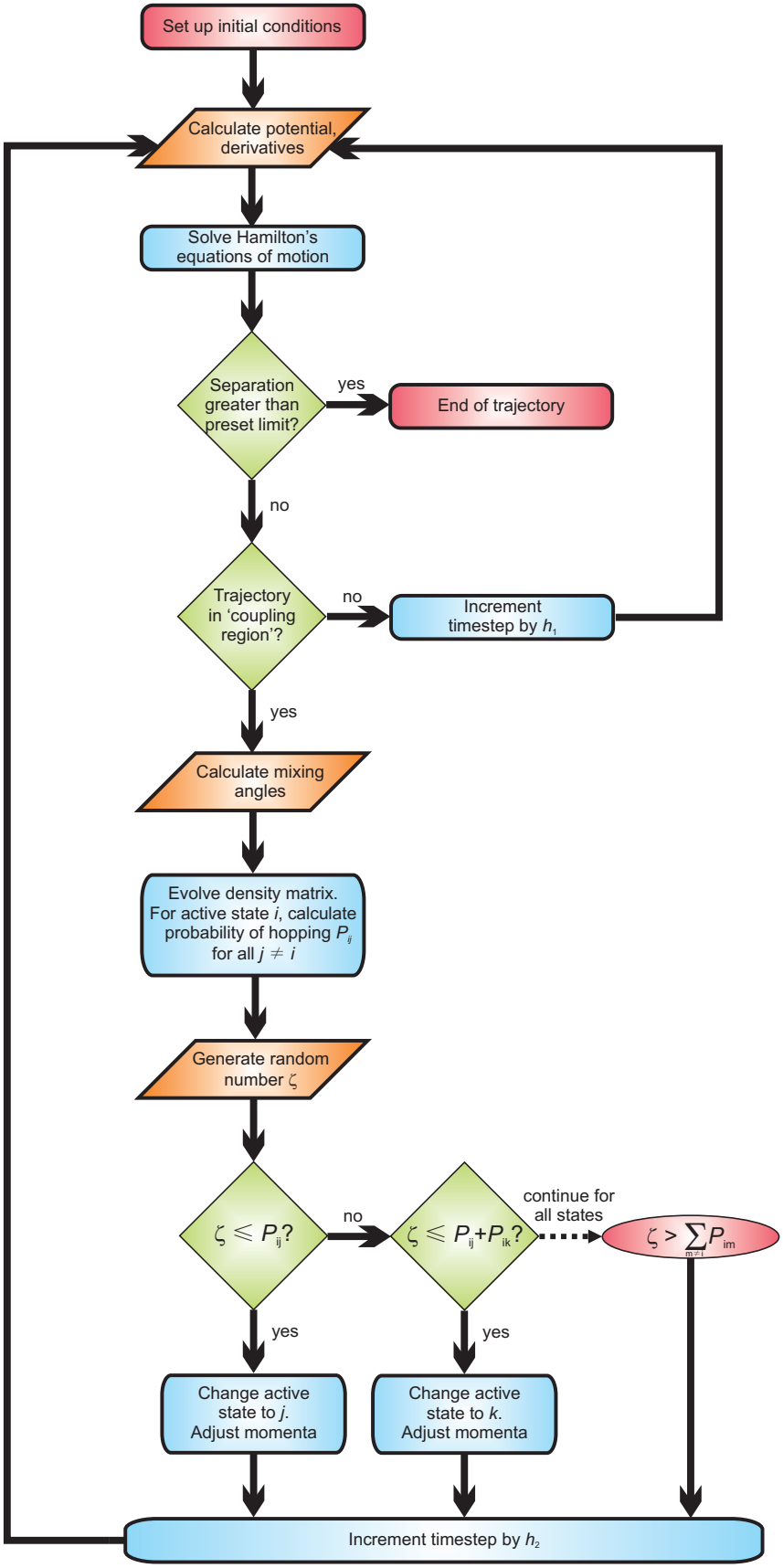

Figure 6.1: Flowchart of the fewest switches surface hopping (FSSH) algorithm.

function (propagated simultaneously) also describes this information.[242] When *adiabatic* state populations are required from the calculation – as here – this information should be obtained from the surface labels of the individual trajectories, not their electronic wavefunctions.[83,243]

Surface-hopping QCT involves trajectories that move on a single PES at all times, which is necessary to correctly describe the system away from the coupling region. Switches (hops) between these surfaces are instantaneous, which can seem unrealistic when considering a single trajectory. However, it is more correct to compare a whole batch of trajectories with reality – in this case, some will hop earlier and some later, leading to a gradual transfer of population from one state to the other.[83]

The FSSH method is self-consistent, and obeys the conservation of energy.[83] In the implementation in this thesis, energy and angular momentum conservation are not forced in the code and so can be used to check the accuracy and stability of the integration.

Figure 6.2 gives Tully's intuitive justification for the fewest-switches criterion.[83] The left-hand panel shows an average of the $2A'$ and $1A'$ potentials for OH + Kr, which is the potential that would be used in an Ehrenfest-like treatment. Clearly, this potential is unlike either $2A'$ or $1A'$ – no best-trajectory approach can describe the dynamics here.

The centre panel shows a cartoon trajectory (purple dashes) for an 'alternative' hopping scheme, in which the probability of the trajectory propagating on state $|i\rangle$ is ρ_{ii} (where $\boldsymbol{\rho}$ is the electronic density matrix). This leads to a large number of hops – in the limit of infinite hops, this reduces to the Ehrenfest case in the left-hand panel, and so is inappropriate for the same reasons.

The right-hand panel shows an example FSSH trajectory, which displays physically reasonable behaviour. The FSSH algorithm is popular and widely used because it is one of the simplest and most intuitive models that accurately simulates a wide variety of non-adiabatic processes.[41,83]

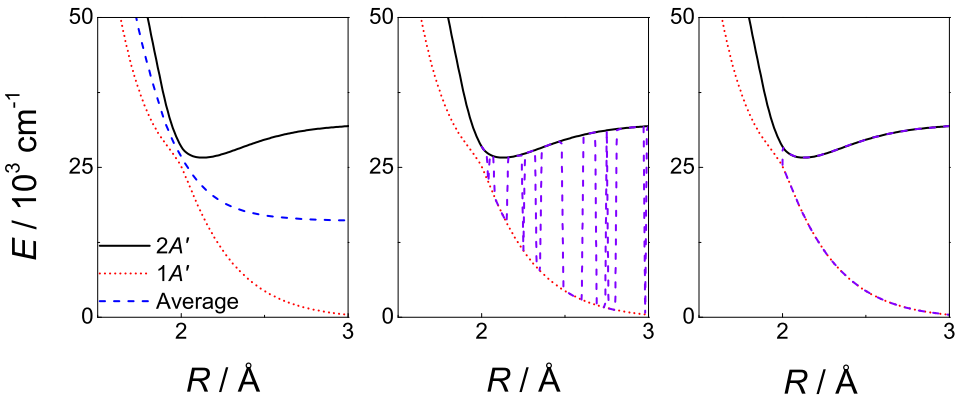

Figure 6.2: Intuitive justification for the FSSH algorithm, following Tully.[83] Left: 'average' (blue dashes) of the adiabatic $2A'$ (black solid line) and $1A'$ (red dots) OH + Kr PESs at $\gamma = 175°$. Centre: cartoon trajectory (purple dashes) for the hopping scheme $P(\text{state } i) = \rho_{ii}$. Right: cartoon trajectory for the FSSH criterion.

6.2 Extension to the $1A''$ state – rovibronic couplings

As explained in chapter 2, it is possible that a rotation of the triatomic system of the correct (A'') symmetry can couple two states of different symmetry: $A' \times A'' \times A'' = A'$ overall – thus enabling coupling between the $1A''$ electronic state and the other two ($1A'$ and $2A'$) states. This rovibronic coupling can be classified into two forms, which in this thesis will be referred to as *Renner-Teller (RT)* and *Coriolis* coupling. Note, however, that a wide variation in nomenclature is found in the literature, and these terms may refer to different things in different sources.

Renner-Teller coupling mixes states of non-zero angular momentum, with $\Delta\Lambda = 0$. It comes about because, in a linear triatomic complex, λ (the projection of the electronic orbital angular momentum, Λ, on the OH bond axis) is a good quantum number, but it ceases to be so on bending away from linearity. Coriolis coupling is caused by a rotation of the whole three-atom system, and mixes states that differ in their orbital angular momentum quantum number by $\Delta\Lambda = \pm 1$.

The scheme set out in this chapter aims to include both of these effects in the TSH-QCT theory set out so far in this chapter. As TSH-QCT is a semiclassical theory, spin-orbit coupling (see section 2.5) will not be included.

Although this is the first attempt to include both Renner-Teller *and* Coriolis effects in a three-state TSH-based theory, competition between these effects has been considered elsewhere. Most relevantly, Santoro *et al.*[131] have incorporated RT coupling into two-state TSH for the study of the $N(^2D) + H_2$ reaction, based on the earlier quantum mechanical study of Goldfield and coworkers.[130] This is a system in which RT effects have been studied extensively quantum mechanically.[128,129,244] An older attempt (before fewest-switches surface hopping in 1990) to look at roto-electronic couplings in surface hopping QCT was made in ref. 245.

The general formalism for non-adiabatic effects in triatomic complexes was set out by Petrongolo[246] and developed in refs. 139,140,247–249, and full three-state quantum mechanical studies have very recently become computationally feasible.[250,251]

Most recently, QM methods have been used to investigate the competition between conical intersection and Renner-Teller pathways in the photolysis of $H_2O(\tilde{B})$, which correlates to OH(A) + H,[134,135,252,253] with reference made to earlier work on this subject.[133,136,254]. The quantum treatment of the $O(^1D) + H_2$ system by Drukker and Schatz[141] also includes Coriolis and electronic couplings.

6.3 Three-state adiabatic to diabatic transformation

As in chapter 2, if couplings to the $1A''$ electronic state are ignored, this state is the same in the adiabatic and diabatic representations. The mixing between the other two states can be fully parametrised by one mixing angle, χ:[28,111]

$$\begin{pmatrix} U_{1A'} & 0 \\ 0 & U_{2A'} \end{pmatrix} = \mathbf{C}_2 \begin{pmatrix} V_{\Pi_{A'}} & V_{12} \\ V_{12} & V_{\Sigma} \end{pmatrix} \mathbf{C}_2^T \tag{6.1}$$

in which

$$\mathbf{C}_2 = \begin{pmatrix} \cos\chi & \sin\chi \\ -\sin\chi & \cos\chi \end{pmatrix} \tag{6.2}$$

For the three-state case, three mixing angles (α, β and ω) are required (for the diabatic electronic basis, see section 6.5.2):

$$\begin{pmatrix} U_{1A'} & 0 & 0 \\ 0 & U_{2A'} & 0 \\ 0 & 0 & U_{1A''} \end{pmatrix} = \mathbf{C}_3 \begin{pmatrix} D_{\text{sum}} & \frac{V_{12}}{\sqrt{2}} & D_{\text{dif}} \\ \frac{V_{12}}{\sqrt{2}} & V_{\Sigma} & \frac{V_{12}}{\sqrt{2}} \\ D_{\text{dif}} & \frac{V_{12}}{\sqrt{2}} & D_{\text{sum}} \end{pmatrix} \mathbf{C}_3^T \tag{6.3}$$

where

$$D_{\text{sum}} = \frac{1}{2}\left(V_{\Pi_{A'}} + V_{\Pi_{A''}}\right) \; ; \; D_{\text{dif}} = \frac{1}{2}\left(V_{\Pi_{A'}} - V_{\Pi_{A''}}\right) \tag{6.4}$$

and

$$\mathbf{C}_3 = \begin{pmatrix} \cos\alpha\cos\beta - \sin\alpha\sin\omega\sin\beta & \sin\alpha\cos\omega & \cos\alpha\sin\beta + \sin\alpha\sin\omega\cos\beta \\ -\sin\alpha\cos\beta - \cos\alpha\sin\omega\sin\beta & \cos\alpha\cos\omega & -\sin\alpha\sin\beta + \cos\alpha\sin\omega\cos\beta \\ -\cos\omega\sin\beta & -\sin\omega & \cos\omega\cos\beta \end{pmatrix} \tag{6.5}$$

Note that, if couplings to the diabatic $\Pi_{A''}$ state are included, the adiabatic states can no longer be given A' and A'' symmetry labels, so are labelled as $U_{1,2,3}$ as in equation (2.31). The addition of rovibrational terms will be dealt with in section 6.5.

The matrix $\mathbf{C}_3$ can be expressed as the product of three matrices in one mixing angle each, as below. This will be used later on in this chapter.

$$\mathbf{C}_3 = \begin{pmatrix} \cos\alpha & \sin\alpha & 0 \\ -\sin\alpha & \cos\alpha & 0 \\ 0 & 0 & 1 \end{pmatrix} \begin{pmatrix} 1 & 0 & 0 \\ 0 & \cos\omega & \sin\omega \\ 0 & -\sin\omega & \cos\omega \end{pmatrix} \begin{pmatrix} \cos\beta & 0 & \sin\beta \\ 0 & 1 & 0 \\ -\sin\beta & 0 & \cos\beta \end{pmatrix} \tag{6.6}$$

6.4 Surface hopping QCT for a three-state system

The fewest switches surface hopping algorithm[83,84] introduced in section 6.1 can be extended to any number of electronic states. At each timestep, the nuclear motion is treated classically, by integrating Hamilton's equations of motion, and the electronic degrees of

freedom are treated quantum mechanically, by integrating the time-dependent Liouville equation for the density matrix $\boldsymbol{\rho}$.

The integration of the density matrix is performed via

$$i\hbar\dot{\rho}_{kj} = \sum_l \left[\rho_{lj}(H_{kl} - i\hbar\dot{\boldsymbol{x}}\boldsymbol{d}_{kl}) - \rho_{kl}(H_{lj} - i\hbar\dot{\boldsymbol{x}}\boldsymbol{d}_{lj})\right] \tag{6.7}$$

noting that $\boldsymbol{d}_{ij} = -\boldsymbol{d}^*_{ji}$, that $\rho_{ij} = \rho^*_{ji}$ and that $\dot{\rho}_{ij} = \dot{\rho}^*_{ji}$. This system of differential equations is integrated by an Adams-Bashforth-Moulton predictor-corrector algorithm.[28] It is ensured that the timestep is short enough that the trace of the density matrix is conserved.

In order to integrate the density matrix, the non-adiabatic coupling matrix elements (NACMEs) $\boldsymbol{d}_{ij}$ are therefore required. For a system of two adiabatic states, $\boldsymbol{d}_{12}$ is given by the derivative of the mixing angle, χ, which is calculated from the PES according to equation (2.59). This can be shown by using the Hellman-Feynman theorem to express $\boldsymbol{d}_{12}$ as a function of V_{11}, V_{22}, V_{12} and χ, as in ref. 255.

For the three state case, the NACMEs are given by

$$\mathbf{d} = \mathbf{C}_3 \nabla_{\boldsymbol{x}} \mathbf{C}_3^T \tag{6.8}$$

Using the reasoning of ref. 256, and the notation '1' for $1A'$, '2' for $2A'$ and '3' for $1A''$,

$$\boldsymbol{d}_{12} = -\sin\omega\nabla_{\boldsymbol{x}}\beta - \nabla_{\boldsymbol{x}}\alpha \tag{6.9}$$

$$\boldsymbol{d}_{13} = -\cos\omega\cos\alpha\nabla_{\boldsymbol{x}}\beta - \sin\alpha\nabla_{\boldsymbol{x}}\omega \tag{6.10}$$

$$\boldsymbol{d}_{23} = \cos\omega\nabla_{\boldsymbol{x}}\beta - \cos\alpha\nabla_{\boldsymbol{x}}\omega \tag{6.11}$$

To obtain the NACMEs, the mixing angles must be calculated, and the method for doing so will be set out in the following sections.

At each step, the transition probabilities from the current state to each other electronic

state are calculated via[83]

$$P_{ij} = \frac{-2\Delta t \mathrm{Re}\left[\rho^*_{ji}\dot{\boldsymbol{x}}\boldsymbol{d}_{ji}\right]}{\rho_{ii}} \tag{6.12}$$

6.5 Basis and coordinates for a three-state system

6.5.1 Axis system

In this work, we use the coordinate system of Petrongolo,[246] in which the z-axis is along the O–H bond and the scattering plane is xz. This is known as r-embedding as the z-axis is along $\boldsymbol{r}$, rather than along $\boldsymbol{R}$. (Recall from figure 2.4 that $\boldsymbol{R}$, $\boldsymbol{r}$ and γ are the Jacobi coordinates of the Rg-OH system, with $\boldsymbol{r}$ being the O–H bond vector from O to H, $\boldsymbol{R}$ being the vector from the OH centre of mass to the rare gas atom, and γ being the angle between them such that $\gamma = 0$ in the Rg–HO configuration.)

6.5.2 Diabatic electronic basis

Equation (6.3) above can be written as

$$\mathbf{A} = \mathbf{C}_3\mathbf{D}\mathbf{C}_3^T \tag{6.13}$$

in which the diabatic potential energy matrix $\mathbf{D}$ is diagonalised to give the adiabatic potential energy matrix $\mathbf{A}$.

This subsection concerns the choice of diabatic electronic basis used for $\mathbf{D}$. Electronic states can be partitioned into spin and orbital terms,[109,257] of which the orbital term is labelled $|\Lambda\rangle$. In the present system, there are three definite-Λ states, with Λ = -1, 0, 1. $\Lambda = 0$ is a Σ state, and $\Lambda = \pm 1$ are the two degenerate components of the Π state.

Alexander and Corey[109,112] use definite-symmetry states:

$$|\Pi\eta\rangle = \frac{\sqrt{2}}{2}\left[|\Lambda\rangle + \eta|-\Lambda\rangle\right] \tag{6.14}$$

where the states $|\pm\Lambda\rangle$ are eigenfunctions of $\hat{L}_z$ but the definite symmetry states are not.

$$|\pm\Lambda\rangle = \pm\,(-1)^{\Lambda} e^{\pm i\Lambda\phi} \tag{6.15}$$

$$\hat{L}_z|\pm\Lambda\rangle = \pm\,\Lambda|\pm\Lambda\rangle \tag{6.16}$$

$$\sigma_{xz}|\pm\Lambda\rangle = (-1)^{\Lambda}|\mp\Lambda\rangle \tag{6.17}$$

$$\sigma_{xz}|\Pi\eta\rangle = (-1)^{\Lambda}\eta|\Pi\eta\rangle \tag{6.18}$$

This results in a block-diagonal $\hat{H}_{\mathrm{el}}$ matrix, elements of which are shown in Table 6.1. **D** in this basis is the same as that given in equation (6.3).

The only off-diagonal matrix elements in this basis are between $|\Pi(\eta=-1)\rangle$ and $|\Sigma\rangle$, so, writing the two-state mixing angle as χ,

$$|1A'\rangle = \cos\chi|\Pi(\eta=-1)\rangle + \sin\chi|\Sigma\rangle \tag{6.19}$$

$$|2A'\rangle = -\sin\chi|\Pi(\eta=-1)\rangle + \cos\chi|\Sigma\rangle \tag{6.20}$$

$$|1A''\rangle = |\Pi(\eta=+1)\rangle \tag{6.21}$$

ALEXANDER	$\Pi(\eta=-1)$	Σ	$\Pi(\eta=+1)$
$\Pi(\eta=-1)$	$V_{\Pi_{A'}}$	V_{12}	0
Σ	V_{12}	V_{Σ}	0
$\Pi(\eta=+1)$	0	0	$V_{\Pi_{A''}}$

Table 6.1: Matrix elements of $\hat{H}_{\mathrm{el}}$ in the basis of Alexander and Corey[109,112]

However, there is no coupling to the $1A''$ state in this basis – it will be necessary to include Renner-Teller and Coriolis couplings in the present case. In their two-state studies of Renner-Teller couplings between states of A' and A'' symmetry, Goldfield *et al.* and Santoro *et al.* use a diabatic basis whose states are eigenfunctions of $\hat{L}_z$.[130,131] This has the advantage of making the calculation of RT effects much easier, but the excited $|2A'\rangle$ state is not included.

To form a unified basis that includes all three states, we follow the QM studies of

Drukker and Schatz,[141] and, more recently, Zhou and coworkers.[135] However, note that the equations here will be slightly different from those given in ref. 135, as the definition of the two-state mixing angle χ here follows section 2.3, rather than ref. 109 – here the $^2\Pi$ state is the ground state, and $^2\Sigma^+$ is the excited state, in contrast to the cited references.

The diabatic electronic basis used in this thesis defines wavefunctions $|\lambda = \pm 1, 0\rangle$ as[141]

$$|\pm\lambda\rangle \propto e^{\pm i\lambda\phi} \tag{6.22}$$

$$|0\rangle = |\Sigma^+\rangle \tag{6.23}$$

which are not the same as the $|\pm\Lambda\rangle$ states of Alexander and Corey.[109] Their behaviour under reflection in the scattering plane, and with the $\hat{L}_z$ operator, is

$$\hat{L}_z|\pm\lambda\rangle = \pm\,\lambda\hbar|\pm\lambda\rangle \tag{6.24}$$

$$\sigma_{xz}|\pm\lambda\rangle = |\mp\lambda\rangle \tag{6.25}$$

meaning of course that the $|\lambda = 0\rangle$ state is an eigenfunction of both.

Expressing this $|\pm\lambda\rangle$ basis in terms of the adiabatic states,[135,258]

$$|\lambda = \pm 1\rangle = \frac{\sqrt{2}}{2}\left[\cos\chi|1A'\rangle - \sin\chi|2A'\rangle \pm i|1A''\rangle\right] \tag{6.26}$$

$$|\lambda = 0\rangle = \sin\chi|1A'\rangle + \cos\chi|2A'\rangle \tag{6.27}$$

The matrix elements of $\hat{H}_{\rm el}$ in this basis are given in table 6.2 — these are the same as those of Drukker and Schatz.[141] In this table, the shorthand notations $D_{\rm sum}$ and $D_{\rm dif}$ refer to $\frac{1}{2}\left(V_{^2\Pi_{A'}} + V_{^2\Pi_{A''}}\right)$ and $\frac{1}{2}\left(V_{^2\Pi_{A'}} - V_{^2\Pi_{A''}}\right)$ respectively. In addition, the same convenient $\hat{L}_z$ matrix elements apply here as in the Goldfield *et al.* basis:

$$\langle\lambda'|\hat{L}_z|\lambda\rangle = \delta_{\lambda'\lambda}\lambda\hbar \tag{6.28}$$

$$\langle\lambda'|\hat{L}_z^2|\lambda\rangle = \delta_{\lambda'\lambda}\lambda^2\hbar^2 \tag{6.29}$$

For matrix elements of $\hat{L}^2$, we will also approximate $\hat{L}^2 \simeq \hat{L}_z^2$, as in ref. 130.

$H_{\lambda'\lambda}$	$\lambda = -1$	$\lambda = 0$	$\lambda = 1$
$\lambda' = -1$	D_{sum}	$\frac{\sqrt{2}}{2}V_{12}$	D_{dif}
$\lambda' = 0$	$\frac{\sqrt{2}}{2}V_{12}$	V_{Σ}	$\frac{\sqrt{2}}{2}V_{12}$
$\lambda' = 1$	D_{dif}	$\frac{\sqrt{2}}{2}V_{12}$	D_{sum}

Table 6.2: Matrix elements of $\hat{H}_{\text{el}}$ in the basis of Zhou *et al.*,[135,141] where the shorthand $D_{\text{sum}} = \frac{1}{2}\left(V_{\Pi_{A'}} + V_{\Pi_{A''}}\right)$ and $D_{\text{dif}} = \frac{1}{2}\left(V_{\Pi_{A'}} - V_{\Pi_{A''}}\right)$.

Matrix elements of $\hat{L}_x$ will also be required in the following sections. In the basis used here, these can be expressed as

$$\langle 0|\hat{L}_x|0\rangle = 0 \tag{6.30}$$

$$\langle \pm 1|\hat{L}_x|\mp 1\rangle = 0 \tag{6.31}$$

$$\langle \pm 1|\hat{L}_x|\pm 1\rangle = \pm i\left[\cos\chi\langle 1A'|\hat{L}_x|1A''\rangle - \sin\chi\langle 2A'|\hat{L}_x|1A''\rangle\right] \tag{6.32}$$

$$\langle 0|\hat{L}_x|\pm 1\rangle = \langle \pm 1|\hat{L}_x|0\rangle = \pm i\frac{\sqrt{2}}{2}\left[\sin\chi\langle 1A'|\hat{L}_x|1A''\rangle + \cos\chi\langle 2A'|\hat{L}_x|1A''\rangle\right] \tag{6.33}$$

(using the fact that $\langle 1A'|\hat{L}_x|1A''\rangle$ and $\langle 2A'|\hat{L}_x|1A''\rangle$ are purely imaginary).

The functions $\text{Im}\left[\langle 2A'|\hat{L}_x|1A''\rangle\right]$ and $\text{Im}\left[\langle 1A'|\hat{L}_x|1A''\rangle\right]$ have been calculated from *ab initio* data by Kłos,[21,28,90,236] and are shown in figure 6.3. Note that $\text{Im}\left[\langle 1A'|\hat{L}_x|1A''\rangle\right]$ has not been calculated for OH + Xe. Because this matrix element is much smaller than $\text{Im}\left[\langle 2A'|\hat{L}_x|1A''\rangle\right]$ in OH + Kr, it is taken to be zero in OH + Xe for the present calculations.

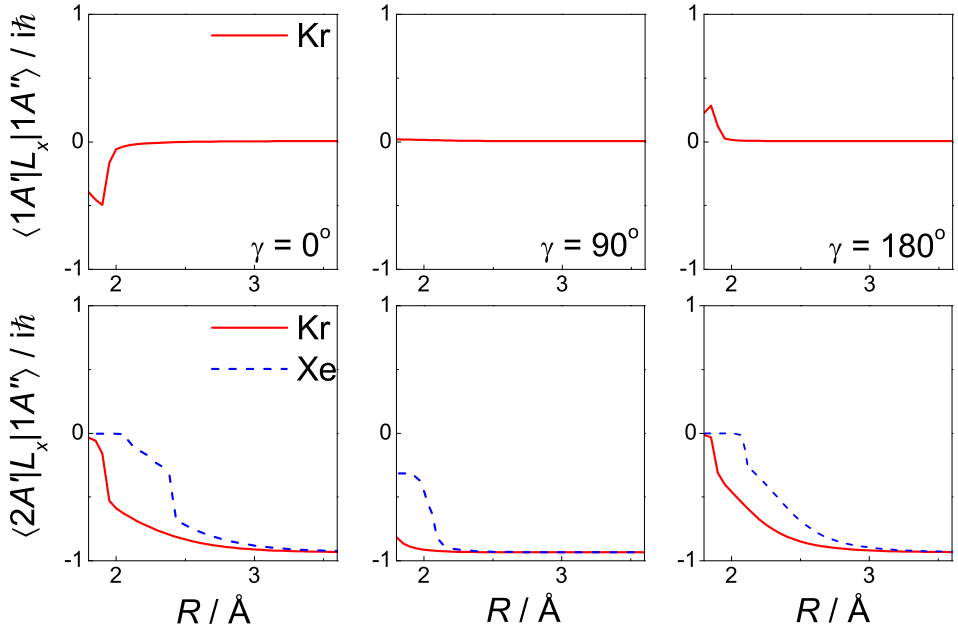

Figure 6.3: Plots of the matrix elements $\mathrm{Im}\left[\langle 1A'|\hat{L}_x|1A''\rangle\right]$ (top panels) and $\mathrm{Im}\left[\langle 2A'|\hat{L}_x|1A''\rangle\right]$ (bottom panels) for OH(A,X) + Kr[21,28] (red solid lines) and OH(A,X) + Xe[90] (blue dashed lines) at three values of γ: 0° (left), 90° (centre) and 180° (right).

6.5.3 Rotational basis

As in refs. 130,131, the rotational basis used here will be Wigner rotational functions labelled $|K\rangle$:

$$|K\rangle = \sqrt{\frac{2J+1}{8\pi^2}} D^J_{KM}(\phi,\theta,\zeta) \tag{6.34}$$

$$\hat{J}^2|K\rangle = J(J+1)\hbar^2|K\rangle \tag{6.35}$$

$$\hat{J}_\pm|K\rangle = \lambda^{JK}_\pm|K\pm 1\rangle \tag{6.36}$$

$$\hat{J}_z|K\rangle = K\hbar|K\rangle \tag{6.37}$$

where $\boldsymbol{K}$ is the projection of $\boldsymbol{J}$ (the total angular momentum of the triatomic complex) onto the O–H bond axis, and

$$\lambda^{JK}_\pm = \hbar\left[J(J+1) - K(K\pm 1)\right]^{\frac{1}{2}} \tag{6.38}$$

6.6 Matrix elements and mixing angles

The full rotational Hamiltonian, $\hat{T}_{\text{rot}}$, for a triatomic system is given by Petrongolo's 1988 paper.[246] This uses the same axis system and r-embedding as the present thesis; conversion to R-embedding can easily be accomplished by exchanging b_r and B_R in equation (6.39).[259] The printing error in the original paper,[246] that substituted $\hat{J}_z - \hat{J}_x \cot\gamma$ for $\hat{L}_z - \hat{L}_x \cot\gamma$, is also corrected here.

$$\begin{aligned}\hat{T}_{\text{rot}} =& \frac{b_r}{2}\left(\hat{J}^2 - 2\hat{J}_z^2 + \hat{L}^2 - 2\hat{L}_z^2 + 2\hat{L}_x\hat{L}_z\cot\gamma - 2i\hat{L}_y\frac{\partial}{\partial\gamma}\right) + \frac{b_r + B_R}{2\sin^2\gamma}\left(\hat{J}_z^2 + \hat{L}_z^2\right) \\ &+ \frac{b_r}{2}\left[\hat{J}_+\left(\hat{J}_z\cot\gamma + \frac{\partial}{\partial\gamma} + i\hat{L}_y\right) + \hat{J}_-\left(\hat{J}_z\cot\gamma - \frac{\partial}{\partial\gamma} - i\hat{L}_y\right)\right] \\ &+ \hat{J}_z\left[b_r\left(\hat{L}_z - \hat{L}_x\cot\gamma\right) - (b_r + B_R)\frac{\hat{L}_z}{\sin^2\gamma}\right] - \frac{b_r\left(\hat{J}_+ + \hat{J}_-\right)}{2}\left(\hat{L}_x + \hat{L}_z\cot\gamma\right)\end{aligned} \tag{6.39}$$

Here, b_r and B_R are $(\mu_{\text{OH}} r^2)^{-1}$ and $(\mu_{\text{Kr-OH}} R^2)^{-1}$ respectively, with μ denoting a reduced mass:

$$\mu_{\text{OH}} = \frac{m_{\text{O}} m_{\text{H}}}{m_{\text{OH}}}\,; \quad \mu_{\text{Kr-OH}} = \frac{m_{\text{Kr}} m_{\text{OH}}}{m_{\text{Kr}} + m_{\text{OH}}} \tag{6.40}$$

The surface hopping QCT method relies on separating the 'fast' and 'slow' coordinates; the electronic degrees of freedom are treated quantum mechanically while the the nuclear motion is dealt with using classical mechanics.[82,83] Although the aim in this chapter is to incorporate terms from $\hat{T}_{\text{rot}}$ into the electronic Hamiltonian in order to deal with rovibronic interactions, this separation must be maintained as far as possible. Therefore, only the terms from equation (6.39) that are necessary for Renner-Teller and Coriolis couplings are taken as a 'perturbation,' $\hat{H}'$, to the electronic Hamiltonian $\hat{H}_{\text{el}}$:

$$\hat{H} = \hat{H}_{\text{el}} + \hat{H}' \tag{6.41}$$

These terms are

$$\begin{aligned}\hat{H}' =& \frac{b_r}{2}\hat{L}^2 + \hat{L}_z^2\left(\frac{b_r + B_R}{2\sin^2\gamma} - b_r\right) + \hat{J}_z\hat{L}_z\left(b_r - \frac{b_r + B_R}{\sin^2\gamma}\right) \\ & - \hat{J}_z\hat{L}_x b_r\cot\gamma - \frac{b_r}{2}\left(\hat{J}_+ + \hat{J}_-\right)\left(\hat{L}_x + \hat{L}_z\cot\gamma\right)\end{aligned} \tag{6.42}$$

First, this is integrated over the rotational basis:

$$\begin{aligned}\langle K'|\hat{H}'|K\rangle =& \delta_{K'K}\left\{\frac{b_r}{2}\hat{L}^2 + \hat{L}_z^2\left(\frac{b_r + B_R}{2\sin^2\gamma} - b_r\right) + K\hbar\hat{L}_z\left(b_r - \frac{b_r + B_R}{\sin^2\gamma}\right) - K\hbar\hat{L}_x b_r\cot\gamma\right\} \\ & - \delta_{K',K\pm1}\left\{\frac{b_r}{2}\lambda_\pm^{JK}\left(\hat{L}_x + \hat{L}_z\cot\gamma\right)\right\}\end{aligned} \tag{6.43}$$

Since the value of K' after a collision cannot be known in a classical trajectory calculation until the collision has taken place, we make the approximation that $K' = K \pm 1 \simeq K$. This is justified because the regions where it becomes a poor approximation are those regions where $\gamma \to 180°$, so the coupling goes to zero by symmetry. In this case,

$$\lambda_\pm^{JK} \simeq \lambda_0^{JK} = \hbar\left[J(J+1) - K^2\right]^{\frac{1}{2}} \tag{6.44}$$

and so

$$\begin{aligned}\langle K'|\hat{H}'|K\rangle =& \frac{b_r}{2}\hat{L}^2 + \hat{L}_z^2\left(\frac{b_r + B_R}{2\sin^2\gamma} - b_r\right) + \hat{L}_z\left(K\hbar b_r - \frac{K\hbar(b_r + B_R)}{\sin^2\gamma} - \frac{b_r}{2}\lambda_0^{JK}\cot\gamma\right) \\ & - \hat{L}_x\left(\frac{b_r}{2}\lambda_0^{JK} + K\hbar b_r\cot\gamma\right)\end{aligned} \tag{6.45}$$

Next, this matrix element must be integrated over the electronic basis. The matrix elements of $H_{\lambda'\lambda} = \langle\lambda'|\langle K'|\hat{H}_{\rm el} + \hat{H}'|K\rangle|\lambda\rangle$ are given in table 6.3, in which the shorthand notations $D_{\rm sum}$ and $D_{\rm dif}$ again refer to $\frac{1}{2}\left(V_{^1\Pi_{A'}} + V_{^1\Pi_{A''}}\right)$ and $\frac{1}{2}\left(V_{^1\Pi_{A'}} - V_{^1\Pi_{A''}}\right)$ respectively. Comparison of this to table 6.2 reveals which are the added rotational terms. The diabatic

$\hat{L}_x$ matrix elements in the table are given explicitly in equations (6.32) to (6.33), and

$$\mathcal{A} = \frac{b_r + B_R}{\sin^2\gamma} - b_r \tag{6.46}$$

$$\mathcal{B} = K\hbar b_r - \frac{K\hbar(b_r + B_R)}{\sin^2\gamma} - \frac{b_r}{2}\lambda_0^{JK}\cot\gamma \tag{6.47}$$

$$\mathcal{C} = \frac{b_r}{2}\lambda_0^{JK} + K\hbar b_r \cot\gamma \tag{6.48}$$

From these matrix elements, the mixing angles are calculated in a pairwise fashion, taking advantage of equation (6.6).

$$\alpha = \frac{1}{2}\arctan\left(\frac{2H_{+1,0}}{H_{+1,+1} - H_{0,0}}\right) \tag{6.49}$$

$$\beta = \frac{1}{2}\arctan\left(\frac{2H_{+1,-1}}{H_{+1,+1} - H_{-1,-1}}\right)(1 - S_K)(1 - S_\gamma) \tag{6.50}$$

$$\omega = \frac{1}{2}\arctan\left(\frac{2H_{0,-1}}{H_{0,0} - H_{-1,-1}}\right) \tag{6.51}$$

The angles resulting from this pairwise procedure were carefully checked against those obtained from diagonalisation of the full 3x3 matrix **C**. In all cases, it was found that there was little difference between the two procedures, and so the pairwise method was chosen for its advantages in terms of speed.

The functions S_K and S_γ are damping functions aimed at preventing unphysical spikes in the mixing angles. They are explained in full in the next section (section 6.7).

6.7 Numerical stability

Equation (6.50) above uses two switching functions, S_γ and S_K, to avoid instabilities that could cause spurious spikes in the mixing angles – often, this is when the expressions used to calculate them contain 0/0. The first, S_γ, deals with the situation when $\gamma \to 180°$, *i.e.* when the Rg–OH complex approaches linearity. On approach to this limit, terms in $\cot\gamma$ and $1/(\sin^2\gamma)$ quickly become very large and dominate equations they appear in. However, at linearity, there should be no RT coupling (as the $1A'$ and $1A''$ states become

$H_{\lambda'\lambda}$	$\lambda = 1$	$\lambda = 0$	$\lambda = -1$
$\lambda' = 1$	$D_{\text{sum}} + \frac{\hbar^2}{2}\mathcal{A} + \hbar\mathcal{B} - \mathcal{C}\langle+1\vert\hat{L}_x\vert+1\rangle$	$\frac{\sqrt{2}}{2}V_{12} - \mathcal{C}\langle+1\vert\hat{L}_x\vert0\rangle$	D_{dif}
$\lambda' = 0$	$\frac{\sqrt{2}}{2}V_{12} - \mathcal{C}\langle+1\vert\hat{L}_x\vert0\rangle$	V_Σ	$\frac{\sqrt{2}}{2}V_{12} + \mathcal{C}\langle+1\vert\hat{L}_x\vert0\rangle$
$\lambda' = -1$	D_{dif}	$\frac{\sqrt{2}}{2}V_{12} + \mathcal{C}\langle+1\vert\hat{L}_x\vert0\rangle$	$D_{\text{sum}} + \frac{\hbar^2}{2}\mathcal{A} - \hbar\mathcal{B} + \mathcal{C}\langle+1\vert\hat{L}_x\vert+1\rangle$

Table 6.3: Matrix elements of the *full* Hamiltonian $\hat{H}$ in the basis of Zhou *et al.*,[135,141] where the shorthand $D_{\text{sum}} = \frac{1}{2}\left(V_{\Pi_{A'}} + V_{\Pi_{A''}}\right)$ and $D_{\text{dif}} = \frac{1}{2}\left(V_{\Pi_{A'}} - V_{\Pi_{A''}}\right)$. The matrix elements of $\hat{L}_x$ are given explicitly in equations (6.32) to (6.33), and $\mathcal{A}$, $\mathcal{B}$ and $\mathcal{C}$ are given in equations (6.46) to (6.48).

the two components of a Π state) or Coriolis coupling (the states are of different symmetry – Σ and Π). So that the coupling tends to zero as it should, a Gaussian damping function is applied:[131]

$$S_\gamma = \exp\left(\frac{-\sin^2\gamma}{\delta_\gamma^2}\right) \tag{6.52}$$

The full width at half-maximum (FWHM; δ_γ) is set at an appropriate level by trial and error such that β is still calculated correctly, but is free of unphysical spikes – see figure 6.5. (It was found that there was no need to apply this function to α or ω). In the calculations performed in this thesis, δ_γ was $\sqrt{0.05}$, but testing revealed that the results were relatively insensitive to its magnitude – the FWHM could be altered by up to 4 times with little noticeable difference.

The other instability occurs when K tends to zero. This occurs periodically throughout a trajectory, as the rotation of the OH radical takes it through an angle where $\boldsymbol{J}$ and $\boldsymbol{r}$ (the OH bond vector) are perpendicular. As the expression for β contains $(H_{+1,+1} - H_{-1,-1})$ in the denominator of a fraction, this angle takes unreasonable values when $K \to 0$ and the splitting between $H_{+1,+1}$ and $H_{-1,-1}$ becomes very small, and this instability propagates forwards to the other two mixing angles as well. As there should be no coupling when $K = 0$, another damping function is employed:

$$S_K = \exp\left(\frac{-K^2}{\delta_K^2}\right) \tag{6.53}$$

(Note the form of the expression used: $K^2\hbar^2/\delta_K^2\hbar^2$ is rather unwieldy to work with.) This is set to cut off regions where K is too small, but should not be set too high due to the risk of missing true couplings. Therefore, δ_K is set carefully to ensure it removes spikes in the mixing angles but keeps the coupling – in this thesis, a value of 0.25 (dimensionless) is chosen.

Figure 6.4 shows how the mixing angles α, β and ω change over the course of a 'typical' OH + Kr trajectory. The variation is seen to be smooth and almost free of unphysical spikes. In the left hand panel, χ (the two-state mixing angle obtained from the PES) is

plotted alongside α to show their similarity. The middle panel shows the effect of the damping functions S_γ and S_K on β, with the grey dotted line being what β would look like without this damping.

The effects of these switching functions are drawn out further in figure 6.5. It can be seen that, in this case, S_γ plays the major part in moderating the behaviour of β, with S_K helping to a lesser degree. The overall variation of β with R is made as smooth as possible by the inclusion of these switching functions.

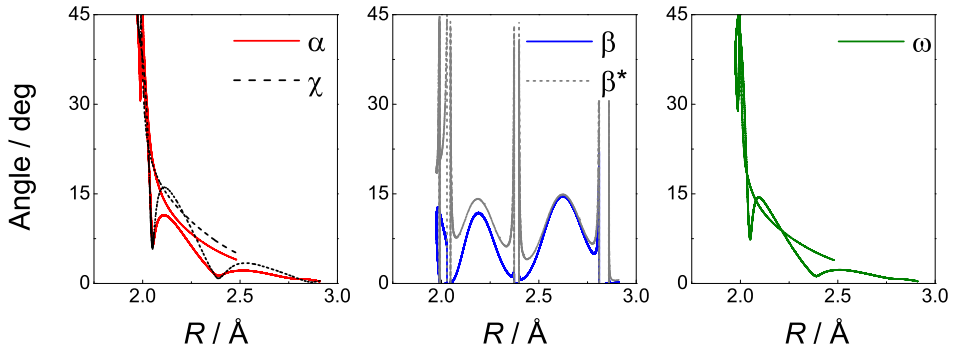

Figure 6.4: Mixing angles α, β and ω plotted over the course of a single trajectory (OH + Kr). Left panel: α (red), χ (black dots). Centre panel: β (blue), β^* (*undamped* β, grey dots). Right panel: ω (green).

Another numerical issue to consider is that the trace of the electronic density matrix (*i.e.* the total populations of all the adiabatic states) must be conserved, and that the population of each individual state must not take unphysical values (less than 0, or greater than 1). This constraint accompanies those carried forward from the adiabatic QCT code, namely that the total energy and angular momentum of the system must be conserved. Figure 6.6 presents the diagonal elements of the electronic density matrix $\boldsymbol{\rho}$, showing that these display physically reasonable behaviour. In addition, their sum (the black dotted line) is seen to be unity, as required.

6.8 Calculation details

The present theory is an extension of the two-state TSH-QCT code discussed at the beginning of this chapter, which itself is a modification of the single-surface QCT code.

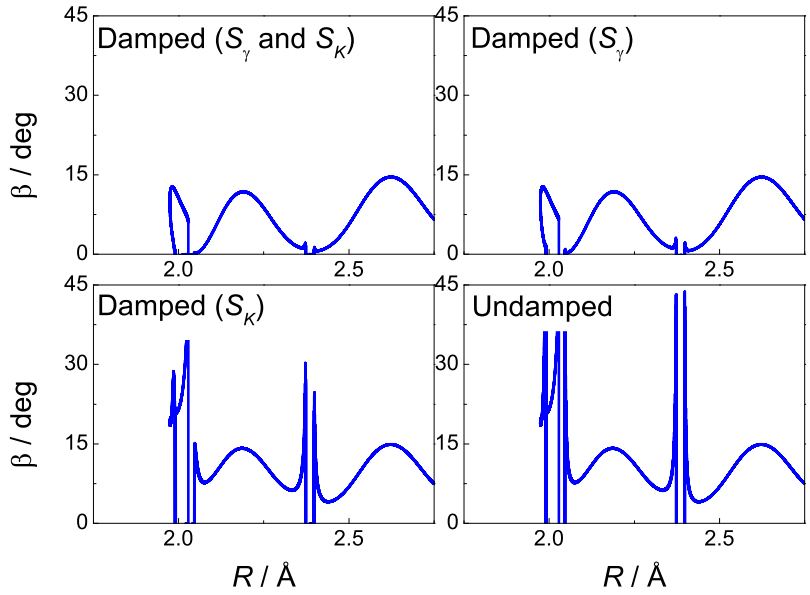

Figure 6.5: Mixing angle β plotted over the course of a single trajectory (OH + Kr). Top left: damped using S_K and S_γ, top right: damped using S_γ only, bottom left: damped using S_K only, bottom right: no damping functions applied.

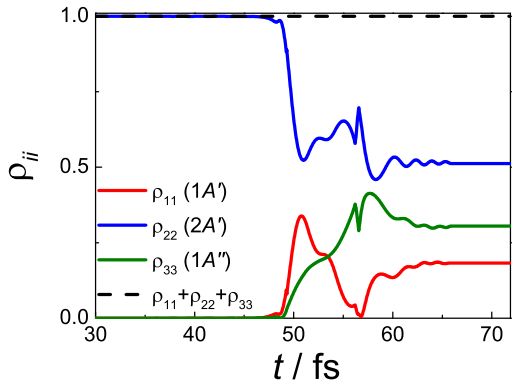

Figure 6.6: Adiabatic electronic state populations (diagonal density matrix elements) plotted over the course of a single trajectory (OH + Kr) against time. Red: ρ_{11} ($1A'$), blue: ρ_{22} ($2A'$), green: ρ_{33} ($1A''$). The black dotted line shows the trace of the density matrix ($\rho_{11} + \rho_{22} + \rho_{33}$). This particular trajectory hopped from $2A'$ to $1A''$.

Therefore the integration of the equations of motion and electronic density matrix is carried out as described in chapter 5 and section 6.4 respectively. Around 5×10^4 trajectories are run for each initial N, with the initial separation being set to 12 Å for OH + Kr and 20 Å for OH + Xe, just as in the single-surface case.

As there is only appreciable coupling between the potentials in certain, close-in configurations, two timesteps were used in the integration in order to speed up the calculations. In the 'outer' region, set to be $\gamma < 150°$ and at distances R between 2.9 and 12 Å (Kr) / 3.5 and 20 Å (Xe), the trajectory was propagated as in the single-surface QCT code, with a timestep of 60 as. At lower R, the timestep was 20 as (Kr) / 25 as (Xe), with the couplings 'turned on'. Comparison of the results to those obtained using only the shorter timestep revealed little to no difference caused by this time-saving method.

For the calculation of the potential couplings, the FWHMs for the switching functions δ_K and δ_γ were set as described in section 6.7. The matrix elements of $\hat{L}_x$ were provided[236] as a grid of points in R and γ, and interpolated using a bivariate method based on piecewise bicubic polynomials.[260]

Quenching cross-sections can be obtained from the number of trajectories ending up on the $1A'$ or $1A''$ adiabatic potentials via the analogue to equation (5.9),

$$\sigma_Q = \pi b_{\max}^2 \frac{\mathcal{N}_{1A'}}{\mathcal{N}_{\text{tot}}} \tag{6.54}$$

with the statistical uncertainty (standard deviation) given by

$$\Delta\sigma_Q = \sigma_Q \sqrt{\frac{1}{\mathcal{N}_{1A'}} - \frac{1}{\mathcal{N}_{\text{tot}}}} \tag{6.55}$$

However, the ratio between these numbers of trajectories on the two ground state potentials is not the same as the lambda-doublet ratio, because A' and A'' are symmetry labels for reflection in the *scattering* plane – as opposed to the plane of *rotation* of the molecule, which gives the $\Pi(A')$ and $\Pi(A'')$ labels to the lambda-doublets (in the high-j limit – see section 2.1). If OH(X) is treated as a $^1\Pi$ molecule, then quenched molecules

with a final rotational state of N'' have reflection symmetry in the scattering plane of[89,261]

$$\langle \sigma_v \rangle = -\epsilon \frac{N''}{N''+1} \tag{6.56}$$

where ϵ is the parity of the wavefunction. This means that a trajectory ending on the $1A'$ adiabatic PES contributes $\frac{1}{2}\left(\frac{N''}{N''+1}+1\right)$ to the $\Pi(A')$ lambda-doublet level (*i.e.* $\mathcal{N}_{1A'}$) and $\frac{1}{2}\left(1-\frac{N''}{N''+1}\right)$ to the $\Pi(A'')$ level. For a trajectory ending on $1A''$, these proportions are reversed. Note that this is only an important correction at low N'', where the present semiclassical theory is a poorer approximation to quantum mechanics anyway.

When considering the final rotational state in OH(X) that a quenched trajectory ends up in, consideration must also be given to the different bond lengths in OH(X) and OH(A). These are taken as 0.970 Å and 1.012 Å respectively.[91] The final rotational energy of OH is first converted to a *continuous* quantum number – n' in equation (5.5). Then, the rotational energies of OH in its X and A electronic states are equated:

$$B_X n'_X(n'_X+1) = B_A n'_A(n'_A+1) \tag{6.57}$$

where B_i is the rotational constant for state i. These have the ratio $x_r = B_X/B_A = (r_A/r_X)^2$, which takes a value around[91] 1.08. Therefore

$$n'_X = -\frac{1}{2} + \sqrt{\frac{1}{4} + \frac{{n'_A}^2}{x_r} + \frac{n'_A}{x_r}} \tag{6.58}$$

and the corrected n'_X is binned to a quantum number, N', in the usual way.

6.8.1 Momentum rescaling

On hopping from one potential energy surface, $|i\rangle$, to another, $|j\rangle$, the potential energy associated with a trajectory changes suddenly from U_i to U_j. In order to conserve the total energy, the nuclear velocities must therefore be adjusted to compensate for this. The most common choice is to adjust the velocities in the direction of the $\boldsymbol{d}_{ij}$ vector,[262,263] although

other methods have been used as well.[102]

This rescaling does *not* guarantee that linear or angular momentum will be conserved.[262] However, hops usually occur between surfaces that are not far apart in energy, so the adjustments to the momenta will be small. In the calculations presented in this thesis, conservation of total E and J is found to be excellent.

For some surface hops (upward in energy), it is not possible to adjust the nuclear momenta sufficiently to compensate for the change in energy between the surfaces. In these cases, the hop is termed *frustrated* and rejected, with the nuclear velocities simply being reversed. Various schemes have been presented to improve upon the treatment of frustrated hops, for example allowing a frustrated hop to occur if the system can reach an 'allowed' hopping point within the limit defined by time uncertainty,[264,265] but these are not employed in this thesis.

To derive the adjustment needed to the nuclear momenta, we split the momenta into two parts for the two reduced masses, r and R:[266] (i and j refer to the two potentials)

$$\boldsymbol{p}_j = \boldsymbol{p}_i - \gamma_{ij}\boldsymbol{d}^r_{ij} \; ; \quad \boldsymbol{P}_j = \boldsymbol{P}_i - \gamma_{ij}\boldsymbol{d}^R_{ij} \tag{6.59}$$

in which γ_{ij} is the scaling factor, $\boldsymbol{d}^r_{ij} = \langle\phi_i|\nabla_r|\phi_j\rangle$ and $\boldsymbol{d}^R_{ij} = \langle\phi_i|\nabla_R|\phi_j\rangle$.

The overall kinetic energy change can be written as[262]

$$\Delta\mathrm{KE} = \gamma^2_{ij}a_{ij} - \gamma_{ij}b_{ij} \tag{6.60}$$

in which

$$a_{ij} = \frac{1}{2}\left[\frac{|\boldsymbol{d}^r_{ij}|^2}{\mu_{BC}} + \frac{|\boldsymbol{d}^R_{ij}|^2}{\mu_{ABC}}\right] \tag{6.61}$$

$$b_{ij} = \frac{1}{2}\left[\dot{\boldsymbol{r}}_i \cdot \boldsymbol{d}^r_{ij} + \dot{\boldsymbol{R}}_i \cdot \boldsymbol{d}^R_{ij}\right] = \langle\phi_i|\frac{\partial}{\partial t}|\phi_j\rangle \tag{6.62}$$

and the reduced masses are

$$\mu_{BC} = \frac{m_B m_C}{m_B + m_C} \; ; \quad \mu_{ABC} = \frac{m_A m_{BC}}{m_A + m_{BC}} \tag{6.63}$$

In order to conserve total energy, $\Delta\mathrm{KE} = U_i - U_j$, so

$$\gamma_{ij}^2 a_{ij} - \gamma_{ij} b_{ij} - (U_i - U_j) = 0 \tag{6.64}$$

A hop is forbidden (frustrated) if $b_{ij}^2 + 4a_{ij}(U_i - U_j) < 0$. In this case, the velocities are reversed:[262] $\gamma_{ij} = b_{ij}/a_{ij}$.

Otherwise, the scaling factor is[262]

$$\gamma_{ij} = \frac{1}{2a_{ij}} \left[b_{ij} \pm \sqrt{b_{ij}^2 + 4a_{ij}(U_i - U_j)} \right] \tag{6.65}$$

with + for $b_{ij} < 0$ and − for $b_{ij} \geq 0$.

6.9 Results: quenching

In this section, the focus is on evaluating the results of the theory presented in this chapter, rather than its ability to predict experimental results. A full discussion of the experimental quenching cross-sections will be dealt with later on, in chapter 7. Here, the present section will begin with a short discussion of the centrifugal sudden (CS) approximation, before comparing the results of three state TSH-QCT theory to fully non-adiabatic quantum mechanics.[236] After this, a comparison will be made of several models in which different couplings (electronic, Coriolis and Renner-Teller) are turned on and off, in order to gauge the relative importance of each.All results considered here are for OH(A) + Kr; the results with Xe are all contained in chapter 7.

6.9.1 Centrifugal sudden approximation

Between equations (6.43) and (6.45), the approximation was made that $K \pm 1 \simeq K$, justifying the inclusion of terms in $\delta_{K'K}$ and $\delta_{K',K\pm1}$ in the same equation. An alternative strategy is to restrict the theory to the case where $K' = K$, which Santoro *et al.* refer to as the *centrifugal sudden* (CS) approximation.[131] In this approach, also known as the *coupled states* treatment,[109,267] the centrifugal coupling term (in $L(L+1)$) is dropped from the Hamiltonian, such that K is a constant during the collision.

Taking an analogous approach in the present case involves ignoring all terms in $\delta_{K',K\pm1}$ in equation (6.43). The effect of this is demonstrated in Table 6.4. As can be seen, the absolute difference is slight, though the inclusion of the extra coupling terms in the non-CS theory results in increased quenching. (The present section is focused on comparing results with and without the CS approximation; a full comparison of theory with experiment is deferred until the experimental results are presented in chapter 7.) For this reason, the CS approximation will not be used in the remainder of this thesis.

It is interesting to note that Kłos, Dagdigian and Alexander,[236] in as-yet unpublished work, have carried out three state non-adiabatic QM calculations on this system (discussed further in section 6.9.2). They find little to no difference in the OH(A) + Kr quenching cross-sections calculated with the full close-coupled (CC) equations and using the CS approximation.[236] These results will be compared to those presented here in more detail in section 6.9.2.

	σ_Q / Å^2	
N	Non-CS	CS
0	16.5	14.1
2	7.4	5.3
4	3.0	2.2
6	0.2	0.3

Table 6.4: Comparison of calculated OH(A) + Kr quenching cross-sections as a function of initial rotational state, N. 'Non-CS' and 'CS' refer to calculations including and omitting terms in $\delta_{K',K\pm1}$ respectively.

6.9.2 Comparison to quantum mechanics

As briefly touched upon in section 6.9.1, non-adiabatic quantum scattering calculations for the OH + Kr system have been carried out by Kłos, Dagdigian and Alexander.[236] Although the results of these calculations have not (at the time of writing) yet been published, other non-adiabatic three state QM models have been described in the literature – see the introduction to this chapter (section 6.2) for examples.

Preliminary quenching cross-sections from J. Kłos,[236] using the CS approximation, are compared to the three state TSH-QCT model presented in this chapter in figure 6.7. It was found that CC and CS calculations gave very similar σ_Q, but the CC calculations were prohibitively expensive – note, however, that the QM calculations are at a very early stage and should not be taken as the final word on the subject.

Agreement between the theory presented here and full quantum mechanics is encouraging, with most disagreement occurring at the lowest N. The lack of significant discrepancies points to spin-orbit coupling playing a relatively minor role in the quenching, though this is a point that would require further investigation for OH(A) + Xe. If this agreement is borne out by further QM studies, the three state TSH-QCT model has the great advantage of computational efficiency over a full quantum calculation, which will be even more relevant for larger systems with more atoms.

6.9.3 Combinations of couplings

The present theory includes electrostatic coupling between the diabatic $\Pi_{A'}$ and Σ potentials, as well as rovibronic (Coriolis and Renner-Teller) couplings. To examine the importance of each kind of coupling, calculations were run using four different models, as below:

2 state TSH

Electrostatic coupling only (links $2A'$, $1A'$; β, $\omega = 0$)

Coriolis, no RT

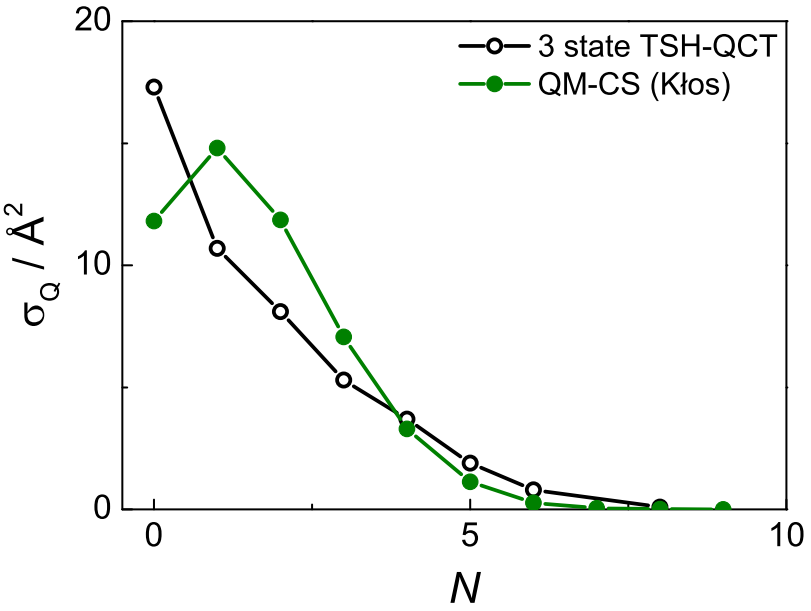

Figure 6.7: Theoretical electronic quenching cross-sections for OH(A) + Kr. Open black circles: full 3 state TSH-QCT, filled green circles: non-adiabatic coupled states (CS) QM.[236]

Electrostatic coupling and $2A' - 1A''$ Coriolis coupling only ($\beta = 0$)

RT, no Coriolis

Electrostatic coupling and $1A' - 1A''$ Renner-Teller coupling only ($\omega = 0$)

Full model

All three kinds of coupling included.

Figure 6.8 shows the results from each model. Note that, from equation (6.11), hops from $2A'$ to $1A''$ are possible even when ω is zero, provided that β is non-zero, meaning that Renner-Teller coupling provides an indirect way of linking $2A'$ and $1A''$. Comparing the results in the figure, it can be seen that the full three state method offers significantly increased electronic quenching over the two state method. As will be seen in chapter 7, the inclusion of rovibronic couplings is essential for a complete description of the OH(A) + Kr quenching dynamics. It is clear that RT coupling is the major 'missing piece' of the theory, with Coriolis coupling providing an extra improvement on top of this.

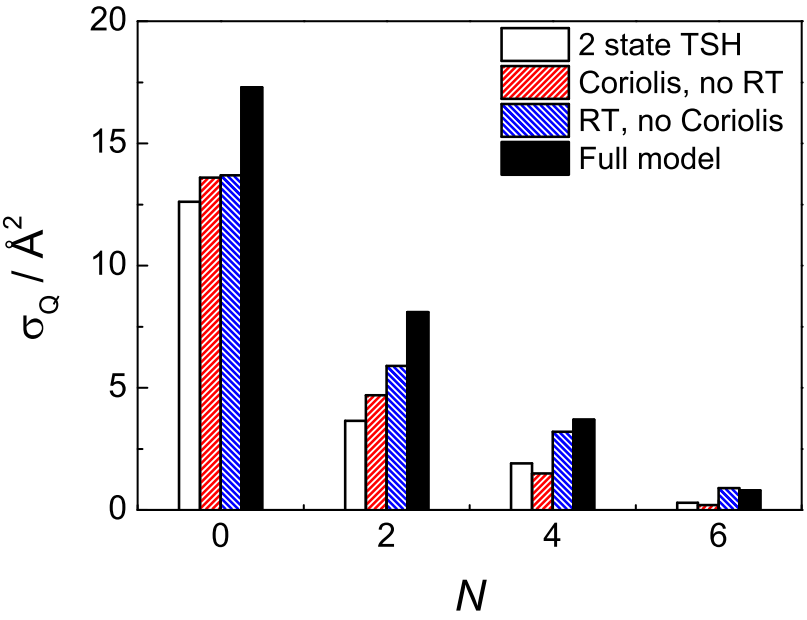

Figure 6.8: Comparison of theoretical electronic quenching cross-sections for OH(A) + Kr. Empty columns: 2 state TSH-QCT, red stripes: including Coriolis but not Renner-Teller couplings, blue stripes: including Renner-Teller but not Coriolis couplings, filled black columns: full model (all couplings included).

6.10 Results: OH(X) product state distributions

As well as looking at the collisional depopulation of OH(A) to its ground electronic state via the quenching cross-sections in the previous section, the calculations in this chapter offer the opportunity to investigate what happens to OH radicals once they are quenched. The rotational and lambda-doublet state distributions of the quenched OH(X) provide a wealth of information on the passage through the conical intersection region.[28]

These product state distributions can be compared to those measured very recently (for OH(A) + Kr) in the molecular beam experiments of Lester and coworkers.[28,268] In those studies, OH(A, $N = 0$) collided with Kr atoms in a molecular beam and the nascent OH(X) products of electronic quenching were probed via LIF spectroscopy, as in several previous studies by Lester's group.[28,115,268–272] Note that experimental data was collected using Kr quencher gas, but not with Xe, so the calculations in this section will all involve the OH(A) + Kr system.

Experimentally, the product state distribution (PSD) of OH(X) from quenching with

Kr is found to be rotationally hot and vibrationally cold – mostly in $v'' = 0$, with a bimodal distribution of N'' peaking around $N'' = 9$ and 17.[28†] This is similar to observations with other quenchers such as H_2 and D_2,[115,269,272] N_2[270] and O_2,[271] as reviewed recently in ref. 268, except that the product rotational distribution is unimodal for all of these. In quenching with CO_2, the rotational PSD is colder, perhaps reflecting the extended time spent in a collision complex.[271]

In all the experimental studies mentioned above, the F_1 and F_2 spin-orbit levels of OH(X) are populated almost equally and, if a preference for one lambda-doublet over another is observed, it is a slight propensity for $\Pi(A')$. For quenching with Kr, no significant lambda-doublet preference is seen at the range of N'' probed.[28]

A quantitative measure of preferential lambda-doublet population is given by the *degree of electron alignment*, or DEA. This is defined as[28]

$$\mathrm{DEA} = \frac{P_{\Pi(A')} - P_{\Pi(A'')}}{P_{\Pi(A')} + P_{\Pi(A'')}} \tag{6.66}$$

such that positive and negative values (ranging between +1 and -1) imply a preference for $\Pi(A')$ and $\Pi(A'')$ respectively.

In this section, results will first be presented for collisions of OH(A) + Kr at a fixed collision energy of 0.039 eV, just as for the quenching results in the rest of this chapter. This will give further insights into the nature of surface hops and which kinds of collisions lead to quenching (and what the outcome of those collisions will be). Then, calculations for a fixed collision energy of 0.012 eV will be compared to the experiments of Lehman *et al.*[28] This collision energy is chosen to correspond approximately to the molecular beam temperature used in those experiments ($\simeq 100$ cm^{-1}).

†We use quantum numbers without primes for the OH(A) produced by laser excitation. Single primes denote OH(A) post-collision, and double primes are for quenched OH(X).

6.10.1 39 meV

TSH-QCT calculations were run at a fixed collision energy of 0.039 eV using the two state model of ref. 23,28 as well as the three state model described in this chapter. The resulting OH(X) product rotational state distributions, or PSDs, are presented in the top row of figure 6.9.

As remarked upon above, the OH(X) rotational distribution is found to be hot, reflecting the large torques experienced by the molecule as it undergoes quenching. The experimental observation[28] that most OH(X) is born in $v'' = 0$, and the similarity of the OH bond lengths in the X and A electronic states, justify keeping r_{OH} fixed in these calculations.

The most interesting feature of these PSDs is that they are bimodal, at least in the two state model – some remnant of this can be seen in the three state model, but it is nowhere near as apparent. To explain this, the bottom row of the figure shows the surface hops binned into the Kr–OH distance, R, where the hop took place. In the two-state model, there are clearly two regions where hopping occurs: a spread-out region at lower values of R, and a sharp spike at higher R.

Taking 1.978 Å as a cut-off between these two regions, the PSDs in the figure are split into those deriving from low-R hops, which tend to have lower final N'', and the distribution resulting from high-R hops, which is rotationally hotter. This nicely accounts for the two peaks observed in the summed PSD.

The same behaviour is observed for hops to the $1A'$ PES in the three state model. The peak from high-R hops looks much the same as in the two state model, but there are fewer hops leading to low N'' (and there is less separation between these two hopping regions). In fact, the hops at lower R that yield rotationally colder OH(X) actually end up going to $1A''$ in this model – hops to this surface take place at shorter distances than hops to $1A'$. The $1A''$ PSD is also separated to some extent into two regions, with low-R hops giving a distribution centred at low N'', and hops at higher R giving the higher-N'' peak.

In order to explore this further, figure 6.10 shows opacity functions for quenching, split

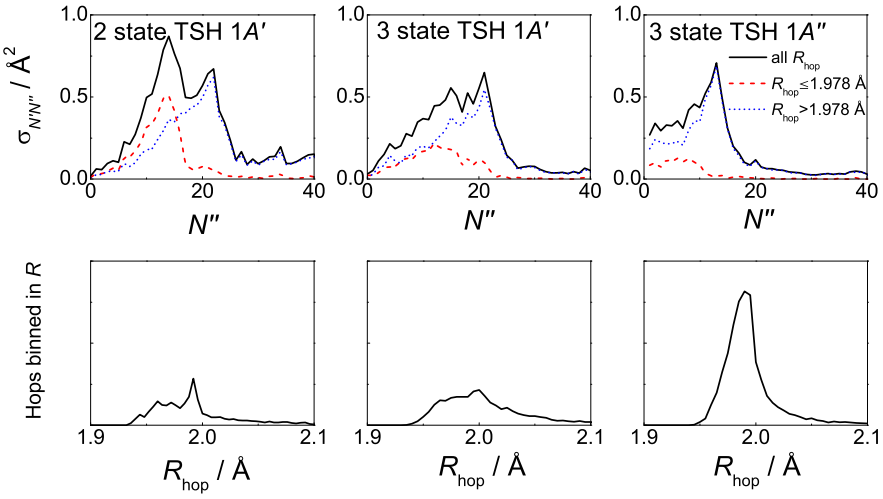

Figure 6.9: Top row: OH(X) product rotational state distributions for quenching of OH(A) + Kr, $N = 0$, 0.039 eV at all R_{hop} (black solid line), $R_{\mathrm{hop}} \leq 1.978$ Å (red dashed line) and $R_{\mathrm{hop}} > 1.978$ Å (blue dotted line). Bottom row: surface hops binned into R at point of hopping. The left-hand column shows the two state TSH-QCT model; the centre and right-hand columns show the three state model (trajectories ending on the $1A'$ and $1A''$ PESs respectively).

according to where the hops took place into 'low' and 'high' R_{hop} regimes. This reveals a stark difference in that trajectories hopping at low R, which lead to lower final N'', tend to be more head-on in character than trajectories hopping at higher R. This is not surprising – a more head-on collision would be required for OH and Kr to approach closer.

The same behaviour is seen for the three state TSH-QCT calculations as for the two state model, though the difference is not as strong. The probability of a hop to $1A''$ is seen to drop dramatically at low impact parameter, because the smaller orbital angular momentum implies a smaller value of K, thus reducing rovibronic couplings.

The OH(X) PSDs resulting from quenching of OH(A) in different rotational states are compared in figure 6.11. The first point to note is that fewer trajectories hop for initial $N = 2$ than for $N = 0$ – as OH rotates faster, it becomes more difficult for Kr to approach at the right angle to reach the position of greatest potential couplings. Much the same peaks are observed in the PSDs for both initial rotational states, but their relative magnitudes are quite different, with the higher N'' peak being much more favoured for $N = 2$. Quenching to high N'' derives from surface hops at larger separations; at higher

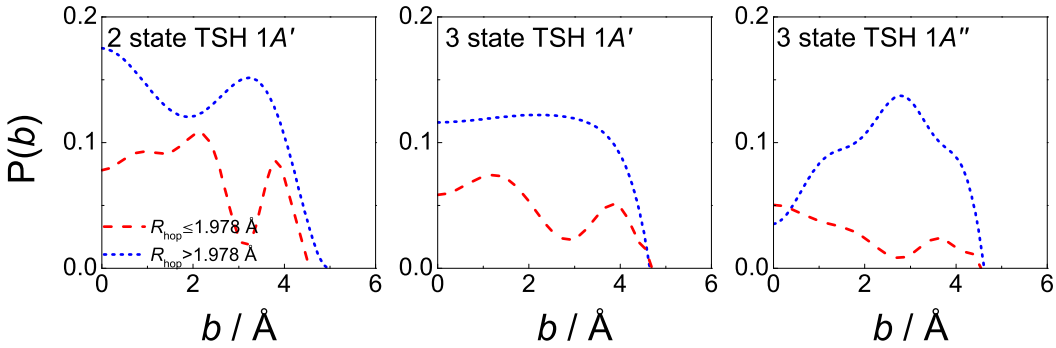

Figure 6.10: Opacity functions for collisions leading to quenching for OH(A) + Kr, $N = 0$, 0.039 eV, for hops at $R_{\text{hop}} \leq 1.978$ Å (red dashed line) and $R_{\text{hop}} > 1.978$ Å (blue dotted line). The left-hand column shows the two state TSH-QCT model; the centre and right-hand columns show the three state model (trajectories ending on the $1A'$ and $1A''$ PESs respectively).

initial N, more head-on collisions are needed to reach the hop positions that would give low N''.

Finally, figure 6.12 compares surface hops to the $1A'$ and $1A''$ potentials in terms of the Jacobi angle, γ, at which they take place. It is clear that hops to the $1A''$ surface occur further off linearity than those to $1A'$. At near-linear configurations, rovibronic couplings should go to zero as detailed in section 6.7, explaining the fall-off in hops in this region. The approximately equal split between trajectories ending up on the $1A'$ and $1A''$ potentials shows the importance of including all three relevant electronic states in any description of the collision process.

6.10.2 12 meV

TSH-QCT calculations were also run at a fixed collision energy of 0.012 meV ($\simeq 100$ cm^{-1}) for comparison with the experimental data of Lester and coworkers.[28] Note that, in ref. 28, the collision energy for this molecular beam experiment is given as 0.025 eV; the work in this subsection was performed before this information was known and as such the choice of 0.012 eV was a 'best guess' for molecular beam conditions. As the general trends in this subsection are broadly similar to those for 0.039 eV (section 6.10.1), the comparison to this experiment should still be appropriate.

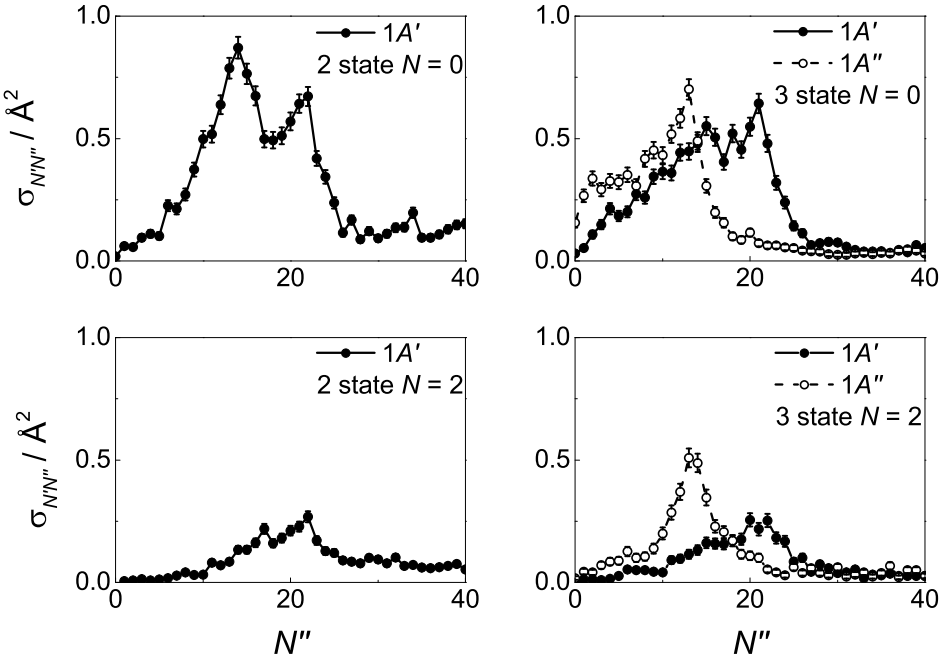

Figure 6.11: OH(X) product rotational state distributions for quenching from OH(A) + Kr, $N = 0$ (top row) or $N = 2$ (bottom row), at a fixed collision energy of 0.039 eV. The left-hand column shows the two state TSH-QCT model and the right-hand columns shows the three state model (trajectories ending on the $1A'$ and $1A''$ PESs denoted with filled and open circles respectively).

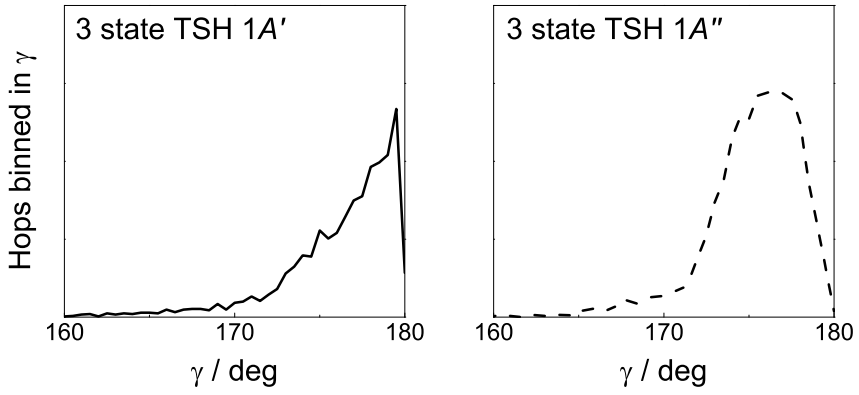

Figure 6.12: Surface hops binned into γ at point of hopping for OH(A) + Kr, $N = 0$, 0.039 eV, using the three state TSH-QCT model. Left: trajectories ending on $1A'$, right: trajectories ending on $1A''$.

It is also worth noting that the experiments of Lester *et al.*[28] give *relative*, rather than absolute cross-sections. Therefore, the experimental data is scaled 'by eye' to give the best match with theory in the comparisons below.

Figure 6.13 presents a comparison between the experimental OH(X) product rotational state distributions and the theoretical PSDs calculated using the full three state TSH-QCT model, including all rovibronic couplings. The agreement between theory and experiment is very encouraging – firstly, the lambda-doublet ratio is correct, with no overwhelming preference for A' over A'', or vice versa. At high N'', the correspondence between the theoretical and experimental rotational state distributions is almost quantitative, with some discrepancies for lower final rotational states. It would be very interesting to see experimental data for $1A''$ states at low N'', but, because of spectroscopic limitations such as overlapping line positions in a crowded spectrum, this may not be possible.

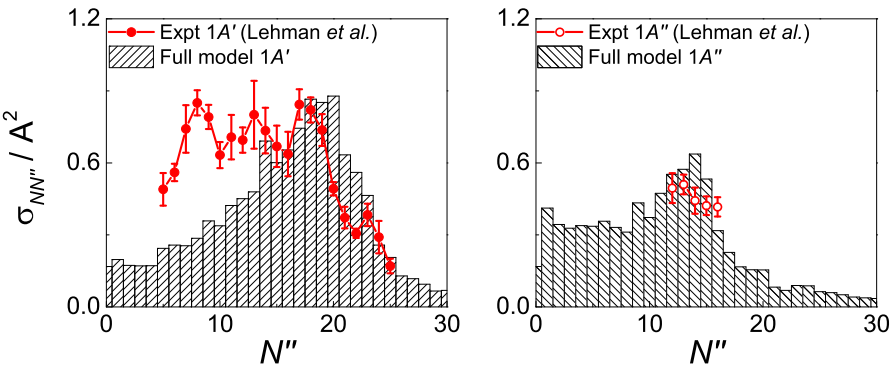

Figure 6.13: OH(X) product rotational state distributions for quenching from OH(A) + Kr, $N = 0$. Left: molecules ending up in the $1A'$ state, right: molecules ending up in the $1A''$ state. The bars are 3 state TSH-QCT calculations at a fixed collision energy of 0.012 eV and the red circles are the experimental results of Lester and coworkers[28].

To enable a more in-depth analysis of the data, 0.012 eV calculations were run using the four models of section 6.9.3. The results are displayed in figure 6.14.

The rotational state distributions for trajectories ending on the $1A'$ PES are fairly similar across the four models – even the two state TSH-QCT calculations do a decent job of modelling the experimental distribution (as seen in ref. 28). However, inclusion of the $1A''$ state is essential as almost half of the experimental quenching is seen to be to this state. This shows that most of the increase in the total quenching cross-section when

going from the two state model to a three state model is due to added quenching to $1A''$, rather than enhanced quenching to $1A'$.

Looking at the results from the three state models, Coriolis coupling favours the production of OH(X) in low rotational states, with the addition of Renner-Teller coupling leading to higher values of N''. This could mean that more torque is applied to OH on passage from $2A'$ to $1A'$ (with subsequent hopping to the $1A''$ surface) than during a direct hop from the $2A'$ to the $1A''$ PES. In general, though, trajectories ending on the $1A''$ PES tend to have a lower degree of rotational excitation than those ending up on the $1A'$ PES.

The PSDs from the full three state model appear as a combination of those from the two partial models ('Coriolis, no RT' and 'RT, no Coriolis'). The theoretical DEA predicts a propensity for the $1A''$ surface in low final rotational states, with quenching to $1A'$ leading preferentially to higher N''. The experimental DEA of 0.06 ± 0.07 at N'' between 11 and 16 is in accord with theory, but, if it were possible to measure this over a wider range of product rotational states, this would give a much better idea of whether Coriolis or Renner-Teller couplings predominate.

6.11 Summary

In this chapter, a TSH-QCT model has been presented for the OH(X,A) + Kr, Xe systems. Chapter 7 will use the theory developed here to model and analyse the experimental results for OH(A) + Kr, Xe that will be presented and discussed in detail there. The $1A'$, $1A''$ and $2A'$ potential energy surface are all included, with all electronic and rovibronic (Coriolis and Renner-Teller) couplings between them. Special attention has been given to details of the diabatic electronic basis and adiabatic to diabatic transition, as well as numerical considerations in the program. Finally, the model has been demonstrated with the presentation of results for quenching of OH(A) and for the resulting state distributions of quenched OH(X), and these results are compared to non-adiabatic quantum scattering calculations[236] and experimental data[28] respectively.

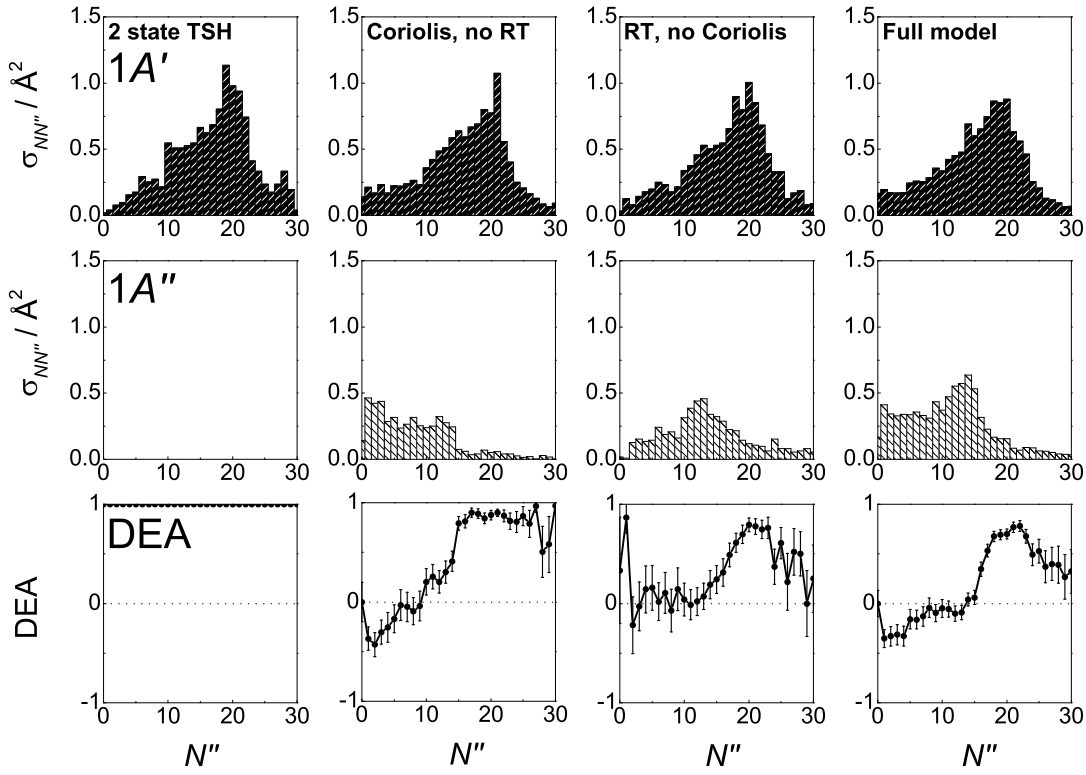

Figure 6.14: Theoretical OH(X) product rotational state distributions for quenching from OH(A) + Kr, $N = 0$, at a fixed collision energy of 0.012 eV. Top row: trajectories ending on the $1A'$ PES, middle row: trajectories ending on the $1A''$ PES, bottom row: degree of electron alignment (equation (6.66)). The columns are the four models of section 6.9.3, from left to right: 2 state TSH-QCT, 3 state TSH-QCT including Coriolis but not RT couplings, 3 state TSH-QCT including RT but not Coriolis couplings, 3 state TSH-QCT including all couplings.

Chapter 7

OH($A^2\Sigma^+$, $v = 0$) + Kr and Xe: experimental and theoretical results

This chapter will present experimental results for electronic quenching, rotational energy transfer (RET), and collisional depolarisation in rotationally elastic* and inelastic collisions for OH($A^2\Sigma^+$, $v = 0$) + Kr and Xe. As set out in chapter 2, the most attractive region of either OH(A) + Rg potential energy surface (PES; Rg = rare gas) is the 'oxygen well,' the near-linear configuration close in where the oxygen atom of OH(A) is pointing at the rare gas atom. It is this feature of the PES that is responsible for a good deal of the RET and inelastic depolarisation, as in refs. 13,16,21–23 and as will be further shown in this chapter. However, chapter 2 also demonstrated that electrostatic coupling between the excited and ground state diabatic OH-Rg potentials[21,28] is greatest in this near-linear HO–Rg configuration, with a conical intersection at linearity in the oxygen well.[28] This means that electronic quenching will compete directly with RET and inelastic depolarisation, since the same features of the PES are partly responsible for both. The competition between these different outcomes is one of the main themes of this chapter.

These experimental results will be compared with calculations using the adiabatic (single-surface) and surface-hopping quasi-classical trajectory (QCT) methods presented in chapters 5 and 6, and also with previous results for other, similar systems. Theoretical

*As in previous chapters, an 'elastic' collision is one in which $j' = j$.

insights will be used in conjunction with experimental data in order to probe the competition between the electronically elastic and inelastic channels open to these systems.

It is important to note that the PESs and couplings will be responsible for the overwhelming majority of differences observed here between the behaviour of the OH(A) + Kr and OH(A) + Xe systems. The reduced masses (OH–Kr: 2.378×10^{-26} kg, OH–Xe: 2.500×10^{-26} kg) are too similar for kinematic effects to have much relevance, as will be shown theoretically in this chapter.

7.1 Electronic quenching

7.1.1 Experimental data

Rate constants for electronic quenching were measured for selected (N, j) states of OH(A) with Kr and Xe at thermal collision energy, and converted to thermal flux average cross-sections, σ_Q, according to equation (4.4). For the OH(A) + Kr system, the quenching cross-sections presented here extend and improve on the set of results reported in ref. 21, and have been published in ref. 28. Chapter 6 has already evaluated different theoretical models in terms of their ability to reproduce these cross-sections, so the comparison of different theories will be dealt with only briefly here. Instead, more focus will be placed on examining the experimental data, comparing Kr to Xe and also to other systems in the literature.

Figure 7.1 compares experimental quenching cross-sections for OH(A) + Kr and Xe, and these cross-sections are also tabulated in table A.1 in appendix A. In both cases, excellent agreement with the data of Hemming *et al.*[27] is observed, and there is seen to be no significant difference in quenching from f_1 ($j = N + S$) and f_2 ($j = N - S$) levels within experimental error.

For both the OH(A) + Kr and OH(A) + Xe systems, quenching cross-sections fall with increasing rotation. As N increases, the angle of approach required for Kr to reach the position of the potential crossing (low on the repulsive wall of the HO–Kr well, or near the

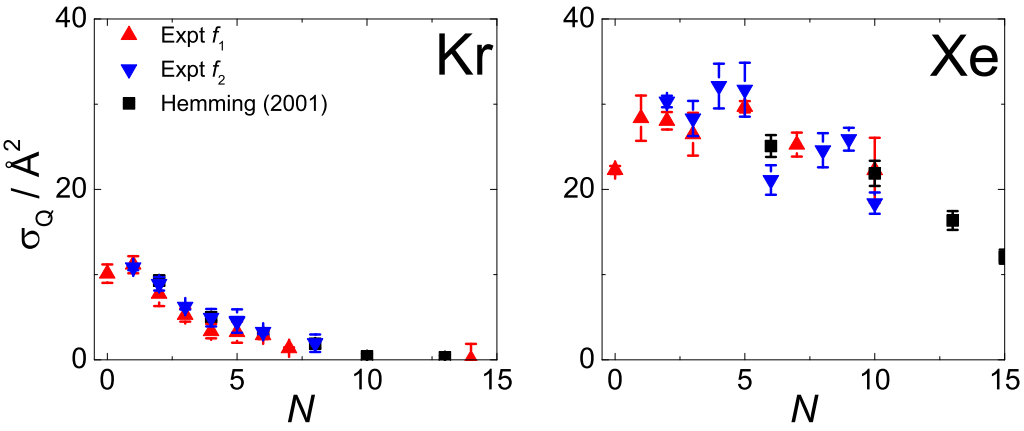

Figure 7.1: Experimental cross-sections for electronic quenching of OH(A) by Kr (left) and Xe (right). Red triangles: f_1 levels, blue triangles: f_2 levels, black squares: Hemming *et al.*[27] The spin-rotation level employed by Hemming *et al.* is not specified in their paper.

bottom of the HO–Xe well) becomes more difficult to reach. Quenching in OH(A) + Kr is highest at $N = 0$, and falls to zero by around $N = 10$. By this point, QCT calculations show that trajectories can no longer sample the correct region of the oxygen well. In contrast, quenching in OH(A) + Xe extends out to the highest N measured, although the same downward trend is seen. The position of the potential crossing is the crucial factor here — classical trajectories are able to access the bottom of the HO–Xe well at all N studied.

The size of the electronic quenching cross-sections is explained by the location of the conical intersection. Quenching is much more extensive with Xe than with Kr because more collisions can sample the relevant features of the PES. Both systems considered here have significant cross-sections for quenching under thermal conditions. This stands in contrast to collisions with lighter rare gases such as Ar and He, where quenching is negligible.[13,27,273,274] Comparing cuts through the diabatic $^2\Sigma^+$ and $^2\Pi$ potentials[236] (figure 7.2), the reason for this is revealed to be that, moving down the noble gas group, the position of the conical intersection in the HO–Rg geometry moves lower in energy. In the case of He or Ar, the crossing is much too high to be accessible at typical thermal collision energies. However, for Kr and Xe, the crossing becomes accessible and quenching

is possible.

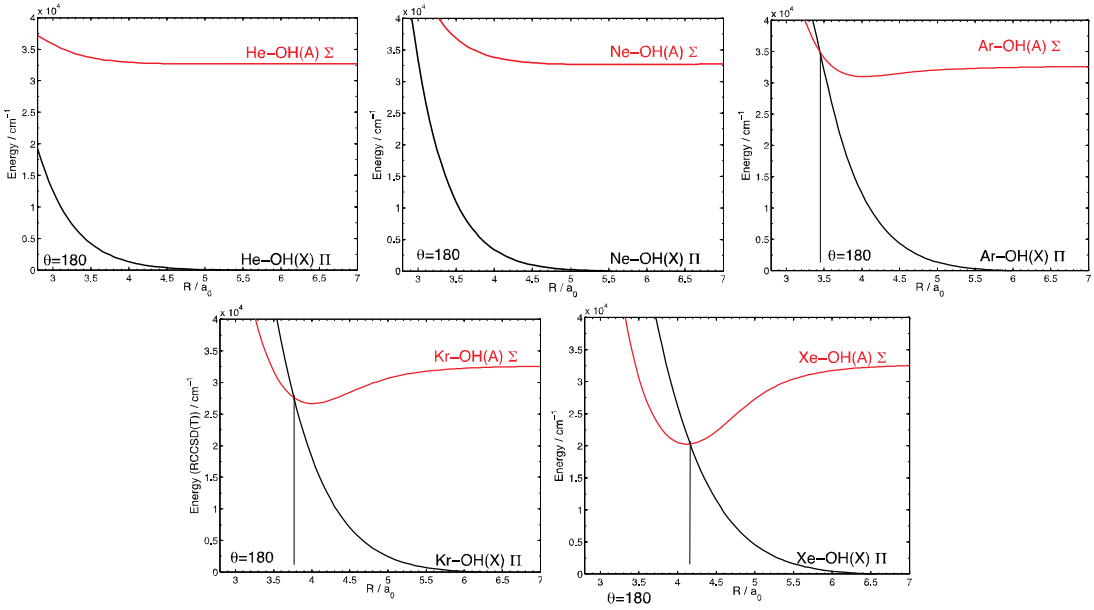

Figure 7.2: Cuts through the diabatic $^2\Sigma^+$ (red) and $^2\Pi$ (black) potentials[236] for OH(X,A) + Rg in the linear HO–Rg geometry. Top row: He, Ne, Ar; bottom row: Kr, Xe. Figure by J. Kłos.[236]

7.1.2 Comparison to theory

In figures 7.3 and 7.4, the experimental quenching cross-sections for OH(A) + Kr, Xe are compared to two state trajectory surface-hopping (TSH) QCT calculations, including only the $2A'$ and $1A'$ adiabatic PESs, and a full three state TSH model including all (non spin-orbit) couplings, as detailed in chapters 5 and 6. The results from the two-state model have been published in ref. 28; the three-state model results are presented here for the first time. A comparison of the various models, including a discussion of quantum mechanical data,[236] has already appeared in chapter 6, so the present discussion will be more general.

The two-state model, neglecting couplings to the $1A''$ PES, is seen to be an inadequate description of both collision systems. For OH(A) + Kr, it recovers around half of the experimental quenching, but captures the correct trend with N, while for OH(A) + Xe, agreement is worse and the cross-sections fall off too quickly. It seems that the inclusion of the third, $1A''$ surface is essential for an appropriate description of the quenching dynamics.

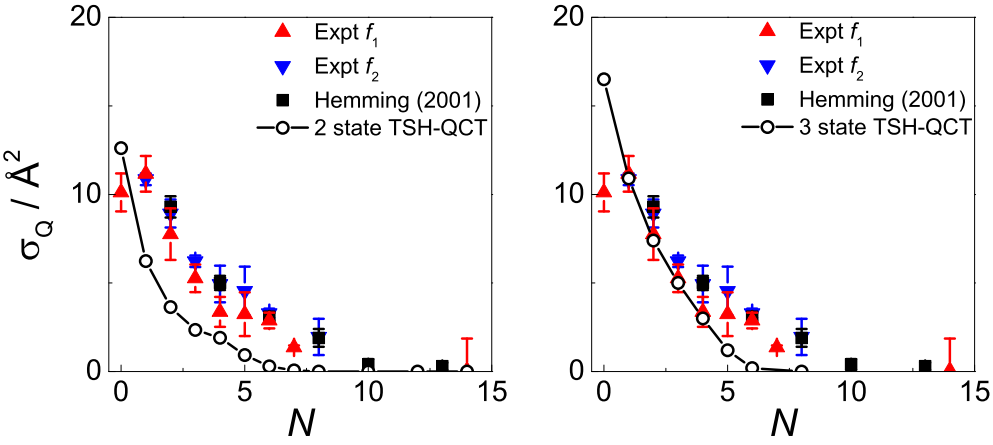

Figure 7.3: Experimental cross-sections for electronic quenching of OH(A) by Kr. Red triangles: f_1 levels, blue triangles: f_2 levels, black squares: Hemming *et al.*[27], open circles: surface-hopping QCT, fixed energy 39 meV (left: 2-state, right: full 3-state). Note that the theory is closed-shell, and that the spin-rotation level employed by Hemming *et al.* is not specified in their paper.

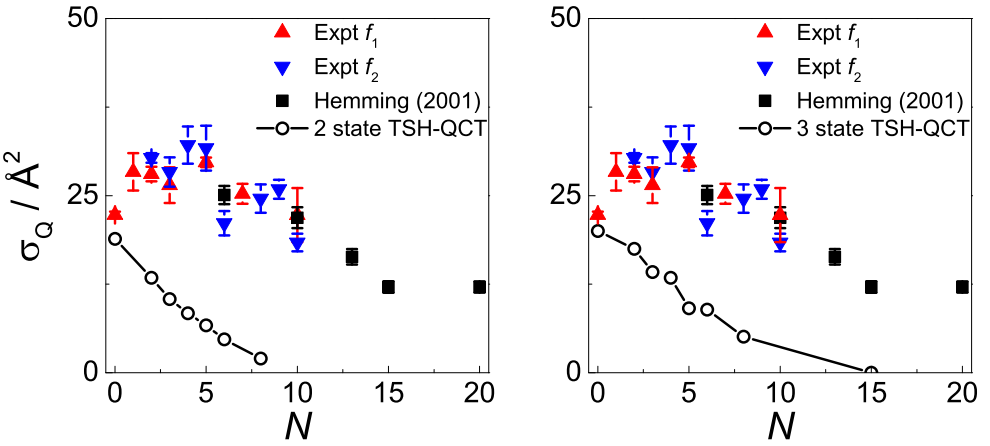

Figure 7.4: Experimental cross-sections for electronic quenching of OH(A) by Xe. Red triangles: f_1 levels, blue triangles: f_2 levels, black squares: Hemming *et al.*[27], open circles: surface-hopping QCT, fixed energy 39 meV (left: 2-state, right: full 3-state). Note that the theory is closed-shell, and that the spin-rotation level employed by Hemming *et al.* is not specified in their paper.

Including roto-electronic couplings in OH(A) + Kr quenching succeeds in reproducing the experimental results reasonably well. The calculated cross-section at $N = 0$ is too large, but after this the trend is a good match for the data. As was shown in chapter 6, about half of the quenched products end up on the $1A''$ PES,[28] so consideration of this surface in the model is important to properly model the results.

The calculations presented here have the OH bond length fixed at its equilibrium bond length. It is not known how the potential energy surfaces (and couplings) would change with r_{OH}, though the evidence in chapter 8 suggests that there is a considerable effect. However, the low degree of vibrational excitation of quenched OH(X) that has been through the conical intersection[28] would indicate that the OH bond is not stretched much by interaction with the oxygen well, so the fixed-bond model here should be appropriate.

The greater extent of quenching in OH(A) + Xe, compared to OH(A) + Kr, comes from the *location* of couplings and these locations' accessibility, not so much the strength of the couplings. In the OH(A) + Xe system, the full three-state TSH model improves upon the two-state model, but agreement with experiment is still not quantitative. One would not expect the extent of roto-electronic coupling in OH(A) + Xe to be significantly greater than in OH(A) + Kr, and this is borne out in the data. Looking at the equations in chapter 6, the main terms that would have a mass dependence are b_r, B_R and K. b_r depends only on the reduced mass of OH, so is the same in both systems. $B_R^{\mathrm{Xe}}/B_R^{\mathrm{Kr}} = \mu_{\mathrm{Kr}}/\mu_{\mathrm{Xe}} \simeq 0.94$, so not much difference is expected here either. As for K, this depends principally on the ratio of ℓ between the two systems, so the difference will go as $\mu_{\mathrm{Xe}}^{0.5}/\mu_{\mathrm{Kr}}^{0.5}$ — not very different. The effect of changing the masses is demonstrated by running calculations on the OH(A) + Kr PESs with the mass of Kr artificially set to that of Xe — in effect, "OH(A) + $^{131.3}$Kr". The value of σ_Q obtained from this mass-adjusted system is within the statistical error of the cross-section calculated with the correct masses.

The disagreement seen between experiment and theory in OH(A) + Xe quenching, compared to the excellent agreement in the case of OH(A) + Kr, is a reminder that calculating *ab initio* potential energy surfaces and diabatic couplings is still a task that

stretches current theory to its limits. The excellent agreement of the experimental data reported here with the earlier results of Hemming and coworkers[27] suggest that the error is in the theory rather than the experiment.

It is also worth noting that spin-orbit coupling is completely neglected in the semi-classical theories used here. The agreement between experiment and theory for OH(A) + Kr suggests its inclusion is not essential in this system. In addition, spin-orbit coupling *is* included in the QM calculations of Kłos *et al.*[236] considered in chapter 6, and these displayed good agreement with the TSH models considered here (for OH(A) + Kr). However, it is possible that such couplings are more important for OH(A) + Xe, and could be a source of the disagreement exhibited here. The spin-orbit coupling constant, ζ, for Xe atoms is almost twice that for Kr, and is on the order of that of lead.[275] Future work should aim to quantify such effects.

More important than this, however, is the approximate nature of the present calculations. The potential energy surfaces and diabatic couplings have been calculated assuming no coupling to the $1A''$ state, and roto-electronic couplings are inserted into the theory later on. This is hampered by the separation between rotational (nuclear) and electronic degrees of freedom required by the TSH method, and reconciling this with the need to include rotational terms in the electronic Hamiltonian used. Further study of these systems would require, ideally, a full quantum mechanical model of all the states and couplings involved. It should be noted, however, that the calculations shown here do a good job for the OH(A) + Kr system, and so their shortcomings are not (primarily) responsible for the discrepancies between experiment and theory for OH(A) + Xe — this disagreement must come from another source, for example the limits of *ab initio* theory.

7.1.3 Continuous collision energy TSH-QCT

The experimental quenching cross-sections presented in this section were obtained from a thermal distribution of molecules at 300 K (see chapter 4). So far, however, these have been compared to calculations performed at a fixed collision energy of 0.039 eV. As set

out in chapter 5, it is possible to carry out TSH-QCT calculations over a range of collision energies, resulting in 300 K thermal (flux averaged) cross-sections.

As lower energy collisions experience more of the attractive part of the intermolecular potential, it is expected that electronic quenching will be more prevalent for these interactions. Conversely, quenching will be less important for high energy collisions, which experience more of the repulsive potential wall. This subsection aims to investigate the differences between calculations carried out at a fixed collision energy and those using a continuous distribution of collision energies, and to see whether the 300 K calculations will better simulate the experimental data.

Figure 7.5 presents such a comparison. For OH(A) + Kr in the left-hand panel, the calculations for a 300 K Boltzmann distribution of collision energies display a small increase in the electronic quenching cross-sections over those performed at a fixed collision energy. The difference is not great, but is more noticeable for higher rotational states, and improves upon the already impressive agreement with experiment displayed by the fixed-energy calculations. Because both sets of calculations (fixed and continuous collision energy) give a fair description of experiment for OH(A) + Kr, and the difference between them is slight, the fixed-energy data will be used in the remainder of this thesis due to the higher number of trajectories it was possible to run.

There is seen to be a much greater difference between the fixed-energy and 300 K theoretical results in the case of OH(A) + Xe than there was for OH(A) + Kr – using the full Maxwell-Boltzmann distribution of collision energies results in significantly greater quenching, and much better agreement with experiment at low N. For high rotational states, however, theoretical quenching drops off too quickly and underestimates the experimental data. These results indicate that lower energy collisions, which experience more of the attractive part of the potential, play an important part in quenching. Because the same trends are evident in both sets of results, and due to the limited number of trajectories it was possible to run using a continuous distribution of collision energies, the rest of this thesis will use fixed-energy data, and so it should be borne in mind that this

underestimates the true extent of non-adiabatic transitions in the OH(A) + Xe system. Future work should certainly focus on further full 300 K simulations of these experiments.

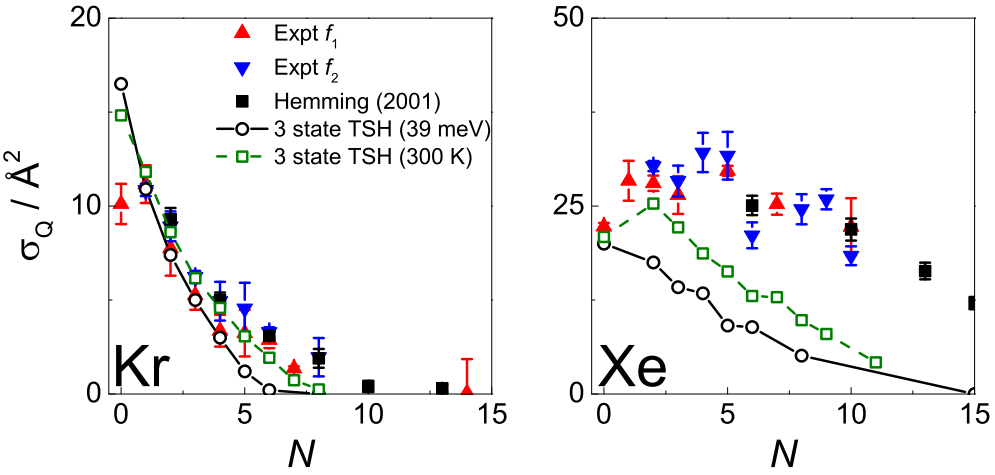

Figure 7.5: Cross-sections for electronic quenching of OH(A) by Kr (left) and Xe (right). Red triangles: f_1 levels, blue triangles: f_2 levels, black squares: Hemming *et al.*[27] The open symbols are three state surface-hopping QCT calculations at a fixed collision energy of 0.039 eV (black circles) and using a 300 K Boltzmann distribution of collision energies (green squares). Note that the theory is closed-shell, that the spin-rotation level employed by Hemming *et al.* is not specified in their paper, and that the two panels of this figure have different scales.

To examine the effects of collision energy on electronic quenching in more depth, figure 7.6 presents excitation functions (collision energy dependent cross-sections) for both electronic quenching and inelastic collisions. Quenching is seen to have an important dependence on the collision energy, with collisions at low energies being much more likely to undergo quenching as they experience more of the relevant, attractive, part of the PES. Inelastic collisions vary less with E_t, though as the variation in cross-section with collision energy can be as great as 10 to 20 Å^2, this is still worth further consideration.

7.2 Rotational energy transfer (RET)

Cross-sections for rotational energy transfer (RET) were measured by resolving emission from a single j state using the monochromator, as described in chapter 4. RET processes include all those for which $N' \neq N$, as well as purely spin-rotation level changing collisions where $N' = N$; $j' \neq j$, and the term 'total RET' here refers to the sum of all these

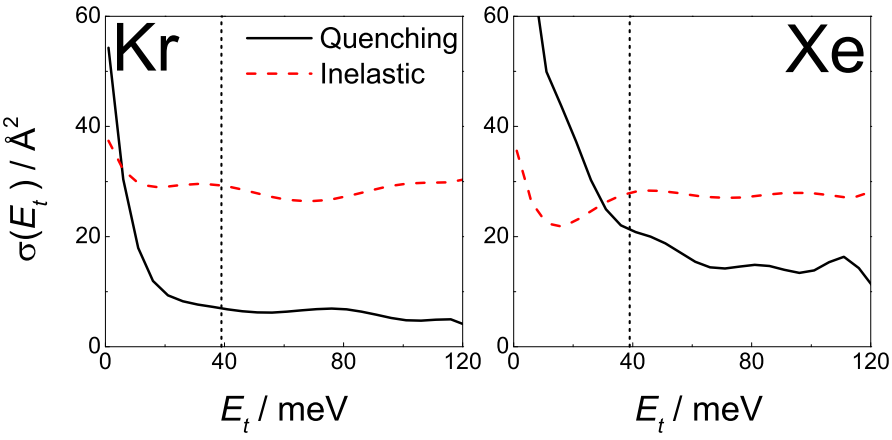

Figure 7.6: Theoretical excitation functions (variation of cross-section with collision energy) for OH(A, $N = 2$) + Kr (left), Xe (right), calculated using 3 state TSH-QCT and expanded in Legendre polynomials. Black solid lines: electronic quenching collisions, red dashed lines: closed-shell inelastic (N-changing) collisions. The vertical dotted lines indicate a collision energy of 0.039 eV, as used in the fixed-energy calculations elsewhere in this chapter.

processes. This total RET is the quantity that is measured experimentally, and will be presented first with a comparison to adiabatic and non-adiabatic theory. The theoretical RET will then be broken down into different contributing collisional processes for a more in-depth analysis.

7.2.1 Total RET versus adiabatic theory

Experimental RET cross-sections for OH(A) + Kr and OH(A) + Xe are presented in figure 7.7, compared to *adiabatic* QCT calculations. Some of the cross-sections for OH(A) + Kr have been published in ref. 21; the present results are an extension of the previous set.

Adiabatic QCT predicts that the RET cross-sections for OH(A) + Xe will be higher than those for OH(A) + Kr. This cannot be a kinematic effect, due to the similar reduced masses of the two systems, so must be down to the potentials. The greater attraction in HO–Rg geometries seen for Xe as opposed to Kr induces more torque on the OH radical, and these attractions also extend to a longer range than for OH(A) + Kr. It is notable that the oxygen well is very deep for HO–Kr, and as such it is surprising that increasing the attraction still further results in more RET, but the range of the interaction plays an

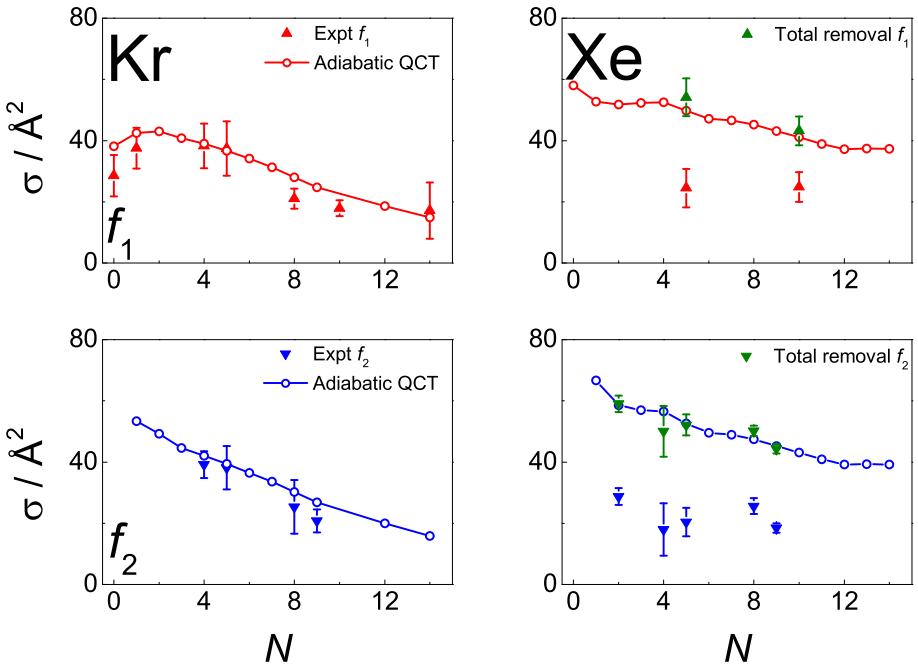

Figure 7.7: Experimental cross-sections for RET in OH(A) + Kr (left) and Xe (right). Red triangles: f_1 levels, blue triangles: f_2 levels, open circles: adiabatic QCT.[21] In the case of Xe, the green triangles are experimental *total removal* cross-sections (quenching plus RET.)

important part as well.

Although adiabatic theory would predict more RET for OH(A) + Xe than for OH(A) + Kr, in reality the cross-sections are found to be much the same in the two systems. The reason for this is quenching, which competes with RET because the same feature of the PES — the deep, attractive oxygen well — is largely responsible for both processes. As quenching is much more extensive in the OH(A) + Xe system (figure 7.1), the adiabatic theory overestimates the RET cross-sections by a larger amount.

The competition between quenching and RET can be seen very clearly in the OH(A) + Xe system by plotting *total removal* cross-sections — the sum of experimental quenching and RET (green triangles in figure 7.7). The excellent agreement between this data and the RET cross-sections predicted by adiabatic QCT shows that the presence of quenching suppresses rotational energy transfer. (For OH(A) + Kr, the magnitude of σ_Q is such that the total removal cross-sections are within the errors of σ_{RET}).

In both collision systems, theory predicts a decrease in σ_{RET} with increasing rotation. This is simply due to the increasing energy separation of rotational levels with N. Because of the longer range of the OH(A) + Xe PES, this decrease is much shallower than for OH(A) + Kr and, indeed, is not observed experimentally — the RET cross-sections are constant across the range of N measured.

To verify that the differences between the experimentally measured and theoretical RET cross-sections are due to quenching and not a failure of the QCT method, the single-surface QCT calculations are compared to full single-surface close-coupled (CC) quantum mechanical (QM) calculations in figure 7.8. The QM calculations for OH(A) + Kr were performed by Kłos,[21,236] and those for OH(A) + Xe were done by McCrudden and Herráez-Aguilar,[235,237] using the HIBRIDON suite of codes.[238] Full details of these QM calculations are contained in the references cited. The excellent agreement shown in figure 7.8 validates the use of the QCT method in this thesis, including the assumption that spin is a spectator in the collision (used to obtain quasi open-shell cross-sections), and supports the conclusion that the disagreement between experiment and (adiabatic) theory is caused by the neglect

of electronic quenching.

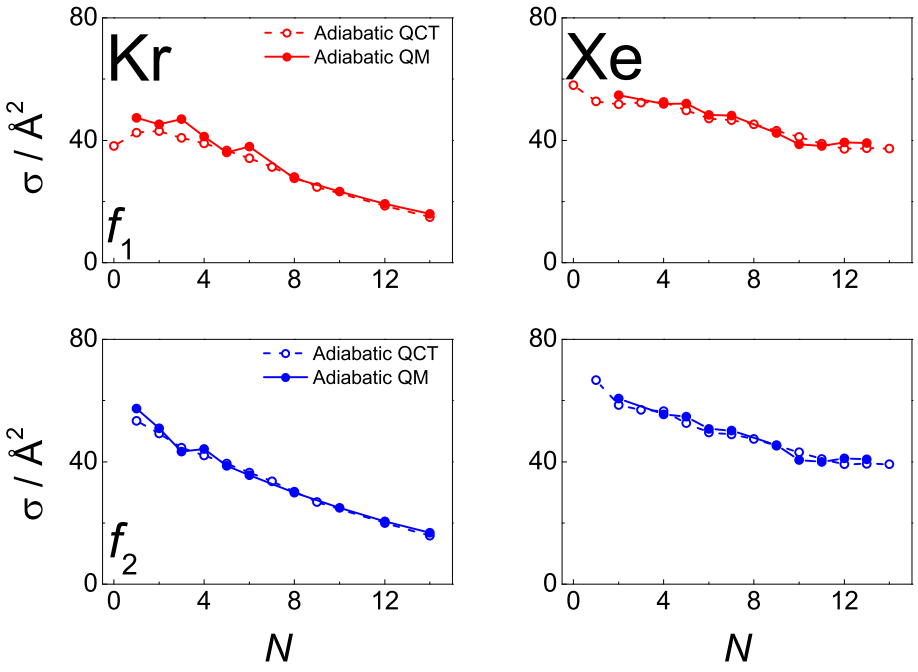

Figure 7.8: Theoretical cross-sections for RET in OH(A) + Kr (left) and Xe (right), for f_1 (top) and f_2 (bottom) spin-rotation levels. Open symbols: adiabatic QCT,[21] filled symbols: adiabatic QM.[21,235–237]

7.2.2 Total RET versus non-adiabatic theory

In this subsection, the three state trajectory surface hopping (TSH) variant of QCT theory presented and developed in chapter 6 is brought into play to try and account for the competition between electronic quenching and rotational energy transfer.

Figure 7.9 compares the experimental RET cross-sections to adiabatic QCT and 3-state surface hopping (TSH) QCT. Note that, for OH(A) + Kr, TSH-QCT calculations have been carried out only up to $N = 8$, as electronic quenching is negligible beyond this point. Because of the inclusion of non-adiabatic effects in the theory, the TSH cross-sections are lower than the adiabatic ones — trajectories that, adiabatically, would have undergone RET are in fact 'lost' to quenching. For OH(A) + Kr, the magnitude of quenching is such that both sets of theoretical data are able to reproduce the experimental results well. In

the case of Xe, the TSH results represent a great improvement over the adiabatic theory, but the failure to capture all of the experimental quenching (see figure 7.4) means that the theoretical cross-sections are not lowered enough to fully account for experiment.

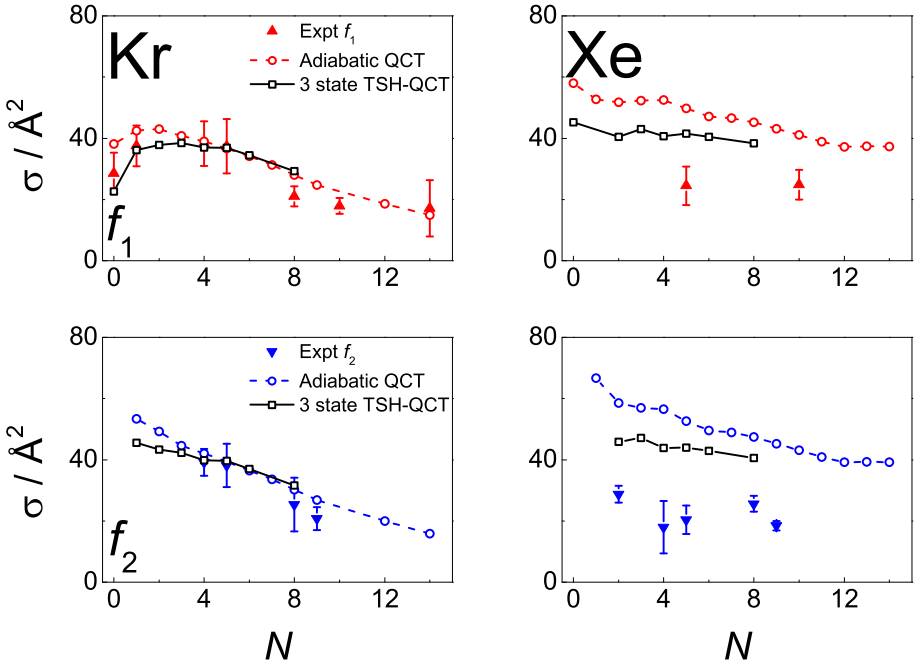

Figure 7.9: Comparison of experimental and theoretical cross-sections for RET in OH(A) + Kr (left) and Xe (right). Red triangles: f_1 levels, blue triangles: f_2 levels, open red and blue circles: adiabatic QCT,[21] open black squares: 3 state TSH-QCT.

The 3-state TSH-QCT calculations are compared to full non-adiabatic quantum scattering calculations by Kłos[236] in figure 7.10, for OH(A) + Kr. The figure shows that the TSH results agree well with full close-coupled (CC) QM calculations, but the coupled-states (CS) QM calculations are significantly different, thus pointing to the need to include all couplings for an accurate description of the system. Such CC-QM calculations are very expensive and can take several weeks to complete on modern computer clusters,[236] showing the benefit of a semiclassical approach.

Theory can be used to further investigate the competition between quenching and RET channels in collisions. Closed-shell opacity functions for inelastic collisions (in this case, $N' \neq N$) and surface-hopping collisions are displayed in figure 7.11, demonstrating the

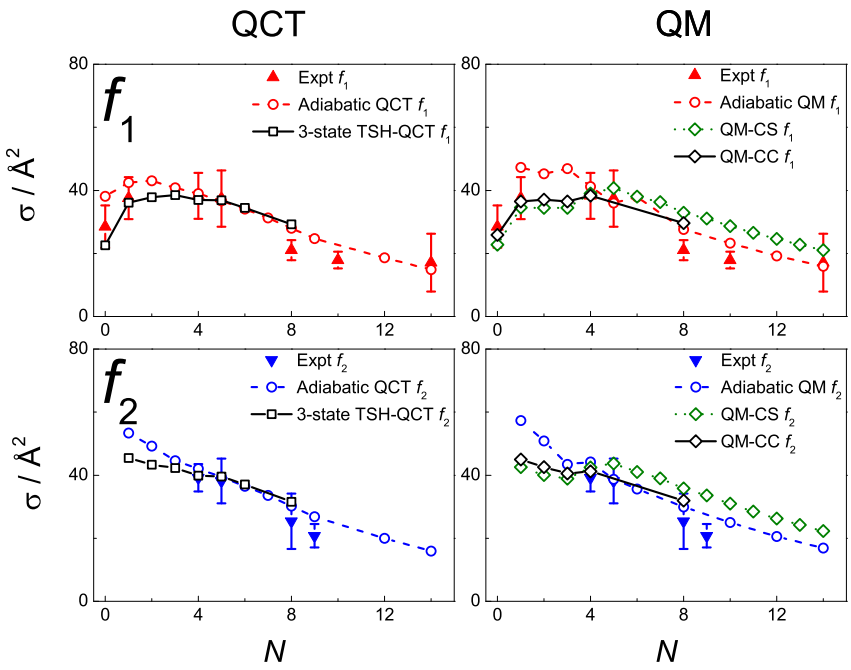

Figure 7.10: Comparison of RET cross-sections for OH(A) + Kr. Red triangles: experimental f_1 levels, blue triangles: experimental f_2 levels, open red and blue circles: adiabatic QCT (left)[21], QM (right)[21]. Open black squares (left): 3 state TSH-QCT, open diamonds (right): non-adiabatic QM[236], with green being CS and black being CC.

similar range of the two processes. This is further evidence that both RET and quenching occur in the deep, oxygen well, and that this is responsible for the competition between them.

7.2.3 Resolved RET

The experimentally determined RET cross-sections are a sum over all the individual state-to-state cross-sections, except the purely elastic cross-section with $j' = j$:

$$\sigma_j = \sum_{j' \neq j} \sigma_{jj'} \tag{7.1}$$

State-to-state resolution of the theoretical RET cross-sections can therefore help to show exactly which electronically adiabatic collisional outcomes compete with electronic quenching – high or low Δj.

Figure 7.12 shows *closed-shell* state-to-state RET cross-sections, $\sigma_{NN'}$, for initial levels

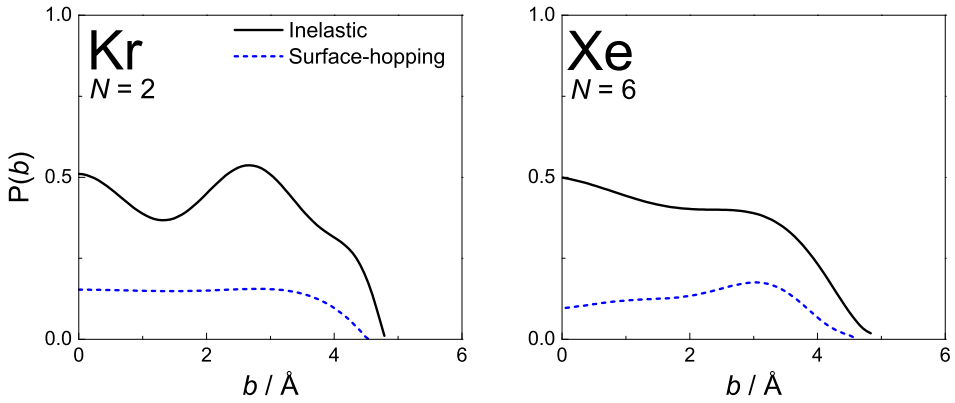

Figure 7.11: *Closed-shell* theoretical opacity functions for OH(A) + Kr ($N = 2$, left) and Xe ($N = 6$, right), using 3 state TSH-QCT. Solid black line: inelastic collisions ($N' \neq N$), dotted blue line: surface-hopping collisions.

$N = 2$ in OH(A) + Kr and $N = 6$ in OH(A) + Xe. These levels were chosen so that quenching would be significant at the values of N studied. Contrasting adiabatic QCT and the three state TSH-QCT model, it can again be seen that the presence of quenching results in lower cross-sections for RET. However, it would appear that quenching competes mainly with collisions that would result in a *lower* change in N — the cross-sections for higher ΔN collisions are more similar between the two models. Of course, the higher ΔN collisions are less likely anyway, but comparing the percentage difference reveals a similar story.[†]

In addition, another instructive way of separating the RET cross-section into different components is to consider the open-shell character of OH(A). Collisions are broken down into three classes depending on the conservation or otherwise of the spin-rotation (SR, f_1 or f_2) level of OH(A), with RET being the sum of:

SR conserving: The relative orientation of $\boldsymbol{N}$ and $\boldsymbol{S}$ is conserved; $\Delta j = \Delta N \neq 0$

Inelastic SR changing: Collisions which are inelastic in rotational level N and also change the relative orientation of $\boldsymbol{N}$ and $\boldsymbol{S}$; $\Delta j = \Delta N \pm 1$

Pure SR changing (PSRC): Collisions which are elastic in N but change the relative

[†]It should be noted that state-to-state QCT cross-sections for $\Delta N = \pm 1$ are known to differ (very) slightly from the corresponding QM values, due to the binning procedure used, so this should be borne in mind in the above discussion.

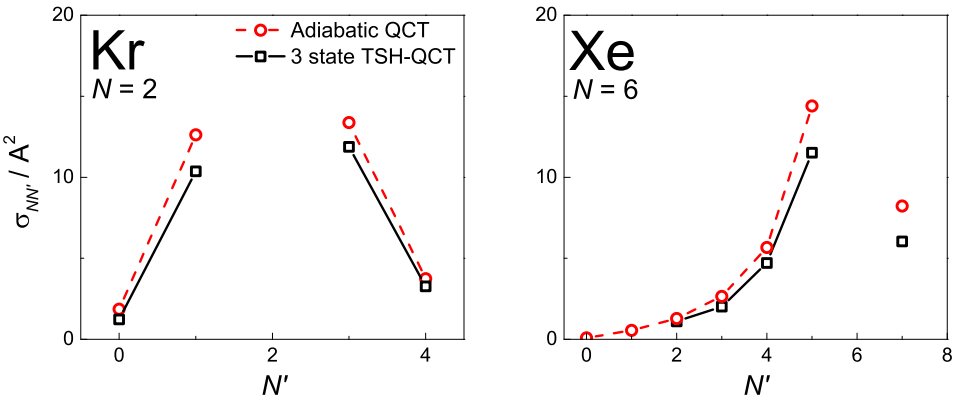

Figure 7.12: Comparison of *closed-shell* theoretical state-to-state RET cross-sections for OH(A) + Kr ($N = 2$, left) and Xe ($N = 6$, right). Red open circles: adiabatic QCT,[21] black open squares: 3 state TSH-QCT.

orientation of $\boldsymbol{N}$ and $\boldsymbol{S}$; $\Delta N = 0$; $\Delta j = \pm 1$

Note that purely elastic ($\Delta j = \Delta N = 0$) collisions are not included, as these cannot be converged using the QCT method. (See chapter 3).

The separation of total RET into these three classes is shown in figures 7.13 and 7.14 for OH(A) + Kr and Xe respectively. These clearly show that the major factor resulting in the total RET cross-sections being reduced in the non-adiabatic calculations is the decrease in N-changing collisions, with pure SR changing collisions (PSRCs) seeming to be affected less by the inclusion of quenching. The trends in N-changing collisions, which fall with increasing N, are very different to those seen for the PSRCs, which are almost constant with N. This means that these collisions will be of increasing importance in the OH(A) + Rg systems as the rotational level increases. (Note that the state $N = 0$ has only one spin-rotation level ($j = 0.5$) and, as such, cannot undergo a purely SR changing collision).

There is seen to be good agreement between the QCT and QM resolved RET cross-sections in figures 7.13 and 7.14, except at low N. As reported previously,[21] this is a consequence of the histogram binning procedure used in the QCT calculations. Nevertheless, the ability of quasi open-shell QCT to produce results close to those from full quantum mechanics is very encouraging.

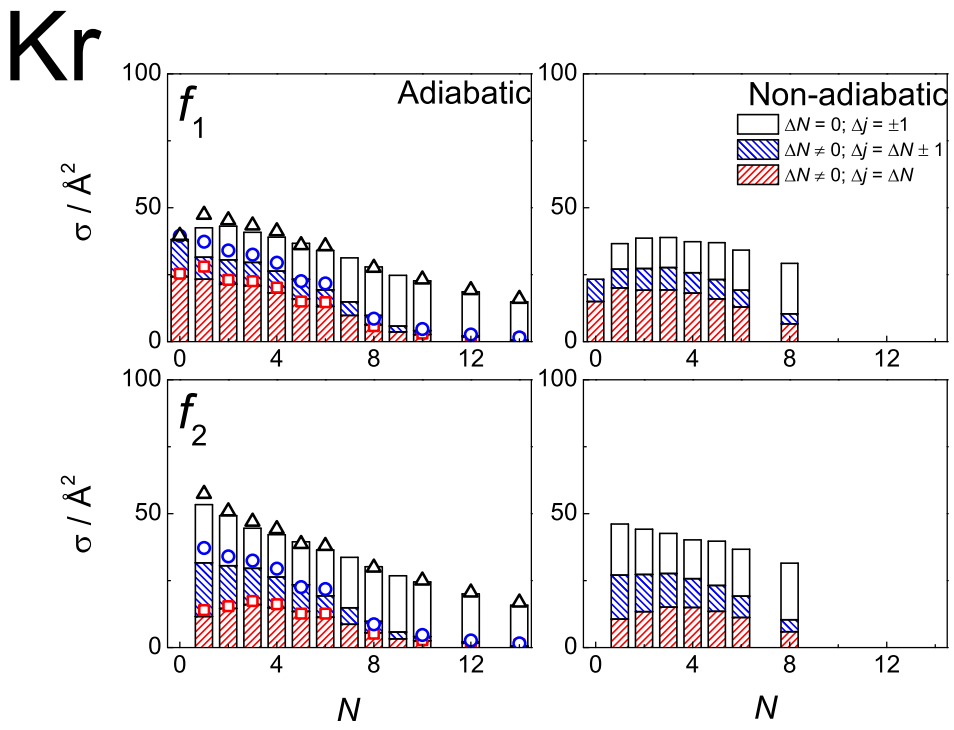

Figure 7.13: Comparison of theoretical RET cross-sections from initial f_1 (top) and f_2 (bottom) spin-rotation levels of OH(A) + Kr, at a fixed collision energy of 0.039 eV. The bars are adiabatic QCT (left) or 3 state TSH-QCT (right) calculations, and the points are single-surface CC QM calculations.[21,258] Total RET is represented by the total height of the bar (QCT), or the triangles (QM). This is made up of *SR conserving* collisions ($\Delta j = \Delta N \neq 0$, red bars, red squares), *inelastic SR changing* collisions ($\Delta N \neq 0$; $\Delta j = \Delta N \pm 1$, blue bars, difference between blue circles and red squares) and *pure SR changing* collisions ($\Delta N = 0$; $\Delta j = \pm 1$, white bars, difference between open triangles and blue circles).

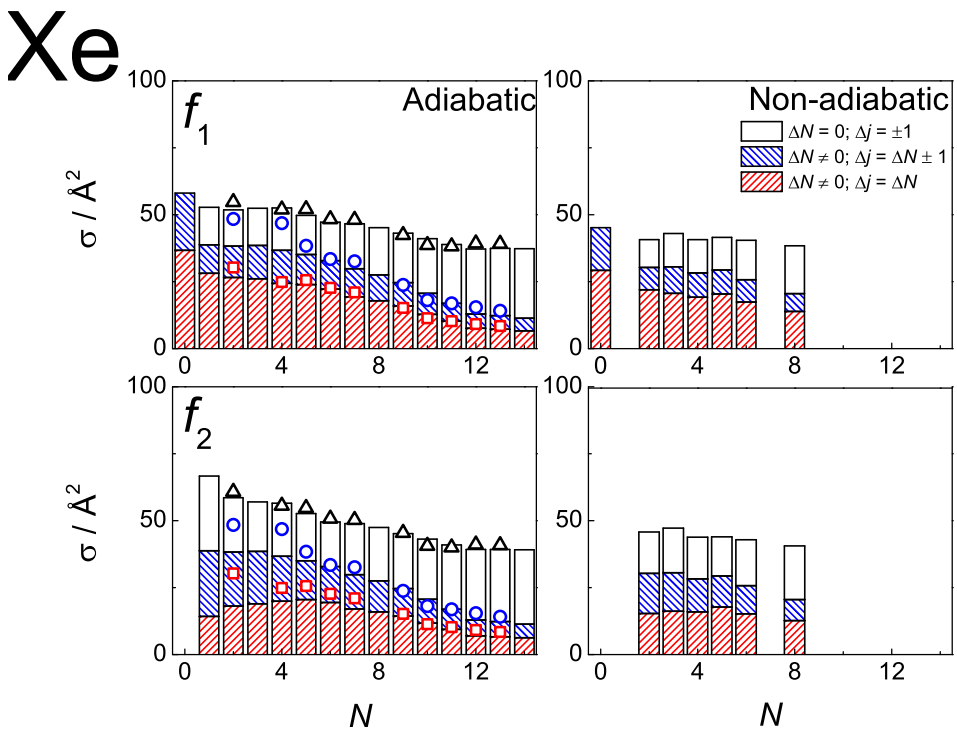

Figure 7.14: Comparison of theoretical RET cross-sections from initial f_1 (top) and f_2 (bottom) spin-rotation levels of OH(A) + Xe, at a fixed collision energy of 0.039 eV. The bars are adiabatic QCT (left) or 3 state TSH-QCT (right) calculations, and the points are single-surface CC QM calculations.[235] Total RET is represented by the total height of the bar (QCT), or the triangles (QM). This is made up of *SR conserving* collisions ($\Delta j = \Delta N \neq 0$, red bars, red squares), *inelastic SR changing* collisions ($\Delta N \neq 0$; $\Delta j = \Delta N \pm 1$, blue bars, difference between blue circles and red squares) and *pure SR changing* collisions ($\Delta N = 0$; $\Delta j = \pm 1$, white bars, difference between open triangles and blue circles).

Opacity functions

For a more detailed picture of exactly which kinds of electronically elastic collisions compete with quenching, figures 7.15 and 7.16 present (quasi) *open-shell* opacity functions (see chapter 5), calculated using adiabatic QCT and three state surface-hopping QCT. It was shown in ref. 21 that the adiabatic QCT opacity functions for OH(A) + Kr display excellent agreement with adiabatic quantum mechanical opacity functions, with the only difference being the absence of quantum oscillations in the QCT functions.

Comparing the opacity functions for $N = 2$ and $N = 8$, rotationally inelastic collisions — whether conserving or changing the spin-rotation level — are less likely to take place at higher N, and occur at lower impact parameters. This is simply due to the greater energy level spacing at higher N making RET a more difficult process, as more energy must be transferred in the collision. The range of impact parameters that can lead to inelastic collisions is greater for OH(A) + Xe than for OH(A) + Kr, reflecting the differences in the two potential energy surfaces.

The rotationally elastic, 'pure' SR-level changing collisions (PSRCs), in the right-hand columns of figures 7.15 and 7.16 mostly take place at high impact parameters, as lower-b collisions tend to lead to a change in N. They show the influence of *long-range* attractive collisions, which can be seen to compete less with quenching — at low impact parameters, the non-adiabatic $P(b)$ is lower than the adiabatic one, but at the high-b peak there is no loss of trajectories to quenching. Rotationally inelastic collisions are seen to have more of a difference between the adiabatic and non-adiabatic opacity functions, because of the competing pathways present in the shorter-range attractive region.

As spin is taken to be a spectator in the collision,[12] changing the spin-rotation level requires significant reorientation of N, so PSRCs are likely to lead to a high degree of elastic depolarisation. The range of impact parameters leading to PSRCs does not fall with N as much as for rotationally inelastic collisions (especially for OH(A) + Xe), showing the importance of these long-range attractive collisions in the systems considered here over the full range of N.

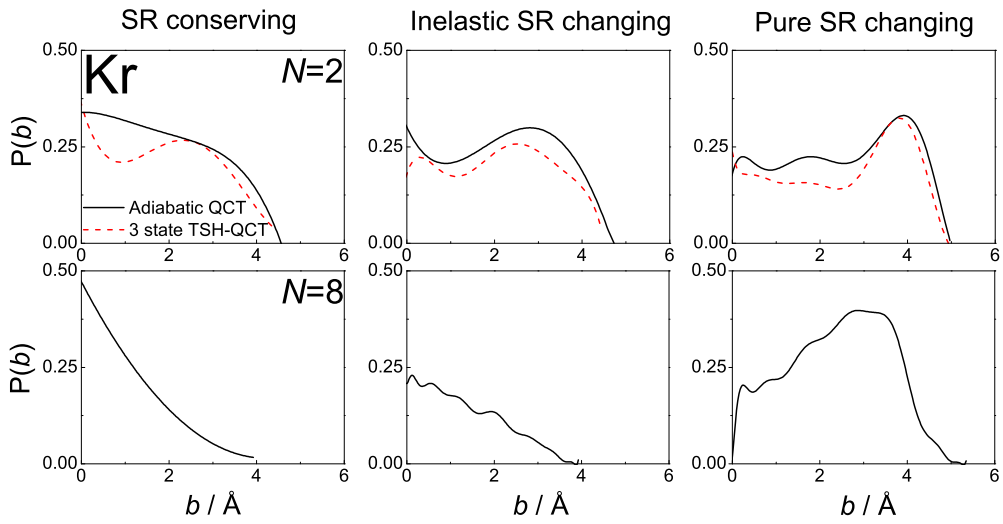

Figure 7.15: Quasi open-shell opacity functions, using adiabatic QCT (black solid lines) and 3 state surface hopping QCT (red dashed lines), for transitions from $N = 2$, $j = 1.5$ (top) and $N = 8$, $j = 7.5$ (bottom) in OH(A) + Kr, at a fixed collision energy of 0.039 eV. Left: spin-rotation level conserving collisions ($\Delta j = \Delta N$), middle: inelastic spin-rotation level changing ($\Delta j = \Delta N + 1$), right: 'pure' spin-rotation level changing (PSRC; $\Delta N = 0$, $\Delta j = 1$). Note that no quenching takes place in the $N = 8$ calculations, so only adiabatic QCT is shown in this row.

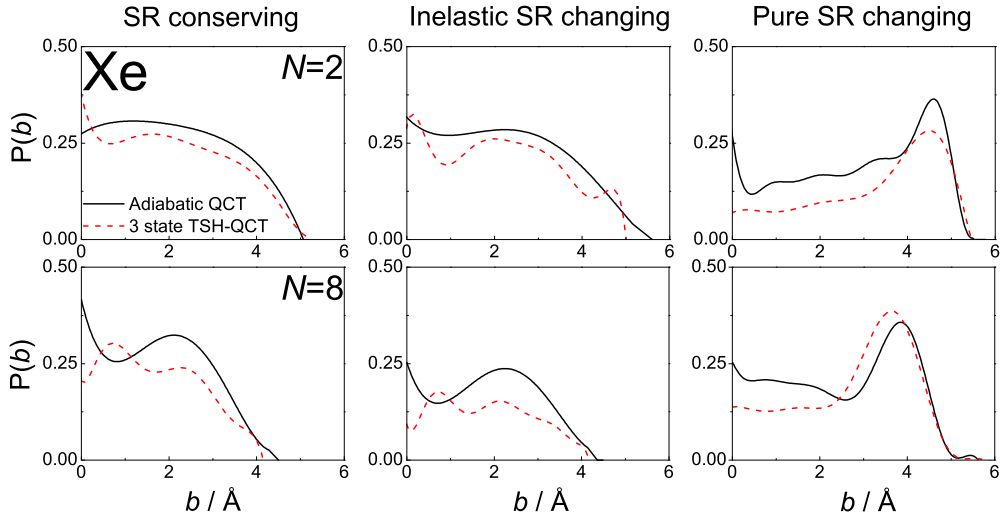

Figure 7.16: Quasi open-shell opacity functions, using adiabatic QCT (black solid lines) and 3 state surface hopping QCT (red dashed lines), for transitions from $N = 2$, $j = 1.5$ (top) and $N = 8$, $j = 7.5$ (bottom) in OH(A) + Xe, at a fixed collision energy of 0.039 eV. Left: spin-rotation level conserving collisions ($\Delta j = \Delta N$), middle: inelastic spin-rotation level changing ($\Delta j = \Delta N + 1$), right: 'pure' spin-rotation level changing (PSRC; $\Delta N = 0$, $\Delta j = 1$).

7.3 Total depolarisation

This section explores the experimentally measured *total* collisional depolarisation (see chapter 4) – the sum of the depolarisation over all final states, j'.

$$\sigma^{(k)} = \sum_{j'} \sigma^{(k)}_{jj'} \tag{7.2}$$

k is 1 or 2 for disorientation and disalignment respectively.

These cross-sections are obtained from the unresolved OH(A) fluorescence. Later on in this chapter, the total depolarisation will be resolved into elastic (j-conserving) and inelastic components, and broken down still further theoretically, for greater insight into the collision dynamics.

7.3.1 Total depolarisation versus theory

Experimental cross-sections for total depolarisation — that is, the sum of elastic ($j' = j$) and inelastic depolarisation — of OH(A) + Kr and Xe are presented in figure 7.17, in comparison with adiabatic QCT theory[22,237] and three-state non-adiabatic TSH-QCT calculations. Note that there is no f_2 spin-rotation level for $N = 0$, and that it is not possible to align levels with $j = 0.5$.

The results show a significant difference in depolarisation between f_1 and f_2 spin-rotation levels. For a given j, N is larger for the f_2 level, so a given change in the direction of $\boldsymbol{N}$ causes more depolarisation for f_2 than for f_1. This is more the case at low N, where S forms a greater proportion of j, and so the f_1 and f_2 cross-sections get closer together for higher rotational levels.

The overall trend in total disorientation and disalignment, for both systems, is a *rise* in depolarisation cross-sections with increasing rotation. For OH(A) + Kr, this flattens off and turns into a fall at higher N; for OH(A) + Xe, the measurements do not extend to a high enough N to reach this regime. Certainly though, this trend is very different to that seen with the lighter noble gases (He, Ar),[12,13,16,17,20] where $\sigma^{(k)}_d$ is seen to fall

with N. This fall can be readily explained by increasing rotation partially averaging out the anisotropy in the PES (more so for the weakly attractive OH(A) + He PES), and the tendency of collisions to be less depolarising at higher N. To change the direction of $\boldsymbol{N}$ through a given angle, a greater transfer of momentum is required in the collision for higher N.

Single-surface QCT calculations fail to capture the unusual trend in cross-sections with N in both systems, and do not do a good job of modelling the magnitudes of the cross-sections. Most strikingly, adiabatic theory predicts that the depolarisation cross-sections for OH(A) + Xe will be larger than those for OH(A) + Kr, due to the greater anisotropy of the PES, while in reality the opposite is the case. The disagreement with experiment is most evident at lower N, especially for OH(A) + Xe, and, for OH(A) + Kr, there is more of a discrepancy in the f_2 results than the f_1 data. This lack of concordance between QCT and experiment is not due to dephasing contributing to the experimental results — figure 7.18 shows that experimental simulations agree well with the QCT data. Neither is the reason to do with a breakdown of the QCT method, as adiabatic quantum scattering calculations[235,236] display excellent agreement with QCT, as shown in the top row of figure 7.18.

Instead, competition between (inelastic) collisional depolarisation and electronic quenching is to blame. Including non-adiabatic effects in the calculations, using the three-state TSH-QCT model, results in better agreement with experiment, particularly in the case of OH(A) + Xe. At lower N, where quenching is most significant, collisions that experience the most attractive parts of the PES (and would therefore be expected to result in significant depolarisation) often end up with OH in its ground electronic state, meaning that adiabatic calculations over-predict the true extent of depolarisation. The greater suppression of depolarisation at low N manifests itself as an initial rise in $\sigma_d^{(k)}$ with N, as observed experimentally.

Despite the better accord between experiment and trajectory surface-hopping QCT, agreement is still not perfect. For OH(A) + Xe, this can be attributed to the failure of

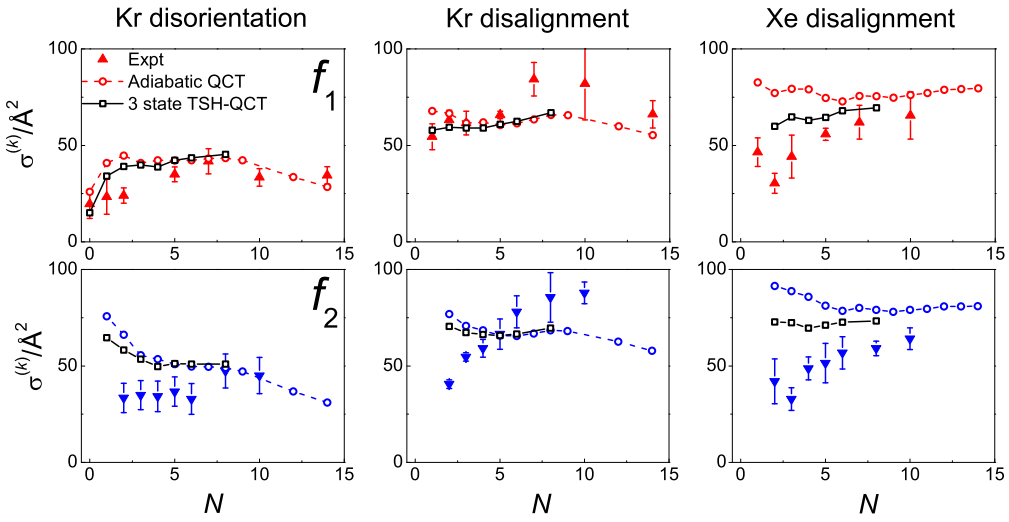

Figure 7.17: Experimental and theoretical cross-sections for *total* (inelastic + elastic) depolarisation of OH(A) in collisions with Kr and Xe. Left: OH(A) + Kr disorientation ($\sigma_d^{(1)}$), centre: OH(A) + Kr disalignment ($\sigma_d^{(2)}$), right: OH(A) + Xe disalignment ($\sigma_d^{(2)}$); top row: f_1 initial levels ($j = N+S$), bottom row: f_2 initial levels ($j = N-S$). Red and blue triangles are experimental data, open circles are adiabatic QCT,[22,237] open squares are 3 state TSH-QCT.

theory to fully capture the full extent of experimental quenching (figure 7.4). If the calculations could recover all of the quenching, it seems likely from figure 7.17 that experimental disalignment would be well modelled too.

However, for the OH(A) + Kr collision system, theory can already explain the observed electronic quenching (figure 7.3). Disagreement with experimental depolarisation cross-sections must be simply because the calculation of *vector* quantities, like the $\boldsymbol{j} - \boldsymbol{j'}$ correlation considered here, requires an extra level of accuracy in the potentials and couplings over and above that necessary for scalar quenching and RET cross-sections. As remarked on in chapter 6, the present TSH-QCT theory agrees well with non-adiabatic quantum mechanical models, so refinement of the theory must come from a full treatment of all three states and couplings, including cross-couplings.

7.3.2 Opacity functions

For a deeper consideration of the processes involved in collisional depolarisation, and the extent of competition with electronic quenching, closed-shell opacity functions (calculated

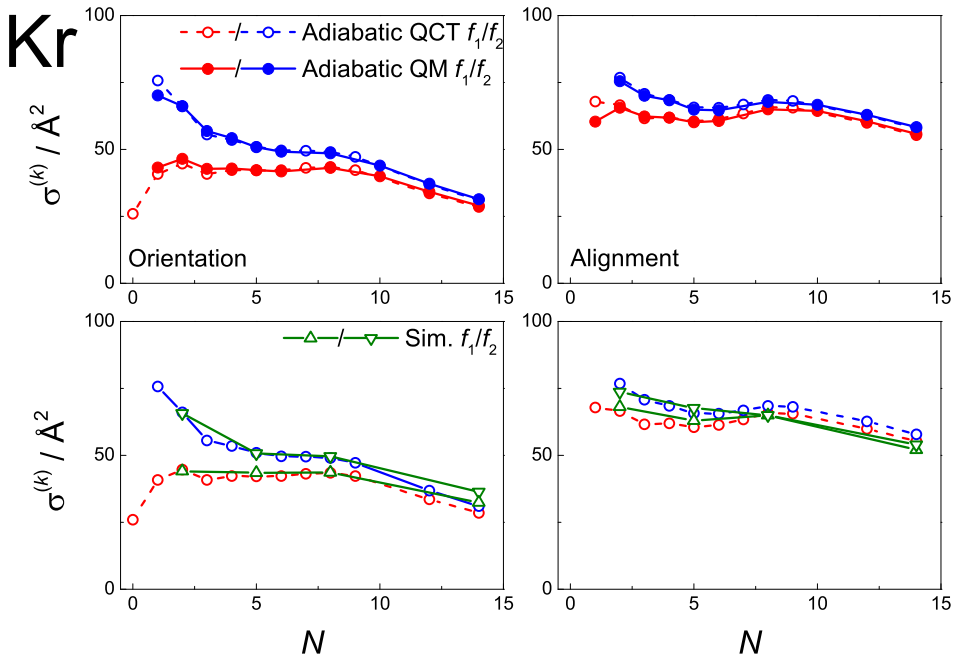

Figure 7.18: Theoretical cross-sections for *total* (inelastic + elastic) depolarisation of OH(A) in collisions with Kr. Left: disorientation ($\sigma_d^{(1)}$), right: disalignment ($\sigma_d^{(2)}$). Top row: Comparison between adiabatic QCT[22] (open circles) and adiabatic QM[235,237] (filled circles); bottom row: comparison between adiabatic QCT (open circles) and experimental simulations (open triangles). Red and blue symbols represent f_1 and f_2 spin-rotation levels respectively.

with the three state TSH-QCT theory) for OH(A) + Kr and OH(A) + Xe are presented in figure 7.19. These functions represent the probability, as a function of impact parameter, b, of an inelastic collision ('inelastic' in the closed-shell case meaning $N' \neq N$), inelastic depolarisation, and electronic quenching (represented here by surface hopping). The opacity function for inelastic disalignment, $P^{(2)}(b)$, is given by (see chapter 5)

$$P^{(2)}(b) = P(b)(1 - a^{(2)}(b)) \tag{7.3}$$

and the opacity functions are expanded in Legendre polynomials as described in chapter 5. Note that the comparison here is to depolarisation in inelastic collisions, rather than all collisions, as this makes a better comparison to the other quantities presented.

It is very noticeable from figure 7.19 that the probability of inelastic disalignment is almost the same as the probability of an inelastic collision, across all N for both systems. This indicates that a single (inelastic) collision is enough to completely depolarise the OH(A) radical, even out to high N. Similar behaviour was observed for OH(A) + Ar at *low* N,[20] but the 'following' collisions responsible (those in which the H of OH(A) is pulled around by the passing Rg atom, leading to very efficient scrambling of polarisation) occurred only for low rotational states. In the systems considered here, the potentials are so anisotropic that these highly depolarising collisions are possible not only over a wide range of rotational states, but across the full range of impact parameters for all levels studied. This is hardly surprising, considering the magnitude of the attractive forces at play in these systems (chapter 2).

The range of impact parameters at which collisions can change the rotational state of OH(A), and cause inelastic depolarisation, is greater for OH(A) + Xe than for OH(A) + Kr due to the longer range of the potential. The greater anisotropy of the OH(A) + Xe PES is also evident in that this range of b does not fall significantly with increasing N, in contrast with OH(A) + Kr — with Kr, most collisions are elastic (in N) by $N = 14$, which is certainly not the case with Xe. This explains why, for OH(A) + Kr, $\sigma_d^{(k)}$ begins

to fall at high N, which is not observed for OH(A) + Xe.

Comparing the opacity functions for rotationally inelastic collisions and surface-hopping, the ranges of these processes are quite similar. Some RET will occur in both the HO–Rg and OH–Rg wells, but, for that subset of RET occuring in or near the oxygen well, competition with electronic quenching will be noticeable over most of the range in b where inelastic collisions occur. The opacity functions for surface-hopping do not show a decline with N, instead remaining relatively constant until they suddenly drop off at a value of b where collisions can no longer reach the relevant region of the PES.

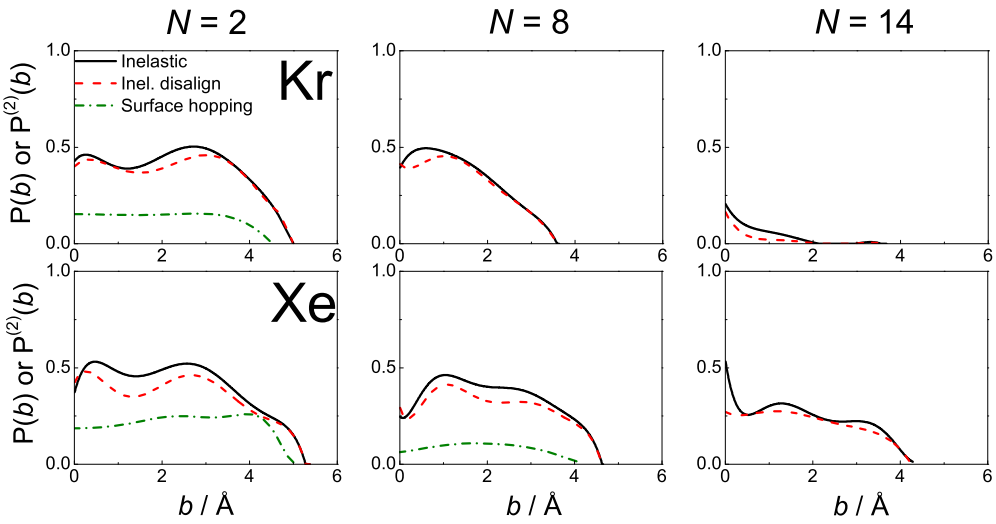

Figure 7.19: 3 state TSH-QCT *closed-shell* opacity functions for inelastic collisions (black solid lines), inelastic disalignment ($P^{(2)}(b)$, $N' \neq N$; red dashed lines) and surface hopping (green dash-dotted lines) of OH(A) in collisions with Kr (top row) and Xe (bottom row). Left, middle and right columns for initial N = 2,8,14 respectively.

7.4 Resolved depolarisation

By using a monochromator to spectrally resolve the OH(A) fluorescence, cross-sections for collisional depolarisation in *elastic* (that is, $j' = j$) collisions may be recorded (see chapter 4). Subtracting these elastic $\sigma_{\mathrm{el}}^{(k)}$ from the total depolarisation cross-sections yields cross-sections for *inelastic* depolarisation ($j' \neq j$). Breaking down the total depolarisation cross-section into elastic and inelastic components in this manner offers an extra level

of insight into the collision dynamics, and enables us to gauge the different effects of quenching on both kinds of collision.

In this section, experimental elastic and inelastic depolarisation cross-sections will be presented and compared to theoretical calculations. This will be supplemented by further theoretical data, such as opacity functions. Then, the collisional depolarisation will be resolved still further, using the categories from section 7.2.3. These were *SR conserving* collisions ($f_1 \rightarrow f_1$ or $f_2 \rightarrow f_2$, with a change in N), *inelastic SR changing* collisions ($\Delta N \neq 0$, $f_1 \leftrightarrow f_2$), *pure SR changing* collisions ($\Delta N = 0$, $f_1 \leftrightarrow f_2$) and purely *elastic* collisions ($\Delta N = \Delta j = 0$).

7.4.1 Elastic and inelastic depolarisation

Experimental elastic depolarisation cross-sections for OH(A) + Kr and OH(A) + Xe are presented in figure 7.20, compared to the results of adiabatic QCT calculations[22,237] and 3 state TSH-QCT calculations. The first point to note is that the cross-sections — both experimental and theoretical — are more-or-less constant with N. In fact, a small rise is noticeable at low rotational states, before the trend levels out. This kind of trend with N is also seen for OH(A) + Ar,[16] and can be attributed to the the character of the potential energy surfaces involved. The OH(A)+ Kr and OH(A) + Xe PESs are both very anisotropic, with deep attractive wells, and extend out to long range. Rotation of the OH radical will not average out these interactions, as can be the case in less attractive systems such as OH(A) + He (where the elastic depolarisation cross-sections *do* fall with N).[16] 'Following' collisions, where the passing Rg atom pulls the H atom of OH around, are common and lead to extensive depolarisation.

The slight rise in $\sigma_{\mathrm{el}}^{(k)}$ for low rotational states can be attributed to the fact that collisions are more likely to be inelastic at low N, as seen in section 7.2. As N increases, collisions changing N and/or j become more restricted to the HO–Rg well and compete less with elastic depolarisation, which can occur in other regions of the potential.

Subtracting the elastic depolarisation cross-sections from those for total depolarisation

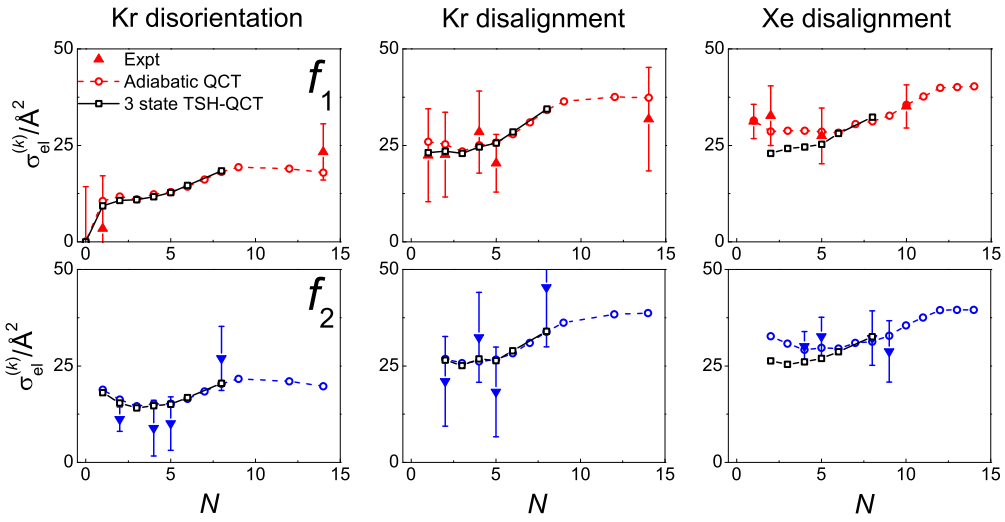

Figure 7.20: Experimental and theoretical cross-sections for *elastic* ($j' = j$) depolarisation of OH(A) in collisions with Kr and Xe. Left: OH(A) + Kr disorientation ($\sigma_{\mathrm{el}}^{(1)}$), centre: OH(A) + Kr disalignment ($\sigma_{\mathrm{el}}^{(2)}$), right: OH(A) + Xe disalignment ($\sigma_{\mathrm{el}}^{(2)}$); top row: f_1 initial levels ($j = N + S$), bottom row: f_2 initial levels ($j = N - S$). Red and blue triangles are experimental data, open circles are adiabatic QCT,[22,237] open squares are 3 state TSH-QCT.

gives cross-sections for *inelastic* ($j' \neq j$) depolarisation, which are presented in figure 7.21. It can be seen that this is where the main competition with quenching lies — this is more visible for OH(A) + Xe, due to the greater extent of quenching. The experimental error in these inelastic results, being propagated from the combined error in $\sigma_d^{(k)}$ and $\sigma_{\mathrm{el}}^{(k)}$, is larger than for the other results, making a comparison with theory slightly more difficult. Nevertheless, it does seem that three state TSH-QCT is an improvement on the adiabatic QCT, and f_2 results display worse agreement with theory.

In contrast to inelastic processes, elastic depolarisation does not appear to compete with quenching. The experimental cross-sections are well modelled by adiabatic QCT, with the TSH-QCT results being very close to the adiabatic ones (more so for Kr than Xe). The reason for this difference is explored further in the next subsection.

7.4.2 Elastic versus inelastic depolarisation: opacity functions

Figure 7.22 compares closed-shell opacity functions for inelastic collisions (in the case of this figure, $N' \neq N$), elastic *depolarising* collisions (again, in the closed-shell case $N' = N$)

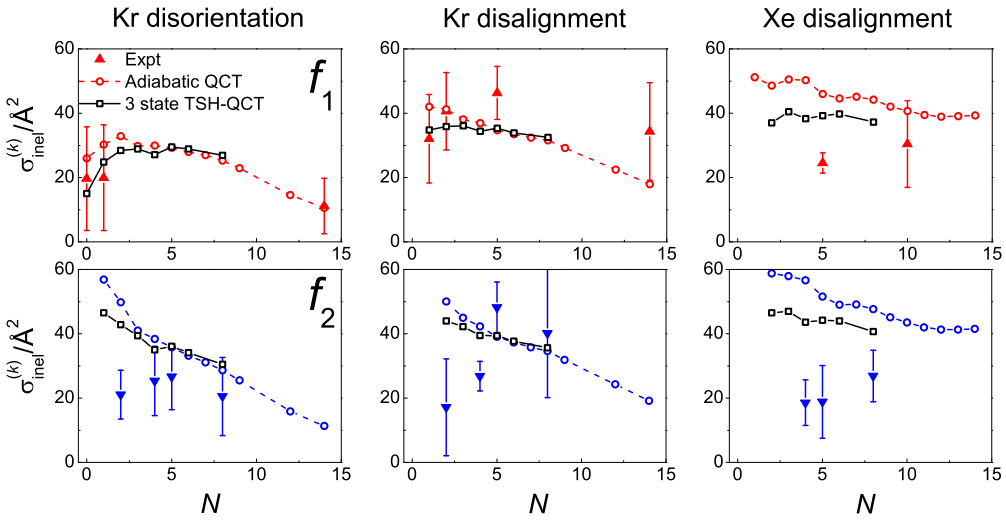

Figure 7.21: Experimental and theoretical cross-sections for *inelastic* ($j' \neq j$) depolarisation of OH(A) in collisions with Kr and Xe. Left: OH(A) + Kr disorientation ($\sigma^{(1)}_{\text{inel}}$), centre: OH(A) + Kr disalignment ($\sigma^{(2)}_{\text{inel}}$), right: OH(A) + Xe disalignment ($\sigma^{(2)}_{\text{inel}}$); top row: f_1 initial levels ($j = N + S$), bottom row: f_2 initial levels ($j = N - S$). Red and blue triangles are experimental data, open circles are adiabatic QCT,[22,237] open squares are 3 state TSH-QCT.

and surface-hopping collisions. As remarked earlier, the ranges of RET and quenching are broadly similar, indicating that the same features of the PES (HO–Rg well) are mainly responsible for both. The opacity function for elastic depolarisation (disalignment), on the other hand, peaks at high impact parameters and extends out further than the inelastic processes. The peak at high b is because there is no competition with inelastic processes there, and the magnitude of $P^{(2)}(b)$ increases with N as RET becomes less likely. It is also interesting to note the lack of an appreciable fall in the range of elastic depolarisation with increasing rotation, as the potential's anisotropy is not 'washed out' by rotation sufficiently to make a difference.

To gauge how depolarising elastic collisions are, figure 7.23 shows the elastic depolarisation opacity functions mentioned above, plotted with the opacity functions for elastic collisions. Note that, in QCT, the elastic opacity functions do not converge and instead tend to unity at high b, as discussed in chapter 5. It is also possible for $P^{(2)}(b) > P(b)$, as $a^{(2)}$ can take negative values. The figure shows that, at low to middle impact parameters, elastic collisions are very depolarising — a single collision can effectively depolarise

OH(A). At high b, elastic collisions begin to become more 'glancing-blow' in nature, so depolarisation falls off.

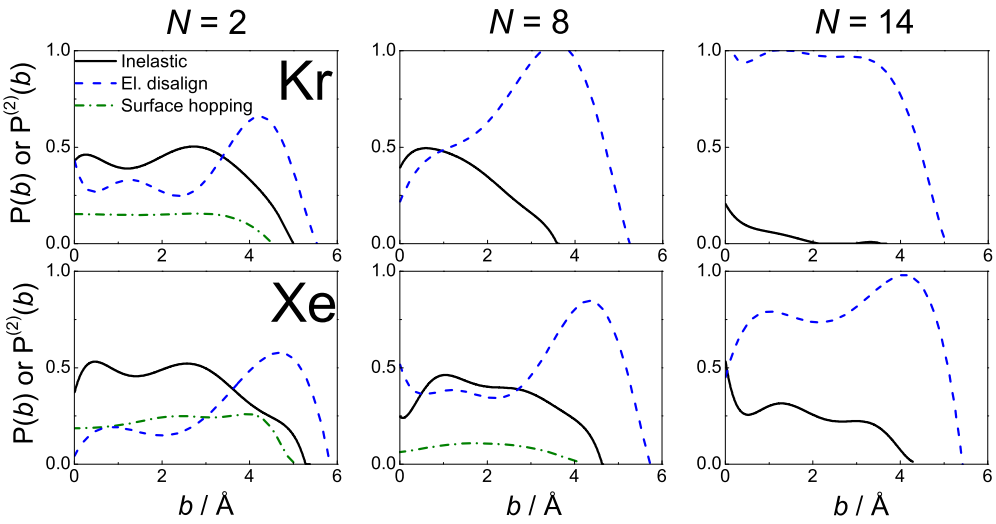

Figure 7.22: 3 state TSH-QCT *closed-shell* opacity functions for inelastic collisions (black solid lines), *elastic* disalignment ($P^{(2)}(b)$, $N' = N$; blue dashed lines) and surface hopping (green dash-dotted lines) of OH(A) in collisions with Kr (top row) and Xe (bottom row). Left, middle and right columns for initial N = 2,8,14 respectively.

7.4.3 Spin-rotation level resolved depolarisation

So far, this section has separated the total depolarisation cross-sections into elastic ($j' = j$) and inelastic components. This is the most separation that is possible experimentally (with the resolution available), but it is possible to use theory to go further.

In the studies of spin-rotation (SR) level resolved rotational energy transfer in section 7.2.3, inelastic collisions were separated into three categories: those that conserve N but change the SR level, known as *pure spin-rotation changing* collisions (PSRCs); those that change N but conserve the SR level, known as *SR conserving* collisions; and collisions which change both N and the SR level, which are labelled *inelastic SR changing* collisions.

This subsection uses the same separation to look at depolarisation in each type of collision, and explores exactly which kinds of collisional depolarisation compete the most with electronic quenching. It is also possible to include the purely *elastic* depolarisation in these comparisons, as these cross-sections can be converged theoretically, unlike the

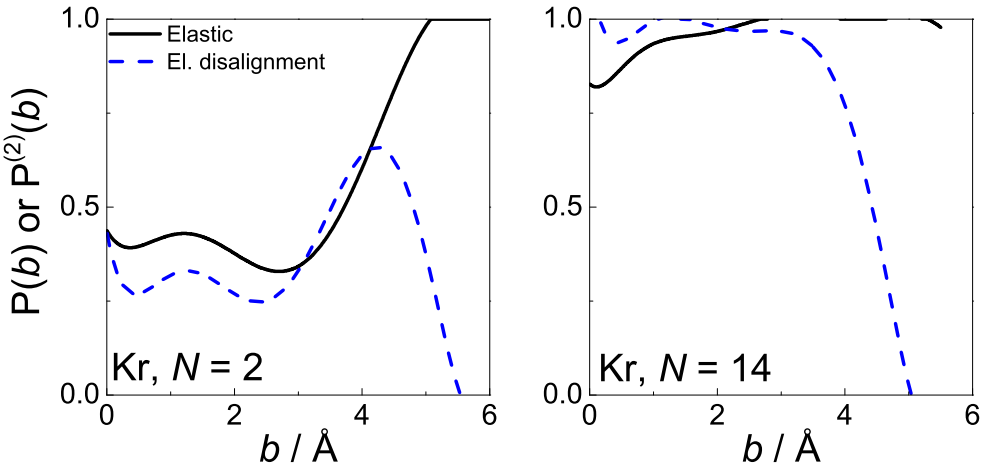

Figure 7.23: 3 state TSH-QCT *closed-shell* opacity functions for elastic collisions (black solid lines) and elastic disalignment ($P^{(2)}(b)$, $N' = N$; blue dashed lines) of OH(A) + Kr. Left and right panels for initial N = 2,14 respectively.

collision cross-section σ_{NN} (see chapter 3).

Figures 7.24 and 7.25 show, for OH(A) + Kr and Xe respectively, collisional disalignment resolved into disalignment in elastic, SR conserving, inelastic SR changing and pure SR changing collisions. These figures are laid out in a similar way to the resolved RET figures, 7.13 and 7.14.

The inelastic depolarisation is also separated into its N-changing and N-conserving, j-changing components in figures 7.26 and 7.27, which demonstrate the changing make-up of 'inelastic' depolarisation in a clearer way.

As N increases, single-surface QCT predicts a fall in the inelastic disalignment cross-sections, more so for Kr than for Xe. The figures here show that this is entirely due to the drop in depolarisation from N-changing collisions, with the PSRC disalignment cross-sections displaying no fall at all.

The reason for the decrease in N-changing, depolarising collisions with N is simply the increasing rotational level spacing, exactly as discussed for RET earlier in this chapter. The relationship between N-changing and pure SR changing depolarisation cross-sections in figures 7.26 and 7.27 suggests that, as the rotational level spacing increases and changing N in a collision becomes less likely, these N-changing collisions become PSRCs, explaining the

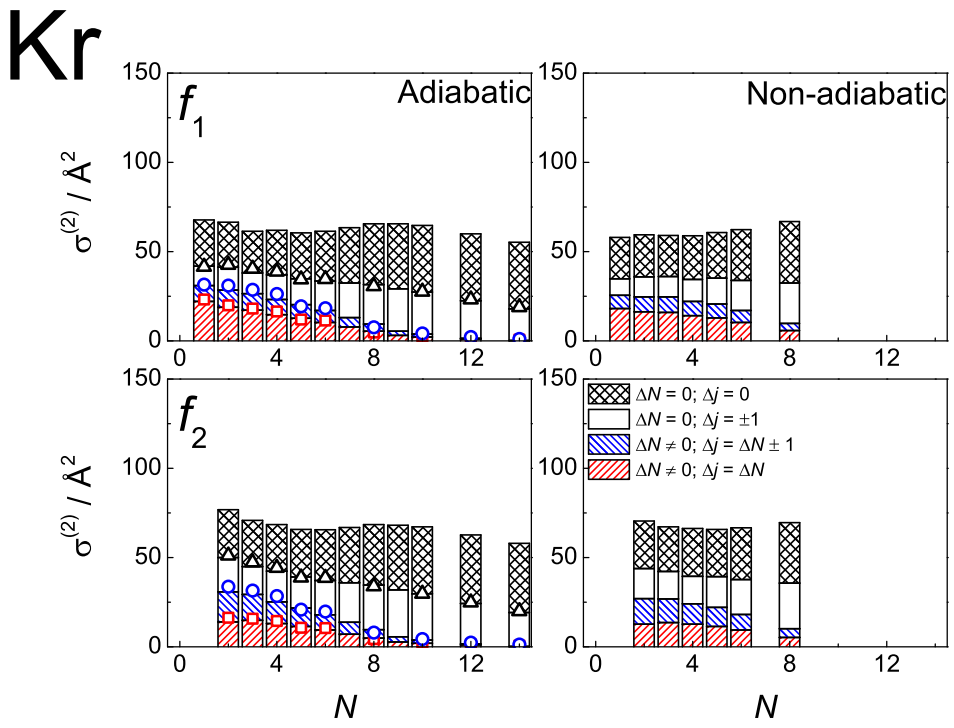

Figure 7.24: Comparison of theoretical disalignment cross-sections $\sigma^{(2)}$ from initial f_1 (top) and f_2 (bottom) spin-rotation levels of OH(A) + Kr, at a fixed collision energy of 0.039 eV. The bars are adiabatic QCT (left) or 3 state TSH-QCT (right) calculations, and the points are single-surface CC QM calculations.[258] Total depolarisation is represented by the total height of the bar. This is made up of *purely elastic* depolarisation ($\Delta j = \Delta N = 0$, crosshatched grey bars) and inelastic depolarisation (the rest of the bars). The inelastic depolarisation is in turn composed of *SR conserving* collisions ($\Delta j = \Delta N \neq 0$, red bars, red squares), *inelastic SR changing* collisions ($\Delta N \neq 0$; $\Delta j = \Delta N \pm 1$, blue bars, difference between blue circles and red squares) and *pure SR changing* collisions ($\Delta N = 0$; $\Delta j = \pm 1$, white bars, difference between open triangles and blue circles).

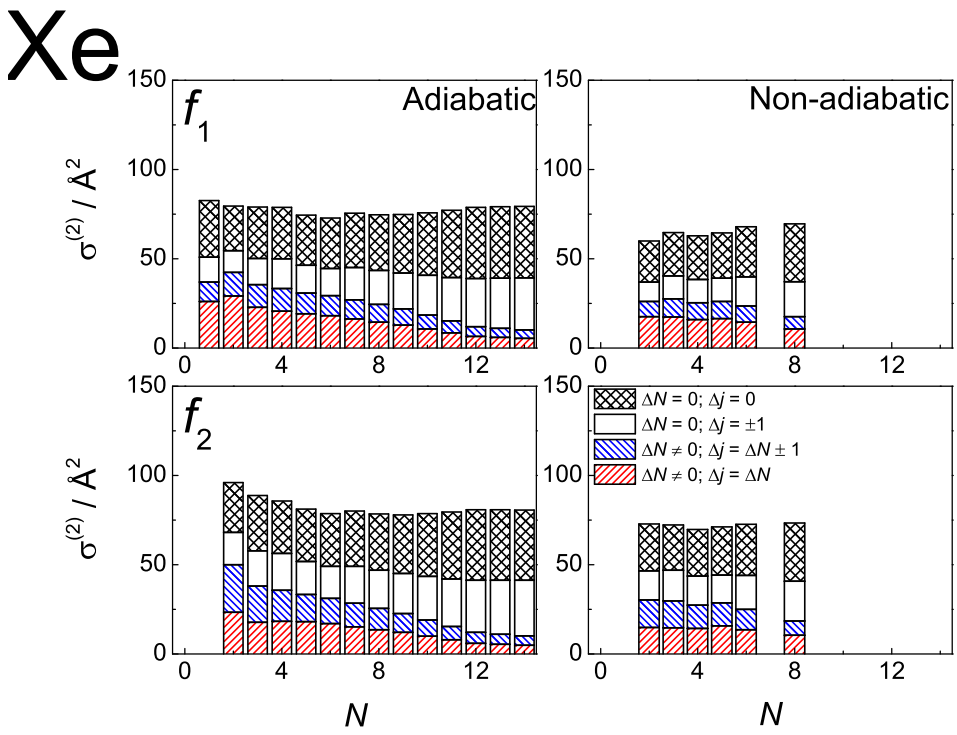

Figure 7.25: Comparison of theoretical disalignment cross-sections $\sigma^{(2)}$ from initial f_1 (top) and f_2 (bottom) spin-rotation levels of OH(A) + Xe, at a fixed collision energy of 0.039 eV. The bars are adiabatic QCT (left) or 3 state TSH-QCT (right) calculations. Total depolarisation is represented by the total height of the bar. This is made up of *purely elastic* depolarisation ($\Delta j = \Delta N = 0$, crosshatched grey bars) and inelastic depolarisation (the rest of the bars). The inelastic depolarisation is in turn composed of *SR conserving* collisions ($\Delta j = \Delta N \neq 0$, red bars), *inelastic SR changing* collisions ($\Delta N \neq 0$; $\Delta j = \Delta N \pm 1$, blue bars) and *pure SR changing* collisions ($\Delta N = 0$; $\Delta j = \pm 1$, white bars).

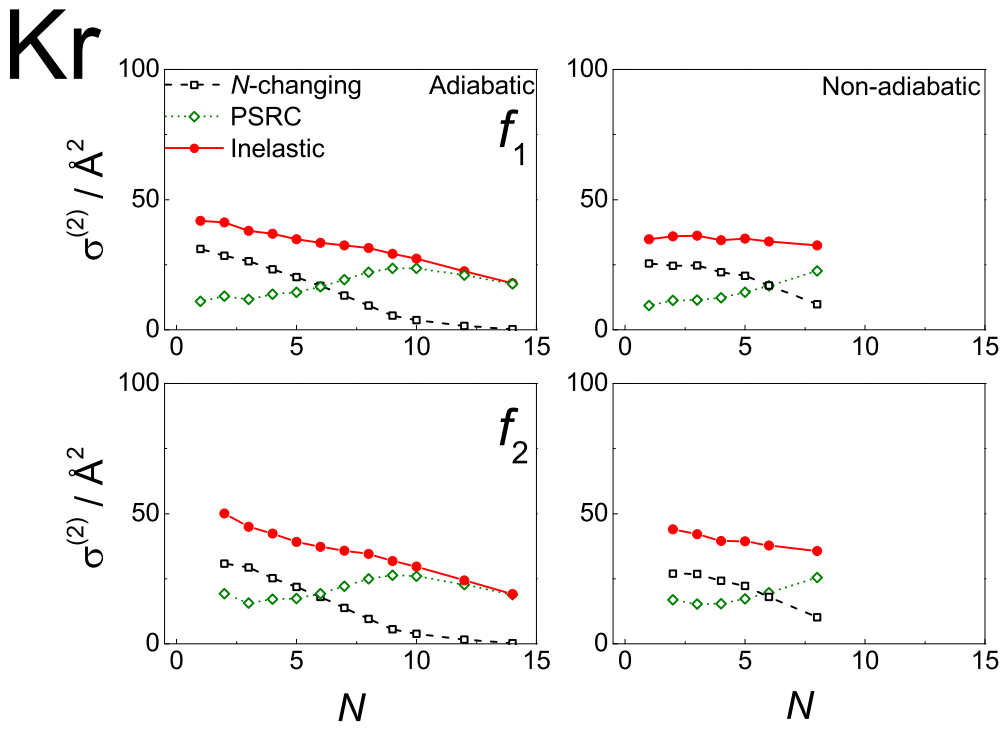

Figure 7.26: Theoretical disalignment cross-sections $\sigma^{(2)}$ from initial f_1 (top) and f_2 (bottom) spin-rotation levels of OH(A) + Kr, at a fixed collision energy of 0.039 eV. *Inelastic* ($j' \neq j$) disalignment (red circles) is here resolved into disalignment in collisions that change N (black squares) and collisions that conserve N, but change j (green diamonds). The left panels are adiabatic QCT and the right panels are 3 state TSH-QCT.

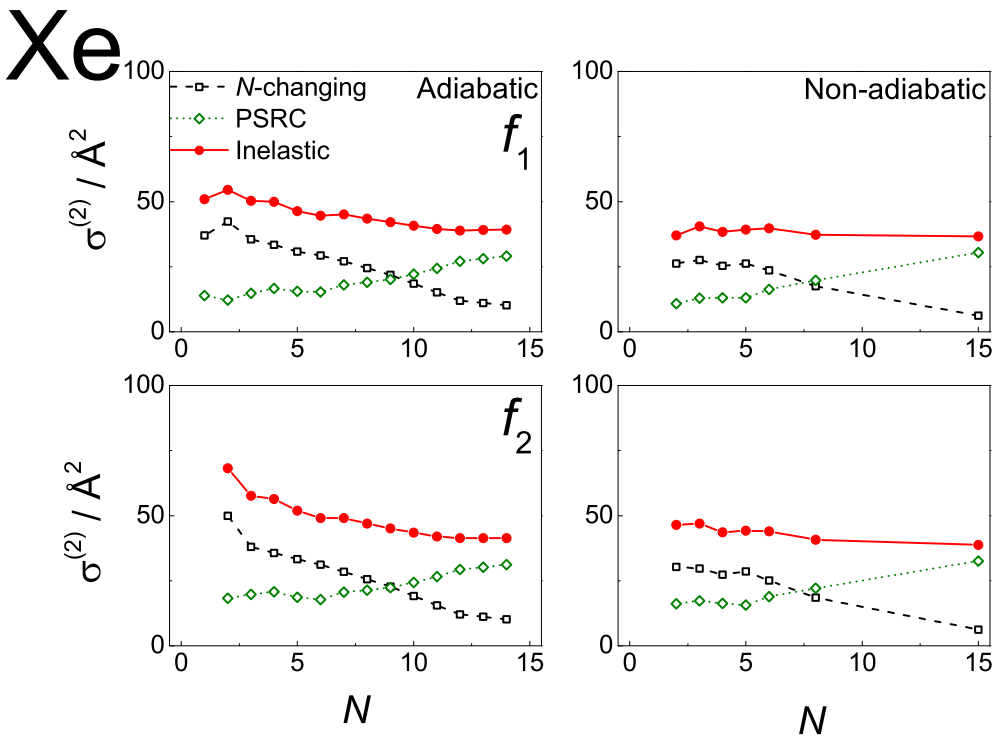

Figure 7.27: Theoretical disalignment cross-sections $\sigma^{(2)}$ from initial f_1 (top) and f_2 (bottom) spin-rotation levels of OH(A) + Xe, at a fixed collision energy of 0.039 eV. *Inelastic* ($j' \neq j$) disalignment (red circles) is here resolved into disalignment in collisions that change N (black squares) and collisions that conserve N, but change j (green diamonds). The left panels are adiabatic QCT and the right panels are 3 state TSH-QCT.

rise in pure spin-rotation changing depolarisation with N. (The reasons behind the elastic depolarisation being relatively constant with N were explored earlier in this section).

Looking now at the non-adiabatic calculations, and at the experimental data, no significant fall in inelastic depolarisation is observed – in contrast to the adiabatic predictions. The figures here reveal that this is because it is overwhelmingly the N-changing depolarisation which is suppressed by quenching at low N, with much less change in the purely SR changing depolarisation. This suggests that purely SR changing depolarisation is similar to elastic depolarisation in that it occurs away from the HO–Rg well and does not compete so much with quenching.

7.4.4 Comparison with OH(X) + Xe

Elastic depolarisation cross-sections for collisions of OH(X) with Xe have been measured by Paterson *et al.*,[25,276] using the TCPS (two-colour polarisation spectroscopy) technique, and compared to quantum scattering calculations by Kłos. The OH(X) + Xe PESs are much less attractive than the excited state OH(A) + Xe PES; the deepest point on the potentials used in ref. 276 (those of Groenenboom *et al.*[100]) is -224 cm^{-1}, and occurs in a T-shaped geometry ($\gamma = 90°$) on the $1A'$ PES. The OH(X) + Xe PESs used in the present work (see chapter 2) are very similar, except the T-shaped well on the $1A'$ PES is a little shallower, so that the global minimum is now in the OH–Xe geometry.

Figure 7.28 compares elastic disalignment cross-sections for OH(A) + Xe with those obtained by Paterson *et al.*,[25,276] for OH(X) + Xe. As can be seen, the magnitudes of the cross-sections are fairly similar — a trend with N is not visible in the left hand panel due to the number of points measured. However, as noted in the comparison of OH(X) and OH(A) with Ar in ref. 16, $\sigma_{\mathrm{el}}^{(2)}$ for OH(X) is better compared to the *closed-shell* elastic depolarisation (that is, $N' = N$) of OH(A), to better reflect the depolarisation of N (including depolarisation in purely spin-rotation changing collisions, $j' \neq j$; $N' = N$). This is because, in collisions of OH($X^2\Pi$), even-λ terms of the Legendre expansion of V_{sum} (equation (7.4)) govern elastic depolarisation;[277,278] in collisions of a $^2\Sigma^+$ radical such as

OH(A), even-λ terms of the Legendre-expanded potential are responsible for both elastic depolarisation and pure spin-rotation changing collisions.[279]

$$V(R,\gamma) = \sum_{\lambda=0} V_\lambda(R) P_\lambda(\cos\gamma) \tag{7.4}$$

These cross-sections, the sum of those for depolarisation in elastic *and* purely spin-rotation changing collisions in OH(A), are the same as the 'closed-shell' elastic (i.e. $N' = N$) depolarisation cross-sections.[16] They can be seen to be significantly larger for OH(A) + Xe than the elastic depolarisation cross-sections for OH(X) + Xe, as expected due to the much more attractive PES in this case.

In both cases, for OH(X) and OH(A), simply comparing the depth of the potential wells is not enough to gauge the effectiveness of elastic depolarisation. As remarked above, elastic depolarisation in OH(A) + Xe tends to occur at longer range than processes in the HO–Xe well (which are more often inelastic). For OH(X) + Xe, the symmetry of anisotropy plays a crucial role: when the potential $V_{\text{sum}} = (V_{1A'} + V_{1A''})/2$ is expanded in Legendre polynomials, *odd*-λ terms $V_{\lambda 0}$ favour lambda-doublet changing collisions, and *even*-λ terms favour elastic depolarisation.[277,278] The $\lambda = 0$ term is isotropic and does not take part in depolarisation. (Note that the V_{dif} potential also plays an important role in elastic depolarisation of OH(X), so the present discussion is somewhat simplified.)[280] A simple consideration of the well depth may miss the propensity for lambda-doublet transfer over elastic depolarisation.

7.5 Summary

This chapter has presented experimental results for electronic quenching, rotational energy transfer and collisional depolarisation in elastic ($j' = j$) and 'total' (elastic + inelastic) collisions. The results have been compared to adiabatic QCT calculations as well as three-state surface-hopping QCT (as in chapter 6), to tease out the effects of competition between electronic quenching and electronically adiabatic processes. The various features

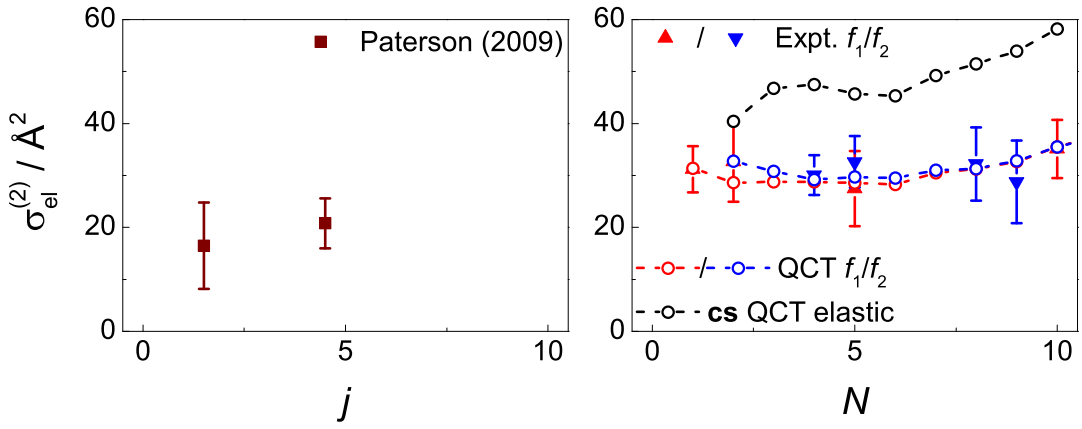

Figure 7.28: Comparison of elastic disalignment cross-sections between OH(X) + Xe (Paterson *et al.*,[276] left) and OH(A) + Xe (right). Left: experimental[276] $\sigma_{el}^{(2)}$, right: experimental (triangles) and adiabatic QCT[237] (circles) elastic disalignment. Black line in right panel: *closed-shell* elastic disalignment cross-sections.

of the potential energy surfaces involved have been examined for their influence on each possible outcome of a collision, and it was found that quenching competes directly with those rotationally inelastic processes that take place in the HO–Rg well (as opposed to the OH–Rg configuration), while rotationally elastic depolarising collisions tend to take place at longer range.

Agreement with theory has been seen to be better for scalar quantities such as quenching and RET cross-sections than it is for depolarisation cross-sections, and better for OH(A) + Kr than for OH(A) + Xe. Future work should aim to extend the theory presented here to a full, consistent quantum mechanical treatment.

Chapter 8

OH($A^2\Sigma^+$, $v = 1$) + Kr: experimental results

In this chapter, the study of the OH(A) + Kr system will be extended to include another collisional process: vibrational energy transfer (VET). When OH(A) is in a vibrationally excited state (here, $v = 1$), a collision with Kr can induce electronic quenching or rotational energy transfer (RET), as in $v = 0$, but also VET, which presents an extra available channel. The extent to which collisions take this pathway, and its competition with the other pathways available, is an interesting question that will be investigated in this chapter.

In addition, the introduction of one quantum of vibrational energy to OH(A) will affect its behaviour in other energy transfer processes. There may be a vibrational enhancement or decrease of the rate of electronic quenching, due to vibronic coupling. Moreover, the potential energy surface (PES) for OH(A) + Kr may have a dependence on the OH bond length, r_{OH}, meaning that collisions of vibrationally excited OH could access regions of the potential where coupling to the ground state is increased, or decreased. Any change to the quenching rate caused by vibration will have an associated effect on the rate of RET, which has been shown to compete with quenching in chapter 7. The results of this chapter will provide information about this other dimension of the PES, r_{OH}, which has so far been held constant in the *ab initio* calculations[21] (see chapter 2).

The experimental results presented here, collected according to the methods set out in chapter 4, will begin with a discussion of electronic quenching in $v = 1$, compared to $v = 0$. Vibrational energy transfer cross-sections will be examined, and discussed in the

context of other systems examined in the literature. Also measured here are cross-sections for rotational energy transfer within $v = 1$, which can be compared to those measured for $v = 0$ in chapter 7. The results presented here are also tabulated in Appendix B.

Because the potential energy surfaces for OH(X,A) + Kr used in this thesis[21,28] (chapter 2) have r_{OH} fixed at the potential minimum for this coordinate, QCT or TSH-QCT calculations of OH(A, $v = 1$) + Kr have not been performed in this thesis. If the full-dimensional potentials were available, this would present an interesting extension of the work in this chapter, though the quasi-classical nature of the theory used in this thesis would require careful treatment of quantisation and zero-point energy. Alternatively, a *vibrationally averaged* PES, with r_{OH} fixed at the correct value for the relevant vibrational state, could be employed — provided that the neglect of vibrational energy transfer was reasonable.

8.1 Electronic quenching

As described in chapter 4, cross-sections for electronic quenching of OH(A, $v = 1$) + Kr were measured by recording unresolved emission on the (1,0) band, which furnished a rate constant for the *sum* of quenching and VET. Subtracting the separately measured VET rate constant provides the rate constant for electronic quenching. These rate constants, converted into cross-sections using the thermal relative velocity, are displayed in figure 8.1.

Comparing the quenching cross-sections for OH(A, $v = 1$) + Kr to those for OH(A, $v = 0$) + Kr — which, for convenience, will henceforth be referred to as Q1 and Q0 respectively — it can immediately be seen that Q1 is significantly greater than Q0. For some rotational states, Q1 is over twice the magnitude of Q0. While quenching in $v = 0$ falls from its highest value around $N = 0$ to zero by $N \simeq 8$ to 10, Q1 rises to a peak at $N = 2$ and then falls off, becoming near-zero in the same region as Q0.

The fact that Q1 does not extend to higher N than Q0 indicates that vibration does

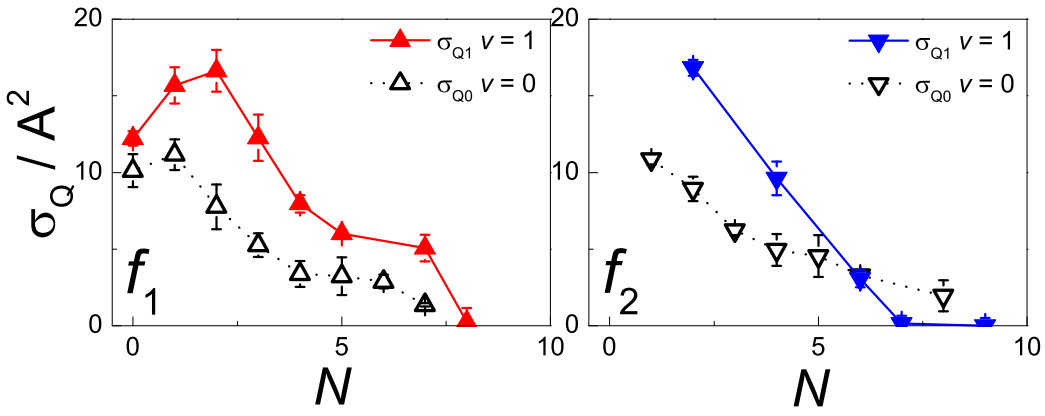

Figure 8.1: Experimental cross-sections for electronic quenching of OH(A) by Kr. Left: f_1 levels, right: f_2 levels; solid triangles: $v = 1$ quenching, open triangles: $v = 0$ quenching.

not help the system access the HO–Kr well, but rather that it enhances the probability of quenching once the system is in that well. This could be because the potential crossing between the X and A states shifts to a more accessible position (lower down on the repulsive wall) at values of r_{OH} sampled by OH(A, $v = 1$).

A similar effect was seen in quenching of OH(A) + Kr by Paul,[281] who observed that Q1 was approximately 70% greater than Q0 under shock tube conditions (1900-2300 K). The same behaviour was observed in OH(A) + Xe. At these high temperatures, quenching cross-sections are lower than those reported here, as the collision samples the repulsive part of the potential more than the attractive wells (where the potential crossing lies).

Other collider gases for which the rates of quenching of OH(A, $v = 0, 1$) have both been measured include oxygen[227,282] and nitrogen.[227,282] (A few points have been measured for Q1 with H_2,[224,283] among other gases, but there are not enough for a meaningful comparison with $v = 0$ data.) Figure 8.2 compares quenching cross-sections Q0 and Q1 for quencher gases O_2 and N_2; the $v = 0$ data is from ref. 282 and the $v = 1$ data is from ref. 227. The O_2 data shows hints of the behaviour observed here with Kr, where Q1 is greater than Q0 at low N but falls to the same values at higher rotational levels. It is not possible to investigate such trends in the N_2 data due to the magnitudes of the errors.

Apart from a possible vibronic coupling enhancing the rate of quenching, the most

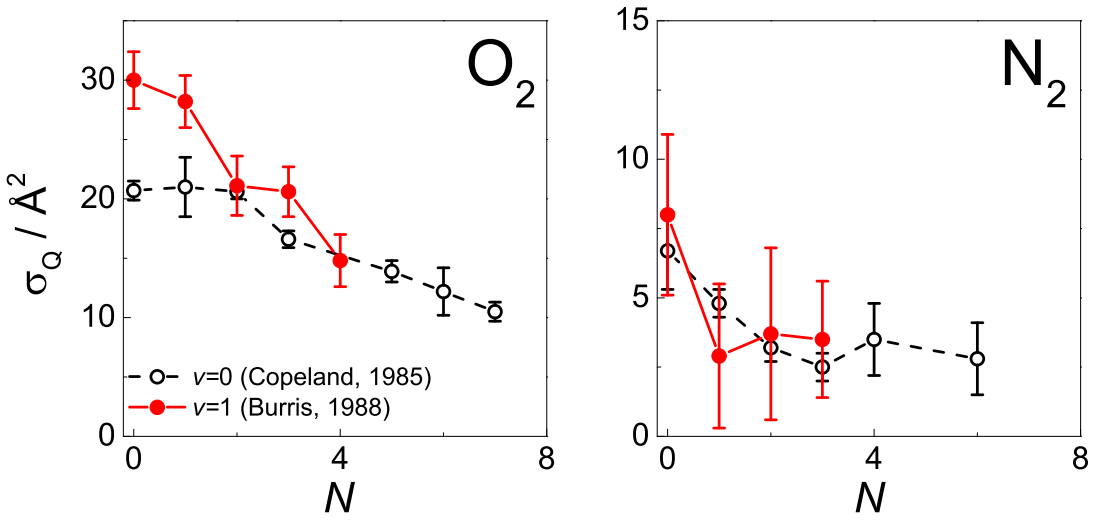

Figure 8.2: Experimental literature cross-sections for electronic quenching of OH(A) by O_2 (left) and N_2 (right). Solid circles are $v = 1$ quenching (Q1),[227] open triangles are $v = 0$ quenching (Q0).[282] Note the different scales in the two panels.

likely explanation for the increased electronic quenching observed from $v = 1$ as opposed to $v = 0$ is the variation of the potential energy surfaces with r_{OH}. The PESs used in this work (chapter 2) were calculated with a fixed OH bond length,[21] so it is not possible to look further into how the position of the conical intersection would vary in this respect. It would be very interesting to run TSH-QCT calculations on a set of vibrationally averaged $v = 1$ PESs, to see if this can explain the quenching observed here.

However, a *full-dimensional* adiabatic PES for OH(A) + Ar has been calculated by Kłos[284] at the MRCISD+Q level of theory. By looking at how the HO–Ar well changes with the OH bond length, it may be possible to gain some insight into the OH(A) + Kr system. Of course, the OH(X) + Kr state, and the diabatic coupling, will change with r_{OH} too, and this must be borne in mind. Sumiyoshi *et al.* reported full-dimensional semi-empirical adiabatic PESs for OH(X) + Kr, which give information on changes in the ground state.[285]

Cuts through the 3D OH(A) + Ar PES[284] at $\gamma = 180°$ (HO–Ar geometry) at various values of r_{OH} are shown in the left hand panel of figure 8.3, demonstrating that the oxygen well becomes *shallower* moving from the equilibrium bond length of OH($v = 0$) to that of OH($v = 1$). These equilibrium bond lengths were obtained from the rotational constants

B_v tabulated by Huber and Herzberg,[91] with

$$B_v = \frac{h}{8\pi^2 c I_v} \tag{8.1}$$

with I_v being the vibrational state-dependent moment of inertia.

What this behaviour implies is that, if the same occurs in OH(A) + Kr, the intersection with the ground state PES will occur closer to the bottom of the oxygen well in $v = 1$ than in $v = 0$ (as the well is 'moving up'). The right hand panel of figure 8.3 shows a section through the full-dimensional OH(A) + Ar PES, at $\gamma = 180°$ and as a function of the Ar to OH centre of mass distance (R) and the OH bond length (r), showing again how the oxygen well gets shallower with increasing r_{OH}. This strong dependence of the potential on r_{OH} gives an idea of how vibrational excitation could enhance quenching.

Again, it is important to emphasise that the ground state potentials will also shift with r_{OH}, as will the diabatic couplings, which may affect the conclusions drawn here. Figure 7(f) in the paper of Sumiyoshi and coworkers[285] shows the changes in the OH(X) + Kr V_{sum} PES at $\gamma = 180°$ as r_{OH} is varied, which are only on the order of 20 cm^{-1} – much less than the changes in the OH(A) + Ar PES discussed above. For this reason, variation in the excited state PES with OH bond length will be the major factor affecting quenching.

To investigate this vibrational enhancement of quenching further, a target for theory should be to obtain r_{OH}-dependent potentials (or vibrationally averaged potentials) for the OH + Kr system.

8.2 Vibrational energy transfer (VET)

When considering OH(A, $v = 1$) + Kr, an extra collisional outcome is possible compared to collisions in $v = 0$: vibrational energy transfer (VET).

$$\mathrm{OH(A},\, v = 1) + \mathrm{Kr} \xrightarrow{k_{VET}} \mathrm{OH(A},\, v = 0) + \mathrm{Kr} \tag{8.2}$$

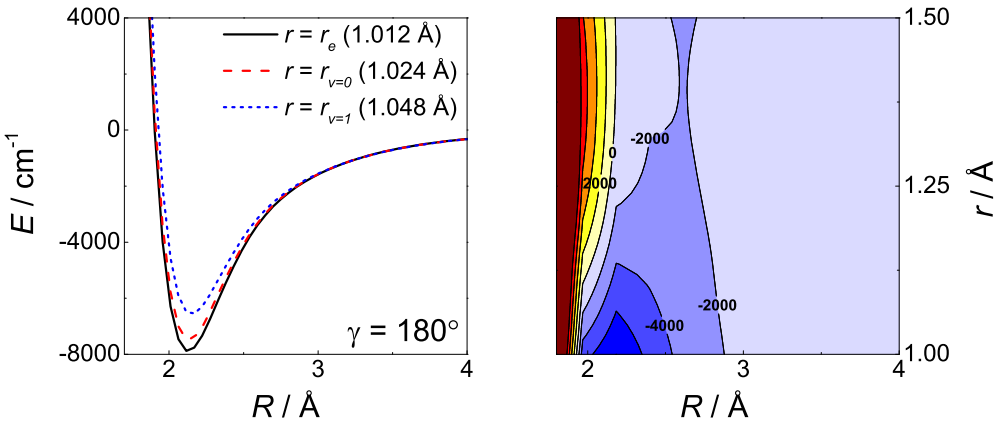

Figure 8.3: Left: potential energy versus centre of mass distance, R, for HO–Ar geometry at various OH bond lengths. Black: r_e for OH, red: equilibrium r_{OH} for $v = 0$, blue: equilibrium r_{OH} for $v = 1$. Right: potential energy versus R (Ar to OH centre of mass distance) and r (OH bond length) for OH(A) + Ar. All data from the PES of Kłos.[284].

Experimental cross-sections for VET were measured using the method in chapter 4, and are presented in figure 8.4. These cross-sections are found to be extremely small (around 0.5 Å^2) and do not vary appreciably with N, within experimental error — though this may be a consequence of the fact that they were measured only up to $N = 7$. Comparing the extent of VET to that of RET and electronic quenching, these results show that it would certainly be possible to model the system assuming no vibrational energy transfer — for example, with the existing TSH-QCT theory on a vibrationally averaged $v = 1$ set of potentials.

The near-negligible degree of vibrational energy transfer in the OH(A, $v = 1$) + Kr system is in agreement with that seen with other monatomic colliders. Both He and Ar have very small VET cross-sections with OH(A, $v = 1$)[224,226,286] with the cross-section for Ar being within the errors of that for Kr. This can be readily explained by a consideration of the relative timescales of translation and vibration. A molecule that vibrates on a femtosecond timescale will not transfer much energy in a collision that could last orders of magnitude longer[8,287] — a *sudden* collision is necessary for efficient energy transfer. VET can be successfully modelled in many cases by a purely impulsive interaction with the repulsive part of the potential.[8,288] For example, the simple Landau-Teller model[8,288,289]

gives an analytical expression for the probability of VET where the potential is taken to be an exponential, $V(R) = Ce^{-\alpha R}$:

$$P_{10} = \exp\left[-3\left(\frac{2\pi^4\mu\nu^2}{\alpha^2 k_B T}\right)^{\frac{1}{3}}\right] \tag{8.3}$$

where μ is the reduced mass and ν the vibrational frequency. A brief consideration of this equation reveals that the probability of VET in a typical collision will be very small.

However, significant vibrational energy transfer in collisions of OH(A, $v = 1$) + Kr (and Xe) has been observed under superthermal collisions (T = 1900 K) in a shock tube.[281] There, the VET cross-sections are around 4 Å^2 for Kr and 10 Å^2 for Xe, which are in fact *larger* than the corresponding cross-sections for quenching (which fall with temperature). This can be explained by the increasing impulsiveness of the collisions at higher temperatures.

Presenting quite a different picture to that seen with monatomic collision partners, collisions of OH(A, $v = 1$) with diatomic (and larger) molecules can result in effective VET. Systems that have been investigated include H_2,[224,226] D_2,[224,226] N_2[226,227,286] and O_2,[227,286] all of which exhibit VET cross-sections comparable to (and in some cases greater than) those for quenching. The internal degrees of freedom of the diatomic are what makes the difference,[226] rather than resonant energy transfer, as verified by a comparison of OH(A) + H_2 with OH(A) + D_2.[226]

8.3 Rotational energy transfer (RET)

In chapter 7, it was found that competition between electronic quenching and electronically adiabatic rotational energy transfer (RET) resulted in an overprediction of the RET cross-sections for OH(A, $v = 0$) + Kr by single-surface QCT. As there is more quenching in OH(A, $v = 1$) + Kr, one would expect a concomitant decrease in the RET cross-sections. This is what is experimentally observed, as seen in the left hand panel of figure 8.5.

At low values of N, the rotational quantum number, where quenching is most signif-

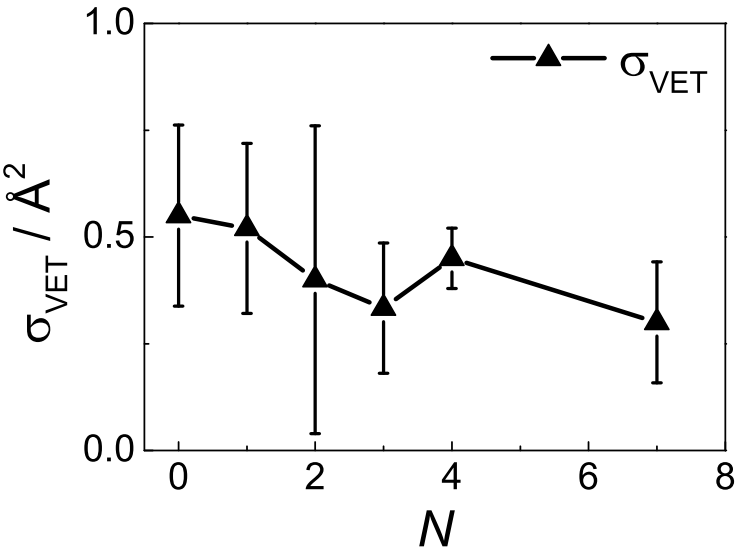

Figure 8.4: Experimental cross-sections for vibrational energy transfer (VET) of OH(A, $v = 1$) + Kr as a function of initial rotational state, N, all f_1 $(N + S)$ levels.

icant, there is the greatest difference between the $v = 1$ and $v = 0$ RET cross-sections. Moving to higher rotational states, the difference gets smaller as there is less quenching.

The right-hand panel of figure 8.5 shows cross-sections for *total removal*, which is (as in chapter 7) the sum of RET and electronic quenching. (For $v = 1$ collisions, total removal also includes vibrational energy transfer, but this was shown to be negligible in the previous section). The total removal cross-sections for collisions in $v = 0$ and $v = 1$ agree to within experimental error, demonstrating that the difference between RET cross-sections in the two vibrational states can be assigned to the competition between RET and quenching.

8.4 Summary

In this chapter, the investigation of collisional pathways in OH(A) + Kr was extended to include vibrational energy transfer (VET). The probability of VET under thermal conditions was found to be low, as it is favoured by impulsive collisions on the repulsive part of the potential energy surface, but vibration caused significant enhancements to the rate of electronic quenching. The increased quenching also caused the cross-sections for

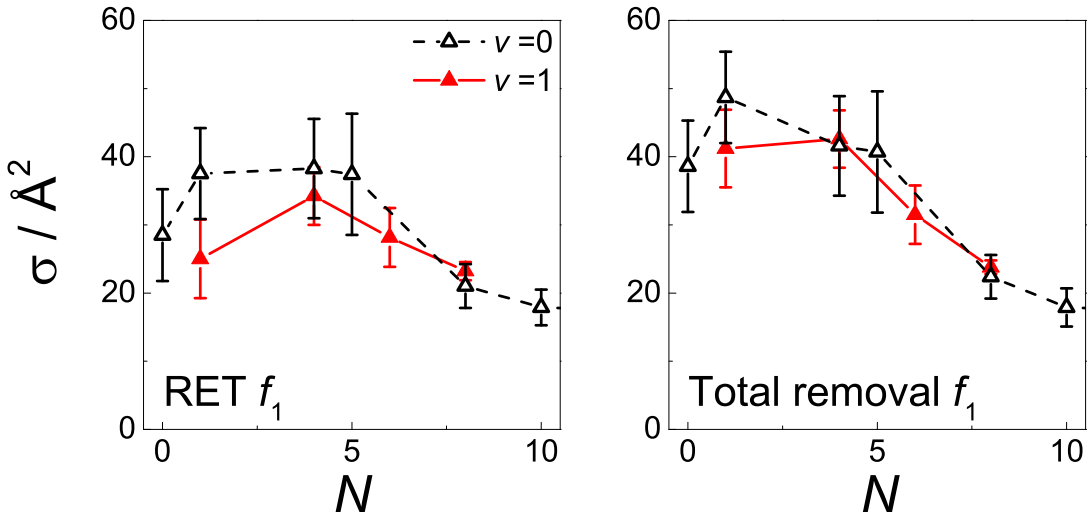

Figure 8.5: Experimental cross-sections for rotational energy transfer (RET, left) and total removal (sum of quenching and RET, right) of OH(A, $v = 1$) + Kr (red triangles) and OH(A, $v = 0$) + Kr (black open triangles). All f_1 ($N + S$) levels.

rotational energy transfer in OH(A, $v = 1$) to be lower than the corresponding cross-sections in $v = 0$ — which can be explained through competition between quenching and RET, as in chapter 7.

The increase in quenching for OH(A, $v = 1$) + Kr over OH(A, $v = 0$) + Kr has been attributed to the change in the location of the crossing between the OH(A) + Kr and OH(X) + Kr potentials with r_{OH}. To confirm this hypothesis, it would be interesting to see *ab initio* potentials calculated at different fixed r_{OH}, perhaps vibrationally averaged, or even a set of full-dimensional PESs. With these potentials, the theory set out in chapter 6 could be extended to the current case, in an attempt to model the results in this chapter.

One useful point in this regard is that it would likely not be necessary to explicitly treat the OH vibration. As VET is almost negligible, it may well be enough to run fixed-r_{OH} calculations on a set of vibrationally averaged potentials, which would be a good deal easier.

Chapter 9

Conclusions and future work

9.1 Conclusions

The primary focus of the work in this thesis has been to investigate the competition between electronically adiabatic and non-adiabatic processes in collisions of OH(A) with Kr and Xe. From the experiments and accompanying theory presented here, it is possible to conclude that quenching competes directly with rotationally inelastic collisions (including the inelastic depolarisation of angular momentum), as both processes are governed by the same region of the potential energy surface – principally, the deep linear HO–Rg well. Rotationally *elastic* depolarising collisions, on the other hand, tend to occur at longer range and so do not compete with electronic quenching so much.

The experiments used here took advantage of polarised laser excitation to prepare a distribution of OH(A) radicals in which the angular momentum vectors were oriented or aligned. The collisional loss of polarisation was monitored by examining quantum beats in the fluorescence induced by a magnetic field; the decreasing beat magnitude over time gave the rate of depolarisation. By resolving fluorescence from different excited vibrational or spin-rotation states, or collections thereof, it was possible to obtain cross-sections for energy transfer processes such as electronic quenching and rotational or vibrational energy transfer.

Quenching was found to be significant for both the OH(A) + Kr, Xe systems examined

here, but more so in the case of Xe. This is because the region of the excited state PES close to the conical intersection – the region where quenching is most likely – is more accessible at thermal collision energies, lying as it does close to the bottom of the attractive HO–Xe well. In the case of OH(A) + Kr, the conical intersection lies slightly higher on the repulsive wall of the potential, requiring more head-on collisions to result in quenching. This explains why electronic quenching cross-sections for OH(A) + Kr are smaller than those for OH(A) + Xe, and fall faster with increasing rotation.

When OH(A) is vibrationally excited, this is found to increase the amount of quenching seen with Kr, presumably due to the crossing region becoming more accessible at different values of r_{OH}. More quenching leads to a concomitant decrease in the cross-sections for rotational energy transfer. Collisional transfer from OH(A, $v = 1$) to OH(A, $v = 0$) is not observed to be a significant process, as expected on kinematic grounds.

In the first instance, single surface quasi-classical trajectory (QCT) theory was used to model the experimental results. In contrast to previous studies of OH(A) + He, Ar,[12,13,16,18,22] significant discrepancies were observed between experiment and theory. As quantum scattering calculations displayed the same behaviour, it was attributed to electronic quenching rather than a deficiency in the QCT method. The competition between rotationally inelastic collisions (RET, inelastic depolarisation) and electronic quenching results in single surface QCT overpredicting the RET and depolarisation cross-sections. However, elastic collisional depolarisation is well simulated by QCT due to the absence of competition from quenching.

Following on from this, trajectory surface hopping (TSH) QCT was employed in an attempt to include non-adiabatic effects into the QCT theory and thereby better model the experimental data. Agreement between experimental and theoretical RET and collisional depolarisation cross-sections was improved, but the inability of two state TSH-QCT to capture the full magnitude of quenching meant that this improvement was not enough to fully explain the observed results.

To this end, the existing TSH-QCT theory, which included only the symmetric $1A'$

and $2A'$ electronic states, was extended to incorporate rovibronic couplings (Coriolis and Renner-Teller) to the antisymmetric $1A''$ state. The development of this extension to the theory was detailed in chapter 6. Inclusion of this third electronic state resulted in much improved agreement between calculated and experimental quenching cross-sections; in the case of OH(A) + Kr the agreement was almost quantitative. Agreement with the experimental RET and collisional depolarisation data also displayed a significant improvement. Notably, the new theory also succeeded in modelling the related experiments of Lester *et al.*,[28] in which the rotational state distribution of quenched OH(X) products was measured. This theoretical modelling added insight into how the balance of different quenching pathways leads to the observed lambda-doublet ratio in the products, and also the rotational state distribution – with Coriolis coupling tending to form OH(X) in lower rotational states than Renner-Teller coupling. Some interesting trends in these state distributions were also explained in terms of the kinds of collisions that led to them.

In conclusion, the experiments and calculations presented here have shown that electronic quenching is a significant channel in collisions of OH(A) with both Kr and Xe. Quenching competes directly with electronically elastic, rotationally inelastic collisional processes, but not as much with j-conserving depolarising collisions. As such, inclusion of non-adiabatic effects is crucial for a complete understanding of the systems here; in particular, the effects of rovibronic couplings to the $1A''$ potential energy surface must be taken into account. It is likely that similar behaviour will be exhibited in collisions of OH(A) with other quenchers and, indeed, in many other collision systems. The work here will therefore be of value in the further study of collisional energy transfer and vector correlations where breakdown of the Born-Oppenheimer approximation is likely to be significant.

9.2 Future work

The results presented in this thesis naturally lead to a number of interesting directions for future study. The OH(A) + Kr, Xe systems still have many more secrets to give up, but, moreover, the present results form a springboard from which to make further leaps in the understanding of collisional dynamics in systems with electronically non-adiabatic channels. As explained in the introduction (chapter 1), one of the aims of the study of simple, three atom systems such as these is the applicability of the conclusions and insights drawn from them to studies of larger, more complex systems. It is to be hoped that this will be the case in the future. To this end, several potential directions for future work are set out in this section.

9.2.1 Experimental

The present results on the OH(A) + Kr and Xe collision systems form the final part of a set of results encompassing 300 K measurements of collisional depolarisation of OH(A) with rare gases in recent years.[24] Together with similar work on other prototypical radicals such as OH($X^2\Pi$), NO($X^2\Pi$), NO($A^2\Sigma^+$) and CN($A^2\Pi$), reviewed in refs. 24–26, these results add to the current understanding of atom-diatom collision dynamics. A direct continuation of the present experiments could be the study of OH(A, $v = 1$) + Xe, or perhaps the use of isotopically substituted OD(A). However, a more interesting possible extension of this work would be to supplement the $\boldsymbol{j} - \boldsymbol{j'}$ correlation measured here with other vectors.

The use of a crossed molecular beam configuration would offer the opportunity to include the vectors $\boldsymbol{k}$ and $\boldsymbol{k'}$ in the correlations investigated. An interesting first direction could be to measure the differential cross-sections for collisions of OH(A) with Kr and Xe, in a similar fashion to the very recent crossed-beam experiments (and accompanying theoretical studies) on NO(A) performed by the groups of Costen, Chandler and Alexander.[290–292] For this experiment, a REMPI detection scheme for OH(A) would be

useful. Further extensions could include $\boldsymbol{j}$ or $\boldsymbol{j'}$, for example looking at the polarisation of collisional products (see ref. 292). Alternatively, the OH(X) products of non-reactive quenching could also be studied via ion imaging (or another suitable technique).

Looking to other systems, the collisional depolarisation of OH(A) by H_2 has been investigated recently in our group.[5] The reactive channel could be investigated, as both H_2O and H are amenable to detection (for example, REMPI or Rydberg tagging). This would follow a variety of previous work on this channel, for example refs. 293–298.

9.2.2 Theoretical

As emphasised several times already in this thesis, an excellent priority for theoretical development would be full close-coupled three state quantum scattering calculations for OH(X,A) + Kr, Xe, extending the unpublished work of Kłos, Alexander and Dagdigian,[236] to put the results of chapter 6 on a more secure footing. However, such calculations are still rather expensive – and certainly not an easy task! – at the present time. Some preliminary non-adiabatic quantum calculations on three coupled PESs have begun to appear in the literature, for example the recent study of the quenching of $O(^1D)$ by $N_2(X^1\Sigma_g^+)$ in ref. 250.

Concentrating more on the existing theory in this thesis, though, an interesting extension would be to model the results of chapter 8, *i.e.* collisions of OH(A, $v = 1$) by Kr. For this task, vibrationally averaged potentials and couplings would be required; if a full-dimensional calculation (where r_{OH} can vary) is considered, then thought needs to be given to the zero-point energy of the OH vibration. In addition, if the experiments in section 9.2.1 are to go ahead, it would be useful to model them using an extension of the theory developed in this work.

The extension of the present QCT code to a four atom (diatom + diatom) system has been recently dealt with by Seamons[5] in the context of OH(A) + H_2 collisional depolarisation. In common with the OH(A) + Kr, Xe systems considered in this work, OH(A) + H_2 collisions can also undergo electronic quenching, and efforts are underway in several

groups to simulate this.[272,299–305] One added complication here is the reactive channel, which accounts for most of the products[306] – this would need to be included in the calculations. In addition, previous QCT calculations on the OH(A) + H_2 system met with some difficulties due to the large rotational spacing of H_2: energy leaked out in collisions, changing the rotational state of OH, but H_2 was still binned to the same final quantum state as it started in.[5] Innovative binning schemes alleviate this problem somewhat,[5] but it would still need to be considered in any extension to multiple states. Alternatively (if full quantum scattering calculations were unfeasible) some sort of semiclassical trajectory method could be considered – for example, treating rotation quantum mechanically but translation classically.[307–311]

Appendix A

Tabulated results for OH(A, $v = 0$) + Kr, Xe

		σ_Q / Å^2				
	N	f_1	f_2	Hemming[27]	TSH2	TSH3
Kr	0	10.1(1.1)	–	–	12.6	16.5
	1	11.2(1.0)	10.9(0.3)	–	6.2	10.9
	2	7.8(1.5)	8.9(0.8)	9.3(0.6)	3.6	7.4
	3	5.3(0.8)	6.2(0.3)	–	2.3	5.0
	4	3.4(0.8)	4.9(1.0)	5.0(0.4)	1.9	3.0
	5	3.2(1.2)	4.5(1.4)	–	0.9	1.2
	6	2.9(0.4)	3.3(0.3)	3.1(0.2)	0.3	0.2
	7	1.4(0.1)	–	–	0.1	–
	8	–	2.0(1.0)	1.9(0.5)	0	0
	10	–	–	0.4(0.3)	0	0
	13	–	–	0.3(0.2)	0	0
	14	0.0(1.8)	–	–	0	0
	20	–	–	0.8(0.3)	0	0
Xe	0	22.3(0.5)	–	–	18.9	20.0
	1	28.4(2.7)	–	–	–	–
	2	28.1(1.0)	30.3(0.7)	–	13.4	17.5
	3	26.5(7.5)	28.3(2.1)	–	10.4	14.2
	4	–	32.1(2.6)	–	8.4	13.4
	5	29.7(0.7)	31.7(3.2)	–	6.7	9.1
	6	–	21.1(1.7)	25.1(1.3)	4.7	8.9
	7	25.3(1.4)	–	–	–	–
	8	–	24.6(2.0)	–	2.0	5.1
	9	–	25.9(1.3)	–	–	–
	10	22.2(3.8)	18.4(1.2)	21.9(1.5)	–	–
	13	–	–	16.4(1.1)	–	–
	15	–	–	12.1(0.8)	–	0
	20	–	–	12.1(0.8)	–	–

Table A.1: Electronic quenching cross-sections for OH(A) + Kr, Xe under thermal conditions. Errors (in brackets) represent one standard deviation. Closed-shell surface-hopping calculations were carried out at a fixed collision energy of 0.039 eV. Note that the spin-rotation level employed by Hemming *et al.* is not specified in their paper. 'TSH2' and 'TSH3' refer to two-state and three-state trajectory surface-hopping QCT calculations respectively.

		σ_{RET} / Å^2				
	N	Expt	Adiabatic QCT[21]	Adiabatic QM[21]	TSH2	TSH3
Kr, f_1	0	29(7)	38	–	26	23
	1	38(7)	43	47	38	36
	2	–	43	45	41	38
	3	–	41	47	40	39
	4	38(7)	39	41	41	37
	5	37(9)	37	36	41	37
	6	–	34	38	34	34
	7	–	31	–	35	–
	8	21(3)	28	28	29	29
	9	–	25	–	–	–
	10	18(3)	23	23	24	–
	12	–	19	19	20	–
	14	17(9)	15	16	16	–
Kr, f_2	1	–	53	57	48	46
	2	–	49	50	47	43
	3	–	45	43	44	42
	4	39(4)	42	44	44	40
	5	38(7)	39	39	44	40
	6	–	37	36	37	37
	7	–	34	–	33	–
	8	25(9)	30	30	31	32
	9	21(4)	27	–	–	–
	10	–	25	25	26	–
	12	–	20	21	21	–
	14	–	16	17	17	–

Table A.2: Rotational energy transfer cross-sections for OH(A) + Kr under thermal conditions. Errors (in brackets) represent one standard deviation. Adiabatic[21] and surface-hopping QCT calculations were carried out at a fixed collision energy of 0.039 eV, as were the adiabatic QM calculations of Kłos.[21] 'TSH2' and 'TSH3' refer to two-state and three-state trajectory surface-hopping QCT calculations respectively.

		σ_{RET} / Å^2				
	N	Expt	Adiabatic QCT	Adiabatic QM[235,237]	TSH2	TSH3
Xe, f_1	0	–	58	–	47	45
	1	–	53	–	43	–
	2	–	52	55	43	41
	3	–	53	–	45	43
	4	–	52	52	44	41
	5	24(6)	50	52	44	42
	6	–	47	48	44	40
	8	–	46	–	41	38
	10	25(5)	41	39	37	–
	14	–	37	–	35	–
	15	–	–	–	–	33
Xe, f_2	1	–	67	–	54	–
	2	29(3)	59	61	49	46
	3	–	57	–	49	42
	4	18(8)	56	56	47	44
	5	20(3)	53	55	46	44
	6	–	50	51	46	43
	8	26(2)	48	–	43	41
	9	18(2)	45	45	–	–
	10	–	43	41	39	–
	14	–	39	–	37	–
	15	–	–	–	–	35

Table A.3: Rotational energy transfer cross-sections for OH(A) + Xe under thermal conditions. Errors (in brackets) represent one standard deviation. Adiabatic and surface-hopping QCT calculations were carried out at a fixed collision energy of 0.039 eV, as were the adiabatic QM calculations of McCrudden and Herráez-Aguilar.[235,237] 'TSH2' and 'TSH3' refer to two-state and three-state trajectory surface-hopping QCT calculations respectively.

		N											
Kr, f_1		0	1	2	3	4	5	6	7	8	10	12	14
$\sigma^{(1)}$	Expt total	20(7)	23(9)	24(4)	—	—	35(4)	—	42(7)	—	33(5)	—	34(5)
	Expt elastic	0(14)	3(14)	—	—	—	—	—	—	—	—	—	23(7)
	QCT total	26	41	45	41	42	42	42	43	43	40	34	28
	QCT elastic	0	11	12	11	12	13	14	16	18	20	19	18
	QM total	—	43	47	43	43	42	42	—	43	40	34	29
	QM elastic	—	9	11	11	11	13	13	—	18	19	19	18
	TSH2 total	18	37	42	41	41	48	43	45	45	43	36	31
	TSH2 elastic	0	10	11	11	11	15	14	16	18	20	20	19
	TSH3 total	15	34	39	40	39	42	44	—	45	—	—	—
	TSH3 elastic	0	9	11	11	12	13	15	—	18	—	—	—
$\sigma^{(2)}$	Expt total	—	54(7)	63(5)	62(6)	—	66(2)	—	84(9)	—	82(19)	—	66(7)
	Expt elastic	—	22(12)	23(11)	—	28(11)	20(7)	—	—	—	—	—	32(13)
	QCT total	—	68	67	62	62	60	61	63	66	65	60	55
	QCT elastic	—	26	25	23	25	26	28	31	34	37	38	37
	QM total	—	60	66	62	62	60	61	—	65	64	61	56
	QM elastic	—	19	23	22	23	26	26	—	34	37	37	37
	TSH2 total	—	62	64	61	61	67	62	65	66	66	62	58
	TSH2 elastic	—	25	25	24	24	30	28	31	34	37	38	38
	TSH3 total	—	58	59	59	59	61	62	—	67	—	—	—
	TSH3 elastic	—	23	24	23	25	26	29	—	34	—	—	—

Table A.4: Cross sections for collisional disorientation ($\sigma^{(1)}/\text{Å}^2$) and disalignment ($\sigma^{(2)}/\text{Å}^2$) of OH(A) by Kr under thermal conditions, for f_1 ($N + S$) spin-rotation levels. The adiabatic QCT,[22] adiabatic QM[236] and surface-hopping QCT calculations ('TSH2' and 'TSH3' for two-state and three-state TSH respectively) were performed at a collision energy of 0.039 eV. The error bars (indicated in brackets on the experimental data) represent 95 % confidence limits (2 standard deviations).

		N										
Kr, f_2		1	2	3	4	5	6	7	8	10	12	14
$\sigma^{(1)}$	Expt total	—	33(8)	35(8)	34(8)	37(8)	33(8)	—	47(9)	45(9)	—	—
	Expt elastic	—	11(3)	—	9(7)	10(7)	—	—	27(8)	—	—	—
	QCT total	76	66	56	54	51	50	50	49	44	37	31
	QCT elastic	19	16	15	15	15	16	18	20	22	21	20
	QM total	70	66	57	54	51	49	—	49	44	37	31
	QM elastic	6	15	14	14	15	15	—	20	21	21	19
	TSH2 total	69	63	56	53	58	50	52	51	47	40	34
	TSH2 elastic	18	16	15	14	18	17	19	20	22	22	21
	TSH3 total	65	58	54	50	51	51	—	51	—	—	—
	TSH3 elastic	18	15	14	15	15	17	—	21	—	—	—
$\sigma^{(2)}$	Expt total	—	41(2)	55(2)	59(5)	67(8)	78(8)	—	86(13)	88(6)	—	—
	Expt elastic	—	21(12)	—	32(12)	18(12)	—	—	45(15)	—	—	—
	QCT total	—	77	71	69	66	66	67	68	67	63	58
	QCT elastic	—	27	26	26	27	28	31	34	37	38	39
	QM total	—	76	70	68	65	65	—	68	67	63	58
	QM elastic	—	24	23	24	26	26	—	34	37	37	37
	TSH2 total	—	75	70	70	73	66	68	69	68	64	60
	TSH2 elastic	—	27	27	26	31	29	31	34	37	38	39
	TSH3 total	—	71	67	66	66	67	—	70	—	—	—
	TSH3 elastic	—	27	25	27	26	29	—	34	—	—	—

Table A.5: Cross sections for collisional disorientation ($\sigma^{(1)}/\text{Å}^2$) and disalignment ($\sigma^{(2)}/\text{Å}^2$) of OH(A) by Kr under thermal conditions, for f_2 ($N - S$) spin-rotation levels. The adiabatic QCT,[22] adiabatic QM[236] and surface-hopping QCT calculations ('TSH2' and 'TSH3' for two-state and three-state TSH respectively) were performed at a collision energy of 0.039 eV. The error bars (indicated in brackets on the experimental data) represent 95 % confidence limits (2 standard deviations).

Xe, $\sigma^{(2)}$		N									
		1	2	3	4	5	6	7	8	10	14
f_1	Expt total	47(7)	30(5)	44(11)	—	56(3)	—	62(9)	—	66(12)	—
	Expt elastic	31(4)	33(8)	—	—	—	—	—	—	35(6)	—
	QCT total	83	77	79	79	75	73	76	75	76	80
	QCT elastic	31	29	29	29	29	28	31	31	36	40
	TSH2 total	66	64	68	68	68	72	—	72	—	—
	TSH2 elastic	26	24	26	26	27	29	—	33	—	—
	TSH3 total	—	60	65	63	65	68	—	70	—	—
	TSH3 elastic	—	23	24	25	25	28	—	32	—	—
f_2	Expt total	—	42(12)	33(6)	49(6)	51(10)	57(8)	—	59(4)	64(6)	—
	Expt elastic	—	—	—	30(4)	33(5)	—	—	32(7)	29(8)	—
	QCT total	—	91	89	86	81	79	80	79	79	81
	QCT elastic	—	33	31	29	30	30	31	31	36	40
	TSH2 total	—	77	77	75	75	77	—	76	—	—
	TSH2 elastic	—	28	27	27	28	30	—	33	—	—
	TSH3 total	—	73	72	70	71	73	—	73	—	—
	TSH3 elastic	—	26	25	26	27	29	—	33	—	—

Table A.6: Cross sections for collisional disalignment ($\sigma^{(2)}/\text{Å}^2$) of OH(A) by Xe under thermal conditions, for f_1 ($N+S$) and f_2 ($N-S$) spin-rotation levels. The adiabatic QCT[237] and surface-hopping QCT calculations ('TSH2' and 'TSH3' for two-state and three-state TSH respectively) were performed at a collision energy of 0.039 eV. The error bars (indicated in brackets on the experimental data) represent 95 % confidence limits (2 standard deviations).

Appendix B

Tabulated results for OH(A, $v = 1$) + Kr

	σ / Å^2			
N	Quenching f_1	Quenching f_2	VET	RET
0	12.2(0.5)	—	0.6(0.2)	—
1	15.7(1.2)	—	0.5(0.2)	25.0(5.8)
2	16.6(1.4)	16.8(0.5)	0.4(0.4)	—
3	12.3(1.5)	—	0.3(0.2)	—
4	8.0(0.6)	9.6(1.1)	0.5(0.1)	34.2(4.3)
5	6.0(0.2)	—	—	—
6	—	3.1(0.6)	—	28.2(4.3)
7	5.1(0.9)	0.1(0.5)	0.3(0.1)	—
8	0.2(0.9)	—	—	23.2(1.3)
9	—	0.0(0.5)	—	—

Table B.1: Experimental results for OH(A, $v = 1$) + Kr under thermal conditions. Errors (in brackets) represent one standard deviation. Vibrational (VET) and rotational energy transfer (RET) are for f_1 ($N + S$) spin-rotation levels, electronic quenching as labelled.

Bibliography

[1] M. J. Pilling and P. W. Seakins, *Reaction Kinetics*, OUP, 1997.

[2] P. O. Wennberg, R. C. Cohen, N. L. Hazen, L. B. Lapsen, N. T. Allen, T. F. Hanisco, J. F. Oliver, N. W. Lanham, J. N. Demusz, and J. G. Anderson, *Rev. Sci. Instrum.*, **65**, 1858 (1994).

[3] D. R. Bates and M. Nicolet, *J. Geophys. Res.*, **106**, 1385 (1950).

[4] D. R. Crosley, *J. Atmos. Sci.*, **52**, 3299 (1995).

[5] S. A. Seamons *D. Phil. Thesis* PhD thesis, University of Oxford, (2014).

[6] K. Liu, R. G. MacDonald, and A. F. Wagner, *Int. Rev. Phys. Chem.*, **9**, 187 (1990).

[7] R. D. Levine, *Molecular Reaction Dynamics*, CUP, 2005.

[8] M. Brouard and C. Vallance (eds.), *Tutorials in Molecular Reaction Dynamics*, RSC, 2010.

[9] H. Eyring and M. Polanyi, *Z. Phys. Chem. Leipzig Abt. B*, **12**, 279 (1931).

[10] M. S. Child, *Molecular Collision Theory*, Dover, 1996.

[11] J. Kłos, M. H. Alexander, M. Brouard, C. J. Eyles, and F. J. Aoiz, *J. Chem. Phys.*, **129**, 054301 (2008).

[12] F. J. Aoiz, M. Brouard, C. J. Eyles, J. Kłos, and M. P. de Miranda, *J. Chem. Phys.*, **130**, 044305 (2009).

[13] M. Brouard, A. Bryant, Y.-P. Chang, R. Cireasa, C. J. Eyles, A. M. Green, S. Marinakis, F. J. Aoiz, and J. Kłos, *J. Chem. Phys.*, **130**, 044306 (2009).

[14] M. Brouard, H. Chadwick, Y.-P. Chang, R. Cireasa, and C. J. Eyles, *Physica Scripta*, **80**, 048120 (2009).

[15] M. Brouard, H. Chadwick, Y.-P. Chang, R. Cireasa, C. J. Eyles, A. O. La Via, N. Screen, F. J. Aoiz, and J. Kłos, *J. Chem. Phys.*, **131**, 104307 (2009).

[16] M.L. Costen, R. Livingstone, K.G. McKendrick, G. Paterson, M. Brouard, H. Chadwick, Y.-P. Chang, C. J. Eyles, F.J. Aoiz, and J. Kłos, *J. Phys. Chem. A*, **113**, 15156 (2009).

[17] Y.-P. Chang *Novel Probes of Angular Momentum Polarisation,* PhD thesis, University of Oxford, (2010).

[18] C. J. Eyles *An Experimental and Theoretical Study of the Dynamics of Atom-Molecule Scattering,* PhD thesis, University of Oxford, (2010).

[19] M. Brouard, H. Chadwick, C. J. Eyles, F. J. Aoiz, and J. Kłos, *J. Chem. Phys.*, **135**, 084305 (2011).

[20] M. Brouard, H. Chadwick, Y.-P. Chang, C. J. Eyles, F. J. Aoiz, and J. Kłos, *J. Chem. Phys.*, **135**, 084306 (2011).

[21] H. Chadwick, M. Brouard, Y.-P. Chang, C. J. Eyles, T. Perkins, S. A. Seamons, J. Kłos, M. H. Alexander, and F. J. Aoiz, *J. Chem. Phys.*, **137**, 154305 (2012).

[22] H. Chadwick *Angular Momentum Polarisation Effects in Inelastic Scattering,* PhD thesis, University of Oxford, (2012).

[23] H. Chadwick, M. Brouard, Y.-P. Chang, C. J. Eyles, G. McCrudden, T. Perkins, S. A. Seamons, J. Kłos, M. H. Alexander, P. J. Dagdigian, D. Herráez-Aguilar, and F. J. Aoiz, *J. Chem. Phys.*, **140**, 054306 (2014).

[24] H. Chadwick, M. Brouard, T. Perkins, and F. J. Aoiz, *Int. Rev. Phys. Chem.*, **33**, 79 (2014).

[25] G. Paterson, M. L. Costen, and K. G. McKendrick, *Mol. Phys.*, **109**, 2565 (2011).

[26] G. Paterson, M. L. Costen, and K. G. McKendrick, *Int. Rev. Phys. Chem.*, **31**, 69 (2012).

[27] B. L. Hemming, D. R. Crosley, J. E. Harrington, and V. Sick, *J. Chem. Phys*, **115**, 3099 (2001).

[28] J. H. Lehman, M. I. Lester, J. Kłos, M. H. Alexander, P. J. Dagdigian, D. Herráez-Aguilar, F. J. Aoiz, M. Brouard, H. Chadwick, T. Perkins, and S. A. Seamons, *J. Phys. Chem. A*, **117**, 13481 (2013).

[29] D. A. Case and D. R. Herschbach, *Mol. Phys.*, **30**, 1537 (1975).

[30] D. A. Case and D. R. Herschbach, *J. Chem. Phys*, **64**, 4212 (1976).

[31] D. A. Case, G. M. McClelland, and D. R. Herschbach, *Mol. Phys.*, **35**, 541 (1978).

[32] J. D. Barnwell, J. G. Loeser, and D. R. Herschbach, *J. Phys. Chem*, **87**, 2781 (1983).

[33] D. R. Herschbach, *Eur. Phys. J. D*, **38**, 3 (2006).

[34] D. R. Herschbach, *Angew. Chem. Int. Ed.*, **26**, 1223 (1987).

[35] M. Born and R. Oppenheimer, *Ann. Phys.*, **389**, 457 (1927).

[36] G. Herzberg and H. C. Longuet-Higgins, *Discuss. Faraday Soc.*, **35**, 77 (1963).

[37] H. C. Longuet-Higgins, *Proc. Roy. Soc. London Ser. A*, **344**, 147 (1975).

[38] D. R. Yarkony, *Rev. Mod. Phys.*, **68**, 985 (1996).

[39] G. A. Worth and L. S. Cederbaum, *Ann. Rev. Phys. Chem.*, **55**, 127 (2004).

[40] L. J. Butler, *Ann. Rev. Phys. Chem.*, **49**, 125 (1998).

[41] J. C. Tully, *J. Chem. Phys.*, **137**, 22A301 (2012).

[42] M. Beer and H. C. Longuet-Higgins, *J. Chem. Phys.*, **23**, 1390 (1955).

[43] M. J. Bearpark, F. Benardi, S. Clifford, M. Olivucci, M. A. Robb, B. R. Smith, and T. Vreven, *J. Am. Chem. Soc.*, **118**, 169 (1996).

[44] M. Garavelli, P. Celani, F. Benardi, M. A. Robb, and M. Olivucci, *J. Am. Chem. Soc.*, **119**, 6891 (1997).

[45] A. L. Sobolewski and W. Domcke, *Phys. Chem. Chem. Phys.*, **12**, 4897 (2010).

[46] C. E. Crespo-Hernández, B. Cohen, P. M. Hare, and B. Kohler, *Chem. Rev.*, **104**, 1977 (2004).

[47] S. Matsika and P. Krause, *Ann. Rev. Phys. Chem.*, **62**, 621 (2011).

[48] A. Wodtke, J. C. Tully, and D. J. Auerbach, *Int. Rev. Phys. Chem.*, **23**, 513 (2004).

[49] J. Kłos, F. J. Aoiz, J. E. Verdasco, M. Brouard, S. Marinakis, and S. Stolte, *J. Chem. Phys.*, **127**, 031102 (2007).

[50] F. J. Aoiz, J. E. Verdasco, M. Brouard, J. Kłos, S. Marinakis, and S. Stolte, *J. Phys. Chem. A*, **113**, 14636 (2009).

[51] C. J. Eyles, M. Brouard, C. H. Yang, J. Kłos, F. J. Aoiz, A. Gijsbertsen, A. E. Wiskerke, and S. Stolte, *Nature Chemistry*, **3**, 597 (2011).

[52] C. J. Eyles, M. Brouard, H. Chadwick, B. Hornung, B. Nichols, C. H. Yang, J. Kłos, F. J. Aoiz, A. Gijsbertsen, A. E. Wiskerke, and S. Stolte, *Phys. Chem. Chem. Phys.*, **14**, 5403 (2012).

[53] C. J. Eyles, M. Brouard, H. Chadwick, F. J. Aoiz, J. Kłos, A. Gijsbertsen, X. Zhang, and S. Stolte, *Phys. Chem. Chem. Phys.*, **14**, 5420 (2012).

[54] J. Kłos, F. J. Aoiz, M. Menéndez, M. Brouard, H. Chadwick, and C. J. Eyles, *J. Chem. Phys.*, **137**, 014312 (2012).

[55] M. Brouard, H. Chadwick, C. J. Eyles, B. Hornung, B. Nichols, F. J. Aoiz, P. G. Jambrina, S. Stolte, and M. P. de Miranda, *J. Chem. Phys.*, **138**, 104309 (2013).

[56] M. Brouard, H. Chadwick, C. J. Eyles, B. Hornung, B. Nichols, F. J. Aoiz, P. G. Jambrina, and S. Stolte, *J. Chem. Phys.*, **138**, 104310 (2013).

[57] M. Brouard, H. Chadwick, C. J. Eyles, B. Hornung, B. Nichols, J. M. Scott, F. J. Aoiz, J. Kłos, S. Stolte, and X. Zhang, *Mol. Phys.*, **111**, 1759 (2013).

[58] F. Filsinger, G. Meijer, H. Stapelfeldt, H. N. Chapman, and J. Küpper, *Phys. Chem. Chem. Phys.*, **13**, 2076 (2011).

[59] Y.-P. Chang, K. Długołecki, J. Küpper, D. Rösch, D. Wild, and S. Willitsch, *Science*, **342**, 98 (2013).

[60] M. C. Heaven, *Science*, **342**, 46 (2013).

[61] H. L. Bethlem, G. Berden, and G. Meijer, *Phys. Rev. Lett.*, **83**, 1558 (1999).

[62] H. L. Bethlem and G. Meijer, *Int. Rev. Phys. Chem.*, **22**, 73 (2003).

[63] N. Vanhaecke, U. Meier, M. Andrist, B. H. Meier, and F. Merkt, *Phys. Rev. A*, **75**, 031402 (2007).

[64] A. Trottier, D. Carty, and E. Wrede, *Mol. Phys.*, **109**, 725 (2011).

[65] W. G. Doherty, M. T. Bell, T. P. Softley, A. M. Rowland, E. Wrede, and D. Carty, *Phys. Chem. Chem. Phys.*, **13**, 8441 (2011).

[66] D. W. Chandler and P. L. Houston, *J. Chem. Phys.*, **87**, 1445 (1987).

[67] A. T. J. B. Eppink and D. H. Parker, *Rev. Sci. Instrum.*, **68**, 3477 (1997).

[68] A. M. Arthurs and A. Dalgarno, *Proc. Roy. Soc. London Ser. A*, **256**, 540 (1960).

[69] M. Karplus, R. N. Porter, and R. D. Sharma, *J. Chem. Phys.*, **43**, 3259 (1965).

[70] F. J. Aoiz, L. Bañares, and V. J. Herrero, *J. Chem. Soc. Faraday Trans.*, **94**, 2483 (1998).

[71] J. C. Tully In *Modern Methods for Multidimensional Dynamics Computations in Chemistry*, D. L. Thompson, Ed., World Scientific, 1998.

[72] N. Ananth, C. Venkataraman, and W. H. Miller, *J. Chem. Phys.*, **127**, 084114 (2007).

[73] R. Kapral and G. Ciccotti, *J. Chem. Phys.*, **110**, 8919 (1999).

[74] A. Kelly and T. E. Markland, *J. Chem. Phys.*, **139**, 014104 (2013).

[75] M. Ben-Nun and T. J. Martínez, *J. Chem. Phys.*, **108**, 7244 (1998).

[76] J. C. Burant and J. C. Tully, *J. Chem. Phys.*, **112**, 6097 (2000).

[77] N. Zamstein and D. J. Tannor, *J. Chem. Phys.*, **137**, 22A518 (2012).

[78] R. Marquardt, *ChemPhysChem*, **14**, 1350 (2013).

[79] R. B. Gerber, V. Buch, and M. A. Ratner, *J. Chem. Phys.*, **77**, 3022 (1982).

[80] D. A. Micha, *J. Chem. Phys.*, **78**, 7138 (1983).

[81] M. H. Beck, A. Jäckle, G. A. Worth, and H.-D. Meyer, *Phys. Rep.*, **324**, 1 (2000).

[82] J. C. Tully and R. K. Preston, *J. Chem. Phys.*, **55**, 562 (1971).

[83] J. C. Tully, *J. Chem. Phys.*, **93**, 1061 (1990).

[84] J. C. Tully, *Faraday Discuss.*, **110**, 407 (1998).

[85] G. Herzberg, *Spectra of Diatomic Molecules*, Van Nostrand, second ed., 1950.

[86] G. H. Dieke and H. M. Crosswhite, *J. Quant. Spec. Radiat. Trans.*, **2**, 97 (1961).

[87] T. Bergeman and R. N. Zare, *J. Chem. Phys.*, **61**, 4500 (1974).

[88] R. N. Zare, *Angular Momentum, Understanding Spatial Aspects in Chemistry and Physics*, John Wiley and Sons, 1988.

[89] M. H. Alexander, P. Andresen, R. Bacis, R. Bersohn, F. J. Comes, P. J. Dagdigian, R. N. Dixon, R. W. Field, G. W. Flynn, K.-H. Gericke, E. R. Grant, B. J. Howard, J. R. Huber, D. S. King, J. L. Kinsey, K. Kleinermanns, K. Kuchitsu, A. C. Luntz, A. J. McCaffery, B. Pouilly, H. Reisler, S. Rosenwaks, E. W. Rothe, M. Shapiro, J. P. Simons, R. Vasudev, J. R. Wiesenfeld, C. Wittig, and R. N. Zare, *J. Chem. Phys.*, **89**, 1749 (1988).

[90] J. Kłos, M. H. Alexander, M. Brouard, G. McCrudden, T. Perkins, F. J. Aoiz, and D. Herráez-Aguilar, *In preparation.*

[91] K. P. Huber and G. Herzberg, *Molecular Spectra and Molecular Structure: IV. Constants of Diatomic Molecules*, Van Nostrand Reinhold, 1979.

[92] A. Degli Esposti and H.-J. Werner, *J. Chem. Phys.*, **93**, 3351 (1990).

[93] C. C. Carter, H.-S. Lee, A. B. McCoy, and T. A. Miller, *J. Mol. Struct.*, **525**, 1 (2000).

[94] C. C. Carter, T. A. Miller, H. S. Lee, P. P. Korambath, A. B. McCoy, and E. F. Hayes, *J. Chem. Phys.*, **110**, 1508 (1999).

[95] S. L. Fei, X. N. Xheng, and M. C. Heaven, *J. Chem. Phys.*, **96**, 4821 (1992).

[96] G. W. Lemire and R. C. Sousa, *J. Phys. Chem.*, **96**, 4821 (1992).

[97] S. W. Benson, *J. Chem. Educ.*, **42**, 502 (1965).

[98] L. Lodi and J. Tennyson, *J. Phys. B*, **43**, 133001 (2010).

[99] S. R. Langhoff and E. R. Davidson, *Int. J. Quant. Chem.*, **8**, 61 (1974).

[100] J. J. Gilijamse, S. Hoekstra, S. Y. T. van der Meerakker, G. C. Groenenboom, and G. Meijer, *Science*, **313**, 1617 (2006).

[101] L. S. Cederbaum, *J. Chem. Phys.*, **138**, 224110 (2013).

[102] M. D. Hack and D. G. Truhlar, *J. Phys. Chem. A*, **104**, 7917 (2000).

[103] C. A. Mead and D. G. Truhlar, *J. Chem. Phys.*, **77**, 6090 (1982).

[104] H. S. W. Massey, *Rep. Prog. Phys.*, **12**, 248 (1948).

[105] C. Zener, *Proc. Roy. Soc. London Ser. A*, **137**, 696 (1932).

[106] C. Wittig, *J. Phys. Chem. B*, **109**, 8428 (2005).

[107] F. T. Smith, *Phys. Rev.*, **179**, 111 (1969).

[108] F. Rebentrost and W. A. Lester Jr., *J. Chem. Phys*, **64**, 3879 (1976).

[109] M. H. Alexander and G. C. Corey, *J. Chem. Phys.*, **84**, 100 (1986).

[110] R. Abrol and A. Kuppermann, *J. Chem. Phys.*, **116**, 1035 (2002).

[111] M. Brouard, G. McCrudden, T. Perkins, F. J. Aoiz, D. Herráez-Aguilar, and J. Kłos, *In preparation.*

[112] H.-J. Werner, B. Follmeg, and M. H. Alexander, *J. Chem. Phys.*, **89**, 3139 (1988).

[113] E. Teller, *J. Phys. Chem.*, **41**, 109 (1937).

[114] B. C. Hoffman and D. R. Yarkony, *J. Chem. Phys.*, **113**, 10091 (2000).

[115] P. A. Cleary, L. P. Dempsey, C. Murray, M. I. Lester, J. Kłos, and M. H. Alexander, *J. Chem. Phys.*, **126**, 204316 (2007).

[116] J. Dillon and D. R. Yarkony, *J. Chem. Phys.*, **139**, 064314 (2013).

[117] M. V. Berry and M. Wilkinson, *Proc. Roy. Soc. London Ser. A*, **392**, 15 (1984).

[118] M. V. Berry, *Proc. Roy. Soc. London Ser. A*, **392**, 45 (1984).

[119] C. A. Mead, *Rev. Mod. Phys.*, **64**, 51 (1992).

[120] J. C. Juanes-Marcos, S. C. Althorpe, and E. Wrede, *Science*, **309**, 1227 (2005).

[121] J. Jankunas, M. Sneha, R. N. Zare, F. Bouakline, and S. C. Althorpe, *J. Chem. Phys.*, **139**, 144316 (2013).

[122] G. Herzberg, *Electronic Spectra and Electronic Structure of Polyatomic Molecules*, Van Nostrand, second ed., 1966.

[123] P. W. Atkins, M. S. Child, and C. S. G. Phillips Tables for group theory Technical report, Oxford University Press, (2006).

[124] D. Poppe, D. Papierowska-Kaminski, and V. Bonačić-Koutecký, *J. Chem. Phys.*, **86**, 822 (1987).

[125] M. S. Child In *Atom-Molecule Collision Theory: A Guide for the Experimentalist*, R. B. Bernstein, Ed., Plenum, New York, 1979.

[126] H. Lefevbre-Brion and R. W. Field, *Perturbations in the Spectra of Diatomic Molecules*, Academic, New York, 1986.

[127] R. Renner, *Z. Phys.*, **92**, 172 (1934).

[128] J. A. Pople and H. C. Longuet-Higgins, *Mol. Phys.*, **1**, 372 (1958).

[129] J. F. M. Aarts, *Mol. Phys.*, **35**, 1785 (1978).

[130] E. M. Goldfield, S. K. Gray, and L. B. Harding, *J. Chem. Phys.*, **99**, 5812 (1993).

[131] F. Santoro, C. Petrongolo, and G. C. Schatz, *J. Phys. Chem. A*, **106**, 8276 (2002).

[132] M. N. R. Ashfold, J. M. Bayley, and R. N. Dixon, *Chem. Phys.*, **84**, 35 (1984).

[133] R. N. Dixon, *Mol. Phys*, **54**, 333 (1985).

[134] K. Yuan, R. N. Dixon, and X. Yang, *Acc. Chem. Res.*, **44**, 369 (2010).

[135] L. Zhou, B. Jiang, D. Xie, and H. Guo, *J. Phys. Chem. A*, **117**, 6940 (2013).

[136] R. N. Dixon, *J. Chem. Phys.*, **102**, 301 (1995).

[137] T. Suzuki, T. Ebata, M. Ito, and N. Mikami, *Chem. Phys. Lett.*, **116**, 268 (1985).

[138] J. Pearson, A. J. Orr-Ewing, M. N. R. Ashfold, and R. N. Dixon, *J. Chem. Phys*, **106**, 5850 (1997).

[139] P. Defazio, P. Gamallo, M. González, and C. Petrongolo, *J. Phys. Chem. A*, **114**, 9749 (2010).

[140] P. Defazio, B. Bussery-Honvault, P. Honvault, and C. Petrongolo, *J. Chem. Phys.*, **135**, 114308 (2011).

[141] K. Drukker and G. C. Schatz, *J. Chem. Phys.*, **111**, 2451 (1999).

[142] L. Adam, W. Hack, G. C. McBane, H. Zhu, Z.-W. Qu, and R. Schinke, *J. Chem. Phys.*, **126**, 034304 (2007).

[143] P. J. Dagdigian, Spin-orbit coupling matrix element for $^2\Sigma^+$-$^2\Pi$ collision-induced transitions Notes, 2012.

[144] P. J. Dagdigian, Spin-orbit coupling matrix elements involving OH states Notes, 2012.

[145] F. J. Aoiz, L. Bañares, T. Díez-Rojo, V. J. Herrero, and V. Sáez Rábanos, *J. Phys. Chem.*, **100**, 4071 (1996).

[146] P. W. Atkins and R. Friedman, *Molecular Quantum Mechanics*, Oxford University Press, 2005.

[147] K. Blum, *Density Matrix Theory and Applications*, Plenum Press, New York, 2000.

[148] G. M. McClelland and D. R. Herschbach, *J. Phys. Chem*, **83**, 1445 (1979).

[149] F. J. Aoiz, M. Brouard, and P. A. Enriquez, *J. Chem. Phys.*, **105**, 4964 (1996).

[150] M. P. de Miranda and F. J. Aoiz, *Phys. Rev. Lett.*, **93**, 083201 (2004).

[151] M. P. de Miranda, F. J. Aoiz, M. Brouard, and V. Sáez-Rábanos, *J. Chem. Phys.*, **121**, 4509 (2004).

[152] I. V. Hertel and W. Stoll, *Adv. At. Mol. Phys*, **13**, 113 (1978).

[153] B. Hornung *Investigation of Rotational Polarisation Effects in the Inelastic Collisions of NO(X) and Ar,* PhD thesis, University of Oxford, (2013).

[154] A. J. Orr-Ewing and R. N. Zare, *Ann. Rev. of Phys. Chem.*, **45**, 315 (1994).

[155] G. C. Corey, M. H. Alexander, and J. Schaefer, *J. Chem. Phys.*, **85**, 2726 (1986).

[156] M. H. Alexander and S. L. Davis, *J. Chem. Phys.*, **78**, 6754 (1983).

[157] G. C. Corey and F. R. McCourt, *J. Phys. Chem.*, **87**, 2723 (1983).

[158] G. C. Corey and A. D. Smith, *J. Chem. Phys.*, **83**, 5663 (1985).

[159] M. Auzinsh and R. Ferber, *Optical Polarization of Molecules*, Cambridge University Press, 1995.

[160] C. H. Greene and R. N. Zare, *J. Chem. Phys.*, **78**, 6741 (1983).

[161] R. B. Kurzel and J. I. Steinfeld, *J. Chem. Phys.*, **56**, 5188 (1972).

[162] R. E. Drullinger and R. N. Zare, *J. Chem. Phys.*, **59**, 4225 (1973).

[163] H. Kato, R. Clark, and A. J. McCaffery, *Mol. Phys.*, **31**, 943 (1976).

[164] R. Clark and A. J. McCaffery, *Mol. Phys.*, **35**, 617 (1977).

[165] S. R. Jeyes, A. J. McCaffery, and M. D. Rowe, *Mol. Phys.*, **36**, 1865 (1978).

[166] E. A. Brinkman and D. R. Crosley, *J. Phys. Chem. A*, **108**, 8084 (2004).

[167] W. Schade, J. Walewski, A. Offt, and A. Knaack, *Phys. Rev. A*, **53**, 53 (1996).

[168] C. D. Pibel and C. B. Moore, *J. Chem. Phys.*, **93**, 4804 (1990).

[169] R. W. Wood, *Philos. Mag.*, **16**, 184 (1908).

[170] R. G. Gordon, *J. Chem. Phys.*, **45**, 1643 (1966).

[171] K. Johnson, R. Pease, and J. P. Simons, *Mol. Phys.*, **52**, 955 (1984).

[172] H. Bitto and J. R. Huber, *Opt. Comm.*, **80**, 184 (1990).

[173] E. Hack and J. R. Huber, *Int. Rev. Phys. Chem.*, **10**, 287 (1991).

[174] R. T. Carter and J. R. Huber, *Chem. Soc. Rev.*, **29**, 305 (2000).

[175] P. J. Brucat and R. N. Zare, *J. Chem. Phys.*, **78**, 100 (1983).

[176] P. Dupré, P. G. Green, and R. W. Field, *Chem. Phys.*, **196**, 211 (1995).

[177] N. Hemmi and T. A. Cool, *J. Chem. Phys.*, **105**, 7964 (1996).

[178] J. Xin and S. A. Reid, *J. Chem. Phys.*, **112**, 10067 (2000).

[179] J. Xin, S. A. Reid, F. Santoro, and C. Petrongolo, *J. Chem. Phys.*, **115**, 8868 (2001).

[180] J. Xin and S. A. Reid, *J. Chem. Phys.*, **116**, 525 (2002).

[181] P. Schmidt, H. Bitto, and J. R. Huber, *J. Chem. Phys.*, **88**, 696 (1988).

[182] N. Ohta and T. Tanaka, *J. Chem. Phys.*, **99**, 3312 (1993).

[183] J. R. Brandenburger and B. R. Rose, *Opt. Comm.*, **36**, 453 (1981).

[184] M. Brouard, A. Bryant, I. Burak, F. Quadrini, I. Anton Garcia, and C. Vallance, *Mol. Phys.*, **103**, 1693 (2005).

[185] L. D. Snow, R. N. Compton, and J. C. Miller, *J. Chem. Phys.*, **88**, 1652 (1988).

[186] Ph. Bréchignac, A. Picard-Bersellini, and R. Charneau, *J. Phys. B.*, **13**, 135 (1980).

[187] S. J. Silvers, R. A. Gottscho, and R. W. Field, *J. Chem. Phys.*, **74**, 6000 (1991).

[188] G. O. Sitz and R. L. Farrow, *J. Chem. Phys.*, **101**, 4682 (1994).

[189] J. B. Halpern, R. Dopheide, and H. Zacharias, *J. Phys. Chem.*, **99**, 13611 (1995).

[190] A. D. Rudert, J. Martin, W.-B. Gao, J. B. Halpern, and H. Zacharias, *J. Chem. Phys.*, **111**, 9549 (1999).

[191] A. D. Rudert, J. Martin, W.-B. Gao, H. Zacharias, and J. B. Halpern, *J. Chem. Phys.*, **112**, 9749 (2000).

[192] N. C. M. Bartlett, D. J. Miller, R. N. Zare, A. J. Alexander, D. Sofikitis, and T. P. Rakitzis, *Phys. Chem. Chem. Phys.*, **11**, 142 (2009).

[193] S. Williams, L. A. Rahn, and R. N. Zare, *J. Chem. Phys.*, **104**, 3947 (1996).

[194] R. N. Zare, *Berichte der Bunsen-Gesellschaft*, **86**, 422 (1982).

[195] C. H. Townes and A. L. Schawlow, *Microwave Spectroscopy*, Dover, NY, 1975.

[196] H. Ring, R. T. Carter, and J. R. Huber, *Eur. Phys. J. D*, **4**, 73 (1998).

[197] P. J. Brucat and R. N. Zare, *J. Chem. Phys.*, **81**, 2562 (1984).

[198] G. J. Gemmen and N. Rouze, *Am. J. Phys.*, **64**, 147 (1996).

[199] B. L. Hemming and D. R. Crosley, *J. Phys. Chem. A*, **106**, 8992 (2002).

[200] N. Herath, S. C. Everhart, A. G. Suits, and O. S. Vasyutinskii, *J. Chem. Phys.*, **134**, 034311 (2011).

[201] Q. Li, R. T. Carter, and J. R. Huber, *Chem. Phys. Lett.*, **334**, 39 (2001).

[202] T. L. Myers, N. R. Forde, B. Hu, D. C. Kitchen, and L. J. Butler, *J. Chem. Phys.*, **107**, 5361 (1997).

[203] MKS Instruments, Gas Correction Factors for Thermal-based Mass Flow Controllers, 2013, `http://www.mksinst.com/docs/UR/MFCGasCorrection.aspx`.

[204] A. A. Turnipseed, G. L. Vaghjiani, J. E. Thompson, and A. R. Ravishankara, *J. Chem. Phys.*, **96**, 5887 (1992).

[205] F. Biaume, *J. Photochem.*, **2**, 139 (1973).

[206] J. R. Huber, *ChemPhysChem*, **5**, 1663 (2004).

[207] A. Jacobs, K. Kleinermanns, H. Kuge, and J. Wolfrum, *J. Chem. Phys.*, **79**, 3162 (1983).

[208] A. U. Grunewald, K. H. Gericke, and F. J. Comes, *Chem. Phys. Lett.*, **132**, 121 (1986).

[209] A. Jacobs, M. Wahl, R. Weller, and J. Wolfrum, *Appl. Phys. B*, **42**, 173 (1987).

[210] D. Case *Faraday Rotation Studies of Collisional Depolarization,* Master's thesis, University of Oxford, (2006).

[211] Lambda Physik GmbH LPD 3002 Manual, (1992).

[212] J. J. ter Meulen, W. A. Majewski, W. L. Meerts, and A. Dymanus, *Chem. Phys. Lett.*, **94**, 25 (1983).

[213] J. J. ter Meulen, W. Ubachs, and A. Dymanus, *Chem. Phys. Lett.*, **129**, 533 (1986).

[214] F. G. R. Quadrini *Dynamics of OH Generating Photochemical Reactions,* Master's thesis, University of Oxford, (2004).

[215] S. Marinakis, G. Paterson, G. Richmond, M. Rockingham, M. L. Costen, and K. G. McKendrick, *J. Chem. Phys.*, **128**, 021101 (2008).

[216] Magnetic Shields Ltd., 2013, `http://www.magneticshields.co.uk`.

[217] J. Luque and D. R. Crosley, *LIFBASE: Database and simulation program (v. 1.6).*, 1999.

[218] P. Lebow, F. Raab, and H. Metcalf, *Phys. Rev. Lett.*, **42**, 85 (1979).

[219] F. Raab, T. Bergman, D. Lieberman, and H. Metcalf, *Optics Lett.*, **5**, 427 (1980).

[220] F. Raab, T. Bergman, D. Lieberman, and H. Metcalf, *Phys. Rev. A*, **24**, 3120 (1981).

[221] J. Xin, I. Ionescu, D. Kuel, and S. A. Reid, *Chem. Phys.*, **291**, 61 (2003).

[222] S. D. Gatenby *A Stereodynamical Study of the H + N_2O Reaction,* PhD thesis, University of Oxford, (1999).

[223] A. M. Green *Zeeman Quantum Beat Spectroscopy as a Tool for Studies of Collisional Depolarisation,* Master's thesis, University of Oxford, (2007).

[224] R. K. Lengel and D. R. Crosley, *Chem. Phys. Lett.*, **32**, 261 (1975).

[225] R. K. Lengel and D. R. Crosley, *J. Chem. Phys.*, **67**, 2085 (1977).

[226] R. K. Lengel and D. R. Crosley, *J. Chem. Phys.*, **68**, 5309 (1977).

[227] J. Burris, J. J. Butler, T. J. McGee, and W. S. Heaps, *Chem. Phys.*, **124**, 251 (1988).

[228] J. O. Hirschfelder, H. Eyring, and B. Topley, *J. Chem. Phys.*, **4**, 170 (1936).

[229] A. Wheeler, B. Topley, and H. Eyring, *J. Chem. Phys.*, **4**, 178 (1936).

[230] M. Karplus, R. N. Porter, and R. D. Sharma, *J. Chem. Phys.*, **40**, 2033 (1964).

[231] F. J. Aoiz, V. J. Herrero, and V. Sáez Rábanos, *J. Chem. Phys.*, **94**, 7991 (1991).

[232] F. J. Aoiz, V. J. Herrero, and V. Sáez Rábanos, *J. Chem. Phys.*, **97**, 7423 (1992).

[233] F. J. Aoiz, L. Bañares, V. J. Herrero, V. Sáez Rábanos, and L. Tanarro, *J. Phys. Chem. A*, **101**, 6165 (1997).

[234] P. Langevin, *Ann. Chim. Phys.*, **5**, 245 (1905).

[235] G. McCrudden and D. Herráez-Aguilar, 2013.

[236] J. Kłos, 2012.

[237] G. McCrudden *Non-adiabatic effects on the Collision Dynamics of OH(A),* Master's thesis, University of Oxford, (2013).

[238] HIBRIDON is a package of programs for the time-independent quantum treatment of inelastic collisions and photodissociation written by M. H. Alexander, D. Manolopoulos, H.-J. Werner, and B. Follmeg, with contributions by P. F. Vohralik, D. Lemoine, G. Corey, R. Gordon, B. Johnson, T. Orlikowski, A. Berning, A. Degli-Esposti, C. Rist, P. Dagdigian, B. Pouilly, G. van der Sanden, M. Yang, F. de Weerd, S. Gregurick, and J. Klos.

[239] D. E. Manolopoulos, *J. Chem. Phys.*, **85**, 6425 (1986).

[240] M. H. Alexander and D. E. Manolopoulos, *J. Chem. Phys.*, **86**, 2044 (1987).

[241] J. E. Subotnik, W. Ouyang, and B. R. Landry, *J. Chem. Phys.*, **139**, 214107 (2013).

[242] N. Shenvi, J. E. Subotnik, and W. Yang, *J. Chem. Phys.*, **135**, 024101 (2011).

[243] B. R. Landry, M. J. Falk, and J. E. Subotnik, *J. Chem. Phys.*, **139**, 211101 (2013).

[244] S. Y. Lin, H. Guo, B. Jiang, S. Zhou, and D. Xie, *J. Phys. Chem. A*, **114**, 9655 (2010).

[245] P. Archirel and P. Habitz, *Chem. Phys.*, **78**, 213 (1983).

[246] C. Petrongolo, *J. Chem. Phys.*, **89**, 1297 (1988).

[247] P. Defazio and C. Petrongolo, *J. Chem. Phys.*, **125**, 064308 (2006).

[248] P. Defazio and C. Petrongolo, *J. Chem. Phys.*, **127**, 204311 (2007).

[249] P. Gamallo, P. Defazio, M. González, and C. Petrongolo, *J. Chem. Phys.*, **129**, 244307 (2008).

[250] P. Defazio, P. Gamallo, and C. Petrongolo, *J. Chem. Phys.*, **136**, 054308 (2012).

[251] S. Yu. Grebenshchikov, *J. Chem. Phys.*, **138**, 224107 (2013).

[252] P. Gamallo, S. Akpinar, P. Defazio, and C. Petrongolo, *J. Chem. Phys.*, **139**, 094303 (2013).

[253] L. Zhou, G.-S.-M. Lin, and D. Xie, *J. Chem. Phys.*, **139**, 114303 (2013).

[254] J. Weiß, R. Schinke, and V. A. Mandelshtam, *J. Chem. Phys.*, **113**, 4588 (2000).

[255] M. Baer, *Phys. Rep.*, **358**, 75 (2002).

[256] B. Sarkar and S. Adhikari, *J. Chem. Phys.*, **124**, 074101 (2006).

[257] M. H. Alexander, *Chem. Phys.*, **92**, 337 (1985).

[258] D. Herráez-Aguilar, 2014.

[259] J. Tennyson and B. T. Sutcliffe, *J. Mol. Spec.*, **101**, 71 (1983).

[260] H. Akima, *Comm. ACM*, **17**, 18 (1974).

[261] M. H. Alexander and P. J. Dagdigian, *J. Chem. Phys.*, **80**, 4325 (1984).

[262] E. Fabiano, T. W. Keal, and W. Thiel, *Chem. Phys.*, **349**, 334 (2008).

[263] M. F. Herman, *J. Chem. Phys.*, **81**, 754 (1984).

[264] A. W. Jasper, S. N. Stechmann, and D. G. Truhlar, *J. Chem. Phys.*, **116**, 5424 (2002).

[265] A. W. Jasper, S. N. Stechmann, and D. G. Truhlar, *J. Chem. Phys.*, **117**, 10427 (2002).

[266] D. Herráez-Aguilar, 2012.

[267] R. T. Pack, *J. Chem. Phys.*, **60**, 633 (1974).

[268] J. H. Lehman and M. I. Lester, *Ann. Rev. Phys. Chem.*, **65**, 537 (2014).

[269] L. P. Dempsey, C. Murray, P. A. Cleary, and M. I. Lester, *Phys. Chem. Chem. Phys.*, **10**, 1424 (2008).

[270] L. P. Dempsey, T. D. Sechler, C. Murray, M. I. Lester, and S. Matsika, *J. Chem. Phys.*, **130**, 104307 (2009).

[271] L. P. Dempsey, T. D. Sechler, C. Murray, and M. I. Lester, *J. Phys. Chem. A*, **113**, 6851 (2009).

[272] J. H. Lehman, L. P. Dempsey, M. I. Lester, B. Fu, E. Kamarchik, and J. M. Bowman, *J. Chem. Phys*, **133**, 164307 (2010).

[273] K. H. Becker, D. Haaks, and T. Tatarczyk, *Chem. Phys. Lett.*, **25**, 564 (1976).

[274] P. H. Paul, *J. Quant. Spec. Radiat. Transf.*, **51**, 511 (1994).

[275] N. J. Turro, V. Ramamurthy, and J. C. Scaiano, *Principles of molecular photochemistry: an introduction*, University Science Books, 2009.

[276] G. Paterson, S. Marinakis, J. Kłos, M. L. Costen, and K. G. McKendrick, *Phys. Chem. Chem. Phys.*, **11**, 8804 (2009).

[277] P. Dagdigian and M. H. Alexander, *J. Chem. Phys*, **130**, 094303 (2009).

[278] P. Dagdigian and M. H. Alexander, *J. Chem. Phys*, **130**, 164315 (2009).

[279] M. H. Alexander, *J. Chem. Phys.*, **76**, 3637 (1982).

[280] P. Dagdigian and M. H. Alexander, *J. Chem. Phys*, **130**, 204304 (2009).

[281] P. H. Paul, *J. Phys. Chem.*, **99**, 8472 (1995).

[282] R. A. Copeland, M. J. Dyer, and D. R. Crosley, *J. Chem. Phys.*, **82**, 4022 (1985).

[283] K. R. German, *J. Chem. Phys.*, **64**, 4065 (1976).

[284] J. Kłos, *OH(A) + Ar 3D potential energy surface*, 2008.

[285] Y. Sumiyoshi, I. Funahara, K. Sato, Y. Ohshima, and Y. Endo, *Mol. Phys.*, **17**, 2207 (2010).

[286] L. R. Williams and D. R. Crosley, *J. Chem. Phys.*, **104**, 6507 (1996).

[287] P. Ehrenfest, *Konink. Ned. Akad. Wetenschap. Proc.*, **16**, 591 (1914).

[288] E. E. Nikitin and J. Troe, *Phys. Chem. Chem. Phys.*, **10**, 1483 (2008).

[289] L. D. Landau and E. Teller, *Phys. Z. Sow. Un.*, **10**, 34 (1936).

[290] J. J. Kay, G. Paterson, M. L. Costen, K. E. Strecker, K. G. McKendrick, and D. W. Chandler, *J. Chem. Phys.*, **134**, 091101 (2011).

[291] J. J. Kay, J. D. Steill, J. Kłos, G. Paterson, M. L. Costen, K. E. Strecker, K. G. McKendrick, M. H. Alexander, and D. W. Chandler, *Mol. Phys.*, **110**, 1693 (2012).

[292] J. D. Steill, J. J. Kay, G. Paterson, T. R. Sharples, J. Kłos, M. L. Costen, K. E. Strecker, K. G. McKendrick, M. H. Alexander, and D. W. Chandler, *J. Phys. Chem. A*, **117**, 8163 (2013).

[293] D. T. Anderson, M. W. Todd, and M. I. Lester, *J. Chem. Phys.*, **110**, 11117 (1999).

[294] B. R. Strazisar, C. Lin, and H. F. Davis, *Science*, **290**, 958 (2000).

[295] M. W. Todd, D. T. Anderson, and M. I. Lester, *J. Phys. Chem. A*, **105**, 10031 (2001).

[296] M. Ortiz-Suárez, M. F. Witinski, and H. F. Davis, *J. Chem. Phys.*, **124**, 201106 (2006).

[297] J. H. Lehman, J. L. Bertrand, T. A. Stephenson, and M. I. Lester, *J. Chem. Phys.*, **135**, 144303 (2011).

[298] S. Liu, C. Xiao, T. Wang, J. Chen, T. Yang, X. Xu, D. H. Zhang, and X. Yang, *Faraday Discuss.*, **157**, 101 (2012).

[299] E. Kamarchik, B. Fu, and J. M. Bowman, *J. Chem. Phys.*, **132**, 091102 (2010).

[300] P.-Y. Zhang, R.-F. Lu, T.-S. Chu, and K.-L. Han, *J. Chem. Phys.*, **133**, 174316 (2010).

[301] P.-Y. Zhang, R.-F. Lu, T.-S. Chu, and K.-L. Han, *J. Phys. Chem. A*, **114**, 6565 (2010).

[302] O. Tishchenko and D. G. Truhlar, *J. Chem. Phys.*, **132**, 084109 (2010).

[303] M. A. Collins, O. Godsi, S. Liu, and D. H. Zhang, *J. Chem. Phys.*, **135**, 234307 (2011).

[304] J. M. Bowman, G. Csakó, and B. Fu, *Phys. Chem. Chem. Phys.*, **13**, 8094 (2011).

[305] R. Conte, B. Fu, E. Kamarchik, and J. M. Bowman, *J. Chem. Phys.*, **139**, 044104 (2013).

[306] L. P. Dempsey, C. Murray, and M. I. Lester, *J. Chem. Phys.*, **127**, 151101 (2007).

[307] W. B. Neilsen and R. G. Gordon, *J. Chem. Phys.*, **58**, 4131 (1973).

[308] J. Boissoles, C. Boulet, and D. Robert, *Chem. Phys. Lett.*, **122**, 237 (1985).

[309] S. Stenholm, *Phys. Rev. A*, **47**, 2523 (1993).

[310] E. Gindensperger, C. Meier, and J. A. Beswick, *J. Chem. Phys.*, **113**, 9369 (2000).

[311] L. Bonnet, *Int. Rev. Phys. Chem.*, **32**, 171 (2013).